MULTISCALE MODELING AND SIMULATIONS OF POLYELECTROLYTE MULTILAYERS AND POLYELECTROLYTE COMPLEXES

A THESIS SUBMITTED TO
THE GRADUATE SCHOOL OF NATURAL AND APPLIED SCIENCES
OF
MIDDLE EAST TECHNICAL UNIVERSITY

BY

ERHAN ÖZDEMİR

IN PARTIAL FULFILLMENT OF THE REQUIREMENTS
FOR
THE DEGREE OF DOCTOR OF PHILOSOPHY
IN
CHEMISTRY

SEPTEMBER 2023

Approval of the thesis:

MULTISCALE MODELING AND SIMULATIONS OF POLYELECTROLYTE MULTILAYERS AND POLYELECTROLYTE COMPLEXES

submitted by **ERHAN ÖZDEMİR** in partial fulfillment of the requirements for the degree of **Doctor of Philosophy** i**n Chemistry, Middle East Technical University** by,

Prof. Dr. Halil Kalıpçılar
Dean, Graduate School of **Natural and Applied Sciences** _____

Prof. Dr. Özdemir Doğan
Head of the Department, **Chemistry** _____

Prof. Dr. Gülay Ertaş
Supervisor, **Chemistry, METU** _____

Assist. Prof. Dr. Erol Yıldırım
Co-Supervisor, **Chemistry, METU** _____

Examining Committee Members:

Prof. Dr. İrem Erel Göktepe
Chemistry, METU _____

Prof. Dr. Gülay Ertaş
Chemistry, METU _____

Prof. Dr. Nuran Elmacı Irmak
Chemistry, İzmir Institute of Technology (IZTECH) _____

Prof. Dr. Emine Esra Kasapbaşı
MB and Genetics, Haliç University _____

Assoc. Prof. Dr. Hande Toffoli
Physics, METU _____

Date: 11.09.2023

I hereby declare that all information in this document has been obtained and presented in accordance with academic rules and ethical conduct. I also declare that, as required by these rules and conduct, I have fully cited and referenced all material and results that are not original to this work.

Name Last name : Erhan Özdemir

Signature :

ABSTRACT

MULTISCALE MODELING AND SIMULATIONS OF POLYELECTROLYTE MULTILAYERS AND POLYELECTROLYTE COMPLEXES

Özdemir, Erhan
Doctor of Philosophy, Chemistry
Supervisor: Prof. Dr. Gülay Ertaş
Co-Supervisor: Assist. Prof. Dr. Erol Yıldırım

September 2023, 205 pages

Polyelectrolytes are a unique class of polymers that can bear ionizable groups and, hence, can dissociate into ions when dissolved in a solvent, typically water. Polyelectrolytes can exhibit self-assembly behaviors, leading to many nanostructures, such as micelles and hollow spheres, that can be used in diverse applications like drug delivery, sensors, electronics and smart coatings. Layer-by-layer (LbL) assembly can also be used to prepare materials with tuned shapes or properties specific to the desired application.

The significance of polyelectrolytes is vast, as they find applications in numerous fields. Hence, understanding polyelectrolytes at the molecular level is essential for their practical applications. Taking a broad view, the advantages of computational methods at different scales were combined to understand better the role of PEs in three different applications at the molecular level in this thesis study.

In the first part of this thesis, modeling and simulation of polyelectrolyte multilayers with all-atom (AA) and coarse-grained (CG) molecular dynamics (MD) simulations were performed for operating as a substrate in Surface Enhanced Raman

Spectroscopy (SERS) applications. It was demonstrated that the structure parameters of these polyelectrolyte multilayers (PEMs), the type of the polyelectrolyte and the number of layers affect the mobility of the nanoparticles used in SERS substrates and distribution of analyte on the surface. This makes PEMs convenient for preparing optimum substrates by tuning the surface morphology.

In the second part, the effect of acid and solvent treatment on PEDOT:PSS was studied by first principle methods and MD simulations. The major finding in this part was the perfectly uniform distribution of HSO_4^- anions as a dopant in PEDOT crystalline structures in charge of the conductivity enhancement. In addition, insulating layers of PSS-H and PSS-Na can be washed away with the solvent, leading to an increase in electrical conductivity.

In the last application, insoluble deposit formation in lubricant oil was modeled for the first time in the literature. Interactions between the constituents of the deposit model, detergent and dispersant were calculated by first principle calculations, and AA and CG MD simulations unraveled the role of detergents and dispersants in the deposit formation control.

Keywords: Polyelectrolytes, Molecular Dynamics Simulations, Surface Enhanced Raman Spectroscopy, Electrical Conductivity, Lubricant Oil Additives

ÖZ

ÇOK KATMANLI POLİELEKTROLİTLER VE POLİELEKTROLİT KOMPLEKSLERİN ÇOK ÖLÇEKLİ MODELLEME VE SİMULASYONLARI

Özdemir, Erhan
Doktora, Kimya
Tez Yöneticisi: Prof. Dr. Gülay Ertaş
Ortak Tez Yöneticisi: Dr. Öğr. Üyesi Erol Yıldırım

Eylül 2023, 205 sayfa

Polielektrolitler (PE'ler), iyonlaşabilen fonksiyonel gruplar içeren ve bir çözücü içerisinde iyonlaşabilen bir polimer çeşididir. Polielektrolitler, miseller ve boş küreler gibi nanoyapılarda kendiliğinden bir araya gelme davranışları sergileyebilir ve bu yapılar ilaç salımı, sensörler, elektronikler ve akıllı kaplamalar gibi çeşitli uygulamalarda kullanılmaktadır. Katman katman kaplama (LbL) tekniği ile PE'ler kullanılarak farklı uygulama alanları için istenen şekil ve özellikte malzemelerin üretimi de mümkündür.

Polielektrolitler birçok farklı alanda kullanılmaları bakımından önem arz etmektedir. Bu nedenle, polielektrolitlerin moleküler seviyedeki davranışlarının anlaşılması, pratikteki uygulamaları için önemlidir. Bu tez çalışmasında geniş bir bakış açısıyla, farklı ölçeklerdeki hesaplamalı yöntemlerin avantajları, moleküler seviyede üç farklı uygulamada polielektrolitlerin rolünün daha iyi anlaşılması için bir arada kullanıldı.

Tezin ilk bölümünde, tüm atomlu (AA) ve kaba taneli (CG) moleküler dinamik (MD) simülasyonları kullanılarak ile Yüzeyde Güçlendirilmiş Raman Spektroskopisi (YGRS) uygulamalarında çok katmanlı polielektrolitler (PEM) alttaş olarak

kullanılmak üzere modellendi. Bu PEM'lerin, yapısal özellikleri, polielektrolitin türü ve katman sayısının YGRS alttaşlarında kullanılan analit moleküllerin dağılımı ve nanoparçacıkların hareketliliği üzerinde etkili olduğu gösterildi. Bu durum uygun alttaşın hazırlanması amacıyla yüzey morfolojisini ayarlanak için PEM'lerin uygun adaylar olduğunu göstermektedir.

İkinci bölümde, PEDOT:PSS'in iletkenliğine asit ve çözücünün etkisi temel ilke hesaplamaları ve MD simülasyonları ile çalışıldı. Bu bölümdeki en önemli bulgu, PEDOT kristal yapılarda katkı olarak kullanılan HSO_4^- anyonlarının PEDOT zindirleri arasına kusursuz bir şekilde dağılımıdır ki bu, iletkenliği artıran bir parametre olabilir. Bununla birlikte, iletkenliği artırabilecek etki bir mekanizması olarak, yalıtkan PSS-H ve PSS-Na tabakalarının çözücü tarafından uzaklaştırıldığı gösterilmiştir.

Son uygulamada, motor yağı ortamında tortu birikimi detaylı bir şekilde ve literatürde ilk defa modellenmiştir. Tortu modelinin bileşenleri arasındaki etkileşimler temel ilke hesaplamaları ile hesaplandı ve tortu oluşumunu kontrol etmede deterjan ve dispersanların tortu dağıtıcı rolü AA ve CG MD simülasyonları ile gösterildi.

Anahtar Kelimeler: Polielektrolit, Moleküler Dinamik Simülasyon, Yüzeyde Güçlendirilmiş Raman Spektroskopisi, Elektrik İletkenliği, Motor Yağı Katkı Maddeleri

To Sezin and our family

ACKNOWLEDGMENTS

I wish to express my deepest gratitude to my supervisor, Prof. Dr. Gülay Ertaş and co-supervisor Assist. Prof. Dr. Erol Yıldırım for their guidance, advice, criticism, encouragement and insight throughout the research.

I would also like to thank Prof. Dr. İrem Erel Göktepe and Assoc. Prof. Dr. Hande Toffoli for their valuable contributions and advice in thesis monitoring committee meetings and support throughout the thesis.

Many thanks to Prof. Dr. Nuran Elmacı Irmak and Prof. Dr. Emine Esra Kasapbaşı for their valuable comments and contributions to the thesis.

I thank my friends and lab mates, particularly Dr. Yeliz Akpınar, Canan Özkan and Begüm Avcı, for their moral and material support.

I want to thank my co-workers in TÜBİTAK, especially Nuri Özdemir and Dr. Eyüp Yalçınkaya, for their encouragement and motivation for the thesis studies.

Thanks to Dr. Anıl Ağıral from the Lubrizol™ Corporation, Jianyong Ouyang from the National University of Singapore, and Yang Shuo Wang from the Agency for Science, Technology and Research Singapore for their support.

Many thanks to The Lubrizol™ Corporation and METU TTO for the project collaboration and their financial support. This work is partially funded by METU BAP under grant number GAP-103-2021-10774.

Computing resources were provided by the National Center for High-Performance Computing of Turkey (UHeM) under grant number 1008192020 and TÜBITAK ULAKBİM, High Performance and Grid Computing Center (TRUBA).

Finally, yet most importantly, I want to thank my wife, Sezin Özdemir, for advice, tutoring, encouragement and support. Many thanks to the unborn baby for her understanding and harmony in the last periods of the thesis studies.

TABLE OF CONTENTS

ABSTRACT v

ÖZ vii

ACKNOWLEDGMENTS x

TABLE OF CONTENTS xi

LIST OF TABLES xiv

LIST OF FIGURES xv

LIST OF ABBREVIATIONS xxvi

CHAPTERS

1 INTRODUCTION 1

1.1 Computational Methodology 1

1.1.1 Multiscale Modeling 1

1.1.2 First Principle (*ab initio*) Quantum Chemical Methods 2

1.1.3 Density Functional Theory 3

1.1.4 Molecular Dynamics Simulations 4

1.2 Polyelectrolytes 22

1.2.1 Polyelectrolyte Complexes 23

1.2.2 Deposition of Polyelectrolytes on a Surface 24

1.2.3 Layer-by-Layer Assembly 25

1.2.4 Polyelectrolyte Multilayers 26

1.3 Raman Spectroscopy 28

1.3.1 Surface Enhanced Raman Spectroscopy (SERS) 30
1.4 Conducting Polymers 35
1.4.1 Poly(3,4-ethylenedioxythiophene) polystyrene sulfonate (PEDOT:PSS) 37
1.5 Mechanism of Aggregation Control by Detergent and Dispersants 44
1.5.1 Soot and Sludge Formation in Engines 44
1.5.2 Lubricants 45
2 INVESTIGATION OF POLYELECTROLYTE MULTILAYERS FOR SURFACE ENHANCED RAMAN SPECTROSCOPY (SERS) 51
2.1 Computational Methods 51
2.1.1 Aim of the Study 51
2.1.2 Model Preparation 53
2.2 Results and Discussion 63
2.2.1 All-Atom MD Simulations 63
2.2.2 Coarse-Grained MD Simulations 66
3 ELECTRICAL CONDUCTIVITY ENHANCEMENT MECHANISM OF ACID AND SOLVENT TREATED PEDOT:PSS 85
3.1 Aim of the Study 85
3.2 Computational Methods 86
3.2.1 First Principle Calculations 86
3.2.2 All-Atom MD Simulations 88
3.3 Results and Discussion 94
3.3.1 Molecular and Electronic Structure of PEDOT 94
3.3.2 All-Atom MD Simulations 105

4 MECHANISM OF AGGREGATION CONTROL BY DETERGENT AND DISPERSANT IN ENGINE OIL 125
4.1 Aim of the Study 125
4.2 Computational Methods 126
4.2.1 First Principle Calculations 126
4.2.2 All-Atom MD Simulations 126
4.2.3 Coarse-Grained MD Simulations 132
4.3 Results and Discussion 139
4.3.1 First Principle Calculations 139
4.3.2 All-Atom MD Simulations 144
4.3.3 Coarse-Grained MD Simulations 151
5 CONCLUSION 175
5.1 Investigation of Polyelectrolyte Multilayers for SERS 176
5.2 Electrical Conductivity Enhancement Mechanism of Acid and Solvent Treated PEDOT:PSS 177
5.3 Mechanism of Aggregation Control by Detergent and Dispersant in Engine Oil 178
5.4 Outlook and Future Perspective 179
REFERENCES 181
CURRICULUM VITAE 205

LIST OF TABLES

Table 1.1 Type of Martini Beads in Martini 2.0 Force Field [31] 15
Table 3.1. Number of HSO_4^- and H_2O, and density of simulation cells prepared for all-atom MD simulations of PSS and PEDOT. 90
Table 3.2. Concentration, number of chains and charges of PEDOT and PSS added to the simulation cell. 93
Table 3.3.Interaction energies calculated for possible interactions in A-PEDOT-PSS and AB-PEDOT-PSS..... 101
Table 4.1 Types of beads and their mean distances from the origin of the insoluble deposit model prepared in this study. 133
Table 4.2 Distance from the center of the insoluble deposit model and corresponding number of beads in the insoluble deposit model. 134
Table 4.3. Interaction energies for all possible interactions of sulfonate detergent units with other constituents. 141
Table 4.4. Interaction energies for all possible interactions of dispersant units with other constituents. 143

LIST OF FIGURES

Figure 1.1. Different approaches in multiscale modeling based on time and distance scale. 2
Figure 1.2. Procedure of MD simulations[25]. 6
Figure 1.3. Polyanion (red) and polycation (blue) in a polyelectrolyte multilayer (PEM) model from the final snapshot of coarse-grained MD simulations in this study. 27
Figure 1.4. Structure of PEDOT with a total of +1 charge carried in 3 EDOT monomers (top) and styrene sulfonate monomer of PSS having -1 charge (bottom x) and protonated styrene sulfonate monomer (bottom y). 38
Figure 2.1. Gold nanoparticles with 10.0 nm (left) and 5.0 nm (right) diameter consisted of 30920 and 3925 Au atoms, respectively. 55
Figure 2.2. Mapping of one sodium citrate structure into Martini force field. 56
Figure 2.3. One PAH_{20} chain prepared for simulations in LAMMPS, visualized with VMD. 56
Figure 2.4. One PAA_{20} chain prepared for simulations in LAMMPS, visualized with VMD. 57
Figure 2.5. AuNP capped with citrate, together with PAA-PAH (linear) layer. ... 57
Figure 2.6. AuNP capped with citrate, together with PAA-PAH (exponential) layer. 58
Figure 2.7. CG model of AuNP capped with citrate, together with PAH/PAA (linear growth) multilayer. 59
Figure 2.8. CG model of AuNP capped with citrate, together with PAA-PAH (exponential growth) multilayer. 60
Figure 2.9. Mapping of crystal violet and Cl^- anion (left) and initial structure of PAH/PAA-AuNP with crystal violet (right). 61
Figure 2.10. Mapping scheme of tannic acid molecule. 62
Figure 2.11. Initial structure of PAH/TA-AuNP with Crystal Violet. 63

Figure 2.12. RMSD vs time plot for AuNP with linear PAH/PAA layer (red), AuNP with exponential PAH/PAA layer (green). 64
Figure 2.13. RMSF values of Au atoms for linear PAH/PAA layer (red), AuNP with exponential PAH/PAA layer (green). 65
Figure 2.14. AuNP capped with citrate, together with linear (left) and exponentially (right) grown PAA-PAH multilayer after 2.0 ns. 66
Figure 2.15. RMSD vs time plot for AuNP with linear growth PAH/PAA layer (red), AuNP with exponential growth PAH/PAA layer (green). 67
Figure 2.16. RMSF values of Au atoms with CG linear (red) and exponential PAH/PAA layer (green) 68
Figure 2.17. Final snapshot of coarse-grained AuNP capped with citrate, together with linear growth PAH/PAA (left) and exponential growth PAH/PAA (right) layer. 69
Figure 2.18. Initial simulation cell containing PAH/PAA multilayer and citrate-capped AuNP with crystal violet. Initial AuNP distances with respect to each other were 20, 40, 70 and 100 Å, respectively. 70
Figure 2.19. Final structures of PAH/PAA-AuNP with crystal violet molecules. AuNP distances with respect to each other were a) 20, b) 40, c) 70 and d) 100 Å, respectively. 71
Figure 2.20. Top view of final structures of PAH/PAA-AuNP with crystal violet molecules. AuNP distances with respect to each other were a) 20, b) 40, c) 70 and d) 100 Å, respectively. 71
Figure 2.21. RDF analysis of Au atoms with N_a beads (containing N atoms without a charge) and with Q_0 beads (containing N atoms with a positive charge) of crystal violet. 72
Figure 2.22. Final structure of PAH/TA-AuNP (top) and PAH/PAA-AuNP (bottom) with crystal violet (side and top views). AuNP distances with respect to each other were 100 Å. 73
Figure 2.23. Final structure of PAH/PAA (left) and PAH/TA (right) used in the simulations. One bilayer is highlighted in each cases. 74

Figure 2.24. Distance between the Au atoms of AuNP in the center with those of the other two AuNPs in PAH/PAA-AuNP (green) and PAH/TA-AuNP (red) cases... 75
Figure 2.25. RDF analysis of Au atoms with N_a beads (representing dimethyl amine group of CV) and with Q_0 beads (representing the dimethyl ammonium) of crystal violet. 76
Figure 2.26. RDF of AuNPs with crystal violet on PAH/TA (purple) and PAH/PAA (yellow) multilayers. 77
Figure 2.27. RDF analysis of charged beads of crystal violet-citrate in PAH/TA-AuNP (red) and PAH/PAA-AuNP (green). 78
Figure 2.28. RMSD vs time graph for AuNP with 3 bilayers of PAH/PAA (red) and 3 (green), 6 (purple) and 9 (yellow) bilayers of PAH/TA. 79
Figure 2.29. RDF analysis of the Au atoms of AuNP in the center with those of other two AuNPs on 3 (red), 6 (green) and 9 (violet) layers of PAH/TA. 80
Figure 2.30. Final structure of PAH/TA-AuNP with Crystal Violet for 3, 6 and 9 layers of PAH/TA (side and top views). AuNP distances with respect to each other was 100 Å initially. 81
Figure 2.31. RDF analysis of AuNP and crystal violet on 3 (red and yellow), 6 (green and blue) and 9 (purple and black) bilayers of PAH/TA. 82
Figure 2.32. RDF analysis of charged beads of crystal violet and charged beads of citrate in the cell containing 3 (red), 6 (green) and 9 (violet) bilayers of PAH/TA 82
Figure 2.33. RDF analysis of crystal violet and tannic acid (at the uppermost layer) in the cell containing 3 bilayers of PAH/PAA (blue) and 3, 6 (green) and 9 (violet) bilayers of PAH/TA. 84
Figure 3.1. Initial positions of HSO_4^- determined for the interactions of $PEDOT^-$ HSO_4^- using Monte Carlo methods. 87
Figure 3.2. End group protonated $EDOT_6$ structure prepared for this study. 88
Figure 3.3. Initial structures of one SS_8 and two $EDOT_4$ (left), those with H_2O in between (center) and Na^+ in between respectively (right). Total charge of the system in each case is zero. 88

Figure 3.4. a) Initial configuration of PEDOT:PSS in the simulation cell. b) $PEDOT_{12}$ chain containing +4 charge. c) PSS_{24} chain containing -4 charge. 89
Figure 3.5. Initial structure of PEDOT:PSS simulation cell, top view (left) and side view (right) 91
Figure 3.6. Modeling steps for PEDOT a) calculation of monomer atomic charges and structure, b) construction of unit cell, c) building a supercell. 92
Figure 3.7. Initial cell for all-atom MD simulations containing different sizes and charges of PEDOT and PSS chains and H_3O^+, Na^+, H_2O and DMSO. 94
Figure 3.8. ESP for a) $PEDOT_3$, b) $PEDOT_6$, c) $PEDOT_9$. d) Band gap for these structures.....95
Figure 3.9. HOMO, HOMO-1, LUMO, LUMO+1 orbitals for $PEDOT_6$. 96
Figure 3.10. Band gap for $PEDOT_6$, $PEDOT_6^{2+}$ biradical polaron ($PEDOT_6$c-P) and $PEDOT_6^{2+}$ bipolaron structures (PEDOT6c-B).....97
Figure 3.11. a) Structure for the calculations of end group protonated $PEDOT_6$ ($PEDOT_6$-H^+), b) band gap for $PEDOT_3$, $PEDOT_6$ and $PEDOT_9$ with and without end group protonation.....98
Figure 3.12. Backbone monomer (C-C bond) distances (in Å) for a) neutral $PEDOT_6$, b) $PEDOT_6^{2+}$ bipolaron, c) end group protonated $PEDOT_6$-H^+. 99
Figure 3.13. Geometry optimized lowest energy structures for a) $PEDOT_6$-$2HSO_4^-$, b) $PEDOT_6^{2+}$-$2HSO_4^-$, c-d) $PEDOT_6^{2+}$-$2OH^-$, e) $PEDOT_6$-$2OH^-$, f) Na^+-HSO_4^- interactions. 100
Figure 3.14. Geometry optimized lowest energy structures for a) $EDOT_3$-SS_3 b) $EDOT_3^+$-SS_3^-, interactions. Distances between the H atoms of EDOT and O atoms of SS are given in the figures in Å unit. 101
Figure 3.15. PEDOT:PSS where four PEDOT and four PSS are charged. Distances between the atoms of PEDOT and PSS are given in Å unit.....102
Figure 3.16. PEDOT: PSS where some of the PSSH units are coordinated by water molecules (PSSH-w). Distances between the atoms of PEDOT, H_2O and PSS are given in Å unit. 103

Figure 3.17. PEDOT: PSS where some of the PSS^- units are coordinated by Na^+ cations (PSS^--Na^+). Distances between the atoms of PEDOT, Na and PSS are given in Å unit. 104
Figure 3.18. Phase separation of PSS (red) from PEDOT (blue) as suggested in the literature [172]. 105
Figure 3.19. Final snapshot from the simulation cell containing 444 HSO_4^- (yellow) and 2008 water (hidden for simplicity). Blue: PEDOT, Red: PSS. 106
Figure 3.20. Final snapshot from the simulation cell containing 289 HSO_4^- (yellow) and 1001 water (hidden for simplicity). Blue: PEDOT, Red: PSS. 106
Figure 3.21. RDF analysis of two PEDOT chains in the simulation cells containing 756 HSO_4^- anions (red), 444 HSO_4^- anions and 2008 H_2O (green), 444 HSO_4^- anions (purple) and other combinations of H_2O and HSO_4^- listed in the caption of the figure. 107
Figure 3.22. RDF analysis of O atoms of PSS with H atoms of PEDOT in the simulation cells containing 444 HSO_4^- anions and 2008 H_2O (red), 756 HSO_4^- anions (green), 444 HSO_4^- anions (purple), 2863 H_2O (yellow), 367 HSO_4^- anions and 498 H_2O (blue). 108
Figure 3.23. RDF analysis of O atoms of HSO_4^- anions with H atoms of PEDOT in the simulation cells containing 444 HSO_4^- anions and 2008 H_2O (red), 756 HSO_4^- anions (green), 444 HSO_4^- anions (purple), 367 HSO_4^- anions and 498 H_2O (yellow). 109
Figure 3.24. Final structures of PEDOT:PSS simulation cell with 0.0, 1.0 and 2.0 mol/L H_2SO_4. 111
Figure 3.25. RDF of two PEDOT groups containing 8 PEDOT chains in each as described above with each other in the simulation cell containing 0.0, 1.0 and 2.0 M H_2SO_4. 112
Figure 3.26. Equilibrium structure for 6x3x3 supercell with a-b) 72 HSO_4^- and c-d) 72 OH^- molecules (216 PEDOT monomer in the cell) for –xy (for a-c) and –yz (for b-d) directions. 114
Figure 3.27. Concentration profile for HSO_4^- and OH^- molecules in-y direction. 115

Figure 3.28. Average position of supercell from a) –xy and b) –yz directions for A-PEDOT:PSS. Distances between the atoms in the end group of PEDOT and HSO_4^- are given in Å. 116
Figure 3.29. Radial distribution function for $PEDOT_6^-$-HSO_4^- hydrogen bond before (A-PEDOT:PSS) and after NaOH addition (BA-PEDOT:PSS)..... 117
Figure 3.30. Proposed mechanism of Tounakti et.al.[106] for enhanced conductivity with solvent treatment (Green: PSS^-Na^+ and PSSH, Red: Insoluble PSS, Blue: PEDOT). 118
Figure 3.31. RDF analysis of backbone C of PEDOT with O atoms of H_2O molecules after 4 ns (red), 8 ns (green) and 20 ns (purple). 119
Figure 3.32. RDF analysis of backbone C of PEDOT with O atoms of H_3O^+ ions after 4 ns (red), 8 ns (green), 12 ns (purple) and 20 ns (blue). 119
Figure 3.33. RDF analysis for O atoms of PSS with H atoms of H_3O^+ ions 4 ns (red), 8 ns (green) and 20 ns (purple). 120
Figure 3.34. Positioning of H_3O^+ between the SO_3^- ends of a PSS chain. 121
Figure 3.35. RDF analysis of PSS with DMSO molecules 4 ns (red), 8 ns (green) and 20 ns (blue). 122
Figure 3.36. RDF analysis of PEDOT with DMSO 4 ns (red), 8 ns (green) and 20 ns (blue)..... 122
Figure 3.37. RDF analysis of O atoms of PSS with backbone C atoms of PEDOT. 123
Figure 4.1. Insoluble deposit model. Molecular formula: $C_{300}H_{599}O_{100}$. 75% C, 25% O based on the experimental results provided by the company. 128
Figure 4.2. Base oil model used in this study. 128
Figure 4.3. Dispersant model used in this study. 129
Figure 4.4. Sulfonate detergent model used in this study. 129
Figure 4.5. Three simulation cells containing a) 2 NPs, b) 2 NPs and 2 dispersants, c) 2 NPs and 6 detergents. Base oil molecules are hidden in the second and third cell for simplicity. 130

Figure 4.6. Three simulation cells containing a) 3 NPs, b) 2 NPs and 6 dispersants, c) 3 NPs and 12 detergents. Base oil molecules are hidden for simplicity. 131
Figure 4.7. Martini model of nanoparticle, consisting of polar, apolar and non-polar beads in total. Total number of beads are 123, 383 and 984, respectively. Images are resized to fit in-line. 135
Figure 4.8. Martini model of base oil, consisting of 7 apolar (C1-C4) beads..... 135
Figure 4.9. Density vs. time plot of the coarse-grained MD simulation of the cell containing only base oil model. 136
Figure 4.10. Martini model of bis-succinimide dispersant. 36 apolar (C_1, cyan) beads for ends, 6 polar (P_5, blue) beads in center, 4 polar (P_3, P_5; gray) and 2 apolar (C_3, cyan) beads for rings. 137
Figure 4.11. Martini model of sulfonate detergent. 5 apolar (C_1-C_4, green) beads for tail, 3 apolar (STY, yellow) beads for styrene and 1 charged (Qa, pink) bead for sulfonate with -1 charge. 137
Figure 4.12. Martini model of salicylate detergent. 5 apolar (C_1, green) beads for tail, 2 apolar (STY, yellow) and 1 polar (SP_2, blue) beads for styrene and 1 charged (Qa, pink) bead for sulfonate with -1 charge. 138
Figure 4.13. Initial structures in the first part of the study. a) 50 NPs, b) 50 NPs and 80 bis-succinimide dispersants c) 50 NPs and 800 sulfonate detergents. 5000 base oil molecules are hidden for simplicity. 139
Figure 4.14. DFT calculation results for lowest energy structures and interaction energies of sulfonate detergent components with other constituents. Distances are given in Å unit. 140
Figure 4.15. DFT calculation results for lowest energy structures and interaction energies of dispersant components with other constituents. 142
Figure 4.16. Time evolution of radial pair distribution function between oxygen and hydrogen atoms of two NPs. 145
Figure 4.17. RDF of oxygen and hydrogen atoms of one NP with oxygen and hydrogen atoms of the other NP in the cell with two NPs, without dispersant (red) and with 2 dispersants (green). 146

Figure 4.18. RDF of oxygen and hydrogen atoms of one NP with oxygen and hydrogen atoms of the other NP in the cell with two NPs, without detergent (red) and in the presence of 6 detergents and 3 calcium cations (purple).....147
Figure 4.19. Final snapshot of NPs after all-atom simulations of 2 NPs (left), 2 NPs with 2 dispersants (center), and 2 NPs with 6 detergents (right).....147
Figure 4.20. Time evolution of RDF of oxygen and hydrogen atoms of one NP with oxygen and hydrogen atoms of the remaining two NPs in the cell containing three NPs. 148
Figure 4.21. RDF of oxygen and hydrogen atoms of one NP with oxygen and hydrogen atoms of the remaining two NPs in the cell containing three NPs; in the absence of dispersant (red), in the presence of 3 dispersants (green) and 6 dispersants (purple). 149
Figure 4.22. Final snapshot of NPs after all-atom simulations of three NPs (red) and three dispersants. Two dispersants can efficiently interrupt the contact of two NPs (bottom arrow) where remaining single dispersant cannot prevent aggregation of two NPs (top arrow). Polar amine center of the dispersants are shown as green colored beads to highlight their positioning. 150
Figure 4.23. RDF of oxygen and hydrogen atoms of one NP with oxygen and hydrogen atoms of the remaining two NPs in the cell containing three NPs; in the absence of detergent (red), in the presence of 12 detergents (green) and 18 detergents (purple). 151
Figure 4.24. RDF plot for 50 NP (R=2.2 nm) in 5000 base oil, in the absence of dispersant after 4 (red), 12 (green) and 20 ns (purple) simulation time. 152
Figure 4.25. Insoluble deposit models with a) 2.2, b) 3.2 and c) 4.4 nm diameter, together with dispersant with 6 polar center and 18 apolar tail (top), with 12 polar center and 18 apolar tail (center), and with 12 polar center and 36 apolar tail (bottom), respectively. Green colored beads represent the alkyl tail of the dispersants, brown beads represent the polar beads in amine groups and succinimides and red color represent AuNPs. 153

Figure 4.26. RDF plot for 50 NP (R=2.2 nm) + 5000 Base Oil, without dispersant (red), with 80 Dispersant v1 (green), with 80 Dispersant v2 (purple), and with 80 Dispersant v3 (blue). 155
Figure 4.27. Final snapshot of NPs with 2.2 nm (left), 3.2 nm (center) and 3.2 nm (right) diameter. Polar beads of dispersants (green) intercalate between NPs (red) and apolar tails (gray) create a hydrophobic barrier preventing other NPs approaching in each case. While NPs size increases, relative size of the dispersant relative to that of NPs decreases which negatively affects the efficiency of mitigating the aggregation of NPs. 155
Figure 4.28. RMSD plot of 50 NPs having 2.2 nm diameter in 5000 base oil in the absence of dispersant (red) and in the presence of 80 dispersants (green). 156
Figure 4.29. RDF plot for 50 NP (R=3.2 nm) + 5000 Base Oil, without dispersant (red), with 80 Dispersant v1 (green), with 80 Dispersant v2 (purple), and with Dispersant v3 (blue). 157
Figure 4.30. RDF plot for 50 NP (R=4.4 nm) + 5000 Base Oil, without dispersant (red), with 80 Dispersant v1 (green), with 80 Dispersant v2 (purple), and with Dispersant v3 (blue). 158
Figure 4.31. TEM images showing aggregation of insoluble deposit in the base oil (left) and reduced aggregation after addition of extra dispersant in the base oil (right). The Lubrizol ™ Corporation provided the TEM images. 159
Figure 4.32. RDF plot for 50 NP (r = 3.2 nm) + 5000 Base Oil, without dispersant (red), with 20 dispersant (3.22% in the simulation cell), with 40 dispersant (6.23%) and with 80 dispersant (11.74%). 160
Figure 4.33. Final snapshot of NPs (2.2 nm diameter) with salicylate (left) and sulfonate (right) detergents. Difference in the extent of aggregation is not visible by eye. 162
Figure 4.34. RDF plot for 50 NP (r = 2.2 nm) + 5000 Base Oil, without detergent (red), with sulfonate detergent (green) and with salicylate detergent (purple). 162
Figure 4.35. RDF plot for 50 NP (r = 3.2 nm) + 5000 Base Oil, without detergent (red), with sulfonate detergent (green) and with salicylate detergent (purple). 163

Figure 4.36. RDF plot for 50 NP (r = 4.4 nm) + 5000 Base Oil, without detergent (red), with sulfonate detergent (green) and with salicylate detergent (purple). 163
Figure 4.37. Comparison of RDF plot for 50 NP (r = 2.2 nm) + 5000 Base Oil, without detergent (red), with 80 Dispersant v3 (green) and with 800 Salicylate detergent (purple). 164
Figure 4.38. Comparison of RDF plot for 50 NP (r = 3.2 nm) + 5000 Base Oil, without detergent (red), with 80 Dispersant v3 (green) and with 800 Salicylate detergent (purple). 165
Figure 4.39. Comparison of RDF plot for 50 NP (r = 4.4 nm) + 5000 Base Oil, without detergent (red), with 80 Dispersant v3 (green) and with 800 Salicylate detergent (purple). 165
Figure 4.40. RDF plot for 50 NP (r = 3.2 nm) + 5000 Base Oil + 800 Sulfonate detergents having 5 beads (red), 4 beads (green) and 3 beads (purple) in the tail.166
Figure 4.41. RDF plot for 50 NP (r = 3.2 nm) + 5000 Base Oil + 800 Salicylate detergents having 5 beads (red), 4 beads (green) and 3 beads (purple) in the tail.167
Figure 4.42. RDF plot for 50 NP (r = 3.2 nm) + 5000 Base Oil, without detergent (red), with 200 salicylate detergent (3.22% in the simulation cell), with 400 salicylate detergent (6.23%) and with 800 salicylate detergent (11.74%). 168
Figure 4.43. RDF plot for 50 NP (r = 3.2 nm) + 5000 Base Oil, without detergent (red), with 200 sulfonate detergent (3.22% in the simulation cell), with 400 sulfonate detergent (6.23%) and with 800 sulfonate detergent (11.74%).....169
Figure 4.44. RDF plot for 50 NP (r = 3.2 nm) + 5000 Base Oil, with no dispersant and 800 salicylate detergent (red), 20 dispersant and 600 salicylate detergent (green), 40 dispersant and 400 salicylate detergent, 60 dispersant and 200 salicylate detergent, and 80 dispersant and no detergent (yellow). 170
Figure 4.45. RDF plot for 50 NP (r = 3.2 nm) + 5000 Base Oil, with no dispersant and 800 sulfonate detergent (red), 20 dispersant and 600 sulfonate detergent (green), 40 dispersant and 400 sulfonate detergent, 60 dispersant and 200 sulfonate detergent, and 80 dispersant and no detergent (yellow).....171

Figure 4.46. Plot of RDF between polar beads of dispersant and polar bead in the aromatic ring in salicylate detergent (red, purple and yellow) and corresponding apolar bead in the sulfonate detergent (green, blue and pink) for 20 dispersant and 600 detergent (red and green), 40 dispersant and 400 detergent (purple and blue), and 60 dispersant and 200 detergent (yellow and pink)..... 172
Figure 4.47. Plot of RDF between polar beads of dispersant and -1 charged head bead in the salicylate detergent (red, purple and yellow) and corresponding apolar bead in the sulfonate detergent (green, blue and pink) for 20 dispersant and 600 detergent (red and green), 40 dispersant and 400 detergent (purple and blue), and 60 dispersant and 200 detergent (yellow and pink). 173
Figure 4.48. Final snapshot of the simulation cell including 50 NPs, 5000 base oil, 20 dispersant and 600 salicylate detergent..... 173

LIST OF ABBREVIATIONS

AA: All-atom

AMBER: Assisted Model Building with Energy Refinement

AuNP: Gold Nanoparticle

CG: Coarse-Grained

CHARMm: Chemistry at Harvard Macromolecular Mechanics

COMPASS: Condensed-phase Optimized Molecular Potentials for Atomistic Simulation Studies

CP: Conducting Polymer

CV: Crystal Violet

CVFF: Consistent Valence Force Field

DFT: Density Functional Theory

DMF: N,N-dimethyl Formamide

DMSO: Dimethyl Sulfoxide

EG: Ethylene Glycol

ESP: Electrostatic Surface Potential

GROMOS: GROningen Molecular Simulation

HF: Hartree-Fock

LAMMPS: Large-scale Atomic/Molecular Massively Parallel Simulator

LbL: Layer-by-Layer

LED: Light-emitting Diode

LJ: Lennard-Jones

MD: Molecular Dynamics

MSD: Mean Squared Displacement

MSF: Mean Squared Fluctuation

μVT: Grand Canonical Ensemble

NP: Nanoparticle

NPT: Isobaric-isothermal Ensemble

NVE: Microcanonical Ensemble

NVT: Canonical Ensemble

OPLS: Optimized Parameters for Large-scale Simulations

PA: Polyacetylene

PAA: Polyacrylic Acid

PAH: Polyallylamine Hydrochloride

PANi: Polyaniline

PCFF: Polymer Consistent Force Field

PE: Polyelectrolyte

PEC: Polyelectrolyte Complex

PEDOT: Poly (3,4-ethylenedioxythiophene)

PEM: Polyelectrolyte Multilayer

PPPM: Particle-Particle Particle-Mesh

PPy: Polypyrrole

PSS: Polystyrene Sulfonate

PTh: Polythiophene

RDF: Radial Pair Distribution Function

Rg: Radius of Gyration

SER: Surface Enhanced Raman

SERS: Surface Enhanced Raman Spectroscopy

SPR: Surface Plasmon Resonance

TA: Tannic Acid

TDDFT: Time-dependent Density Functional Theory

THF: Tetrahydrofuran

VMD: Visual Molecular Dynamics

CHAPTER 1

INTRODUCTION

1.1 Computational Methodology

1.1.1 Multiscale Modeling

Multiscale modeling refers to a computational approach that involves creating models that span multiple levels of scales to understand and predict complex phenomena which emerge from interactions across these different scales. At each level, specific methodologies are employed to describe the system. Quantum mechanics and classical mechanics encompass disparate length and time scales. Molecular dynamical structures rely on Newton's Laws, while quantum mechanics models employ the Schrödinger equation to capture the electronic properties of structures with higher detail. When working with small-scale models, it is important to utilize theories that offer more comprehensive and precise information about the system. Larger-scale simulations with less computational source can be achieved at the expense of some information on structural details. The boundaries between different scales can vary depending on the system[1]. In multi-scale models, in transition from one scale to the next, the small-scale system is validated, and the models are prepared for the larger system. Multi-scale modeling simulations can be categorized into three primary methods: quantum mechanics calculations, molecular mechanics calculations, and coarse-grained simulations, as summarized in Figure 1.1 based on time and distance scales[2]. This thesis study is mainly focused on molecular dynamics and coarse-grained molecular dynamics studies between ~10-200 nm distance and ~1-20 ns time scales. Quantum mechanics calculations are

utilized whenever calculations for pairwise interactions or electronic or molecular properties such as HOMO-LUMO band-gaps, electrostatic surface potential (ESP) and/or bond lengths are required.

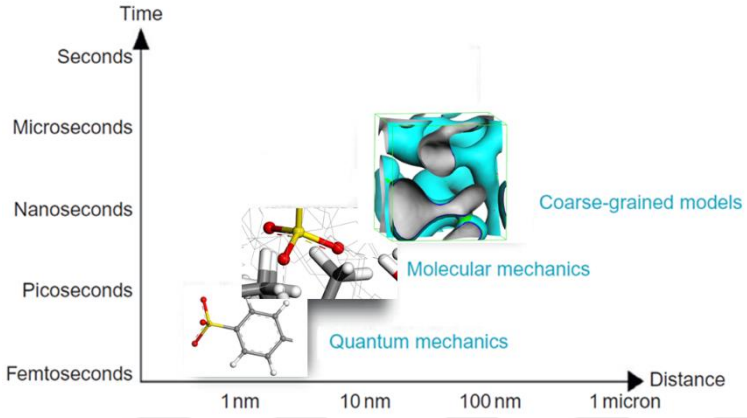


Figure 1.1. Different approaches in multiscale modeling based on time and distance scale.

1.1.2 First Principle (*ab initio*) Quantum Chemical Methods

The first principle quantum chemical methods, which is often called *ab initio* methods, is used to solve the electronic Schrödinger equation for a molecular system without needing empirical data. The equation is given as;

$$\hat{\mathrm{H}}\Psi = E\Psi \tag{1}$$

where $\hat{\mathrm{H}}$ is the Hamiltonian operator, representing the total energy of a quantum system. The Hamiltonian usually includes terms for kinetic and potential energy. Ψ is the wave function of the system. In quantum mechanics, this wave function contains all the information about the state of a quantum system. E is the eigenvalue associated with the wave function, representing the energy of the state. Hamiltonian can be written as;

$$\hat{\mathrm{H}} = -\frac{\hbar^2}{2m}\nabla^2 + V(r) \tag{2}$$

where ħ is the reduced Planck constant, m is the mass of the particle, ∇^2 is the Laplacian operator, which represents the second spatial derivative and V(r) is the potential energy operator, which describes how external forces act on the particle based on its position[3].

These methods start from the fundamental principles of quantum mechanics, and equations do not involve any fitted parameters. Since first principles methods do not rely on empirically adjusted parameters, they can be applied to any molecular system or attribute, even in the absence of experimental evidence. As a result, they might offer higher precision than traditional approaches[3–5]. Quantum chemical computations based on first principles have typically been impractical for larger molecules because they demand high computational resources.

1.1.3 Density Functional Theory

Density functional theory (DFT) approach was introduced by Walter Kohn and Pierre Hohenberg. It was formulated by Walter Kohn and Lu Jeu Sham. Based on Hohenberg-Kohn theorems, the ground-state energy of a many-electron system can be obtained from the electron density. The electron density carries the information about the ground state, and the energy can be considered a functional of this density. Total energy function can be written as;

$$E(n) = F(n) + \int dr V_{ext}(r) n(r) \tag{3}$$

where F(n) is internal electronic energy, V_{ext} is external potential energy, n(r) is electron density and E (n) is total energy function. Among all possible electron densities that integrate into the total number of electrons, the true ground-state electron density minimizes the energy functional. Thus density can be varied until the lowest energy is reached[6,7].

Instead of dealing with the real system of interacting electrons, a fictitious system of non-interacting "Kohn-Sham particles" (electrons) that produce the same ground-state electron density. These single-particle equations describe the motion of each Kohn-Sham particle in an effective potential. The core idea of the Kohn-Sham equation is to construct a single-particle potential V(r) so that the density of a system without interactions matches the density of one with interactions.

$$\left\{-\frac{\nabla^2}{2} + V + \mu_{xc}[\rho]\right\}\Phi_i = \varepsilon_i \Phi_i \tag{4}$$

where μ_{xc} is the exchange-correlation potential[7]. The Kohn-Sham approach essentially transforms the many-body problem of interacting electrons into a set of single-particle problems that are much easier to solve computationally. Once the Kohn-Sham equations are solved, the electron density is used to compute various ground-state properties of the system[3].

The exact functional form is unknown in DFT. Hence, approximations such as Local Density Approximation (LDA) and Generalized Gradient Approximation (GGA) are used. The accuracy of results often depends on the basis set chosen. The basis set is a set of functions, which are used to represent the molecular orbitals of the system. As the basis set size increases, the accuracy of calculations is expected to increase due to improved representation of the orbitals. On the other hand, increasing the basis set requires a higher computational source[3,8–10].

1.1.4 Molecular Dynamics Simulations

Molecular dynamics (MD) is a simulation method which describes the motion of a system consisting of particles (atoms or beads) mathematically, by the impact of forces that are computed using Newton's law of motion. MD simulations are utilized for the estimation of equilibrium properties and dynamics of complex systems such

as biological systems, sensors, membranes, etc. Molecules are not static. On the other hand, including vibrant units where their atoms interact not only with each other but also with their surrounding environment. By observing how the velocity and movements change, we can better understand the different conditions a system might be in. These observations also help to explain how a certain sequence is related to its physical shape and how it works. We can acquire a wealth of information about its structural and dynamic attributes by observing the dynamics of such a molecular arrangement in space over time. Analyzing the dynamic properties of molecular systems can offer significant insights into various aspects such as the shape and energy levels of the molecules, average atomic variations by means of space and velocity, and localized changes like hydrogen bonding or interactions between solvent and other components in the matrix such as ions. It can also help to understand rates of shape-shifting activities like ring inversions or adjustments in nucleic acid structures, as well as enzyme interactions with their substrates and free energy levels and protein folding[3]. MD simulations are used in the investigation of the behavior of proteins and other biomolecules such as conformational changes, ligand binding, protein folding or drug design and targeting[11–14], as well as membrane structure and permeability[15–18], mechanical properties of polymers and polymer nanocomposites[19–23] and sensors[24].

The procedure of MD simulation starts by distributing velocity to all of the particles in the system randomly or with Boltzmann distribution corresponding to the kinetic energy of the system at the temperature specified. Then, step by step numerically solving the equation of force;

$$F_i = m_i \times a_i = m_i \times \frac{dV_i}{dt} = \frac{d^2 r_i}{dt^2} \tag{5}$$

where F_i is the force acting on the particle i, m_i is the mass of the particle i, a is the acceleration of the particle i, acting on the particles results in new positions and velocities of the particles. These positions are saved in a trajectory file within

specified time periods. With this respect, molecular dynamics simulations are time dependent. The procedure of MD simulations is summarized in Figure 1.2.

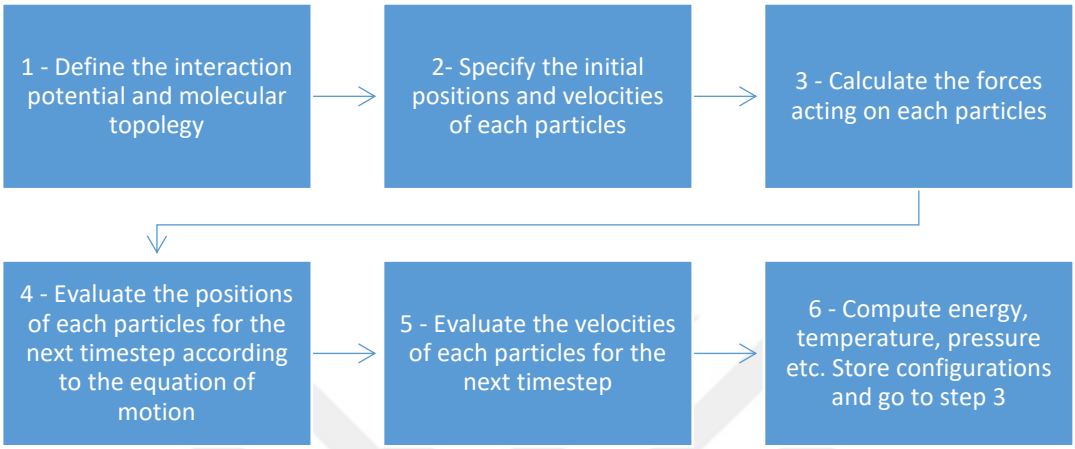


Figure 1.2. Procedure of MD simulations[25].

By solving the equations of motion, real systems consisting of particles are mimicked to explain and/or support experiments[26].

1.1.4.1 Equations of Motion (Verlet-Velocity Verlet)

The position of a single particle at a time is evaluated according to Verlet, velocity Verlet and leapfrog methods. The positions of each particle and forces acting on them at a time are used to determine the positions in the next time step in Verlet method where velocities are used in addition to acceleration and positions in velocity Verlet method. In leapfrog method, positions and forces are used to calculate the velocities in time steps in a leapfrog manner. Specifically, the velocities are known at half time steps, while positions are known at whole time steps [25].

In Verlet algorithm, positions of the particles at time t (r(t)) and t-δt (r(t-δt)) and acceleration (a) of the particles at time t (a(t)) is used to calculate the new positions at time t+δt (r(t+δt)) as shown in the equations (6) and (7) [27].

$$r(t+\delta t) = r(t) + v(t)\delta t + \frac{1}{2}a(t)\delta t^2 \tag{6}$$

$$r(t-\delta t) = r(t) - v(t)\delta t + \frac{1}{2}a(t)\delta t^2 \tag{7}$$

Sum of the equations (6) and (7) gives the equation (8),

$$r(t+\delta t) = 2r(t) - r(t-\delta t) + a(t)\delta t^2 \tag{8}$$

In addition to the position and velocities of the particles at t and t+ δt in equation (6), positions and velocities of the particles are calculated at t and t+ δt/2 in Velocity-Verlet algorithm (Equation (9)). Using equations (6) and (9), equation (10) is derived for the position and velocity of the particles [27].

$$v\left(t+\frac{1}{2}\delta t\right) = v(t) + \frac{1}{2}a(t)\delta t \tag{9}$$

$$v(t+\delta t) = v(t) + \frac{1}{2}a(t)\delta t + \frac{1}{2}a(t+\delta t)\delta t \tag{10}$$

1.1.4.2 Ensembles

Pressure (P), volume (V), temperature (T) and number of particles (N) define thermodynamic state of the system. Position and velocity of the particles are different in many possible microscopic states. Some of these microscopic states have identical thermodynamic states. Collection of all possible systems with identical thermodynamic state is defined as ensemble. Different ensembles are used in MD

such as microcanonical ensemble (NVE) in which N, V and energy (E) are fixed; canonical ensemble (NVT) in which N, V and T are fixed; isobaric-isothermal (Gibbs) ensemble (NPT) in which N, P and T are fixed and grand canonical ensemble (μVT) in which chemical potential (μ), V and T are fixed[25]. In NVT, average temperature is controlled while the total energy of the system fluctuates. Root mean square fluctuations of the energy (σE) of the system is defined as,

$$\sigma_E^2 = \langle H^2 \rangle_{NVT} = k_B T^2 c_v \quad (11)$$

In addition, the instantaneous temperature fluctuation is,

$$\sigma_T^2 = \langle T^2 \rangle_{NVT} = 2_{df}^{-1} T^2 \quad (12)$$

where, c_v is the isochoric heat capacity, k_B is Boltzmann's constant, H is the Hamiltonian and *df* is the number of internal degrees of freedom in the system.

In NPT ensemble, root mean square fluctuation of the volume of the system (σ_v) is defined by the following equation as;

$$\sigma_V^2 = \langle V^2 \rangle_{NPT} = V k_B T \beta_T \quad (13)$$

where β is the isothermal compressibility. At the beginning of the simulations in NVT and NPT ensemble, fluctuation of the temperature and pressure is high between the successive time steps. Magnitude of this fluctuation decreases over the simulation time and it is minimized when the system reaches equilibrium [28,29].

1.1.4.3 Thermostats and Barostats

In MD simulations, the system is often studied at constant temperature. However, as the simulation progresses, the temperature of the system may drift due to the changes in the velocity of the particles, which is caused by various interactions between the particles. Thermostats are algorithms that regulate the temperature of the system to keep it near a target value. Before achieving the target system temperature T, an equilibration process is often required. For instance, in the case of a liquid, the calculated temperature T_c, determined by averaging the velocities of the particles,

may vary significantly from the target temperature T_f. This difference can arise from the exchange of the energy between kinetic and potential energy in the system. Therefore, equilibration is commonly essential before initiating the primary computation cycle in simulation software.

In MD simulations, the temperature of the system is controlled with a thermostat. Berendsen, Nose-Hoover and Andersen thermostats are widely used in literature. Scaling the velocities of the particles depending on the distribution at the desired temperature is realized in the Berendsen thermostat. In Nose-Hoover, the temperature of the system is optimized based on parameters such as heat capacity. Hamiltonian of the system is changed, according to the temperature[29]. To clarify, Hamiltonian is not directly changed. The dynamics (via velocities or system dimensions) is manipulated to mimic the effect of a heat bath or pressure reservoir.

In order to fix the pressure, a barostat is implemented in the system. In this approach, the simulation box is rescaled in order to keep the pressure under control[25].

1.1.4.4 Force Fields

In MD simulations, a force field refers to a mathematical description of the interatomic or intermolecular forces acting on a system of particles. Mathematical functions are used to describe the potential energy of a system consisting of particles. Parameters that are gathered from experimental data and/or quantum mechanical calculations for each kind of particle are stored as a force field term. Interactions and hence the change in the positions and velocities of the particles within the system are determined by these forces. Intermolecular and intramolecular interactions of the particles (i.e. atoms in all-atom MD simulations) with each other, their positions, energies etc. are affected by these forces[3,25].

Force fields are a crucial component of molecular dynamics simulations, as they provide the basis for calculating the motion and interactions of atoms and molecules within a simulated system.

Force fields are constructed for atoms, which can be used in all-atom MD simulations. There are other types of force fields for "beads". Beads are defined as groups of atoms. Example to these types of force fields are Dreiding force field, which is used for organic molecules. In this force-field, every heavy atom with hydrogen atoms bonded to it is represented as one single bead[30]. Another example is Martini force field. In this force field, two to four heavy atoms containing the hydrogen atoms bonded to them are represented as one single bead[31]. Detailed explanation of Martini force field is given under Martini force-field title (1.1.4.4.2.1).

1.1.4.4.1 Force Fields for All-Atom MD Simulations

In all-atom simulations, force fields contain bonded and non-bonded terms for atom types in the system.

Total energy in a system can be written as:

$$E_{total} = E_{bonded} + E_{non\ bonded} \tag{14}$$

where E_{bonded} and $E_{non\text{-}bonded}$ are defined by the following equations:

$$E_{bonded} = E_{bond} + E_{angle} + E_{dihedral} + E_{improper\ torsional} + \cdots \tag{15}$$

$$E_{non-bonded} = E_{coulomb} + E_{van\ der\ Waals} \tag{16}$$

Each term is modelled in several ways for different force fields. Assisted Model Building with Energy Refinement (AMBER), GROningen Molecular Simulation (GROMOS), Optimized Parameters for Large-scale Simulations (OPLS), Condensed-phase Optimized Molecular Potentials for Atomistic Simulation Studies (COMPASS), Consistent Valence Force Field (CVFF), Polymer Consistent Force

Field (PCFF) Chemistry at Harvard Macromolecular Mechanics (CHARMm) are some well-known examples[25].

1.1.4.4.1.1 OPLS all-atom (OPLS-AA)

OPLS all-atom (OPLS-AA) force field was developed and tested by Jorgensen and co-workers for organic molecules and peptides. Bond stretching and angle bending parameters are mostly adopted from AMBER force field. Non-bonded and torsional energy parameters are obtained from gas-phase structures and ab-initio calculations for more than 50 organic molecules and thermodynamic properties of organic liquids.

The non-bonded interactions are described by Coulomb and Lennard-Jones terms as shown in Equation (17), where q_i and q_j are charges on particles a and b; and σ is the distance at which particle-particle potential energy is zero and ε stands for dispersion energy. Bond and angle energies are described as harmonic oscillator as given in Equation (18) and (19) where r_0 and θ_0 are the equilibrium bond distance and angle values, respectively and K_r and K_θ are bond and angle coefficients. Torsional energy is given in Equations (20) where φ_i is the dihedral angle, V_1, V_2, and V_3 are the coefficients in the Fourier series and f_{i1}, f_{i2}, and f_{i3} are phase angles[32].

$$E_{ab} = \sum_{i}^{on\ a} \sum_{j}^{on\ b} \left[\frac{q_i q_j e^2}{r_{ij}} + 4 \in_{ij} \left(\frac{\sigma_{ij}^{12}}{r_{ij}^{12}} - \frac{\sigma_{ij}^{6}}{r_{ij}^{6}} \right) \right] f_{ij} \tag{17}$$

$$E_{bond} = \sum_{bonds} K_r \left(r - r_{eq} \right)^2 \tag{18}$$

$$E_{angle} = \sum_{angles} K_\theta \left(\theta - \theta_{eq} \right)^2 \tag{19}$$

$$E_{torsion} = \sum_i \frac{V_1^i}{2}[1 + \cos(\varphi i + f_i 1)] + \frac{V_2^i}{2}[1 - \cos(2\varphi i + f_i 2)] + \frac{V_3^i}{2}[1 + \cos(3\varphi i + f_i 3)] \quad (20)$$

1.1.4.4.1.2 Polymer Consistent Force Field (PCFF)

Polymer Consistent Force Field (PCFF) was derived from Consistent Force Field (CFF) for organic molecules and polymers. The non-bonded interactions are described by Coulomb and Lennard-Jones terms. Different from OPLS-AA, a 9-6 Lennard-Jones potential is used as given in Equation (21):

$$\mathrm{E} = \sum_{ij} \epsilon_{ij} \left(2\frac{\sigma_{ij}^9}{r_{ij}^9} - 3\frac{\sigma_{ij}^6}{r_{ij}^6} \right) \quad (21)$$

where ε_{ij} is the depth of the potential well, related to the strength of the interaction between the particle i and j. σ_{ij} is the finite distance between the particles i and j, at which the inter-particle potential is zero. r_{ij} is the distance between the particles i and j.

For bonded interactions, common harmonic and Fourrier terms are used which are E_{bond}, E_{angle}, $E_{out\ of\ plane\ bending}$ and $E_{torsion}$ and these terms are given in Equations (22), (23), (24) and (25) [33].

$$E_{bond} = \sum_b \sum_{i=1}^{4} K_{ib}\left(r_b - r_{0,b}\right)^i \quad (22)$$

$$E_{angle} = \sum_\theta \sum_{i=2}^{4} K_{\theta,i}(\theta - \theta_0)^i \quad (23)$$

$$E_{out\ of\ plane\ bending} = \sum_\chi k_\chi \chi^2 \quad (24)$$

$$E_{torsion} = \sum_{\emptyset} \sum_{i=1}^{3} V_i(1 - cos(i\emptyset - \emptyset_0)^2) \quad (25)$$

In these equations, K_b is the bond force constant, which is provided for each type of atom within the force field document. r is the current bond length and r_0 is the equilibrium bond length. K_θ is the angle force constant, θ is the current bond andgle and θ_0 is the equilibrium bond angle. χ in equation (24) represents the out-of-plane displacement of the atom from the plane defined by the other three atoms. k_χ is the force constant associated with out of plane bending. V_n is the torsion amplitude, $\emptyset$ is the torsion angle and n is the periodicity.

1.1.4.4.2 Coarse-Grained MD Simulations

Coarse-graining presents an alternative method for addressing sampling challenges and size limitations. In MD simulations, "sampling" refers to exploring the configuration space of the system, i.e., the various spatial arrangements and conformations the molecules can adopt. For complex molecules or large systems, adequately sampling this space to gather meaningful statistics and insights is computationally intensive. Due to energy barriers, certain conformations or transitions might be rarely observed in a fully atomistic simulation because of the limited timescales that can be feasibly simulated. In addition, simulating large systems with full atomic detail can be computationally prohibitive because of the sheer number of particles and interactions.

Coarse-grained MD simulations approach involves simplifying the complexity of the simulated system by grouping atoms into virtual particles. By reducing the number of particles within the simulated system, the number of calculated interactions decreases, resulting in a smoother energy landscape. This makes CG models computationally faster than traditional all-atom models due to a smaller number of particles and force field terms for a similar size system. In addition, the use of smoother interaction potentials allows for longer time steps in molecular dynamics

simulations, enabling the investigation of time and length scales beyond those accessible with all-atom models. The specific acceleration achieved through CG simulations relies on the intricacies of the models employed. The construction of CG models is contingent upon the specific scientific inquiry they aim to tackle. When decreasing the level of detail in the representation, it is crucial to avoid excessive simplification of the system's description. Instead, the focus should be on preserving the essential features that may affect the properties of the system which are of interest[34].

Various approaches have been employed in the improvement of CG models for polymers, encompassing considerations of chemical specificity. The simplest way of coarse-graining includes modeling beads. One of the force fields generated for this approach is the Martini Force Field[31].

1.1.4.4.2.1 Martini Force Field

The Martini force field is an example of a coarse-grained simulation approach. Four heavy atoms are represented as one polar (P), non-polar (N), apolar (C) or charged (Q) particle (bead) with 18 sub-types based on hydrogen bonding characteristics and degree of polarity. In order to have a more rigid structure, atoms in the ring structures are mapped into different types of beads having slightly changed LJ interaction parameters. Symbol for these type of beads starts with –S (Ex: SN_a or SC_4 etc.).

Table 1.1 Type of Martini Beads in Martini 2.0 Force Field [31]

Type	**Description**	**Sub-types**	**Examples**
Q	Charged beads. For cations with one heavy atom like Na^+, Ca^{2+}, Cl^-. One bead represents the cation with its first hydration shell.	Q_{da}: Both donor and acceptor in hydrogen bonding Q_d: Donor in hydrogen bonding Q_a: Accepter in hydrogen bonding Q_0: none of above	Sodium, chloride, choline, phosphate
P	Polar. Water is a P4 type bead consisting of four water molecules in one bead.	P_1 (least) to P_5 (most) polar.	Water, ethanol, acetic acid, DMSO
N	Nonpolar	N_{da}: Both donor and acceptor in hydrogen bonding N_d: Donor in hydrogen bonding N_a: Accepter in hydrogen bonding N_0: none of above	1-butanol, 2-propanone, methoxyethane
C	Apolar	C_1 (least) to C_5 (most) polar.	Butane, butene, butyne, 1-propanethiol, chloroform

The non-bonded interactions between coarse-grained beads are calibrated against thermodynamic data to accurately reproduce the properties of interest according to the specific aim[31]. These may be stiffness of a specific bond, density of the system, rigidity of a molecule and other possible properties. The Martini force field was

originally developed for simulating lipid bilayers. Currently includes force field parameters for DNA, proteins, and uncharged polymers. It offers advantages such as parameterization for a wide range of chemical building blocks, simple modeling of non-bonded interactions, and relatively easy parameterization of new building blocks[35].

1.1.4.5 Output Analysis

Output files created by the MD simulation software contains information such as energy (kinetic, potential, bond, angle, electrostatic etc.), volume, pressure, temperature of the simulation cell and trajectory files contain the atomic positions of the atoms or beads in the time step where the data is saved. Moreover, specific calculations can be made during the simulation run and saved as an output such as stress-strain behavior. This information can be used to calculate several properties of the simulation cell, as well as the specific components in the simulation cell such as radial pair distribution function (RDF), root mean squared displacement and fluctuation (RMSD and RSMF), radius of gyration (R_g), structure factor.

1.1.4.5.1 Radial Pair Distribution Function (RDF)

The radial pair distribution function (RDF) or Pair Correlation Function is the value of average number density of the particles around a selected particle within the system. In its simplest form, it quantifies the probability of locating a particle at a distance of r from a specified selected reference particle, compared to that of an ideal gas. It is represented as in the following equation;

$$x_\alpha x_\beta \rho g(r) = \frac{1}{N} \langle \sum_{i=1}^{N_\alpha} \sum_{j=1}^{N_\beta} \delta(r - r_i + r_j) \rangle \quad (26)$$

where x_i and N_i is the mole fraction and the number of atoms of selection of type i, ρ is the number density, N is the total number of atoms[36].

1.1.4.5.2 Mean Squared Displacement (MSD)

Mean square displacement (MSD) or root mean square displacement (RMSD) of particles is a statistical measure of deviation of their position with respect to a reference position during the simulation. It is measured throughout the simulation in order to evaluate the extent of random motion. Besides, it is a measure of stability of the system or a specific group of particles the system. If MSD of a particle or a group of particles increases, it shows that the system has not reached equilibrium yet. MSD at time t is calculated as shown in Equation (27), where *N* is the number of particles, *x(i)(0)* is the reference position of particle i and *x(i)(t)* is the position of the particle i at time t. The time-dependent diffusion coefficient is also derived from MSD, which can be calculated Equation (28), where *N* is the number of particles and *r(t)-r(0)* is change in the position over time[37].

$$MSD = \frac{1}{N}\sum_{i=1}^{N}\left|x^{(i)}(t) - x^{(i)}(0)\right|^2 \tag{27}$$

$$D = \frac{1}{6N}\,\frac{d\,\langle (r_i(t) - r_i(0))^2 \rangle}{dt} \tag{28}$$

1.1.4.5.3 Mean Squared Fluctuation (MSF)

Mean squared fluctuation (MSF) of a particle is the deviation of its position over the time interval. It is shown in Equation (29), where, r_i^{ref} is the reference position of particle i, which is the time averaged position of it and t is the time interval. The difference between RMSF and RMSD is that RMSF is an averaged value over time for each particle. On the other hand, RMSD is an average value of all particles[37].

$$RMSF_i = \sqrt{\frac{1}{T}\sum_{t_j=1}^{T}\left|r_i(t_j) - r_i^{ref}\right|^2} \tag{29}$$

1.1.4.5.4 Structure Factor

When X-rays interact with a crystalline material, the resulting diffraction pattern provides a 'fingerprint' of that material's internal atomic arrangement. The structure factor is a mathematical tool used to understand and predict this pattern based on the periodic arrangement of atoms in the crystal. It is calculated from the equation,

$$F_{hkl} = \sum_j f_j e^{[2\pi i(hx_j + ky_j + lz_j)]} \quad (30)$$

where x_j, y_j and z_j are the spatial coordinates and f_j is the scattering factor of the j^{th} atom where f_j is the scattering factor of the atom, which depend on the direction of the scattering and it is independent from the position of the atom.

The clarity and sharpness of the diffraction pattern from a single crystal are influenced by how uniformly the unit cells are repeated and by the coherence length, which refers to the number of neighboring unit cells in every direction. In essence, while the regularity of unit cell repetitions and coherence length define the clarity of the diffraction pattern, the structure factor determines where and how intense each spot in the pattern will be based on the atomic arrangements within the unit cells[38].

1.1.4.5.5 Radius of Gyration (R_g)

The radius of gyration is a measure of the distribution of the particles (atoms or beads) in a structure around its center of mass. In the context of polymer science and molecular dynamics simulations, the radius of gyration (R_g) gives information about the size of a polymer chain or a complex molecule by quantifying how its mass is distributed around its center of mass.

The general formula to compute the radius of gyration (R_g) for a system of N particles is:

$$R_g = \left(\frac{\sum_{i=1}^{N} m_i {s_i}^2}{\sum_{i=1}^{N} m_i} \right)^{1/2} \quad (31)$$

where, r_i is the position vector of the i^{th} particle and r_0 is that of the center of mass in the system. N is the number of particles in the system.

In simple terms, the radius of gyration is a measure of how the particle of the system spreads out around its center of mass. This parameter is used in biophysics and material science for comprehending the arrangement of large molecular complexes like proteins, polymers and colloidal particles[39].

1.1.4.6 Software Used in This Thesis

There is a wide range of software used to carry out MD simulations available as free and paid alternatives. Some examples are Biovia Materials Studio, Schrödinger Desmond[40], Assisted Model Building with Energy Refinement (AMBER)[41], GROningen MAchine for Chemical Simulations (GROMACS)[42], Large-scale Atomic/Molecular Massively Parallel Simulator (LAMMPS)[43], Nanoscale Molecular Dynamics (NAMD)[44]. In addition, there are many number of software with miscellaneous dimensions and with paid and free alternatives ready to use for preparation and processing of input files and conversion of the file types. Many of the MD software offer visual interface included inside the package enabling drawing the initial molecules, constructing nanostructures, polymers, simulation cells etc. and visualizing the final snapshot of the simulation cell and/or the trajectory file as a movie. For the rest of the software, which does not offer interface for visualization, input files are introduced and output files obtained are structured text files. Software packages such as Visual Molecular Dynamics (VMD)[45] and Open Visualization Tool (OVITO)[46] can be used to visualize these files in Cartesian coordinates. Within the scope of this thesis, LAMMPS is used as MD simulation software and VMD is used for visualization. For construction of the model structures, Discovery Studio, Scienomics Materials Atomistic Properties Simulation (MAPS), Moltemplate[47] and Packmol[48] software packages are used throughout this thesis study.

1.1.4.6.1 Large-scale Atomic/Molecular Massively Parallel Simulator (LAMMPS)

LAMMPS is an MD simulations software specifically designed for high-efficiency parallel processing, capable of handling from a small to an extremely large number of particles, in the millions or even billions[43]. Sandia National Laboratories, an institution focused on defense technologies and operated as a Department of Energy (DOE) facility, distributes the software freely under the GNU General Public License (GPL).

1.1.4.6.2 Discovery Studio

Discovery studio is distributed by Dassault Systèmes (formerly: Accelrys). The software serves as a tool for the simulation and study of materials. The software is employed for research into a variety of materials like polymers, carbon nanotubes, catalysts, metals, and ceramics.

1.1.4.6.3 Scienomics Materials Atomistic Properties Simulation (MAPS)

MAPS is a commercial software platform developed by Scienomics. The software is designed for multi-scale modeling and simulation in materials science. This commercial tool aims to streamline the simulation workflow, from model setup and job submission to data analysis. Different from Moltemplate and Packmol, it offers an interface and supports a wide range of computational methods, such as molecular dynamics, quantum mechanics, and mesoscale simulations. MAPS provides integration with multiple third-party simulation engines, allowing to switch between different computational approaches like DFT or MD on the same interface.

1.1.4.6.4 Visual Molecular Dynamics (VMD)

Visual Molecular Dynamics (VMD) is a popular software package used for visualizing and analyzing molecular dynamics simulation input and trajectory files. It is developed and maintained by the Theoretical and Computational Biophysics Group at the University of Illinois at Urbana-Champaign, VMD serves in the field of computational biology and chemistry[45]. It is designed to work with large data sets, enabling visualization of complex molecular structures and their interactions over time. The software supports a variety of file formats and simulation types, offering a broad range of tools for rendering high-quality images and producing animated sequences.

1.1.4.6.5 Moltemplate

Moltemplate is a software package designed for constructing and setting up molecular systems for simulation with text-based editing[47]. It is especially useful for systems that are too complicated to be conveniently set up by a visual interface. It is commonly used for preparation of the LAMMPS input files. It can be useful for other simulation platforms as well. Moltemplate allows users to define complex molecular topologies, including the arrangement of atoms, bonds, angles, and other molecular features, in a text-based format that is both human-readable and scriptable.

Using a hierarchical object-oriented approach, Moltemplate makes it easier to create large and complex molecular structures by enabling users to define a molecule once and then replicate it multiple times. This feature is particularly beneficial for systems containing repeating units, like polymers or crystal lattices.

1.1.4.6.6 Packmol

Packmol is a software package used to generate initial configurations for MD simulations using Monte Carlo approach. It can be used to prepare input structures

for LAMMPS, GROMACS and others. It is particularly useful for creating random yet physically plausible arrangements of molecules within a defined volume. It is compatible with Moltemplate in preparation of LAMMPS input files[48].

One of the key features of Packmol is its ability to efficiently pack molecules in a manner that minimizes overlap and maintains specified constraints, such as distance between molecules or particular orientations of the molecules with respect to each other. This enables the construction of complex multi-component systems like solutions, mixtures, or layered materials (ex. polyelectrolyte multilayers, lipid bilayers, etc.) easily.

Packmol is widely used in computational chemistry, materials science, and biophysics area to generate initial system configurations for molecular dynamics simulations. The generated configurations can then be further equilibrated and studied using molecular dynamics or other computational methods.

1.2 Polyelectrolytes

Polyelectrolytes (PEs) are a class of large molecules or macromolecules having multiple ionizable groups. PEs can bear a significant amount of electric charge per unit length of the polymer chain.

PEs possess a unique combination of polymeric and electrolyte properties, making them highly versatile for a wide range of applications. The solubility of a polyelectrolyte in specific solvents is dependent on some factors e.g. its functional groups, the presence of counter ions, pH, and more. Generally, polyelectrolytes are soluble in water. When dissolved in polar solvents like water, these ionizable functional groups dissociate, resulting in charged polymer chains and the release of counter ions into the solution. Polystyrene sulfonate (PSS), polyacrylic acid (PAA), polymethacrylic acid (PMMA) and their salts, DNA, and other polyacids and polybases are examples of polyelectrolytes. The electrostatic interaction between these charges gives rise to unique properties and features in polyelectrolyte solutions,

e.g. ion condensation, osmotic pressure, swelling, electrophoretic mobility, that are qualitatively distinct from those observed in neutral polymers[49,50].

Polyelectrolytes can be classified based on the charge of the functional groups in their polymer backbone after ionization. They are categorized as cationic[51] or anionic[52] depending on whether they contain positively or negatively charged functional groups, respectively. Ampholytic (or amphoteric) polyelectrolytes are polymers which contain both positively charged and negatively charged groups along their backbone[48].

Copolymers, with include more than one type of monomer can also include dissociating groups in their monomers. More than one dissociating group or monomers with and without dissociating groups may exist in copolymers. The maximum charge of the polyelectrolyte is determined by the chemical composition in this case[53–55].

Additionally, polyelectrolytes can be categorized as "strong" or "weak" based on their degree of ionization. The degree of ionization, or average degree of dissociation, primarily depends on the chemical properties of the ionizable functional groups. Strong polyelectrolytes exhibit a constant degree of ionization over a wide pH range. In contrast, "weak" polyelectrolytes have a pH-dependent ionization degree, and this is characterized by a “intrinsic pK” value, which represents the deprotonation constant. In polymers having weak groups, the average degree of dissociation is adjusted to the physicochemical conditions, e.g., pH, ionic strength, temperature, presence of other species. The charges on the polymers having strong groups are fixed along the chain[55].

1.2.1 Polyelectrolyte Complexes

The electrostatic interaction between two oppositely charged PEs gives rise to the formation of polyelectrolyte complexes (PEC). The formation of PECs is influenced by various properties of polyelectrolytes, such as steric factors, the length and

rigidity of the polymer backbone, the nature and charge density of ionizable functional groups, and the concentration of the polyelectrolyte. Additionally, the formation of PECs can be adjusted by changing pH and temperature, as well as the composition of the system by incorporating different salts or other different polyelectrolytes. By changing the pH, the interactions between oppositely charged polyelectrolytes and potentially the stability, size, or morphology of the PECs can be changed. Temperature changes the overall thermodynamics of the system, leading to formation or dissociation of PECs[56,57]. PECs can have various morphologies, offering a wide range of structural possibilities. These morphologies can be fibers, capsules, nanoparticles, tapes, tubes, and even coacervates[58]. Van der Gucht and coworkers provided a detailed analysis of the phase behavior and driving forces involved in the formation of PECs[57]. They explored the impact of various parameters such as the nature of the polyelectrolyte, ionic strength, and pH on PEC formation, shape, arrangement and organization of the atoms. The authors highlighted the multi-responsive nature of the electrostatic driving force. One of the important findings is that, the driving force is the strongest when the charges of the functional groups in each component, i.e., polycation and polyanions are in a 1:1 ratio. Moreover, adding salt diminishes the driving force, leading to fewer PECs aggregating, which in turn lowers the system's viscosity. This decrease in viscosity is due to reduced entropy, which is accompanied by a rise in the released counter ions as the salt concentration goes up.

1.2.2 Deposition of Polyelectrolytes on a Surface

Polyelectrolyte chains in a semidilute regime exhibit unentangled dynamics over a broader concentration range compared to the solutions of neutral polymers. The crossover to entangled dynamics occurs further away from the chain overlap concentration. When polyelectrolyte chains are near surfaces or interfaces, they can exist in both flat and more three-dimensional configurations. The number of these

chains in a particular area is affected by how the chains interact with the material of the surface or interface.[59].

With an increase in surface charge density, the dilute solution of adsorbed chains undergoes a transformation into a two-dimensional semidilute solution. Further increase in surface charge density leads to the formation of a concentrated PE solution within the adsorbed layer, with the thickness increasing in proportion to the surface charge density. An interesting phenomenon observed in the adsorbed layers is surface overcharging, which refers to the overcompensation of surface charge by adsorbed PE chains. The amount of surface overcharging can be adjusted by varying the ionic strength of the solution. Charge inversion plays a central role in the layer-by-layer deposition technique, a self-assembly method used for fabricating multilayer films. Self-assembly is a process by which individual components spontaneously organize into ordered structures, primarily due to specific local interactions among the components, without external guidance. These multilayer films are not merely simple repetitions of the same layers. Instead, they can possess varied and intricate designs. Importantly, both the designs and functionalities hinge on the deposition method and the materials used. In simpler terms, with reversal of charges on surfaces, one can build up intricate and complex films layer by layer, using the natural attraction between oppositely charged materials to guide the assembly process [57,60].

1.2.3 Layer-by-Layer Assembly

The layer-by-layer (LbL) method is a technique for depositing alternating layers of oppositely charged polymers. This method can be used to functionalize surfaces with a high degree of control, and it has been shown to be effective in improving the mechanical and chemical properties of PEMs[61].

The capability to control the thickness and composition of multilayers, along with the possibility of immobilization of different materials for the specific application,

e.g. DNA, proteins, inorganic platelets, nanoparticles, and viruses, with opposite charges to the PE, renders this method convenient, straightforward, and cost-effective. The LbL method can be employed to prepare multilayer. However, it can be challenging to classify these architectures based on their respective components since they often comprise a variety of materials[62].

1.2.4 Polyelectrolyte Multilayers

When the self-assembly process of PEs is carried out by sequentially depositing oppositely charged PEs on a substrate's interface, it results in the formation of polyelectrolyte multilayers (PEMs). This subclass of PECs in a non-equilibrium state is considered to be part of the self-assembly process[56].

Film growth in this technique involves the alternating deposition of polycations and polyanions on the surface of the substrates in aqueous medium. The simplicity of the electrostatic assembly technique allows for the fabrication of multilayer films using synthetic polyelectrolytes, DNA, proteins, inorganic platelets, nanoparticles, and viruses. Due to its simplicity and the fact that it can work with various types of charged materials (regardless of their shape or nature), it is possible to create intricate multilayer films with a wide range of properties and functions[59].

In the self-assembly of PEMs, electrostatic bonds are established between the PEs through the release of counter ions, similar to the formation of PECs. However, there are some differences between these processes. PECs tend to exhibit a more ordered internal structure due to the limited freedom in the bonding of PEs. In PECs, the electrostatic attraction between oppositely charged groups can lead to a compact structure where the charges are neutralized. This compactness might limit the manifestation of steric effects. On the other hand, PEMs often display a highly disordered and relatively amorphous internal structure, primarily influenced by apparent steric effects. To clarify, PEMs are constructed by the sequential adsorption of oppositely charged polyelectrolytes onto a substrate. An example model of PEMs

is given in Figure 1.3 in which one polyanion and polycation layer is shown in red and blue, respectively. With each added layer, the outermost segments of previously adsorbed polyelectrolyte chains might hinder the close approach of the incoming chains due to their physical bulk. This can result in irregular layering and a less compact structure [63–65].

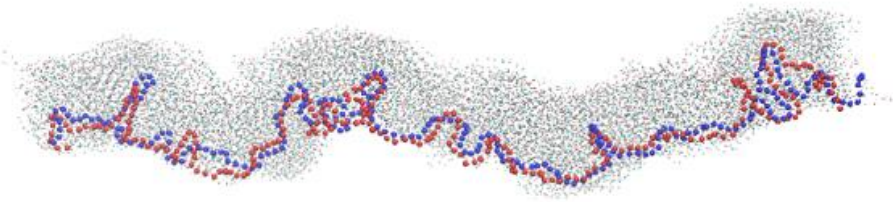


Figure 1.3. Polyanion (red) and polycation (blue) in a polyelectrolyte multilayer (PEM) model from the final snapshot of coarse-grained MD simulations in this study.

Although there are many experimental studies about LbL assembly of polyelectrolytes, there are many points that are open to improvement in the area. These points that are open to improvement can include the discovery of new PEs or other materials that can be incorporated into the LbL process to enhance its capabilities or extend its applicability. Moreover, reducing the time to deposit each layer, which can be especially critical for industrial-scale applications, can be another point for possible improvement. Control and reproducibility of uniform layer thickness or structure across different batches and setups may also be improved[63,66,67].

The growth dynamics of PEMs refer to the patterns in which the thickness of these layers accumulates over successive depositions of polyelectrolytes. There are two primary regimes such as linear and exponential growth. In the linear growth, PEMs thickness increases consistently with each successive deposition of PE, ensuring a steady build-up. In contrast, the exponential growth witnesses an accelerated thickness increase with every additional layer[67,68].

Several factors influence the deposition of specific polyelectrolyte pairs as linear or exponential growth PEM assembly. For instance, the transition from exponential to linear growth is reported to be observed and kinetically determined. This change is due to the way in which polyelectrolyte chains move and spread out within the film. Their distribution becomes more uniform over time[69]. The strength of the interactions between PEs also influences the growth of the PEMs. Strongly exothermic interactions favor linear growth. On the other hand, weakly exothermic or endothermic interactions lead to exponential growth[68]. Overall, the type of the system -whether it grows linearly or exponentially- depends on the strength and the nature of intermolecular interactions between the polyelectrolyte pairs. In the experimental studies conducted in our lab, linear and exponential growth PAH/PAA multilayers were gathered by altering the pH of the dipping solution[60,61].

1.3 Raman Spectroscopy

Raman spectroscopy is an analytical technique used to study vibrational, rotational, and other low-frequency modes in a system. It can give information about the molecular structures, chemical compositions, and interactions of various materials. Similar to spectra derived from other vibrational methods like IR absorption, a Raman spectrum can be considered a unique identifier for a compound. This characteristic of Raman spectroscopy makes it a valuable tool for identifying a range of compounds.

When a sample comes into contact with radiation of a frequency, ν_0, part of this radiation undergoes a scattering process. Scattered radiation with the same frequency as the incident radiation is called Rayleigh scattering or elastic scattering. The scattered radiation exhibits different frequencies compared to that of incident radiation is called Raman scattering or inelastic scattering. The core principle of inelastic scattering revolves around the interaction between a photon with energy $h\nu_0$ and a molecule. This interaction can lead to a virtual state of the sample leading to the effective disappearance of the original photon. This is simultaneously causing

the emergence of a new photon with an energy level of $h(\nu_0 - \nu_M)$. When incident photons are scattered with a loss of energy, the scattered light shifts to a lower frequency (or longer wavelength) compared to the incident light. This phenomenon is observed when the molecule undergoes a transition from its ground vibrational state to an excited vibrational state, resulting in scattered photons which are less energetic than the incident photons. This shift to a lower frequency in the Raman spectrum is termed the Stokes Raman shift. Conversely, when incident photons are scattered with a gain of energy, the scattered light shifts to a higher frequency by $h\nu_M$ (or shorter wavelength) compared to the incident light. This occurs when the molecule is already in an excited vibrational state and drops to a lower energy state upon interaction with the photons. As a consequence, the scattered photons possess higher energy than the incident photons. This shift to a higher frequency in the Raman spectrum is termed the Anti-Stokes Raman shift. For Anti-Stokes Raman shift, the molecule which is exposed to the incident radiation is in its excited state. In practical applications, the Stokes Raman shift is more commonly used than the Anti-Stokes shift because, at ambient temperatures, most of the molecules are typically found in their ground vibrational state.

When a molecule is in an excited virtual state, scattering can occur leading to the disappearance of the initial photon with energy $h\nu_0$ and the emergence of a new photon with energy $h(\nu_0 + \nu_M)$. This event is coupled with the molecule, where the scattering takes place, transitioning to an energy that is lower by $h\nu_M$. Since molecular energy is distinct and quantized, the energy losses of photons follow the same rule, mirroring the energy quantization of photons absorbed during the capturing of the infrared (IR) spectrum. In essence, the information in the vibrational Raman spectrum is similar to that in the IR spectrum, yet, due to unique selection rules, the details in both spectra can vary significantly[70].

1.3.1 Surface Enhanced Raman Spectroscopy (SERS)

Plasmon resonance or the plasmon effect refers to the phenomenon where free electrons in a metal interact with light, the electron cloud in the conduction band of the metal can collectively oscillate at specific frequencies. Incoming photons can trigger substrate electron-hole pairs or surface plasmons. Each can contribute to enhancing photo-induced processes. Specifically, the uptake of light by nanostructures can generate powerful local electric fields at the site of adsorbed molecules[71]. The plasmon effect has found place in several applications. One of these is sensing of substances like proteins. When a metal binds to a metal surface, surface plasmon resonance properties changes which can be used to detect and quantify specific substances[72]. Moreover, the amplified local field dramatically alters the optical properties of the adsorbed substance which is playing a crucial role in causing the significant SERS effect[71].

The way light interacts with the metallic nanostructure relies on the value of the complex dielectric function at the excitation wavelength, which in turn dictates the enhancement noted at a specific excitation frequency. Absorption of the electromagnetic radiation by molecules and scattering of the incident photons are influenced by the shape and size of the metallic nanostructure[73].

In SERS, the substrate is irradiated by a monochromatic radiation source (laser) and scattered radiation is followed by a Raman spectrometer. The Raman cross-section of a substance (analyte) can experience a significant amplification which may be as much as 15 orders of magnitude greater than typical Raman scattering in SERS experiments. Surface enhanced Raman (SER) signals are collected for molecules situated in resonators composed of certain metal nanostructures, like silver (Ag), gold (Au), or copper (Cu). The primary cause of this enhancement in Raman intensity due to the SERS effect stems from the amplification of the electric field at the metal surface. However, a fraction of the SERS enhancement can be attributed to the so-called charge transfer enhancement, which is similar to the standard resonance Raman event seen in metal–ligand associations[70].

The nature of SERS is rooted in the complexity introduced by the multitude of factors that shape the observed spectrum of the output light. This complexity has led to significant confusion in the literature and negatively affected the progression of quantitative analytical applications of SERS. In this context, the absence of reliable and repeatable nanostructures with well-determined enhancement factors remains a significant challenge due to the dispersion, or frequency dependence, of the enhancement[70,74].

1.3.1.1 Mechanism of SERS

There are two mechanisms proposed for enhanced Raman signals which are electromagnetic and chemical enhancement[75]. Contribution to the total SERS enhancement is dominantly originated from electromagnetic enhancement. Localized surface plasmon resonance (LSPR) is the collective oscillation of electrons, which are free on the surface of the metal and excited by incoming light causing selective absorption and scattering. Upon irradiation of metallic clusters at their LSPRs, polarized molecule causing a new surface plasmon coupling with Raman scattered photon and hence, Raman signal increases[76]. This strong field enhancement is known as electromagnetic enhancement. The energy of the plasmon on a smooth surface is confined to the surface, requiring the surface to be textured or made uneven to allow a perpendicular component to the plasmon for scattering to happen. Hence, the creation of the plasmon takes place on a rough surface[77].

Focusing of light primarily happens at hot spots, often the gaps of the plasmonic materials like Ag, Au, and Cu, as they exhibit strong SPR in the visible to near-infrared (NIR) range. It is reported that in the junctions between nanoparticles, hot spots occur[75]. The intensity of the local electric field depends on the proximity between molecules and the surface. Surface roughness creates numerous crevices, protrusions, and gaps where the electromagnetic field can become highly concentrated. By decreasing the distance between nanoparticles, area becomes highly localized (hot spot) and consequently Raman scattering efficiency increases.

This makes surface roughness important. Moreover, rough surfaces offer more surface area giving more space to the analyte molecules. In addition, homogenous dispersion of nanoparticles on the surface of the substrate is important for homogenous Raman signal over the surface[78,79].

Chemical enhancement is realized because of the chemical interaction between the analyte molecule and the nanostructured surface. A charge-transfer state is formed between the surface of the substrate and the analyte molecule, which can specifically be excited resonantly. The incoming radiation interacts with the metal surface and an electron-hole pair is formed. This process results in a transfer of energy to the bonds of the analyte molecule from the metal. Similar to the process in the electromagnetic enhancement mechanism, the energy is transferred back to the metal excluding the scattered radiation, which is directed to the spectrometer. Electromagnetic enhancement is known to be much larger than chemical enhancement.

Plasmons include the collective movement of a bunch of electrons across the surface, making them inherently not a property of individual molecules. There is a considerable number of studies about the plasmon's characteristics to produce effective enhancement. Significant gradients in the field across the molecule are essential. Synergistic effects between surface roughness elements result in highly active areas known as hot spots. Still, the Raman scattering occurs at the individual molecule level, and there is still much investigation required to fully understand the exact characteristic of the enhancement site on a molecular level[77].

The positioning of the analyte on the substrate is critical for the enhancement of the scattering efficiency. The plasmon component perpendicular to the surface is responsible for scattering, which has a direct correlation with molecular polarization which is vertical with respect to the surface. As such, when concentrations are low, pyridine molecules tend to lay on silver in a manner where the ring plane is parallel to the surface. However, as the surface nears monolayer coverage, the pyridine rings tend to arrange themselves with the plane at a right angle to the surface. As a result,

vibrations in-plane involving carbon atom displacements will gain intensity at increased concentrations due to their amplified polarizability, which is vertical with respect to the surface[80].

1.3.1.2 SERS Substrates

In the first implementations of SERS, typical choice of a substrate was to use metal, which were roughened electrochemically.

To enhance the reproducibility and stability of SERS substrates, and to increase the SERS enhancement factors reproducible metallic nano-resonators have been incorporated onto solid substrates. Examples include metal film-over-nanosphere substrates and metal-coated alumina nanoparticles. In some examples, SER signal is so large that even a single molecule can be detected[73,74]. Reproducible SER signals can be achieved even with only 50-100 analytes, which make SERS one of the most sensitive technique[70].

To promote the adsorption of the analyte, SERS-active metal substrates frequently undergo modifications with various adsorption layers. By enveloping the SERS-active metal substrate with a monolayer of species forming distinct complexes with the analyte, a significant increase in selectivity and improvement in the detection limit of SERS-sensors can be accomplished[81].

The adsorption characteristic of the analyte on the surface is influenced by both the surface properties and the nature of the analyte itself. Au and Ag are commonly used as substrates. Au surface typically consists of Au_0 atoms covered with a layer of physically adsorbed inorganic and/or organic ions derived from the media, e.g. sodium citrate, polyethyleneimine (PEI) or polyethylene glycol (PEG). These coatings functionalize the surface for various applications and stabilize the nanoparticles. The choice of capping agent often depends on the intended application and desired properties of the AuNPs. Contrarily, Ag may display a surface layer of

oxide or similar layer consisting of Cl^- or other reagents, which can include organic complexing agents like citrate, in addition to physically adsorbed ions.

The degree of Raman signal enhancement is dependent on characteristics of the nanoparticles, such as their shape and size. Areas of high field gradients, such as the interaction between two nanoparticles, yield larger enhancements. Fractal clusters are aggregates of particles and they exhibit a repeating pattern at different scales. They provide greater enhancements, and larger scattering efficiency were obtained in hot spots of these clusters[82]. These hot spots are regions where the electromagnetic field is greatly amplified due to the close proximity of individual nanoparticles within the cluster. As a result, molecules located in these hot spots experience a much stronger interaction with the incident light, leading to significantly enhanced scattering (or SERS) signals. These findings have guided studies towards optimizing the nanoparticle distance for larger enhancement in Raman scattering process[71].

The substrate should offer reasonable enhancement, be robust, deliver uniform enhancement across its entire surface and it should be fabricated reproducibly. A surface area yielding high enhancement can be possible but producing a substrate that consistently provides the same level of enhancement in every subsequent measurement is more difficult[77].

There are a number of studies with different kinds of effective substrates, including vapor-deposited films, shaped particles and spheres, designed metal surfaces and colloidal suspensions[77,83,84].

The use of multilayer polyelectrolytes in this field is generally based on coating of nanoparticles on film surface or confining inside the film. It is reported in the literature that surfaces having multilayer films containing complexes have porous structure[85]. Thickness, structure and other properties of PEM films can be tuned based on parameters like pH and salt concentration[86]. Thus, homogenous and reproducible substrates can be fulfilled by PEMs prepared by LbL technique. Silicon wafer, glass or quartz can be used as substrates, which are coated with PEMs with

LbL technique. Type of the PE, pH, salt concentration and solvent type can be changed to tune thickness, roughness and other properties of the film[87].

1.4 Conducting Polymers

The concept of conducting polymers (CPs) was first demonstrated by Hideki Shirakawa, Alan Heeger, and Alan MacDiarmid in 1977[88,89]. They showed that a doping process could change the conductivity of polyacetylene many times. The electrical properties of CPs are similar to metals or semiconductors, and their mechanical properties are similar to polymers[90]. CPs are also used in energy conversion and storage devices, such as solar cells and batteries. In addition, they have potential applications in biological electronics, such as sensors and actuators[91,92]. There is a vast number of CPs in the literature. Some of the important examples reported in the literature are polyacetylene (PA), polypyrrole (PPy), polyaniline (PANi) and polythiophene (PTh).

PA is a polymer that can be doped to increase its conductivity. When doped, its conductivity is comparable to that of metals. This led to the hope that PA could be used as a replacement for metals in batteries and conductive wires. On the other hand, conductivity of it decreases with time because of the reactions in which counter ions of the dopants are involved. When oxygen reacts with PA, it forms superoxide anions, which can react with the double bonds in the polymer, breaking them and devastate the conjugation. The breakdown of the conjugation in the polymer chains leads to a decrease in the conductivity of the polymer. This can eventually lead to the degradation of the polymer, as the polymer chains become more and more disordered. This poor stability problem limits the use of PA in commercial applications[93]. Yet, PANi based CPs are reported to be sufficiently stable[94]. Doped PTh and PPy are also reported to be quite stable. Besides, PTh is protected from reaction with oxygen owing to its high ionization potential.

Although conducting polymers have good conductivity and flexibility, their poor stability due to doping and short half-life of conductivity are major challenges to tackle[95]. The problem of stability and insufficient half-life of conductivity is partially solved with the invention of Poly (3, 4-ethylenedioxythiophene) (PEDOT)[96].

The advent of intrinsically conductive polymers was in fact followed by the emergence of polymer composites. These composites gained their conductive properties through the integration of conductive particles into an insulating polymeric matrix. In the initial stages of the experiment, elements like conductive carbon blacks, short graphite fibers, metal-coated glass fibers, and miniature metal particles or flakes were used for the preparation of such composites[97]. There is a noticeable rise in their conductivity once they hit the percolation threshold, the point where the dispersed conductive elements within the non-conductive matrix form a continuous network. After this threshold, their conductivity can potentially reach between 0.5-0.1 Scm^{-1}, if the conductive filler makes up 10-40 % by weight of the overall mixture. The dimensions and configuration of the particles in question heavily influence the percolation threshold. Recently, composites, along with blends and grafts of intrinsically conductive polymers with a non-conductive polymeric substance, have been prepared to enhance their processability and support the mechanical characteristics of them[93].

Over the past decade, significant progress has been achieved in the field of CPs. New conjugated polymers have been synthesized, such as poly(p-phenylene vinylene) (PPV) derivatives, poly(para-phenylene) (PPP) derivatives, polythiophene derivatives etc. [97–99]. Currently, these materials are employed in devices like electrochromic, electroluminescent, and optoelectronic devices, including light-emitting diodes (LEDs) and flat-panel light-emitting displays. They are also used in memory and junction devices, resist and recording materials, biomedical and environmental sensors, shielding materials, corrosion protection, antistatic coatings, catalytic and rectifying electrodes, and conjugated polymer actuators. Further potential applications can be listed as electronically conductive wires and fibers,

batteries, solar cells, Schottky barrier diodes, solid capacitors, and printed circuit board surface finishes, which are also being explored[94,100].

1.4.1 Poly(3,4-ethylenedioxythiophene) polystyrene sulfonate (PEDOT:PSS)

A derivative of polythiophene, PEDOT, offers high conductivity along with excellent transparency and stability. These properties are important in various applications, such as solar cells, electrochromic devices and supercapacitors[101,102]. Structure of PEDOT chain is given in Figure 1.4. It consists of repeating units based on the 3,4-ethylenedioxythiophene (EDOT) monomer. The ethylenedioxy bridges give the polymer chain certain flexibility and help in maintaining its stability, while the thiophene ring imparts the conjugated system which is responsible for its conductive properties[103]. A total of +1 charge is carried in 3 EDOT monomers. The inherent insolubility of PEDOT restricts its optoelectronic applications. PEDOT:PSS is prepared by polymerizing PEDOT emulsion with a surfactant known as polystyrene sulfonate (PSS) [96]. It is a dark blue opaque solution, offering a high degree of versatility in its applications. It can be transformed into a transparent and stable film on the surface of a flexible matrix or rigid substrate through a solution treatment process. Among CPs, PEDOT has gained significant interest in both academic and industrial circles owing to its relatively high conductivity, excellent stability under normal conditions, and the potential to be transparent within the visible light spectrum[104].

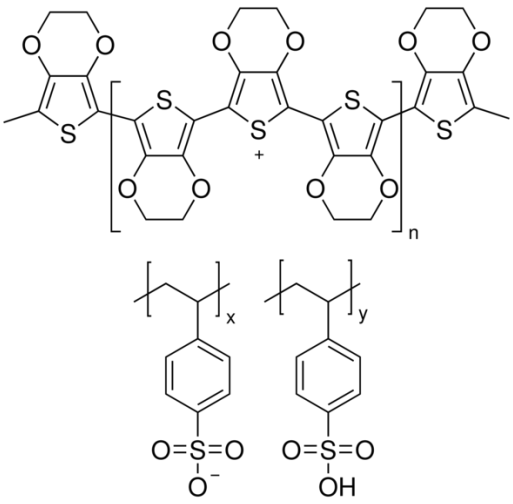


Figure 1.4. Structure of PEDOT with a total of +1 charge carried in 3 EDOT monomers (top) and styrene sulfonate monomer of PSS having -1 charge (bottom x) and protonated styrene sulfonate monomer (bottom y).

PEDOT:PSS is one of the most preferable conjugated polymers used in organic optoelectronics thanks to its improvable conductivity, solubility in water and ability to form high-quality thin transparent films during the manufacturing process of optoelectronic devices[105]. It has gathered considerable interest as a self-sufficient conductive electrode material, as well as thin buffer layers in organic electronic devices like photovoltaic cells. It's important to point out that the aqueous solution of PEDOT:PSS is a commercially available product that comes with varied electrical properties[106].

On the other hand commercial PEDOT:PSS includes excess amount of PSS^-Na^+ and PSSH to provide high solubility to PEDOT:PSS[107]. These moieties affect the charge current adversely. Therefore, they need to be removed from the medium to increase conductivity values. However, PEDOT:PSS becomes water-insoluble with this process since at the right stoichiometric amounts, PEDOT and PSS form a complex that aggregates or clumps togethers[108].

1.4.1.1 Computational Studies on PEDOT:PSS

Since PEDOT was initially synthesized by scientists at Bayer AG[96], a vast wealth of knowledge has been gathered on its material properties. It is used in various studies related to its morphological, structural, electrical, and optical characteristics, as well as its various applications in different types of devices[109]. The properties of PEDOT, e.g. flexibility, conductivity, solubility, are heavily influenced by the counter ion in the solution matrix and the arrangement of the PEDOT chains if it is adsorbed on a substrate. As a result, for PEDOT to be effectively used in its many potential applications, it is important that it is made and prepared in a manner that ensures it has the best possible performance [110].

Techniques such as density functional theory (DFT) and time-dependent DFT (TDDFT) have been employed in the studies related to the electronic structure and optical absorption spectra of PEDOT at a range of oxidation levels of it. Most of the studies in this field is experimental, often using a "trial-and-error" approach. Simulations and molecular modeling offered only minimal information[111]. Although molecular modeling is a commonplace tool in many material science disciplines, its application remains rather unrefined and restricted in PEDOT studies. Consequently, the absence of theoretical knowledge concerning key characteristics of material properties and device operations often results in misunderstandings and contentious issues[111].

1.4.1.2 Conductivity Enhancement in PEDOT:PSS

Since the 1980s, the electronic structure of thiophene-based CPs and their derivatives, including PEDOT, has been a focal point of rigorous theoretical investigation. Previous studies largely hinged on semiempirical models and an assortment of Hartree-Fock (HF) methods[112,113]. Over the past ten years, DFT has ascended to become an important approach for characterizing the electronic properties of a wide range of materials, including CPs[114]. The DFT method is aptly

suited to accurately factor in the Coulomb interaction, which results in the elimination of spin degeneracy[115].

Positively charged polarons and bipolarons are the charge carriers in p-doped conducting polymers including PEDOT[116]. A polaron is a quasiparticle characterized by a charge Q of +1e and a spin S of 1/2, which signifies a hole that is confined within several monomer units due to the potent interaction between the electron and the lattice. This interaction results in the variation of the bond lengths in the polymer chain from an aromatic to a quinoid structure. A bipolaron, on the other hand, is a localized spin-degenerate quasiparticle (S = 0) in which two holes of opposite spins exist in the same spin-degenerate energy level[111].

It was reported that conductivity of PEDOT:PSS was increasing with thermal and light treatment, organic solvent treatment, treatment with ionic liquids, surfactants, salt solutions, zwitterion, acid and alkali treatment[111].

In a study conducted by Ouyang and coworkers[117], 500 fold increase in conductivity of PEDOT:PSS was achieved, from 0.2 Scm^{-1} to 100 Scm^{-1}. Same group treated PEDOT:PSS with aqueous solutions of various salts. They showed that soft cations like Cu^{2+}, Ag^{+} and In^{3+} increased the conductivity by 2 orders of magnitude while the effect of hard cations like Li^{+}, Na^{+}, Mg^{+} was negligible[118].

1.4.1.2.1 Solvent and Post-Treatment with Organic Solvents

Over the past several decades, substantial efforts have been put forth to enhance the conductivity of PEDOT:PSS, with numerous strategies reported to have significantly elevated its conductivity. Beyond the physical techniques such as thermal and light treatments, the integration of a polar organic compound with a high boiling point into a PEDOT:PSS aqueous solution, or treating PEDOT:PSS films with these compounds were used as chemical approaches[119].

In 2002, Kim and his co-workers reported that altering solvents to dimethyl sulfoxide (DMSO), N,N-dimethyl formamide (DMF), or tetrahydrofuran (THF) enhanced the

conductivity of PEDOT:PSS films. There was an approximate two-fold increase in conductivity at room temperature when DMSO was introduced, while the increment was less substantial when DMF or THF were used[120].

Using polar organic solvents (including DMSO, ethylene glycol (EG), DMF, THF, glycerol, sorbitol, methoxyethanol, diethylene glycol, dimethyl sulfate, meso-erythritol, and xylitol) PEDOT:PSS enhanced conductivity values, ranging from 0.61 to 677 S cm $^{-1}$ [111].

Ouyang and his team managed to increase the conductivity of PEDOT:PSS films by more than two orders of magnitude by introducing solvents like EG, meso-erythritol, and 2-nitroethanol into the PEDOT:PSS aqueous solution[121].

Onorato and colleagues found that sorbitol-treated PEDOT:PSS films engage in a cyclodehydration reaction, leading to the formation of 1,6-anhydrosorbitol. They also provided evidence that both sorbitol and 1,6-anhydrosorbitol persist in the film, contributing to the enhancement in the conductivity[122].

1.4.1.2.2 Acid Treatment

Cruz and his co-workers introduced a minor quantity of diluted sulfuric acid to a PEDOT:PSS solution to fabricate thin films. They achieved conductivities of around 100 Scm^{-1}, a value which is approximately 1400 times higher than that of the unmodified PEDOT:PSS films. Intriguingly, when hydrochloric acid, another potent acid, was utilized for comparison, a significant rise in conductivity was not detected. This outcome is attributed to a pH lower than the optimal value and a secondary doping effect[123].

Aleshin and his team reported that PEDOT:PSS films cast from solutions with pH values ranging from 0 to 3.34 could achieve conductivity values as high as 20 S cm^{-1}. Concurrently, Xu and co-workers reported that the conductivity of PEDOT:PSS composite films depends on the pH value when treated with acids, specifically hydrochloric acid or oxalic acid[124].

Treating PEDOT:PSS film with 1M H_2SO_4 at 160 °C for three times, Xia and coworkers measured a conductivity as high as 3065 Scm^{-1} [125]. Kim and coworkers achieved a 4350 Scm^{-1} conductivity with H_2SO_4 treatment. They reported the formation of solution-processed crystalline structures in PEDOT:PSS through post-treatment with H_2SO_4, under strictly controlled conditions. The proposed explanation for this enhancement is that the H_3SO4^+ and HSO_4^- ions, resulting from the autoprotolysis of H_2SO_4, bind PEDOT and PSS nanofibrils together, causing the typically disordered PEDOT:PSS to become highly ordered[126]. Gueye and coworkers reported a conductivity as high as 5400 Scm^{-1} by controlling the crystallization of the PEDOT chains and using HSO_4^- as dopant[127].

Ouyang and his co-workers noted an improvement in the conductivity of PEDOT:PSS when it is subjected to a post-treatment with mild and weak organic acids. These acids included acetic acid, propionic acid, butyric acid, oxalic acid, malonic acid, pyruvic acid and methanesulfonic acid[128]. The effects of acid concentration and temperature on the conductivity have been explored. PEDOT:PSS films displayed metallic properties at room temperature, and this method was considered superior to the use of highly strong and corrosive acids such as sulfuric acid. Notably, the conductivity increased to approximately 3300 Scm^{-1} after treatment with 8 M methanesulfonic acid[129].

In a recent study, McCarthy and his team introduced the idea of using formic acid as a treatment for PEDOT:PSS films. This approach resulted in an astounding increase in conductivity, with improvements up to 4 orders of magnitude[130]. Furthermore, straightforward solution-processed techniques suggested using an organic acid and an organic solvent. Notably, Kang and his research team revealed that immersing PEDOT:PSS films in a HCl-methanol solution significantly improved the conductivity, elevating it by nearly 3 orders of magnitude[131].

1.4.1.2.3 Molecular Mechanism of Conductivity Enhancement

In a study by Crispin and coworkers PEDOT:PSS structure was analyzed with XPS during the addition of organic solvent. They proposed that, PSS was removed from the surface of PEDOT:PSS film during solvent treatment, resulting in the enhancement of conductivity since PEDOT was the conducting part of the film[132]. Mengistie and coworkers suggested that, after organic solvent treatment and removal of PSS, PEDOT with coiled structure turns into extended coil or linear structure[133]. In another study by Ouyang group, conductivity enhancement was as a result of the change in resonant structure of PEDOT from benzoid to quinoid structure[134]. In a study by Yıldırım and coworkers, conductivity enhancement of PEDOT:PSS with DMSO treatment was examined with density functional theory (DFT) calculations, molecular dynamics (MD) studies and hydrophobicity studies. Pairwise interactions between DMSO and different structures derived from PEDOT:PSS system were investigated. Strong hydrogen bonding between sulfonic acid H in PSSH and O in DMSO was shown in this study. Moreover hydrogen bond between methyl H in DMSO and sulfonate oxygens in PSS. It was shown that PSSH-DMSO interaction was the strongest pairwise interaction compared to other possible pairs like PEDOT-DMSO, PSS--DMSO etc. In addition, PSSH is had weak interaction with PEDOT, PSS- and $PEDOT^+$. Since PSSH is the insulating component of PEDOT:PSS system, removal of the PSSH with DMSO was suggested to be the enhancement mechanism. Additionally, the mechanism was confirmed with molecular dynamics simulations[135].

In the study of Tounakti and co-workers, conductivity of the PEDOT:PSS is measured *in situ* during treatment with DMSO with and without water[106]. With the help of XPS and IR measurements, they conclude that PSS structure reorganizes to a planar and stretched form. This process is reported to be realized as soon as the PEDOT:PSS is in contact with the solvent. Additionally, short chains of neutral or charged PSS (HPSS, NaPSS) are removed with the help of the solvent. Similarly, to

the reports in the literature, they propose that remaining PEDOT:PSS chains are insoluble in any solvent and make an organized structure upon drying.

To sum up, while there exist numerous studies on the mechanism behind the enhanced conductivity of PEDOT:PSS, the reasons and methods for this improvement are diverse and frequently disputed. It is commonly agreed that more extensive studies are required to elucidate the mechanism of this enhanced conductivity.

1.5 Mechanism of Aggregation Control by Detergent and Dispersants

1.5.1 Soot and Sludge Formation in Engines

When a passenger car engine does not reach a minimum operational temperature while working, steam and CO_2 may bypass the piston rings, condensing in the cool crankcase and subsequently producing liquid H_2CO_3, which corrodes iron and steel. This situation is particularly common when the engine is cold and runs at low speeds. Under these conditions, the combustion process is inadequate and incomplete[136].

Soot is a kind of ultrafine granular and abrasive particle, which is produced in the engines as a by-product of incomplete oxidation of fuel. These ultrafine particles aggregate over time. Size of sludge, which is another kind of inadequate combustion, is not as large as that of soot. Soot and sludge, both cause an increase in the viscosity of the lubricant oil[137,138].

The process of creating sludge deposits takes place in three primary stages. Initially, sludge forms in the combustion chamber due to an incomplete reaction between oxygen and fuel. Following this, these structures undergo various interactions with the lubricant oil, making the second phase[139,140]. The final phase involves the clumping together of these precursors to yield a substance that is insoluble in oil[141]. Therefore, incorporating detergent and dispersant additives in the lubricating oil is necessary to avoid the formation of these insoluble particles.

A key element, that negatively influences oil usage, is the build-up of deposits in the piston-cylinder assembly. Cylinder liners are shaped using a plateau honing process, resulting in a surface texture with flat plateaus and deep valleys, which hold oil and debris. When these deep valleys are covered with deposits, the operational surface becomes smoother, diminishing its ability to store oil and negatively affecting the role of oil for lubrication. This leads to increased oil consumption and requires additional maintenance[142].

In heavy-duty diesel engines, a significant number of research have been carried out about the piston's oil and deposits. The deposits found on the top land of the piston comprise both organic as organic soot and oxidized oil in the form of resin and inorganic substances, inorganic metals and salts (ash)[143]. Due to the unavailability and the large array of variables in the process, investigating the mechanism of the soot formation is a significant challenge. Additional difficulties are experienced when attempting to measure and inspect these deposits. The method of photographing cylinder running surfaces and subsequently rating the deposits is subjective and inadequate, while employing a scanning electron microscope (SEM) is a time-intensive process[142].

Commonly, surface profilometry is utilized, and a reduction in roughness is often linked with deposit buildup. However, this can be misleading due to simultaneous wear and tear. In the area of contact mechanics and wear modeling, understanding the transformations of the original surface caused solely by wear becomes crucial, emphasizing the significance of accurate measurements and characterizations of the deposits[142].

1.5.2 Lubricants

Lubricants, from ancient times, have evolved into a substantial global industry. The progression of contemporary engine and transmission technologies would have been unattainable without the advancements in lubricant additive chemistry and lubricant

formulation. Regardless of their application, the oils employed for the lubrication of internal combustion engines were exposed to a vast and diverse array of temperatures and operating conditions[136].

A lubricant has to perform several vital tasks simultaneously. Namely, the lubricant has to;

- serve as a medium for heat transfer
- generate a sufficiently thick film to avoid direct metal-on-metal contact
- safeguard all engine components against chemical assault from potentially corrosive by-products arising from fuel combustion or lubricant oxidation
- act as a reservoir for all solid and liquid contaminants that make their way into the lubricated regions[138].

When formulating lubricating oils, it's essential to consider protections against both chemical and mechanical wear for engine parts. Over recent years, there have been significant improvement to the wear resistance of engine oils. This progression has been tremendous due to the integration of relatively minor quantities of additives, rather than alterations in the refining methods used on the petroleum base stocks composing the oils[138].

The ideal lubricant is expected to prevent wear on an engine's piston rings and cylinder liners unless there should be enough lubricant when the pistons start to move up and down. However, in real circumstances, this process may not be as effective as it is expected. Even a few strokes of a dry piston ring on a dry cylinder liner can cause significant surface damage, which takes extensive operation to repair. To ensure proper lubrication is quickly established when an engine starts; the lubricant oil should have the lowest possible viscosity under current operating conditions. This limiting viscosity is mainly determined by oil consumption characteristics, although the temperature of the ring belt and bearing design also plays an important role in protection of the engine components. It is therefore crucial that the lubricant's viscosity remains as stable as possible regardless of temperature changes. In other words, it should possess a high viscosity index[144].

1.5.2.1 Composition of Lubricants

Today, engine oils are composed of a vast array of additives mixed with base oils[145,146]. Lubricants contain a variety of additives, whose type, quantity, and quality are adjusted based on their intended function[147].

Lube oil additives are substances that either introduce a new, beneficial attribute not naturally occurring in the oil or amplify a favorable characteristic already partially present in the oil[148]. Despite the development of numerous types of additives to address specific lubrication requirements, their primary functions are to curb the oxidative or thermal degradation of an oil, minimize wear, stifle rust and corrosion, reduce the formation of detrimental deposits on lubricated components, and avert destructive metal-to-metal contact[149].

Lubricating additives are categorized based on their function and divided into three distinct groups, which are listed as;

- Additives intended to safeguard the finished lubricant during use by inhibiting chemical alterations or decay.
- Additives are meant to shield the machinery either from detrimental residues or from the failure of lubricants to operate correctly.
- Additives are devised to enhance the current physical properties of the lube oils or introduce new attributes[136].

1.5.2.1.1 Dispersants and Detergents

Over the past several years, there has been a significant rise in the utilization of detergent additives and oxidation inhibitors in lubricant oils. Detergents were initially integrated into lubricant oils to deal with the over-accumulation of fuel soot and carbon in the ring zone and piston skirt regions of diesel engines. Oils with detergents have proven remarkably effective in diminishing not only the deposit accumulation but also the wear and tear on piston rings and cylinder liners. Oxidation

inhibitors are included in oils to increase their resistance to oxidation in high-temperature operations, as oil oxidation can lead to the creation of acidic substances which can corrode certain alloy bearings such as copper-lead currently in use, and can also cause undesirable varnish and sludge deposits[138].

Detergents, composed of a surface-active polar group, are capable of chemically bonding to the metal surface, forming a protective layer that helps maintain the cleanliness of engine's metal components. Not only do these detergents clean, but they also neutralize acidic byproducts, thereby curbing corrosion, rust, and engine deposit formation[150].

Conversely, dispersants function to distribute and maintain the suspension of sludge particles. This helps prevent the creation of sludge at low temperatures [151]. Currently, multifunctional additives, serving both as detergents and dispersants, are in use. The primary roles of these multifunctional dispersants and detergents are;

- maintaining engine cleanliness
- neutralizing acids
- solubilizing and dispersing sludge particles in oil
- mitigating deposit formation[152].

Examples of well-recognized detergents include sulfonate (metal, asshless or overbased), salicylates, alkyl phenolates, carboxylate, polyisobutylene succinimides, Mannich adducts, polyethylene glycol esters, polyol poly-(12-hydroxy stearic acid), phosphates, and phosphonates in their structures[152].

While the precise working mechanism is not fully comprehended, it is accepted that dispersant and detergent can function in two distinct manners; they can either suspend particles and precursors of deposits in the oil to mitigate deposit formation, or they can form a protective layer on the metal surface to obstruct deposit formation. This is likely accomplished by mitigating the accumulation of carbon-based deposits from heated surfaces to prevent the clumping of dirt through the creation of stable micelles. The oxidative breakdown of hydrocarbons leads to the formation of

insoluble colloidal particles. The stability of these particles is counteracted by the Van der Waals forces which cause the aggregation due to attractions of these particles. In the absence of any forces resisting the Van der Waals forces, the particles quickly agglomerate. However, when detergent and dispersant are present, this agglomeration decline or does not occur. Dispersant and detergent can either solubilize the oil-insoluble polymerized byproducts whose formation is observed due to oil and fuel breakdown or at least keep it dispersed. This activity prevents or mitigates the precipitation and deposition of colloidal materials on the metal surface in the form of soot and sludge[152].

Initially, neutral metal salts of long-chain organic acids, commonly alkyl-aromatic sulfonates like sodium dodecyl benzene sulfonate, were employed in engine lubricants[136,144]. These compounds function as surfactants because their hydrocarbon tail exhibits enough oleophilicity to ensure the detergent's full compatibility and solubility in the base oil. Currently, the typical hydrophobic part used in commercial applications comprises an 8-20 carbon chain either straight or slightly branched. These detergents have found equally significant applications in various other types of lubricants, including gear oil, hydraulic fluids, automatic transmission fluids, and industrial oils[152].

New generation ash-free additives include copolymers of an oil-solubilizing monomer like decyl methacrylate, vinyl decyl ether, or a high molecular weight olefin, combined with a monomer including polar substituents, such as amino-alkyl acrylate or poly-(oxy-ethylene)-substituted acrylate, amine salts, amides, and imides of oil-soluble monocarboxylic or dicarboxylic acids like stearic acid, oleic acid, tall-oil acid, and high molecular weight alkyl or alkenyl-substituted succinic acid[153].

Typical ashless dispersant and detergent additives include succinimides, high molecular weight ester-amides, and Mannich bases. These ashless lubricating oil detergents and dispersants are more effective than traditional metal salts at controlling the accumulation of sludge and varnish deposits during low-temperature gasoline engine operation. An additional significant benefit of these additives is that

they prevent the formation of ash typically created when metal salt detergents decompose[154].

CHAPTER 2

INVESTIGATION OF POLYELECTROLYTE MULTILAYERS FOR SURFACE ENHANCED RAMAN SPECTROSCOPY (SERS)

2.1 Computational Methods

2.1.1 Aim of the Study

The aim of this study is to use MD simulations to investigate the nature of polyelectrolyte multilayers to determine some of the parameters for SERS applications. Although there are many experimental studies about the LbL assembly of polyelectrolytes, there is a limited number of computation and simulation studies in this field. To the best of our knowledge, there is no computational study including polyallylamine hydrochloride/polyacrylic acid (PAH/PAA) and polyallylamine hydrochloride/tannic acid PAH/TA films in the literature. Kotov contributed to Gibbs energy change as a result of the adhesion of polyelectrolytes on a substrate which is coated with polyelectrolytes with opposite charges and it is reported that hydrophobic attractions play an important role in multilayer formation[155]. In another study by Netz and coworkers, parameters such as pH and ionic strength were studied experimentally. Additionally, hydrodynamic radiuses were calculated in various conditions and confirmed with MD simulations[156]. Cranford and coworkers used steered molecular dynamics (SMD) simulations to determine the bonding interaction between PAA and PAH quantitatively. Binding force between layers was reported between 15 to 40 nN in the pH range of 2.5 to 10[157]. There are few numbers of computational studies with tannic acid either. In a study conducted by Alechinsky and coworkers, the settlement capacity of TA to biological membranes was evaluated with MD simulations and regardless of whether gallic ends were protonated or not, it is reported that TA interacts with the membrane[158].

Within the scope of this study, citrate-capped AuNPs models were constructed for their all-atom and coarse-grained MD simulations on PAH/PAA and PAH/TA multilayers. As discussed in Section 1.3.1.2, it is essential to prepare homogenously dispersed NPs with an optimum distance between them to reach the best enhancement from the Raman scattering of the molecules interacting with these NPs. Aggregation and agglomeration of the NPs are undesired for this purpose. In the junctions between the NPs, hot spots occur because of surface plasmon generated on NPs. At equilibrium conditions, deviation in the positions of the NPs is undesired since it can decrease the efficiency of plasmon generated on the surface and may also cause aggregation of the NPs.

In experimental studies conducted by the members of our lab, different combinations of PEs were used for the preparation of PEMs, e.g. PAH/PAA, Polydiallyldimethylammonium chloride (PDADMAC)/PAA, PAH/PSS, PAH/TA which were used as SERS substrates. In addition to PE types, the number of layers in these PEMs were studied to obtain the best SER signals for crystal violet molecule. Moreover, different procedures for the LbL preparation of PEMs were tested such as linear and exponential growth PEMs. There are many other aspects of these experimental studies, which are out of the scope of this thesis study. Exponential growth PAH/PAA is shown to be increasing the SER signal compared to linear growth PAH/PAA in these experimental studies. The first objective of this chapter was to compare the linear and exponential growth models of the PAH/PAA multilayers by means of the mobility of AuNPs located on the top of the multilayers. As a second objective, the PAH/PAA model was mapped into the Martini force field to run coarse-grained MD simulations. In these simulations, crystal violet was used as an analyte in the experimental studies. They were also mapped into the Martini force field. As discussed in the Introduction (1.3.1.1) part, chemical enhancement is a result of the chemical interaction between the analyte molecule and the NPs on the substrate. Hence, the orientation of the analyte molecules on the surface and their interaction with citrate, AuNPs and PEMs may have significance on the resulting SER signal efficiency. As a part of the second objective, the orientation of the citrate

model on the surface of the substrate model and its interaction with citrate molecules, AuNPs and PEMs were investigated. After completing a successful coarse-grained MD simulation of crystal violet and citrate-capped AuNPs on PAH/PAA multilayers with similar results as in all-atom MD simulations, PAH/TA multilayers were prepared. The third objective of this study was to make a comparison of the mobility of citrate-capped AuNPs on PAH/PAA coarse-grained MD simulation with those on PAH/TA multilayers. Besides, the orientation of crystal violet and its interactions with citrate, AuNPs and PEMs were studied. The last objective of this chapter was to compare the numbers of PAH/TA bilayers by means of mobility of the citrate-capped AuNPs and orientation of citrate molecules.

In this study, an important majority of the interactions rely on 12-6 and 9-6 Lennard-Jones (LJ) potentials, which are defined for non-bonded, i.e. intermolecular interactions. Heinz and coworkers presented 12-6 and 9-6 LJ parameters for some of the metals[159]. Throughout this study, LJ interactions for AuNPs were used as reported in their study. In a study conducted by Salassi and coworkers a coarse-grained model of citrate-capped AuNPs were prepared for their interactions with lipid bilayers [160]. Atom to bead mapping of citrate molecules to Martini force-field is inherited from their study. In the literature, there is no study on tannic acid for coarse-grained MD simulations with Martini force fields. On the other hand, there are studies on coarse-grained MD simulations of gallic acid [161,162].

2.1.2 Model Preparation

All-atom model of PAH/PAA based on the experimental studies being conducted by our group. Initial small molecules, monomers, gold nanoparticles and polymers were modeled using Discovery Studio. For all-atom molecular dynamics simulations, simulation cells were also prepared. Polymer consistent force field (PCFF) was used for bonded and non-bonded interactions. Scienomics MAPS 4.4 and 4.5 were utilized to construct cells and apply PCFF to the prepared models.

For the preparation of coarse-grained models of PAH/PAA, PAH/TA, sodium citrate and crystal violet, MAPS Atomeso Converter tool was used to map the atomic structures to the coarse-grained beads. Once the models were created, Moltemplate was utilized to prepare polyelectrolyte multilayers including the nanoparticles, citrate ions and crystal violet. Scripts were written in Python for the conversion of input files to Moltemplate input files.

Simulations were carried out in LAMMPS. For long-range interactions particle-particle particle-mesh solver (PPPM) was used.

Data visualization and calculations were carried out with VMD. The simulation box had periodic boundary conditions (PBC) in the x, y and z directions.

2.1.2.1 Construction of Gold Nanoparticles (AuNPs)

Gold nanoparticles with 10.0 and 5.0 nm diameter, consisting of 30920 and 3925 Au atoms was modeled as shown in Figure 2.1. For the short-ranged repulsion-dispersion interactions of Au, the LJ parameters were used from the study by Hendrik Heinz and coworkers who presented ε_0 = 5.29 kcal/mol and σ = 2.629 Å[159] in their study. For an AuNP having 10.0 nm diameter, the number of Au atoms to construct the model was 30920.

One Au atom was considered as one Au bead in coarse-grained MD simulations. LJ parameters for interactions Au beads with the other beads were used from the study by Salassi and co-workers[160].

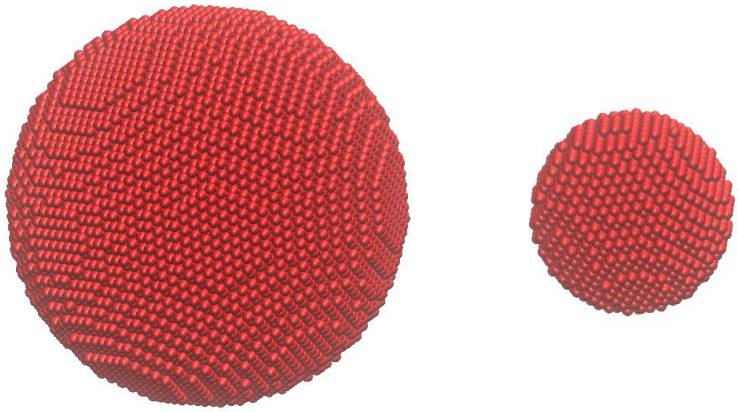


Figure 2.1. Gold nanoparticles with 10.0 nm (left) and 5.0 nm (right) diameter consisted of 30920 and 3925 Au atoms, respectively.

2.1.2.2 Construction of Sodium Citrate

Packmol was used to distribute 300 citrate anions to cap a gold nanoparticle in all-atom simulations. For charge equilibrium, 900 Na^+ cations were located in the same area randomly.

In CG MD simulations, a citrate ion was mapped into four beads as reported in the paper of Salassi and coworkers[160]. In Martini mapping, as mentioned before, up to four heavy atoms are represented as one single bead having the total mass of its constituents. As shown in Figure 2.2, OH group was mapped into an N_{cit} bead in the mapping of a citrate anion. It is a modified version of N_{da} type of bead, which is an apolar type of bead as summarized in Table 1.1. Three COO^- groups of a citrate anion were mapped into a Q_{cit} type of bead, which is modified from a Q_a type of bead. Q_a beads are charged beads having hydrogen bond acceptor characteristics. The charge of citrate was balanced with three Na^+ ions, each of which is represented as a Q_0 type of Martini bead which is considered to include the first hydration shell in the representation.

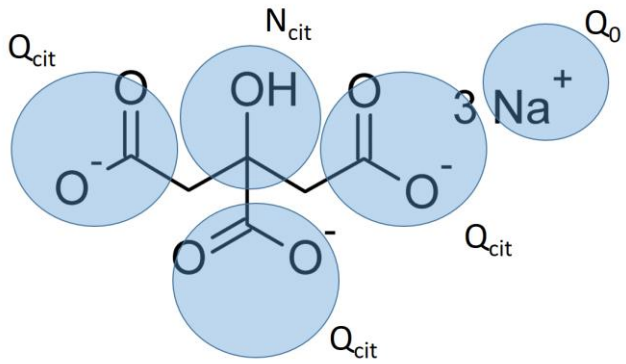


Figure 2.2. Mapping of one sodium citrate structure into Martini force field.

2.1.2.3 Construction of PAH/PAA Multilayer

2.1.2.3.1 All-Atom MD Simulations

PAH/PAA film was modeled based on both linear and exponential growth observed in experimental studies. Linear chains of PAH and PAA were constructed and one linear chain was superimposed to the other linear chain. For the exponential growth model, the linear shape of the chains was distorted manually and again one distorted chain was superimposed on the other distorted chain. One PAH/PAA layer consisted of one PAH containing 80 monomers and 962 atoms and one PAA chain containing 80 monomers and 642 atoms as shown in Figure 2.3 and Figure **2.4**, respectively.

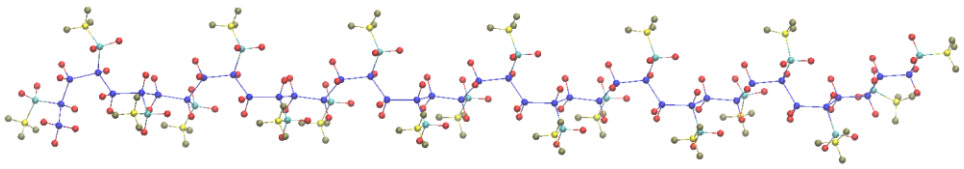


Figure 2.3. One PAH_{20} chain prepared for simulations in LAMMPS, visualized with VMD.

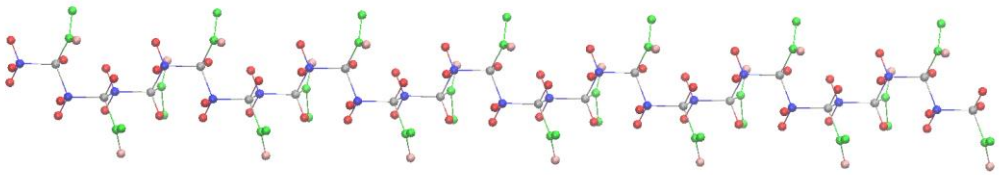


Figure 2.4. One PAA_{20} chain prepared for simulations in LAMMPS, visualized with VMD.

Once the PAA and PAH chain models were constructed, they were placed together to make a PAH/PAA layer and this layer was multiplied 1x3x8 times in x, y and z direction. Then, this multilayer was placed under one Au nanoparticle capped with citrate in simulation box. Total number of atoms was 48721 in the simulation box. The simulation box is shown in Figure 2.5.

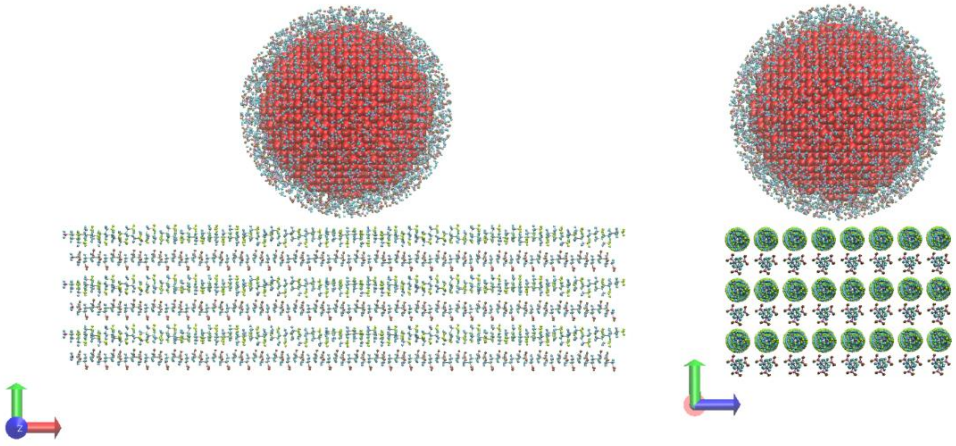


Figure 2.5. AuNP capped with citrate, together with PAA-PAH (linear) layer.

For modeling linear growth process for computational study, PAH chain was positioned at the top of PAA chain as given in Figure 2.5. These planar shaped

structures were bent for preparation of exponential growth model of PAH/PAA layer as given in Figure 2.6.

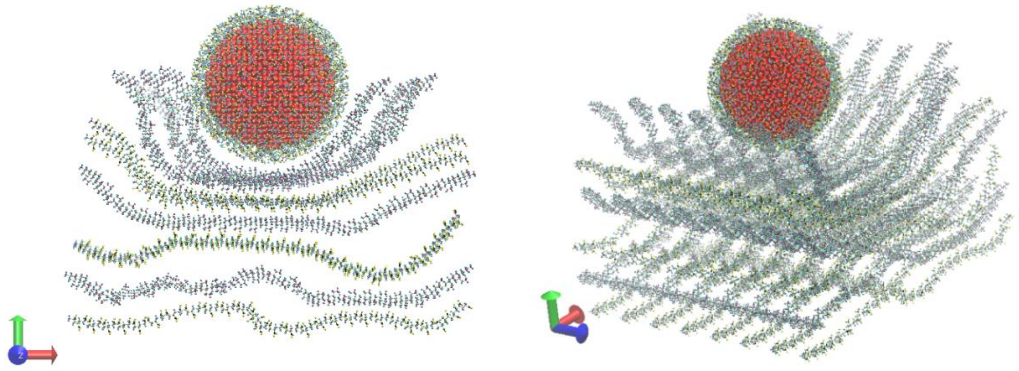


Figure 2.6. AuNP capped with citrate, together with PAA-PAH (exponential) layer.

The initial structure was minimized using the steepest descent algorithm implemented in LAMMPS. The stopping criteria for energy and force are $1.0x10^{-4}$ and $1.0x10^{-6}$ (kcal/mol)/Å, respectively. In the general procedure of minimization, iterations are terminated when one of these tolerances is satisfied for the energy or force in subsequent time steps. Maximum number of iterations was set as 1000 and the maximum number of force and energy evaluations was set as 10.000 at which minimization was terminated. The time step was 1 fs. An NPT ensemble and a Nose-Hoover thermostat and barostat were used at 300 K and 1.0 atm for optimization of the cell for 0.8 ns. Then an NVT ensemble and a Nose-Hoover thermostat at 300 K were used. Temperature was kept constant at 300 K for 1.2 ns.

2.1.2.3.2 Coarse-Grained MD Simulations

In coarse-grained simulations, one acrylic acid monomer in PAA was represented as one charged hydrogen bond acceptor type bead (Q_a) with a -1 charge. Allylamine in PAH was represented as a charged particle (Q_0) with a +1 charge. In all-atom MD

simulations, PAA and PAH chains contained 80 monomers as described in the previous section. Different from all-atom MD simulations, the number of monomers was increased to 240 in order to have 3 AuNPs on the top of PAH/PAA multilayers as shown in Figure 2.7 and Figure 2.8 for linear and exponential growth films, respectively. One PAH/PAA bilayer consisted of one PAA chain containing 240 monomers which were represented as 240 beads and one PAH containing 240 monomers which were represented as 240 particles as shown in Figure 2.7. One PAH/PAA bilayer is multiplied 1x3x12 times in x, y and z directions to prepare a multilayer structure. Then this multilayer structure was placed under three AuNPs capped with citrate in a simulation box.

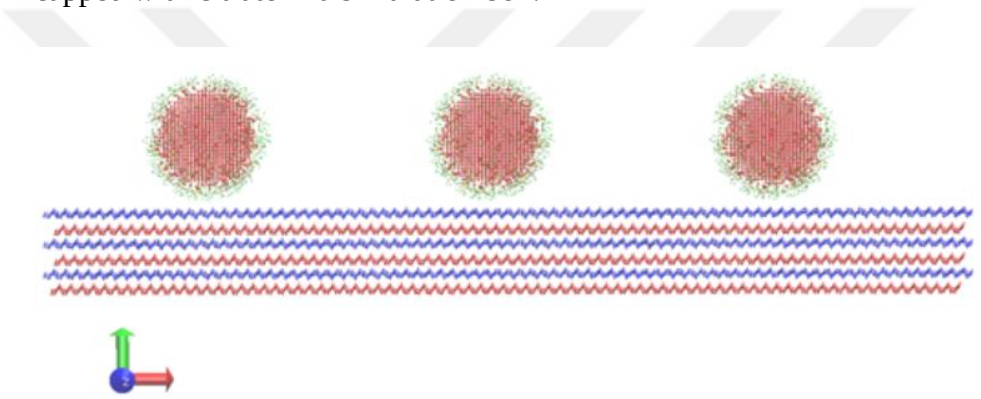


Figure 2.7. CG model of AuNP capped with citrate, together with PAH/PAA (linear growth) multilayer.

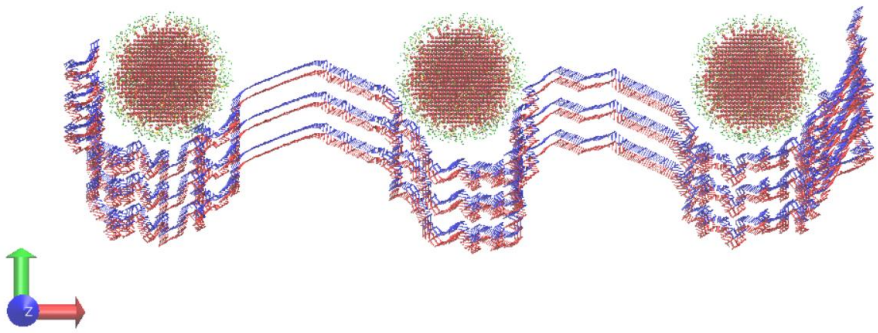


Figure 2.8. CG model of AuNP capped with citrate, together with PAA-PAH (exponential growth) multilayer.

2.1.2.3.3 Construction of Crystal Violet

A crystal violet molecule was mapped into the Martini force field as shown in Figure 2.9 (left). The dimethyl ammonium group having a +1 charge on this structure was mapped into a Q_0 bead, which is a type of charged bead without donating or accepting a hydrogen bonding capability as summarized in Table 1.1. The other two dimethyl amine sides were mapped into N_a type of beads, which is a non-polar type of bead and acceptor for hydrogen bonding. Two aromatic rings connected to these two dimethyl amine ends were mapped into six SC_4 types of beads, which is an apolar type of bead. The "S" character before C_4 indicates a ring structure. The remaining part was mapped into two C_4 types of beads.

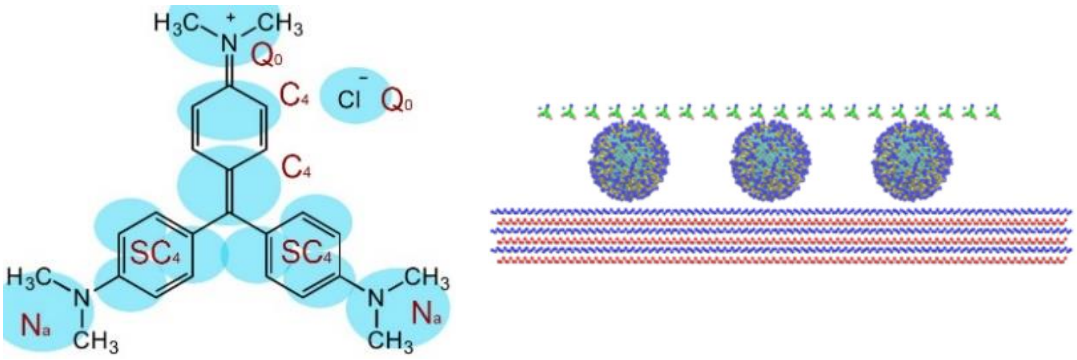


Figure 2.9. Mapping of crystal violet and Cl^- anion (left) and initial structure of PAH/PAA-AuNP with crystal violet (right).

Crystal violet molecules were placed onto the top of AuNPs utilizing Moltemplate Software builder during the initial cell preparation for CG MD simulations.

2.1.2.3.4 Construction of PAH/TA Multilayers

Tannic acid was mapped into the Martini force field as shown in Figure 2.10. Aromatic rings in the gallic acid sides bonded to –OH groups were mapped to polar SP_4 beads. In mapping atoms to Martini beads, the general practice is to map four heavy atoms into one bead as summarized in Table 1.1. Besides, to make a rigid structure having the beads closely connected, two or three heavy atoms were represented as one bead in the ring structures and these types of beads were implemented using the same rules. The only difference is that their type symbols start with an additional "S" character. The atoms in the aromatic rings without polar groups were mapped into SC_4 type beads. $-COO^-$ groups in the gallic acid are represented as non-polar N_a beads, which are beads having acceptor characteristics in hydrogen bonding[162].

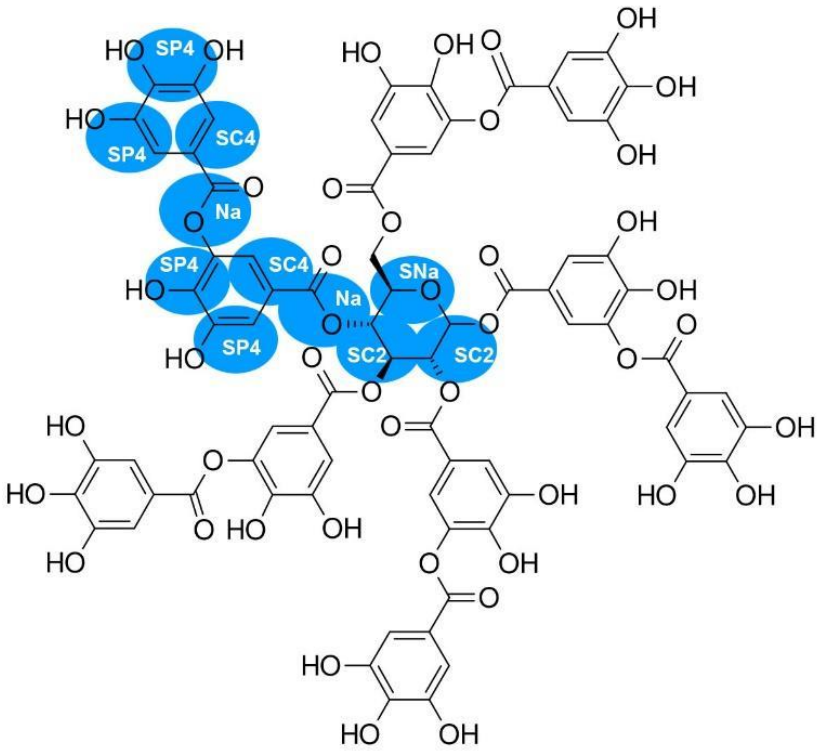


Figure 2.10. Mapping scheme of tannic acid molecule.

In preparation of PAH/TA multilayers, 6 PAH chains having 240 monomers were placed in the YZ plane and 72 TA molecules were placed on the top of these 6 PAH chains as shown in Figure 2.11. This layered structure of PAH/TA was repeated three times in the Z-direction to prepare multilayer films. The charge of one TA molecule was set to -4 to balance the charge with PAH. Similar to the PAH/PAA section, this multilayer film was placed under three AuNPs capped with citrate in the simulation box.

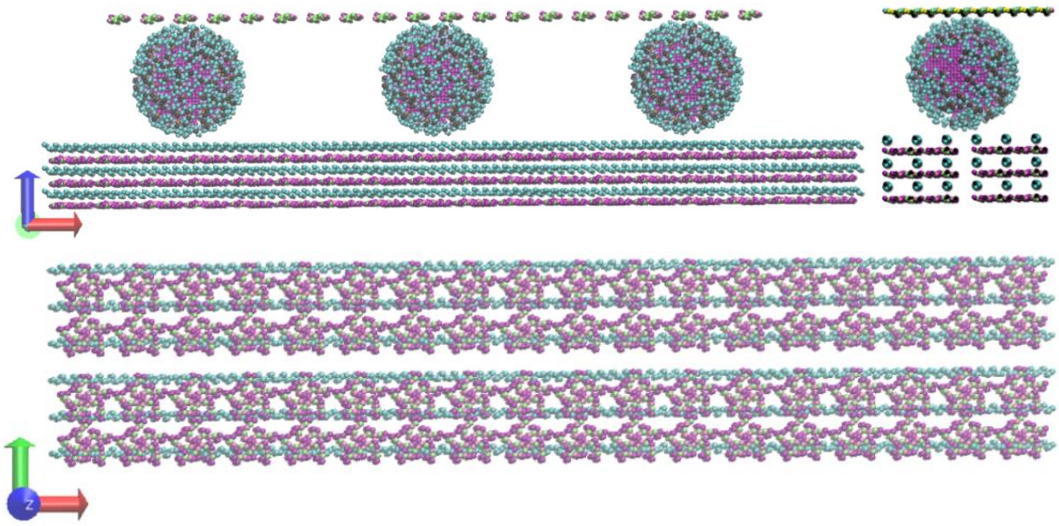


Figure 2.11. Initial structure of PAH/TA-AuNP with Crystal Violet.

2.2 Results and Discussion

The objective of this part is to compare linear and exponential growth models of PAH/PAA multilayers by means of the mobility of AuNPs on these PEMs in all-atom and coarse-grained MD simulations. Moreover, the comparison of PAH/PAA and PAH/TA and different numbers of PAH/TA bilayers by means of the mobility of citrate-capped AuNPs were the other objectives of this chapter. As a part of these objectives, the orientation of crystal violet molecules and their interactions with AuNPs, citrate and PEMs were studied.

2.2.1 All-Atom MD Simulations

In the first section of this chapter, all-atom MD simulations were run as explained in the previous part. The objective of this study was to compare linear and exponential PAH/PAA multilayers by means of the mobility of citrate-capped AuNP positioned on these PEMs. Due to the limitation of the size of the simulation, there is only one AuNP in the simulation cell. However, the results of this simulation by means of the RMSD and RMSF analysis stand as a reference for coarse-grained MD simulations.

2.2.1.1 Citrate-capped AuNPs with PAH/PAA Multilayers

PAH/PAA films were modeled using linear and exponential grown films in experimental studies, as explained in the previous section. After the simulations were performed, the difference between the mobility of AuNPs depending on the shape of PAH/PAA multilayers was investigated in this part of the study.

As shown in Figure 2.12, the RMSD of AuNP located on exponential growth PAH/PAA reaches a constant value well before 100 ps. On the other hand, fluctuation in the RMSD plot continues at 2.0 ns in linear PAH/PAA films.

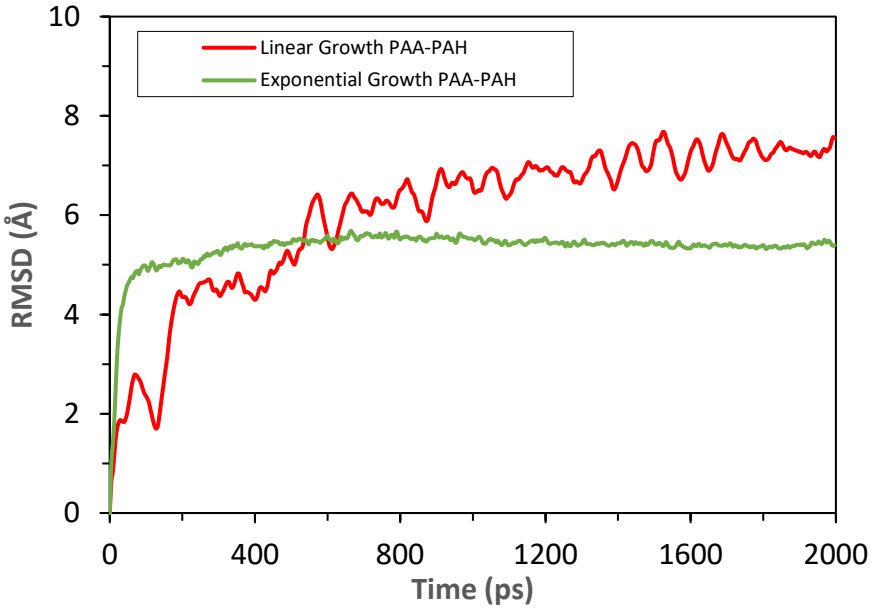


Figure 2.12. RMSD vs time plot for AuNP with linear PAH/PAA layer (red), AuNP with exponential PAH/PAA layer (green).

As mentioned above, the aim of this section is to demonstrate the differences between the mobility of AuNPs on linear and exponential PAH/PAA multilayers. Therefore, RMSF values were plotted and similar results were obtained in RMSF plots. As given in Figure 2.13, the fluctuation of the position throughout the simulation is about 0.5 Å for almost all of the Au atoms under exponential growth

multilayers while the fluctuation of the position of the same Au atom reaches ~3.0 Å on linear growth multilayer. In Figure 2.14, the final snapshot of the simulation boxes containing linear and exponential growth PAH/PAA is given. It can be seen that AuNP was embedded inside the exponential PAH/PAA multilayer deeper compared to linear PAH/PAA. This placement decreases the mobility of AuNP on the PEMs, while it is freer to move on the surface of linear PAH/PAA. This important result indicates the better stability and decreased mobility of Au nanoparticles on the PEM surface with exponential films compared to linear films. This result agrees with the experimental results where exponential growth provided enhanced Raman scattering. In experimental studies conducted in our group, the SER signal for 10^{-5} M crystal violet was below the detection limit when linear PAH/PAA was used as the SERS substrate. On the other hand, when exponential growth PAH/PAA was used; the signal was detectable in the order of ~40 counts/s. This result might be fully or partly due to the decrease in the mobility of nanoparticles. Since the mobility of nanoparticles and thereby the electron density is restricted, the number of hot spots increases, giving rise to enhanced Raman scattering.

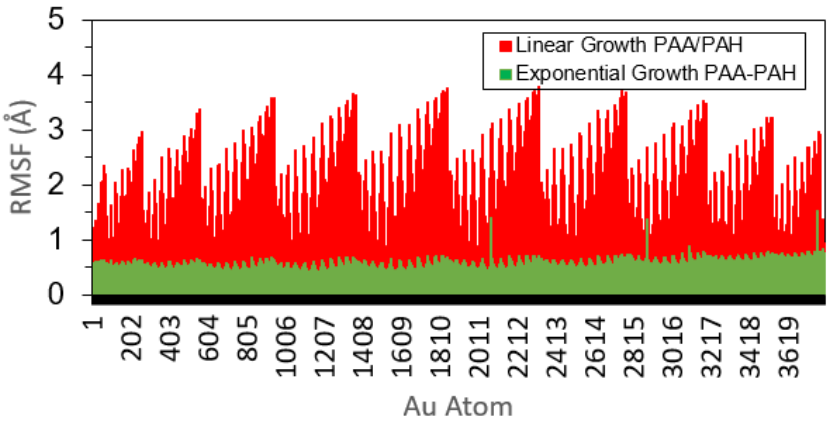


Figure 2.13. RMSF values of Au atoms for linear PAH/PAA layer (red), AuNP with exponential PAH/PAA layer (green).

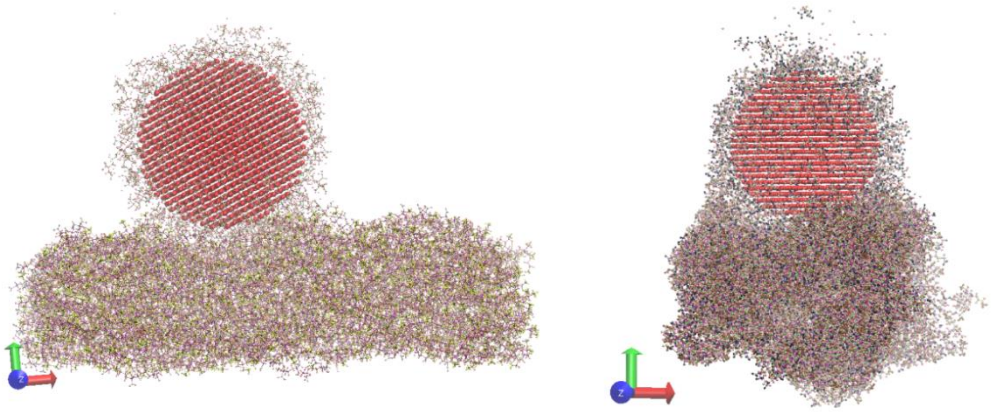


Figure 2.14. AuNP capped with citrate, together with linear (left) and exponentially (right) grown PAA-PAH multilayer after 2.0 ns.

2.2.2 Coarse-Grained MD Simulations

The coarse-grained MD simulations were conducted as explained in the following part of this text. The objective of this study was to create a decent model of citrate-capped AuNPs on PAH/PAA for coarse-grained MD simulations, giving RMSD and RMSF results in agreement with the results of the all-atom MD simulations. Then, the PAH/TA model was prepared for comparison of the performance by means of the mobility of AuNPs, as explained in Section 2.1.1 in detail.

2.2.2.1 Citrate-capped AuNPs with PAH/PAA Multilayers

In all-atom MD simulations, as described in the Computational Methodology (1.1) section, there were 24 PAH and 24 PAA chains, each containing 80 monomers and one AuNP capped with citrate. The total number of beads, which are the coarse-grained units, in the simulation box was 48721. In contrast to this huge number of particles, the simulation box contained only one AuNP having a diameter of 5.0 nm, because it was not possible to determine the distribution of the analyte model

between two nanoparticles. Accordingly, computational resources were not enough to increase the number of PAH/PAA bilayers in the PEM model.

In order to simulate larger cells, a coarse-grained model of PAH/PAA multilayer was prepared together with AuNPs in a similar manner to that of all-atom MD simulation studies. Difference between the mobility of AuNPs was investigated in this part of the study with coarse-grained MD simulations. As given in Figure 2.15, RMSD values reach a constant value before two ns for AuNPs on the top of exponential growth PAH/PAA. On the other hand, the values reach a constant value at beyond three ns for AuNPs on linear PAH/PAA multilayers. As can also be observed in the plot, the noise of the line for the linear growth PAH/PAA is larger, indicating that the fluctuation in the position of Au atoms is higher when they are located on the top of linear growth multilayers. The result is consistent with that of atomistic MD and experimental results as explained in the previous section.

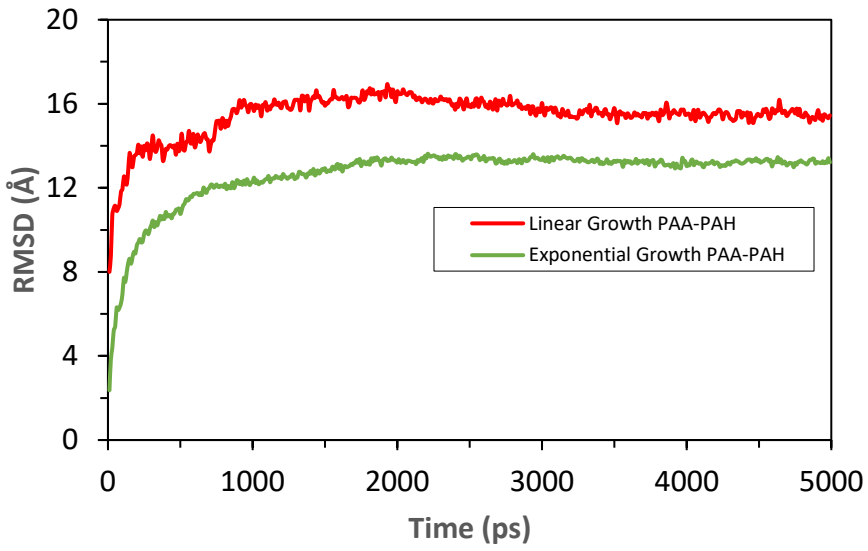


Figure 2.15. RMSD vs time plot for AuNP with linear growth PAH/PAA layer (red), AuNP with exponential growth PAH/PAA layer (green).

A similar conclusion can be extracted from the RMSF analysis given in Figure 2.16. When exponential growth PAH/PAA was located under the AuNPs, within the 3925

Au atoms in the AuNP at the center of the simulation box, fluctuation in the position was in the order of 1.0 Å except for only two Au atoms in the central AuNP. In the remaining 7850 Au atoms in the other two AuNPs, fluctuation in the position was about 2.0 - 2.5 Å except for only two Au atoms. On the other hand, the fluctuations of the same Au atoms increased from 2.0-2.5 to ~3.0 to 4.0 Å when the AuNPs were located on the top of linear growth PAH/PAA multilayers instead of exponential growth multilayers.

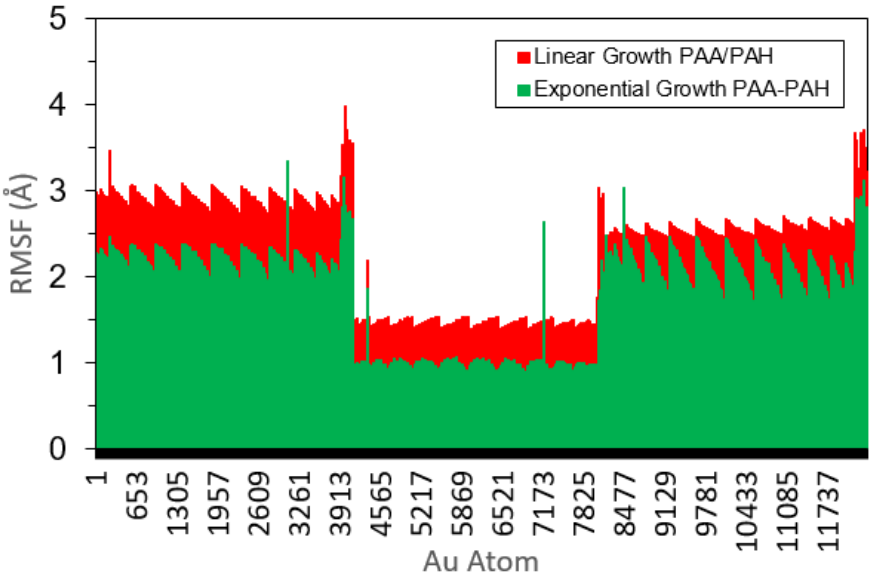


Figure 2.16. RMSF values of Au atoms with CG linear (red) and exponential PAH/PAA layer (green)

It is worth noting that, there is a 6-fold decrease in the fluctuation of the position of Au atoms in all-atom MD simulations, where the magnitude of the decrease is not similar in coarse-grained MD simulations due to the decreased sensitivity of coarse-grained simulations. In repeated simulations, it was demonstrated that the magnitude of the decrease in the fluctuation depends on the morphology of the exponential growth structures. In all cases, however, a decrease in the fluctuation was observed when exponential growth multilayer was used instead of linear growth multilayers independent from the initial structure. Consequently, fluctuation in the position of

AuNPs on exponentially grown multilayers were less compared to those on linear growth multilayers. Therefore, it is possible to use PEM with exponential growth as a SERS substrate. The magnitude of the decrease differs depending on the initial structure of the exponential growth multilayer. In addition, all-atom models work better for these kinds of position-sensitive applications.

The positions of gold nanoparticles in the final snapshot of the simulations are shown in Figure 2.17. Decreased mobility of nanoparticles embedded into the exponential growth multilayers may be used to design the substrate candidate for SERS studies. Decreased mobility of nanoparticles increases the SER signal because it improves the formation of localized hot spots between the AuNPs. The mobility of the NPs may result in their aggregation, disrupting the localized hot spots.

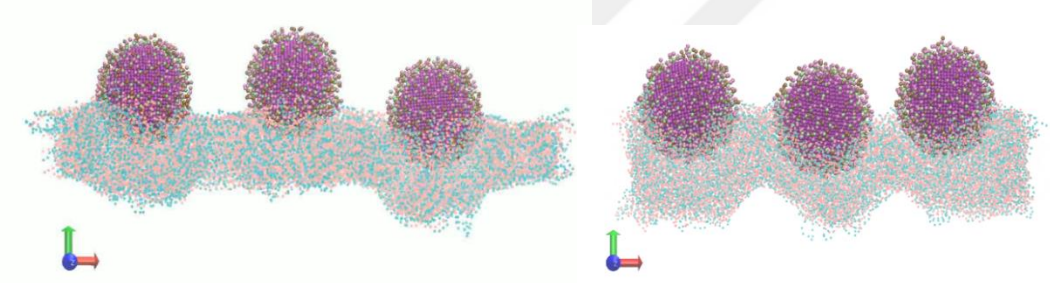


Figure 2.17. Final snapshot of coarse-grained AuNP capped with citrate, together with linear growth PAH/PAA (left) and exponential growth PAH/PAA (right) layer.

2.2.2.2 Crystal Violet (CV) on Citrate-capped AuNPs with PAH/PAA Multilayers

The distribution of crystal violet as a model analyte on the top of AuNPs embedded PAH/PAA multilayer was studied with coarse-grained molecular dynamics simulations. For this purpose, linear PAH/PAA multilayers with 3 AuNPs coated with citrate as shown in Figure 2.18 were constructed in this part of the study. The initial distance between AuNPs was set as 20, 40, 70 and 100 Å, respectively in 4 different simulation cells.

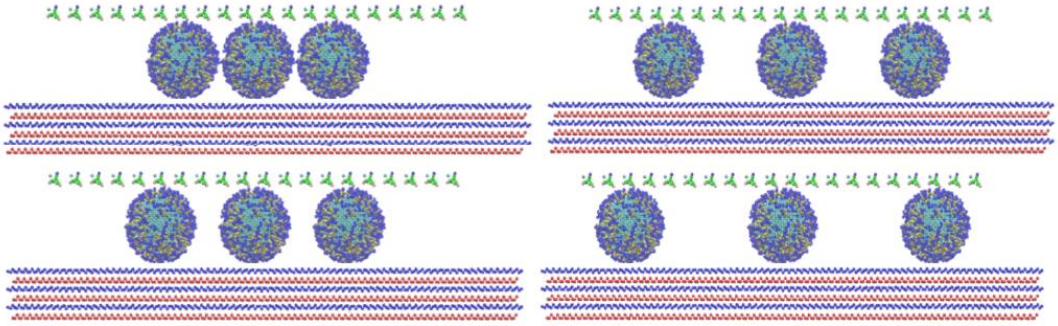


Figure 2.18. Initial simulation cell containing PAH/PAA multilayer and citrate-capped AuNP with crystal violet. Initial AuNP distances with respect to each other were 20, 40, 70 and 100 Å, respectively.

As shown in Figure 2.19 and Figure **2.20**, crystal violet molecules were distributed on the surface of AuNPs, even when the distance between AuNPs was 100 Å. In addition, whether the AuNPs were far away or close to each other, there was no difference in terms of the distribution of crystal violet molecules around the NPs. In some cases, crystal violet molecules self-organized as bridge-like structures leaving a space between the AuNPs. This might be the result of a strong interaction between negatively charged citrate anions and positively charged crystal violet molecules.

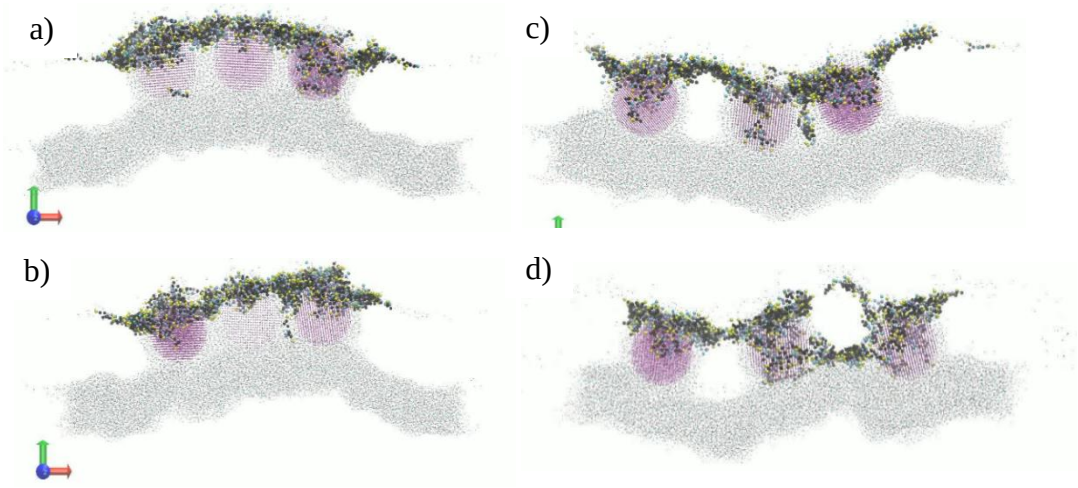


Figure 2.19. Final structures of PAH/PAA-AuNP with crystal violet molecules. AuNP distances with respect to each other were a) 20, b) 40, c) 70 and d) 100 Å, respectively.

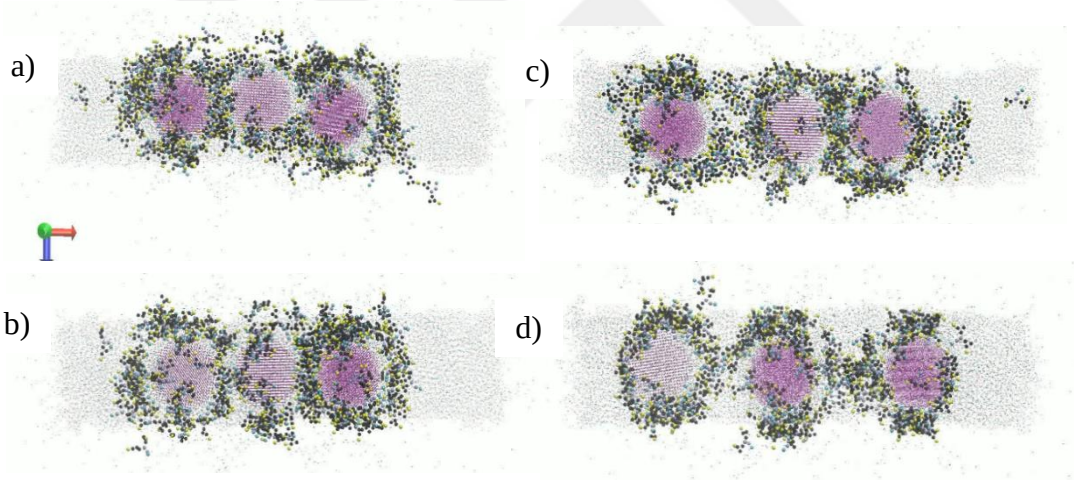


Figure 2.20. Top view of final structures of PAH/PAA-AuNP with crystal violet molecules. AuNP distances with respect to each other were a) 20, b) 40, c) 70 and d) 100 Å, respectively.

Orientation of crystal violet molecules on AuNPs can be estimated from RDF analysis of Au atoms with N_a beads (corresponding to the dimethyl amine group having zero charge) and with Q_0 beads (corresponding to the dimethyl ammonium

group having a +1 charge) of crystal violet molecules. As shown in Figure 2.21, the peak value of RDF for N_a beads is in the order of 0.18. As mentioned previously, N_a was a non-polar and hydrogen bond accepting type of bead, which corresponds to dimethyl amine groups on crystal violet molecules. This value was more than twice that of Q_0 beads, which correspond to the dimethyl ammonium group of crystal violet. The dotted lines show the initial values of g(r). In the beginning, the number density of the Q_0 and N_a beads were almost the same. This result implies that, throughout the simulation, crystal violet molecules moved to the AuNP surface from their dimethyl amine sides.

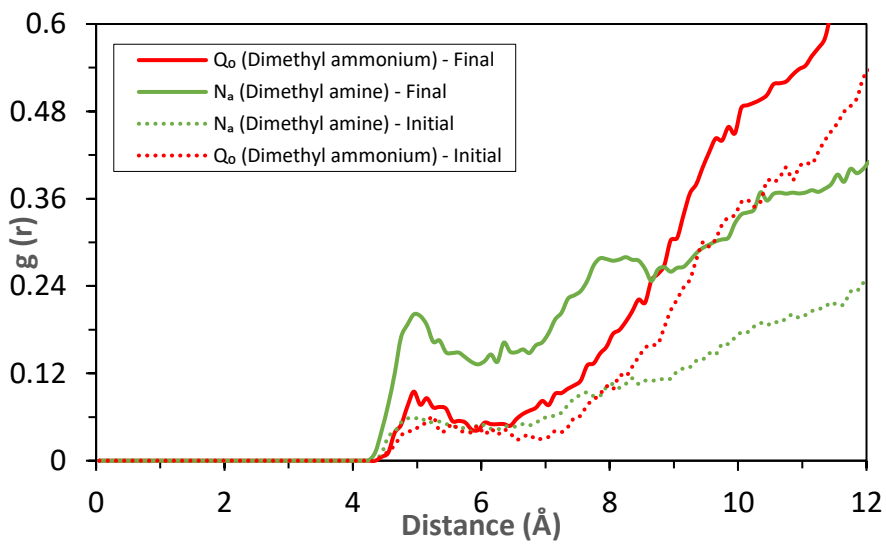


Figure 2.21. RDF analysis of Au atoms with N_a beads (containing N atoms without a charge) and with Q_0 beads (containing N atoms with a positive charge) of crystal violet.

2.2.2.3 Crystal Violet on Citrate-capped AuNPs with PAH/TA Multilayers

In this part of the study, PAH/TA multilayer was modeled for coarse-grained MD simulations to compare the distribution of AuNPs on PAH/PAA and PAH/TA multilayers. Atom to bead mapping details of TA to Martini force field were explained in the Model Preparation (2.1.2.3.4) section. A linear PAH/TA system

with three AuNPs coated with negatively charged citrate ions was used in this part of the study.

Crystal violet molecules were distributed on the surface of AuNPs coated with citrate molecules. However, the bridge-like arrangement of crystal violet molecules between AuNPs looks slightly different compared to Au NPs coated PAH/PAA films as shown in Figure 2.22. In PAH/PAA-AuNP case with a similar distance of AuNPs (i.e. 100 Å), crystal violet molecules organized into a bridge like structure leaving an empty space between the AuNPs as described above. The distribution of CV molecules can be visualized in Figure 2.22 (a and c). Crystal violet molecules are generally distributed on the top of AuNPs in both cases. Crystal violet molecules fill the empty space between the AuNPs more efficiently as shown in Figure 2.22 (a). As it is suggested in the literature, local hot spots in SERS observed in between the NPs and for the analyte molecules located in the hot spots, Raman signal enhancement is expected to be higher. This can be a possible explanation for the ~10-fold increase in SER signal in the experimental studies when PAH/TA was used instead of exponential growth PAH/PAA as a SERS substrate.

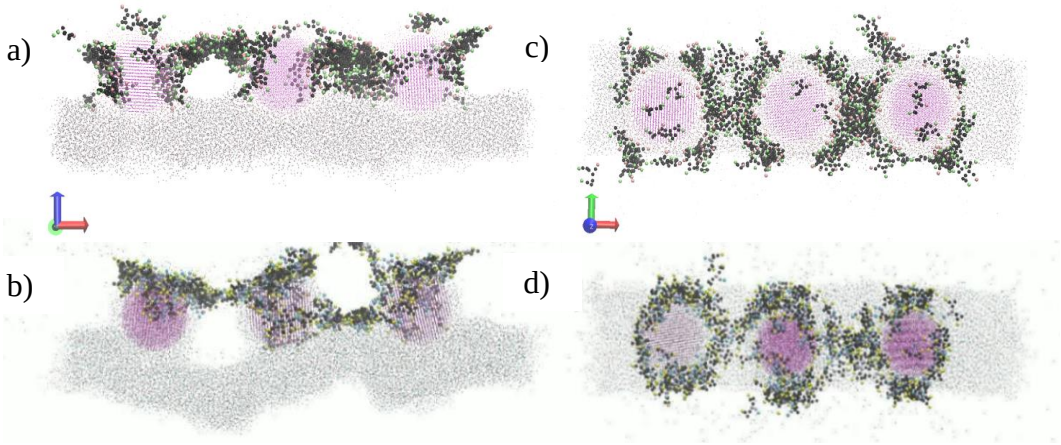


Figure 2.22. Final structure of PAH/TA-AuNP (top) and PAH/PAA-AuNP (bottom) with crystal violet (side and top views). AuNP distances with respect to each other were 100 Å.

In a linear growth PAH/PAA layer, the PAH/PAA complex was formed through $–COO^-$ and $–NH_3^+$ units of the monomers through the polymer chain, on the z-axis, providing the whole PAH/PAA multilayer relatively open to bend or fold in the z-axis. On the other hand, tannic acid, having a structure with the ability to connect and fix PAH chains on the y-axis, can make the PAH/TA complex more rigid. As illustrated in Figure 2.23, one single PAH chain is wrapped up and linked with tannic acid in many directions. This PAH chain is coiled and linked to the other layers more efficiently, making the bilayer rigid and resistant to bending or folding compared to the PAH/PAA bilayer shown in the same figure on the left.

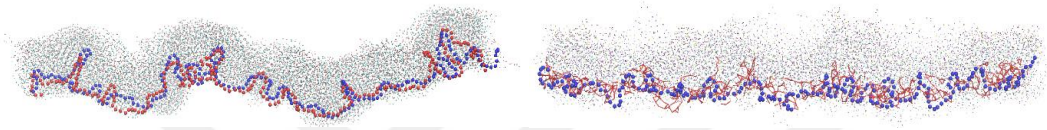


Figure 2.23. Final structure of PAH/PAA (left) and PAH/TA (right) used in the simulations. One bilayer is highlighted in each cases.

Distance between the AuNP in the center and the other two AuNPs was calculated for the case when they were located at the top of a PAH/PAA and a PAH/TA multilayer. As given in Figure 2.24, the shortest distance between the surface Au atoms of AuNPs reached ~51 Å and ~54 Å when they were located on PAH/PAA and PAH/TA multilayers, respectively. It is important to note that, the SER signal increases with decreasing distance of nanoparticles and the highest enhancement can be achieved if one single analyte molecule is located in between two nanoparticles[71]. In this study, rather than the distance between NPs, we focused on the mobility of the AuNPs. The number of AuNPs used in the initial model does not represent the experimental studies due to computational limitations. Moreover, the size of AuNPs in experimental studies can be larger than 10 nm but modeling of larger size of AuNPs is not convenient for this study due to computational inadequacy. Thus, it is difficult to make a realistic estimation of the equilibrium distance of AuNPs, to relate with Raman signal enhancement. In this study, deviations in the mobility and fluctuations of AuNPs were examined related to the enhancement of the Raman

signal. In this study, the surface interaction of gold nanoparticles with PEMs for SERS applications was modeled for the first time to the best of our knowledge.

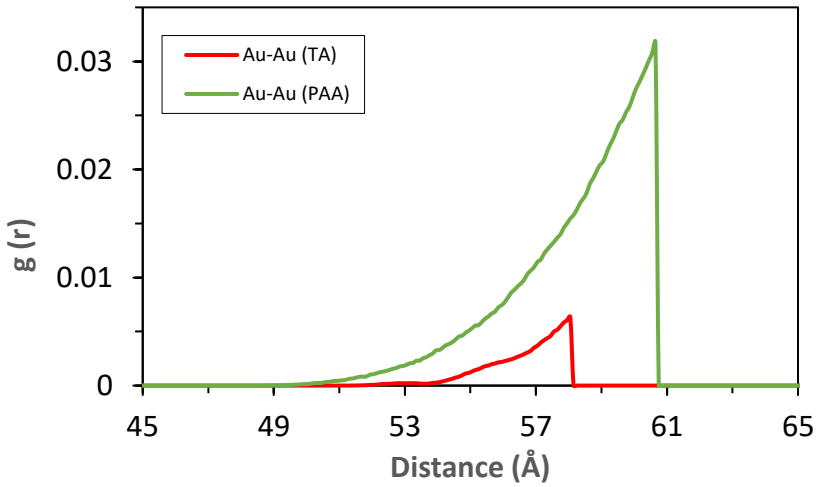


Figure 2.24. Distance between the Au atoms of AuNP in the center with those of the other two AuNPs in PAH/PAA-AuNP (green) and PAH/TA-AuNP (red) cases.

It was shown that citrate molecules interact with AuNPs through their neutral dimethyl amine sides on PAH/PAA. This study was repeated for the AuNPs located on PAH/TA multilayers. On the contrary to the PAH/PAA system, crystal violet molecules reached AuNPs from their +1 charged dimethyl ammonium side in the PAH/TA system. The initial distance of charged Q_0 and neutral N_a beads to the AuNPs on average were close to each other as it was in the case in PAH/PAA-AuNP. At the end of the simulation, in contrast to the PAH/PAA-AuNP system, the N_a bead representing polar dimethyl amine drifted apart from the AuNPs. On the other hand, the Q_0 bead representing +1 charged dimethyl ammonium reached AuNPs. These results indicate that different orientations and distributions of analytes are possible depending on the chemical environment of the PEMs.

Initial positions of the crystal violet molecules were located with Moltemplate software in which one crystal violet molecule was multiplied along the xy plane in the simulation cell with the same orientation. In this orientation, two N_a beads

representing the dimethyl amine groups were close to the AuNPs and the Q_0 bead representing the charged dimethyl ammonium group was on the upside. As described in the previous case for PAH/PAA, the number density of Q_0 beads in CV to AuNPs did not vary at the end of the simulation. However, the average number density of N_a beads increased, indicating that CV approaches AuNPs from their neutral dimethyl amine sides as shown in Figure 2.25. In contrast, in the case of PAH/TA, the RDF peak value of N_a beads decreased and the RDF peak value of Q_0 beads increased at the same time showing that CV approached AuNPs from their +1 charged dimethyl ammonium sides. This change in the orientation of CV may be because of their positioning between the nanoparticles on PAH/TA multilayers. As discussed above, the distance between AuNPs is smaller on PAH/TA films, compared to PAH/PAA since PAH/TA films are filled by crystal violet molecules more efficiently. Comparison of RDF analysis of AuNPs with crystal violet on PAH/TA and PAH/PAA multilayers is given in Figure 2.26.

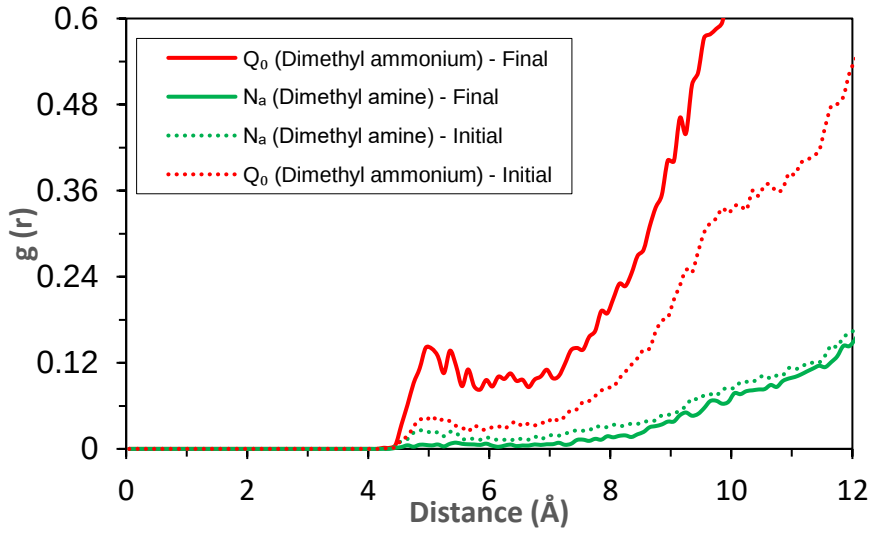


Figure 2.25. RDF analysis of Au atoms with N_a beads (representing dimethyl amine group of CV) and with Q_0 beads (representing the dimethyl ammonium) of crystal violet.

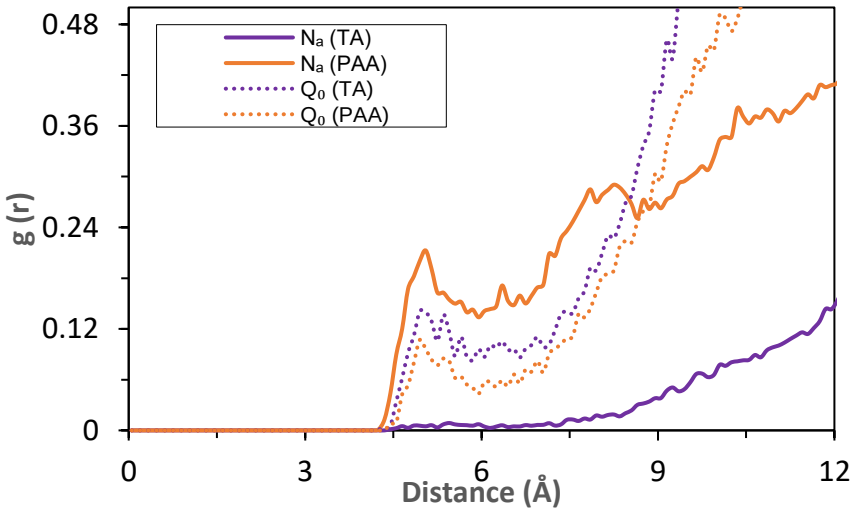


Figure 2.26. RDF of AuNPs with crystal violet on PAH/TA (purple) and PAH/PAA (yellow) multilayers.

At the end of the simulation, in RDF analysis of charged beads of crystal violet and charged beads of citrate, the highest peak for radial distribution was observed in ~5 Å and g (r) values in the order of 10-15, indicating a strong interaction between the +1 and -1 charges of CV and citrate molecules as shown in Figure 2.27. The highest peak value of the RDF was reached as 15.4 in the PAH/TA-AuNP system, which is slightly higher than that of the PAH/PAA-AuNP system. On average, the number density of crystal violet molecules around citrate ions is slightly higher on PAH/TA multilayers compared to PAH/PAA multilayers, indicating a stronger interaction of citrate-CV in PAH/TA multilayers.

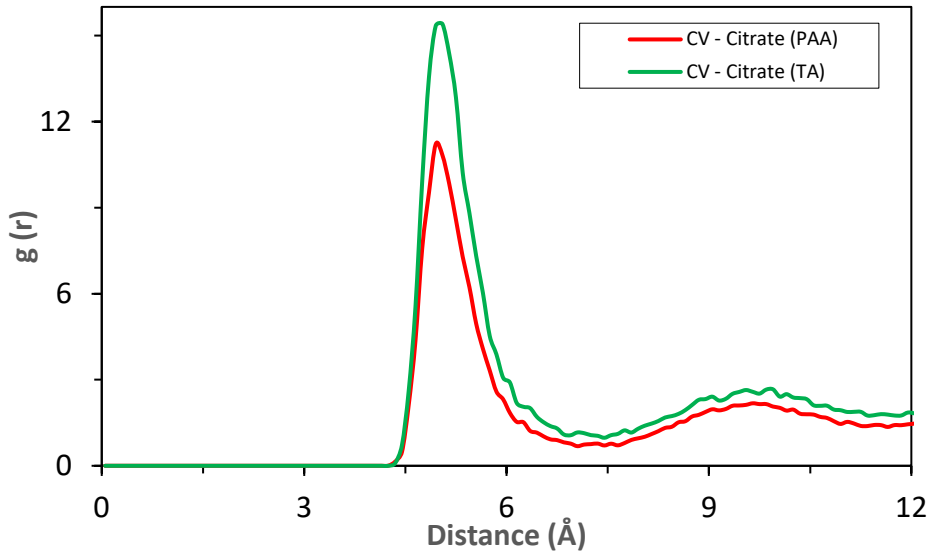


Figure 2.27. RDF analysis of charged beads of crystal violet-citrate in PAH/TA-AuNP (red) and PAH/PAA-AuNP (green).

2.2.2.3.1 Effect of Number of Layers

In this study, as mentioned before, PAH/TA and PAH/PAA multilayers contained 3 bilayers, with 12 PAA and 12 PAH in PAH/PAA, and 72 TA and 6 PAH in PAH/TA. To investigate the effect of the number of layers, 6 and 9 bilayers of PAH/TA were prepared and the results were compared with those in 3 bilayers of PAH/TA.

As expected, the rigidity of the multilayers increased with the increasing number of layers, resulting in a reduced mobility of the multilayers and AuNPs. As can be confirmed in the RSMD plot in Figure 2.28, the use of PAH/TA multilayers instead of PAH/PAA multilayers decreases the mobility of Au nanoparticles significantly. The mobility of AuNPs decreased further with the increasing number of PAH/TA layers. Another important finding is that the relative decrease in the noise is observed given in Figure 2.28. When the number of PAH/TA bilayers is nine, the noise in RMSD is the least compared to other lines, indicating that the deviation of the position of atoms slows down with the increasing number of layers.

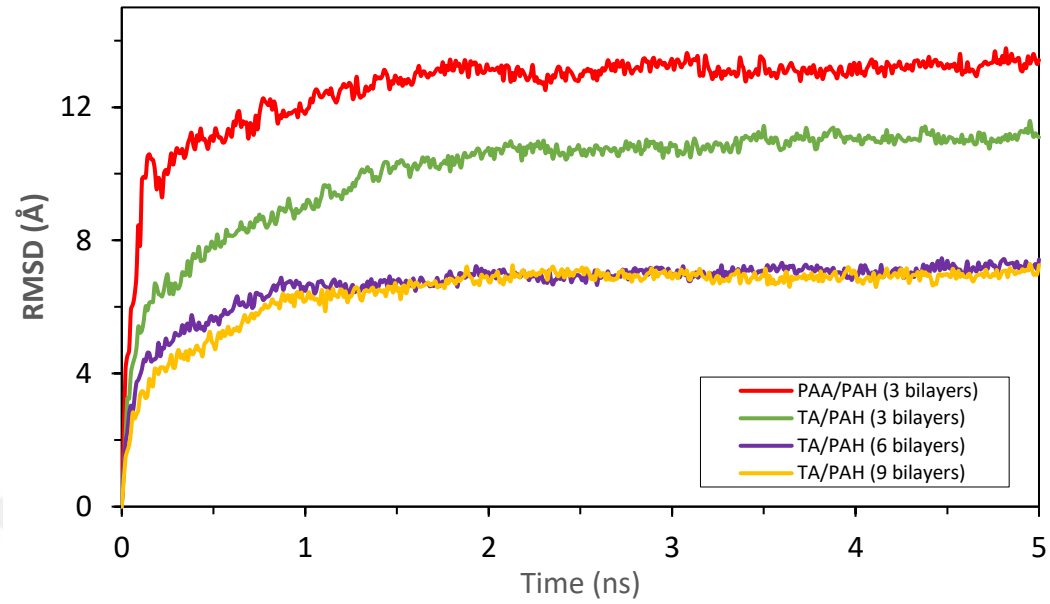


Figure 2.28. RMSD vs time graph for AuNP with 3 bilayers of PAH/PAA (red) and 3 (green), 6 (purple) and 9 (yellow) bilayers of PAH/TA.

The distance of the nearest Au atoms to each other increased with the increasing number of PAH/TA layers. The distance of the nearest Au atoms to each other in AuNPs was ~54 Å when they were located on the top of 3 bilayers of PAH/TA. As given in Figure 2.29 and Figure **2.30**, the distance reaches up to 57-59 Å values due to the decreased chain coiling by packing effect if the number of bilayers is increased to 6 and 9, respectively. The aim of this study does not involve estimating the equilibrium distance of AuNPs due to computational limitations. It is demonstrated in this study that an increase in the number of layers in PAH/TA results in a decrease in the mobility of AuNPs. The AuNPs stick to PAH/TA multilayers stronger and their initial position changes less when the number of layers increases. In the experimental results conducted by our group, the use of PAH/TA resulted in about a 10-fold increase in the intensity of the Raman signal compared to the use of PAH/PAA. With these results, combined with the experimental results produced in our group, it can be concluded that a decrease in the mobility of AuNPs can be related to the increase in the Raman signal.

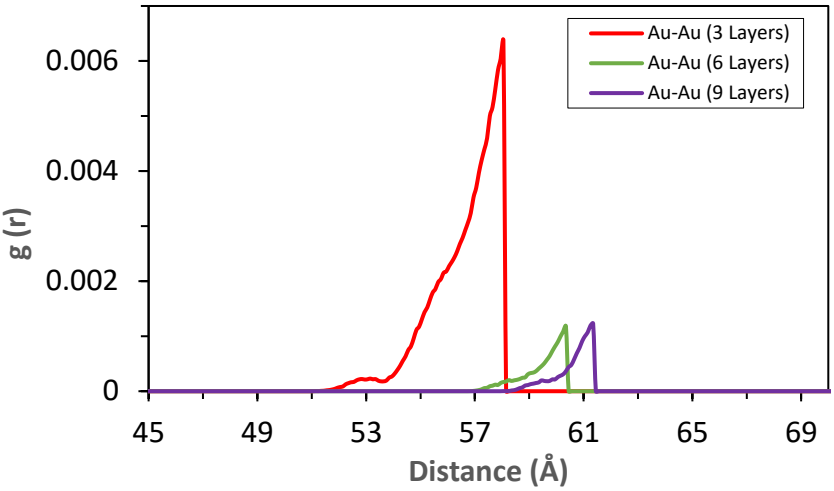


Figure 2.29. RDF analysis of the Au atoms of AuNP in the center with those of other two AuNPs on 3 (red), 6 (green) and 9 (violet) layers of PAH/TA.

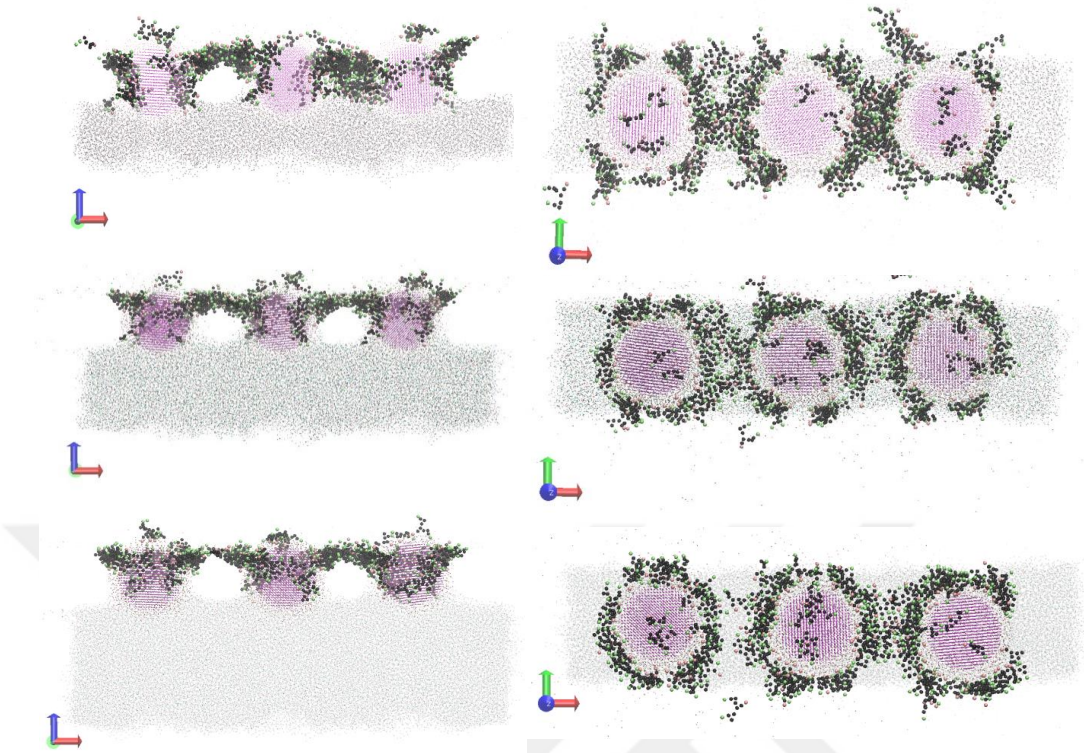


Figure 2.30. Final structure of PAH/TA-AuNP with Crystal Violet for 3, 6 and 9 layers of PAH/TA (side and top views). AuNP distances with respect to each other was 100 Å initially.

Crystal violet molecules interact with AuNPs from the charged side in the cell on the PAH/TA multilayers. This tendency did not change with increasing number of layers. As shown in Figure 2.31, the peak value of RDF for Q_0 beads increased with increasing number of bilayers. The peak value of RDF for N_a beads also increased with an increasing number of bilayers. However, these values did not reach those of Q_0 beads. Similarly in Figure 2.32, the number density of crystal violet molecules around citrate molecules increased with increasing number of bilayers of PEs. In conclusion, as the number of layers increased, crystal violet molecules interacted more with AuNPs.

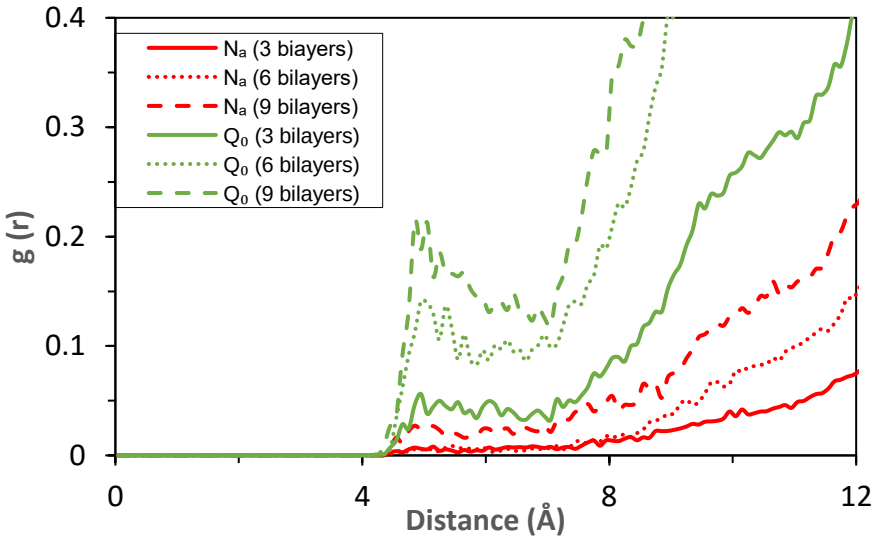


Figure 2.31. RDF analysis of AuNP and crystal violet on 3 (red and yellow), 6 (green and blue) and 9 (purple and black) bilayers of PAH/TA.

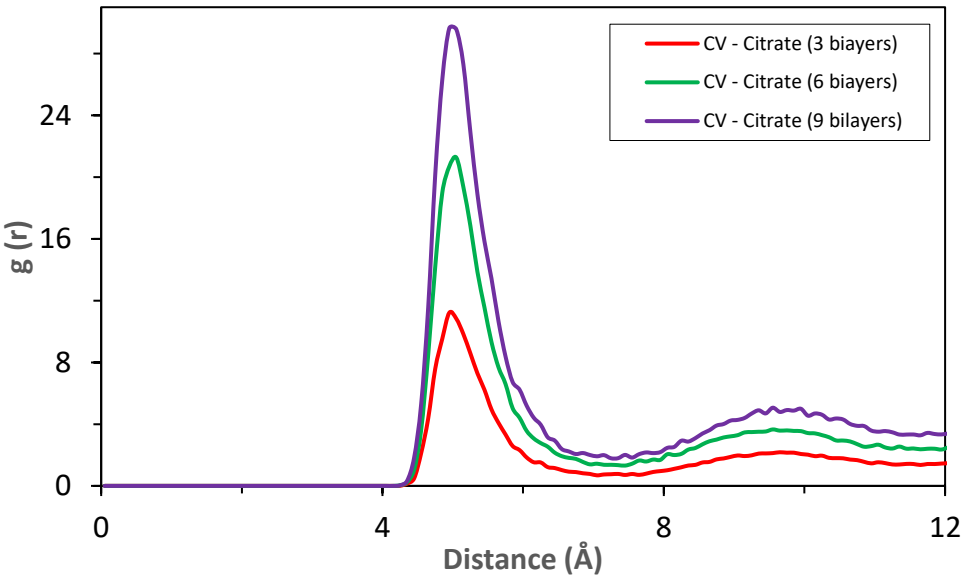


Figure 2.32. RDF analysis of charged beads of crystal violet and charged beads of citrate in the cell containing 3 (red), 6 (green) and 9 (violet) bilayers of PAH/TA

RDF analysis of crystal violet and the uppermost negatively charged polyelectrolyte layer in the PEM structure is given in Figure 2.33. The RDF value was the highest in CV – PAA showing that the number density around the uppermost layer of the PEMs was the highest for CV-PAA couples. This result indicates that the number of CV molecules passing through the AuNPs reaching the surface of PEMs and interacting with the PEMs surface was higher for PAH/PAA. This could be a reason why the number density of crystal violet around AuNPs decreased when PAH/PAA multilayers were used. This decreasing tendency continued when the number of TA bilayers was increased from 3 to 6. When the number of TA bilayers was increased from 3 to 6, there was more than 2 orders of magnitude decrease in the peak value of RDF at the highest point. This could be attributed to the decreased mobility of AuNPs as shown in Figure 2.29, where the distance of the nearest Au atoms in AuNPs was ~54 Å when they were located on the top of 3 bilayers of PAH/TA and reached up to 57-59 Å values when the number of bilayers were 6 and 9, respectively. These results showed that AuNPs were less mobile with the increasing number of bilayers, as explained previously. When the mobility of AuNPs decreased, there was stronger attraction of analyte molecules due to the larger number of localized charges on the surface and the number of analyte molecules reaching the surface of PEMs decreased. The extent of the change in the mobility of AuNPs was less when the number of PAH/TA bilayers was increased from 6 to 9. This can be correlated to the unaffected RDF peak value in the RDF analysis of CV and TA.

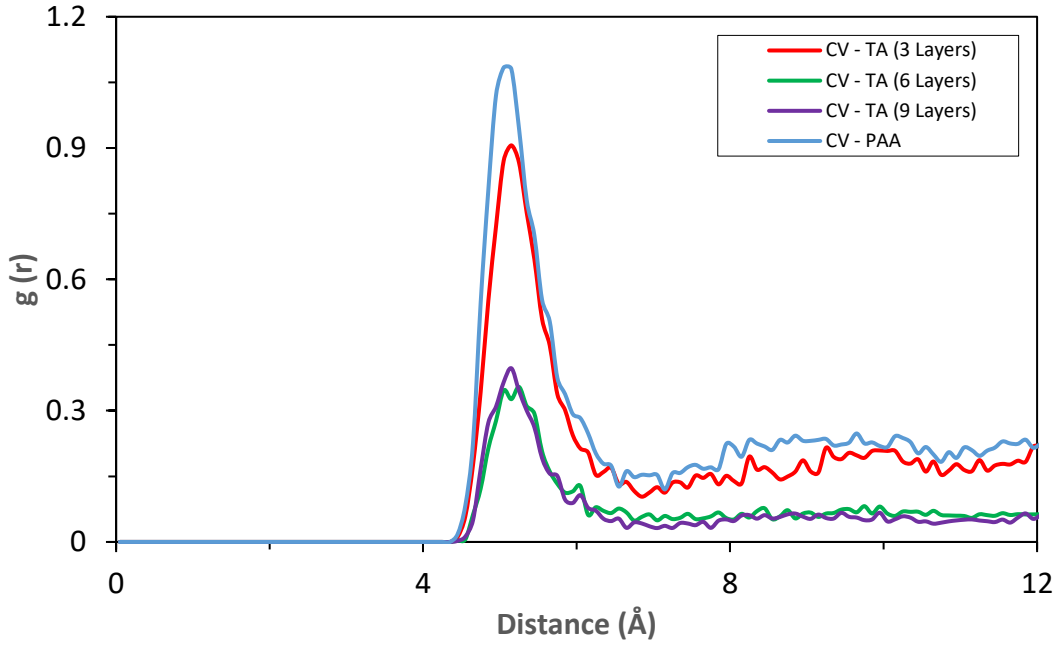


Figure 2.33. RDF analysis of crystal violet and tannic acid (at the uppermost layer) in the cell containing 3 bilayers of PAH/PAA (blue) and 3, 6 (green) and 9 (violet) bilayers of PAH/TA.

CHAPTER 3

ELECTRICAL CONDUCTIVITY ENHANCEMENT MECHANISM OF ACID AND SOLVENT TREATED PEDOT:PSS

3.1 Aim of the Study

The aim of this chapter was to investigate the molecular mechanism of enhancement in the conductivity with the addition of organic solvents and H_2SO_4 using multiscale molecular modeling. As it was summarized in the Introduction chapter (1.4.1.2.3), there are several mechanisms proposed in the literature for the enhancement of the electrical conductivity of PEDOT:PSS. One of these mechanisms includes the phase segregation of PSS from PEDOT After the separation of PSS by organic solvent treatment, PEDOT chains aggregate and assemble in an ordered structure[132]. Another suggestion in the literature is that, after the separation of PSS, PEDOT turns into an extended coil or linear structure from a coiled structure[133]. The transition from benzoid to quinoid structure of PEDOT chains is another suggested mechanism of enhanced electrical conductivity[134]. Recently, another mechanism has been reported in the literature including the separation of short-chained PSS-H and PSS^-Na^+, from PEDOT:PSS aggregate in DMSO. The remaining PEDOT:PSS having a certain stoichiometry is insoluble in DMSO, which turns from disorganized to organized structure[106]. To sum up, while there exist numerous studies on the mechanism behind the enhanced conductivity of PEDOT:PSS, the reasons and methods for this improvement are diverse and frequently disputed. It is commonly agreed that more extensive research is required to elucidate the origins of this enhanced conductivity more clearly.

There are a considerable amount of computational studies on the structure and properties of PEDOT:PSS in the literature[163–165], some of which are on the electrical conductivity enhancement mechanism of it[110,111,135,166–169]. There are studies in

which separation of PSS and self-organization of PEDOT were investigated with coarse-grained MD simulations[110,111,166]. Different from these studies, multiscale modeling techniques were used to demonstrate the experimental findings summarized above.

The first objective of this study was to demonstrate the phase segregation of PSS, which was observed experimentally[123]. As a part of this objective, the molecular and electronic properties of PEDOT were calculated. Moreover, the pairwise interaction energies of possible constituents in the acid and solvent treatment mechanism were calculated. The second objective was to examine the phase separation of PSS from PEDOT and potential interactions between PEDOT and PSS during acid and solvent treatment using all-atom MD simulations. Additionally, their interactions with other elements in the simulation cell were examined.

3.2 Computational Methods

In this part of the study, the enhancement mechanism in the electrical conductivity of PEDOT:PSS polymers was investigated by first principle calculations, all-atom and coarse-grained MD simulations with the addition of solvent and/or H_2SO_4. Additionally, initial structures were prepared and simulations were carried out with the same procedure as in the other chapters of the study. Data visualization and analysis were carried out with VMD.

3.2.1 First Principle Calculations

DFT was used for the calculation of structural and electronic properties such as pairwise interaction energies and frontier orbitals. For pairwise interaction energies to understand the molecular mechanism of phase segregations, $EDOT_3$ and SS_3 oligomers and HSO_4^- structures were prepared. The initial positions of the structures were determined by generating a large number of molecular configurations with excluded-volume constraints to determine energetically favorable configurations by

employing Monte Carlo simulations. Eight structures for PEDOT-HSO_4^- in which the lowest energy structures were determined were given in Figure 3.1. M06-2X functional with 6- 31++G(d) basis set was used in Gaussian 09 software with tight convergence criteria. Counterpoise corrections were performed for basis set superposition error (BSSE).

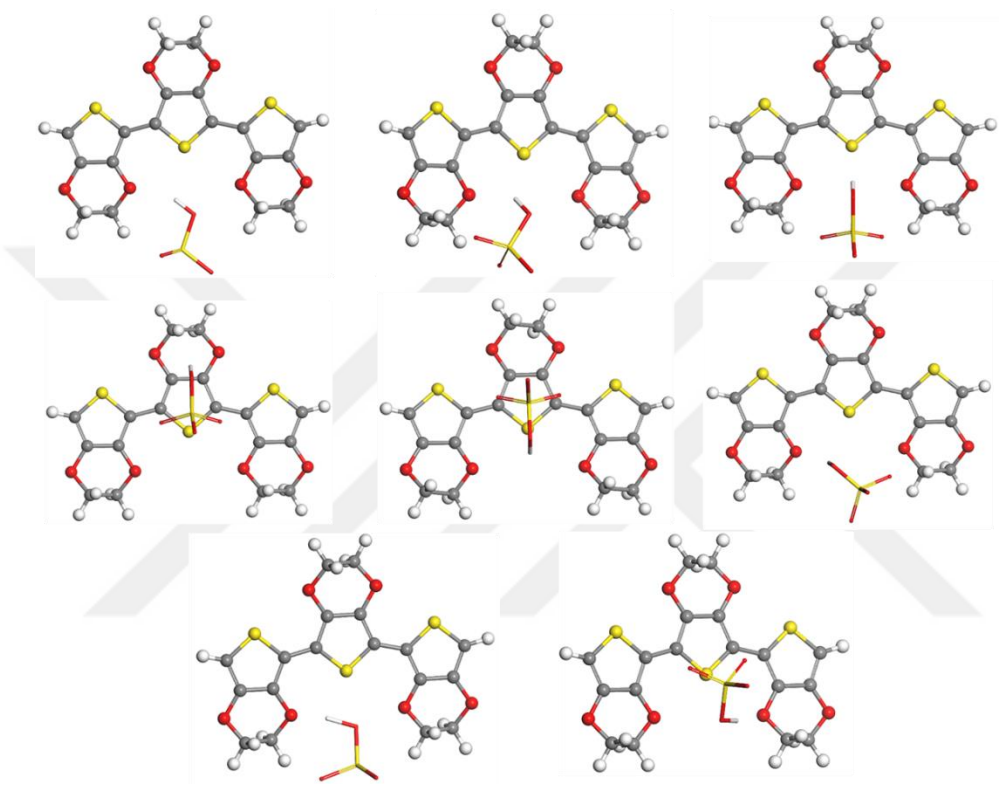


Figure 3.1. Initial positions of HSO_4^- determined for the interactions of PEDOT$^-$ HSO_4^- using Monte Carlo methods.

For HOMO-LUMO band gap calculations, $EDOT_3$, $EDOT_6$ and $EDOT_9$ structures and corresponding end group protonated $EDOT_x^+$ structures were constructed as shown in Figure 3.2 if it is possible to enhance conductivity based on the end group protonation with acid treatment.

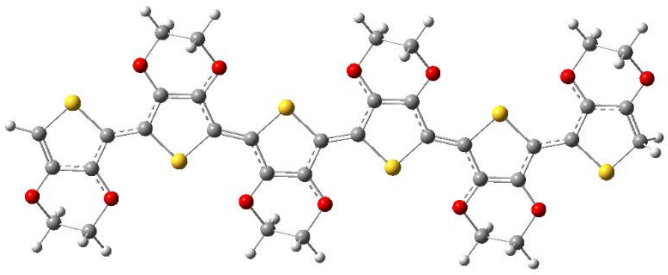


Figure 3.2. End group protonated $EDOT_6$ structure prepared for this study.

For calculation of pairwise interaction energies of H_2O and Na^+ between one SS_8 and two $EDOT_4$, as represented in Figure 3.3. Aim of preparation of each structure and the results will be discussed in the following "Results and Discussion" section.

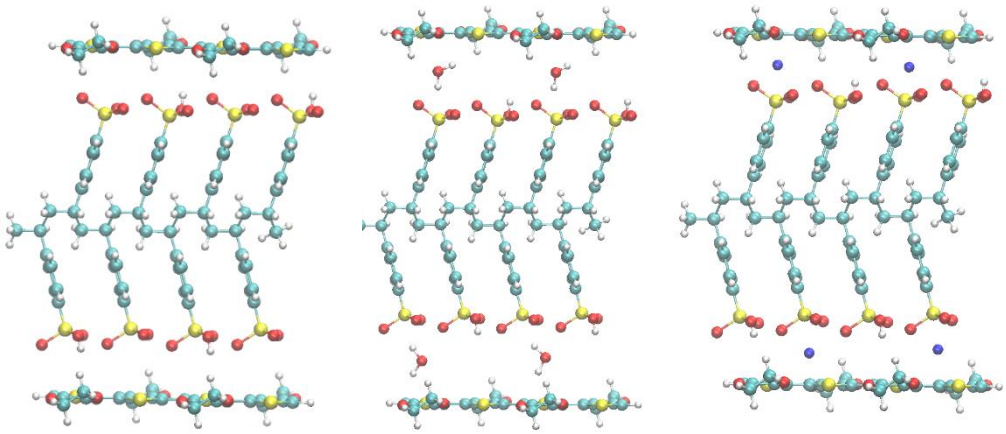


Figure 3.3. Initial structures of one SS_8 and two $EDOT_4$ (left), those with H_2O in between (center) and Na^+ in between respectively (right). Total charge of the system in each case is zero.

3.2.2 All-Atom MD Simulations

In all-atom MD simulations, PCFF was used for bonded and non-bonded interactions of PSS, PEDOT, HSO_4^- and H_3O^+. 9−6 Lennard-Jones (LJ) was used for short-ranged repulsion-dispersion interactions. For long-range interactions particle-particle particle-mesh solver (PPPM) was used. Scienomics MAPS 4.4 was used to assign PCFF force field to the structures in the simulation cells.

In the first part of all-atom MD simulations, simulation cells containing 8 PSS and 2 PEDOT chains were prepared. Each PEDOT involved 12 monomer chains as shown in Figure 3.4. Three monomers of PEDOT hold one positive charge in PEDOT chains as reported in the literature[170]. Therefore, a $PEDOT_{12}$ chain is prepared with a +4 charge. It is also reported in the literature that the ratio of weights of PEDOT and PSS is 1:2.5 experimentally[166]. Simulation cells were prepared considering this value. Each PSS involved 24 monomer chains. For charge equilibrium, two of the PSS chains were ionized, removing a total of 8 protons from $-SO_3H$ ends. The other six PSS chains were used as neutral during simulations.

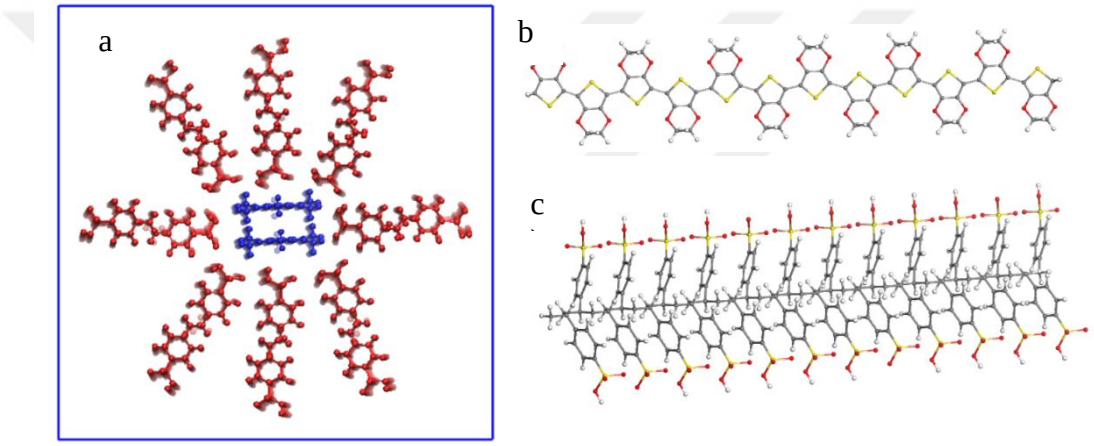


Figure 3.4. a) Initial configuration of PEDOT:PSS in the simulation cell. b) $PEDOT_{12}$ chain containing +4 charge. c) PSS_{24} chain containing -4 charge.

The initial simulation cell was then filled with certain amounts of water, HSO_4^- anion and H_3O^+ cation. Components of 10 cells used in the simulations are summarized in Table 3.1.

Table 3.1. Number of HSO_4^- and H_2O, and density of simulation cells prepared for all-atom MD simulations of PSS and PEDOT.

Cell	HSO_4^-	H_2O	Density	Cell	HSO_4^-	H_2O	Density
1	0	0	0.43	**6**	289	1001	1.0
2	0	2863	1.0	**7**	367	498	1.0
3	133	2006	1.0	**8**	444	0	1.0
4	211	1504	1.0	**9**	444	2008	1.4
5	289	0	0.80	**10**	756	0	1.4

An NVT ensemble with a Nose-Hoover thermostat was utilized for the following procedure. Temperature was increased from 300 K to 600 K in 0.1 ns, kept constant at 600 K for 0.1 ns, decreased to 300 K in 0.5 ns and kept constant at 300 K for 0.1 ns. This cycle was repeated 10 times and then, a production run was followed at constant temperature for 2 ns. RDF measurements were performed for this last 2 ns time interval. Atomic positions were saved in every 20 ps.

In another initial structure shown in Figure 3.5, eight PEDOT chains, each having 12 monomers and +4 charge were placed close to each other and wrapped with 2 PSS chains, each having 96 monomers, 16 of them having -4 charge to provide charge equilibrium. A simulation cell containing two of these PEDOT:PSS structures was prepared. Three replicates of this structure were positioned in a simulation cell. The first cell was filled with water until the density of the simulation cell reached 1.2 g/cm^3. The number of water molecules in this cell was 7395. Other two simulation cells were prepared so that the cells contain 114 and 218 HSO_4^- anions and 13 and 16 SO_4^{2-} anions to ensure 1.0 and 2.0 mol/L sulfuric acid concentration, respectively. The aim of this part is to observe that PSS and PEDOT separate from each other and PEDOT makes an ordered structure.

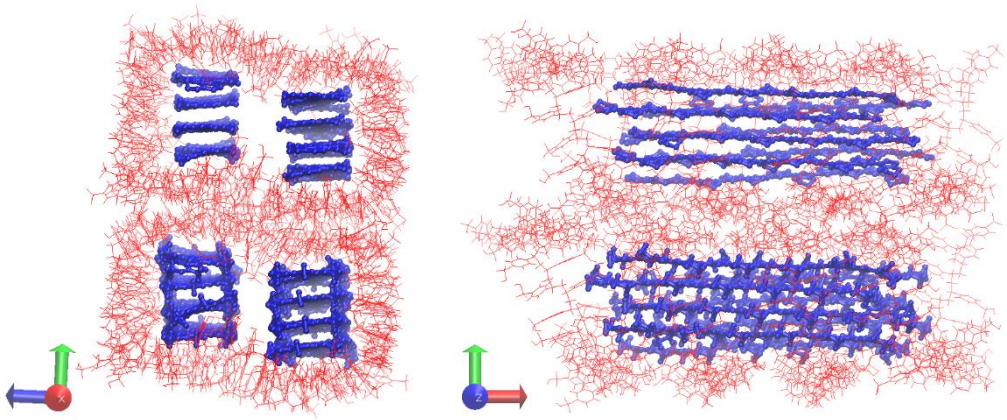


Figure 3.5. Initial structure of PEDOT:PSS simulation cell, top view (left) and side view (right)

Temperature was increased from 300 K to 1000 K in 1.0 ns, kept constant at 1000 K for 1.0 ns, decreased to 300 K in 5.0 ns and kept constant at 300 K for 3.0 ns. The structure in the last frame was saved and used as the initial structure for further studies.

In the next initial structure, an $EDOT_4$ oligomer was prepared and a unit cell was created with this structure. One EDOT monomer had a +0.334 charge similar to the previous parts. A supercell was created by multiplying this unit cell 6x3x3 times in x, y and z directions, respectively. Two cells were prepared by adding 72 HSO_4^- and 72 OH^- anions in the cells by packing with Monte Carlo simulations as given in Figure 3.6.

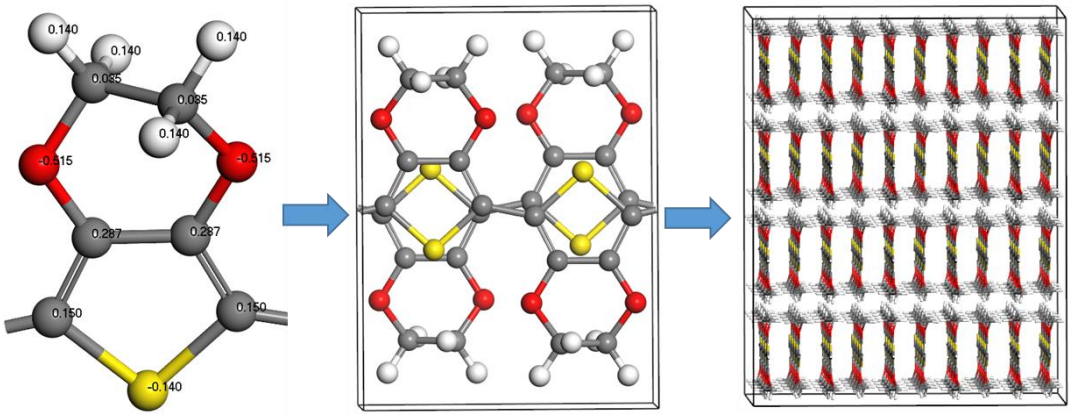


Figure 3.6. Modeling steps for PEDOT a) calculation of monomer atomic charges and structure, b) construction of unit cell, c) building a supercell.

COMPASS force-field was employed in calculations. Charges of each atom in EDOT, $HSO4^-$ and OH^- were assigned from COMPASS force-field charges. The cut-off distance for the van der Waals interactions was 12.5 Å. Electrostatic energy was calculated using the Ewald summation method with accelerated convergence.

An NVT ensemble and a Nose-Hoover thermostat were utilized for 1.0 ns MD simulations at 300 K. The timestep was used as 1.0 fs.

In another initial structure, PEDOT and PSS chains with various numbers of monomers and total charges were added to a simulation cell with Monte Carlo simulations. Details on the composition of the simulation cell are summarized in Table 3.2. The simulation cell is given in Figure 3.7.

An NVT ensemble and a Nose-Hwasoover thermostat were utilized for the following procedure. Cell optimization was performed for 2.0 ns in the NPT ensemble at 300 K and 1.0 atm. Temperature was then increased from 300 K to 600 K in 2.0 ns, kept constant at 600 K for 2.0 ns, decreased to 300 K in 8.0 ns and kept constant at 300 K for 6.0 ns. Data were collected from the last 4.0 ns, the closest time interval for structures to the equilibrium.

Table 3.2. Concentration, number of chains and charges of PEDOT and PSS added to the simulation cell.

Component	**No of Monomers**	**Total Charge**	**No added in the cell**
PEDOT	24	+8	16
PEDOT	12	+4	16
PEDOT	6	+2	8
PSS	48	-36	6
PSS	48	-8	8
PSS	24	-18	6
PSS	24	-4	8
PSS	12	-9	8
PSS	12	-2	8
H_3O^+	-	+1	30
Na^+	-	+1	270
DMSO	-	0	8782
H_2O	-	0	561

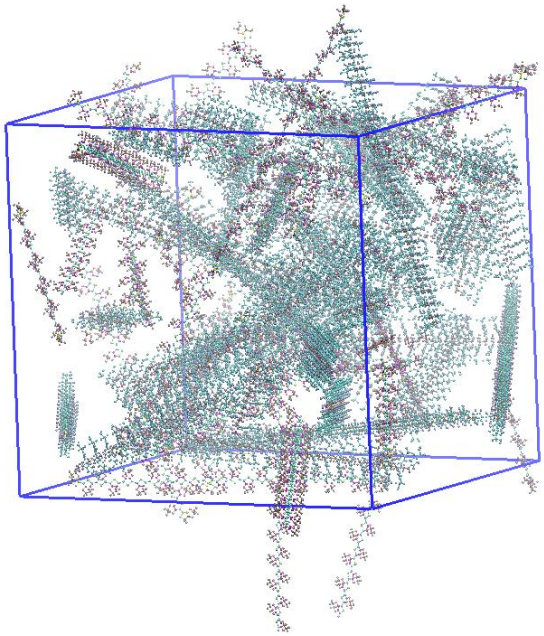


Figure 3.7. Initial cell for all-atom MD simulations containing different sizes and charges of PEDOT and PSS chains and H_3O^+, Na^+, H_2O and DMSO.

3.3 Results and Discussion

3.3.1 Molecular and Electronic Structure of PEDOT

Conjugation length is an important parameter for organic conductors because the band gap of PEDOT decreases with increasing conjugation length, leading to enhanced charge carrier density. As depicted in Figure 3.8 (d), the band gap of the PEDOT chain decreases with the increasing number of monomers from 3 to 9. This result is showing that longer conjugation length resulted in better conductivity for neutral PEDOT chain for increasing chain length. Electrostatic potential surface (ESP) for $PEDOT_3$, $PEDOT_6$, and $PEDOT_9$ demonstrated that the conjugated zone is confined between electron-deficient ethylenedioxy groups in PEDOT. In other words, the addition of the ethylenedioxy group results in a conjugated zone between the ethylenedioxy and thiophene groups of PEDOT. This conjugated zone results in increased conductivity of PEDOT compared to thiophene.

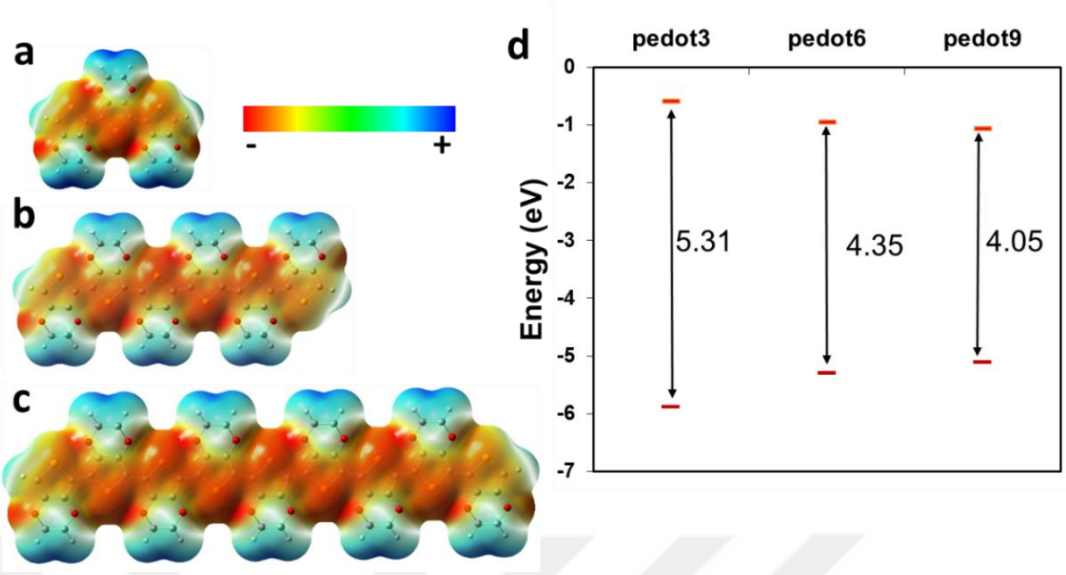


Figure 3.8. ESP for a) $PEDOT_3$, b) $PEDOT_6$, c) $PEDOT_9$. d) Band gap for these structures.

HOMO-LUMO orbitals are visualized for $PEDOT_6$ in Figure 3.9. These orbitals were homogeneously distributed along the conducting zone of PEDOT. This result is also valid for polaron and bipolaron structures of $PEDOT_6^{2+}$. The homogenous distribution of HOMO and LUMO orbitals between the ethylenedioxy and thiophene groups is making a conducting zone in the center of the chain.

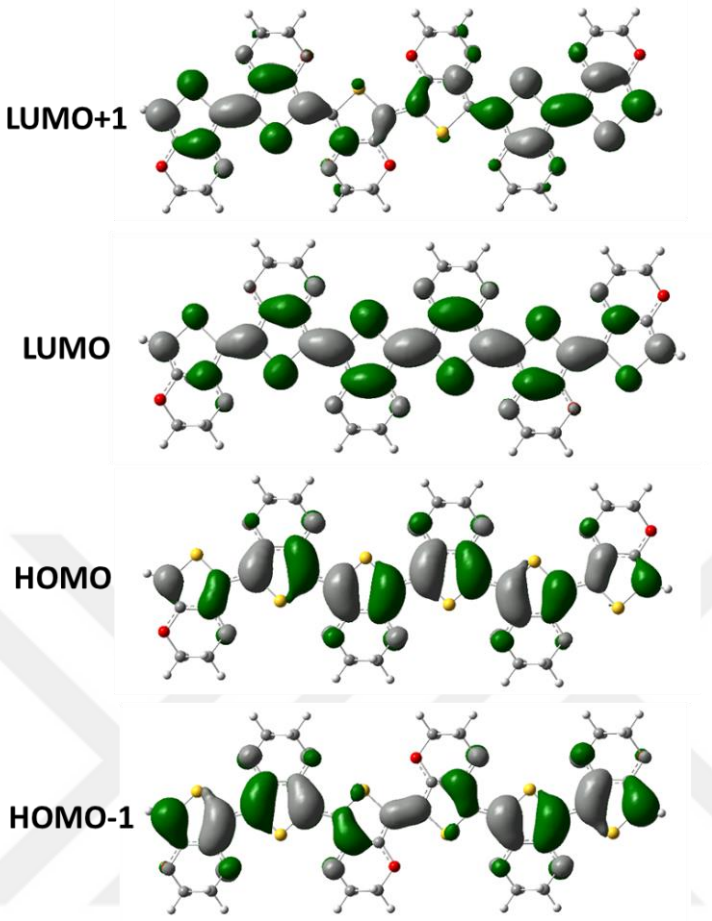


Figure 3.9. HOMO, HOMO-1, LUMO, LUMO+1 orbitals for $PEDOT_6$.

The band gap is decreased significantly with the transition from $PEDOT_6$ to $PEDOT_6^{2+}$ by doping as given in Figure 3.10. C-C backbone monomer-monomer distance is also decreased. This demonstrates the phenomenon reported in the literature, which is called benzoid to quonoid transition of the PEDOT structure. This change leads to improved rigidity and metallic properties. Bipolarons are more stable than polarons and they are mainly responsible for electrical conductivity.

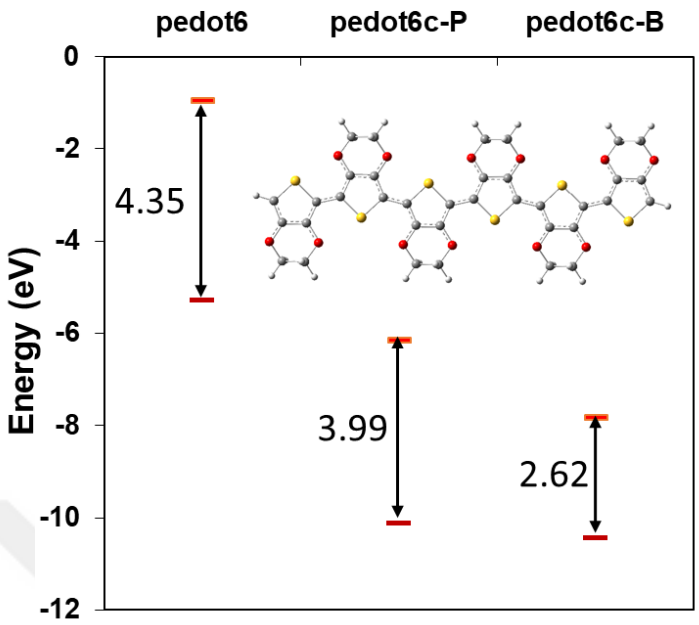


Figure 3.10. Band gap for $PEDOT_6$, $PEDOT_6^{2+}$ biradical polaron ($PEDOT_6$c-P) and $PEDOT_6^{2+}$ bipolaron structures (PEDOT6c-B)

The mechanism for the enhancement in the conductivity by acid treatment can be explained by two mechanisms:

1. Protonation of α-thiophene carbon end group of PEDOT ($PEDOTH^+$ formation)
2. Replacement of PSS^- chains by HSO_4^-

Band gap for $PEDOT_3$, $PEDOT_6$ and $PEDOT_9$ were determined with and without protonation of α-thiophene carbon end group to model A-PEDOT-PSS. As shown in Figure 3.11, the band gap significantly decreased because of the protonation of the end group in the PEDOT chain. Longer conjugation lengths from 3 to 9 also showed a higher amount of decrease in the band gap.

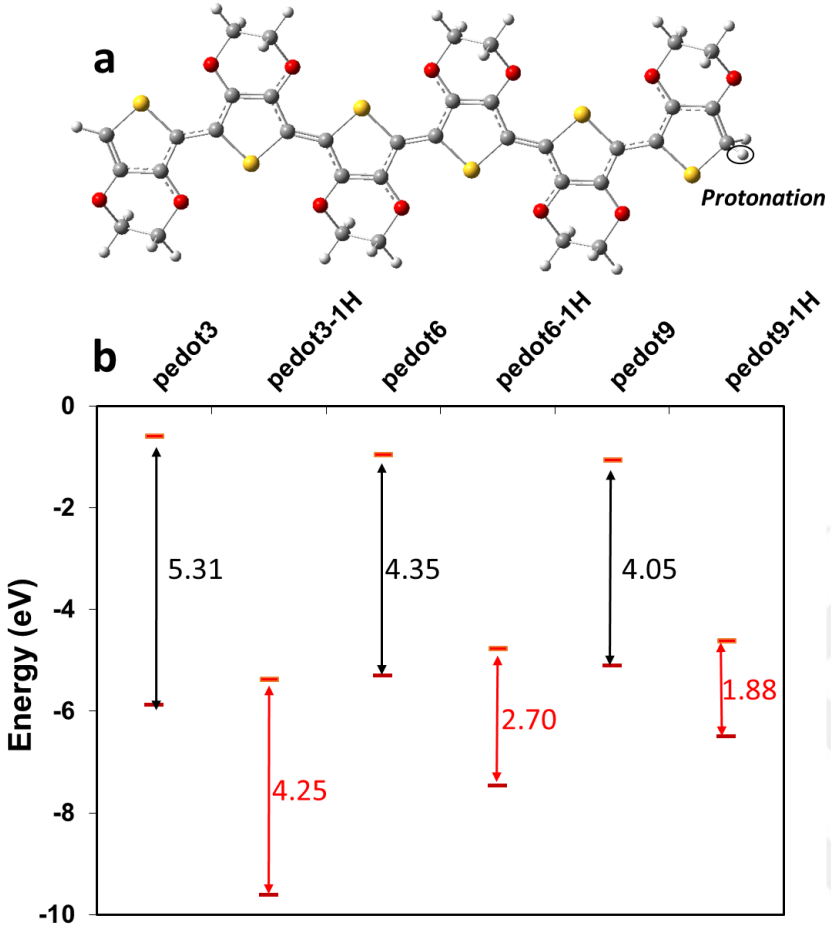


Figure 3.11. a) Structure for the calculations of end group protonated $PEDOT_6$ ($PEDOT_6$-H^+), b) band gap for $PEDOT_3$, $PEDOT_6$ and $PEDOT_9$ with and without end group protonation.

Distance of the bonds connecting PEDOT monomers is given in Figure 3.12 for neutral $PEDOT_6$, $PEDOT_6^{2+}$ bipolaron and end group protonated $PEDOT_6$-H^+. These are measured after geometry optimization. Bond distances are decreased for the end group protonated $PEDOT_6$-H^+ from 1.444 Å to 1.373 Å which is an indication of benzoid to quinoid transition and enhanced chain rigidity by acid treatment reported in the literature as one of the enhancement mechanisms. Enhanced rigidity leads to enhanced packing and crystallization which is the main reason for improved conductivity via the hopping mechanism between PEDOT chains[167,171].

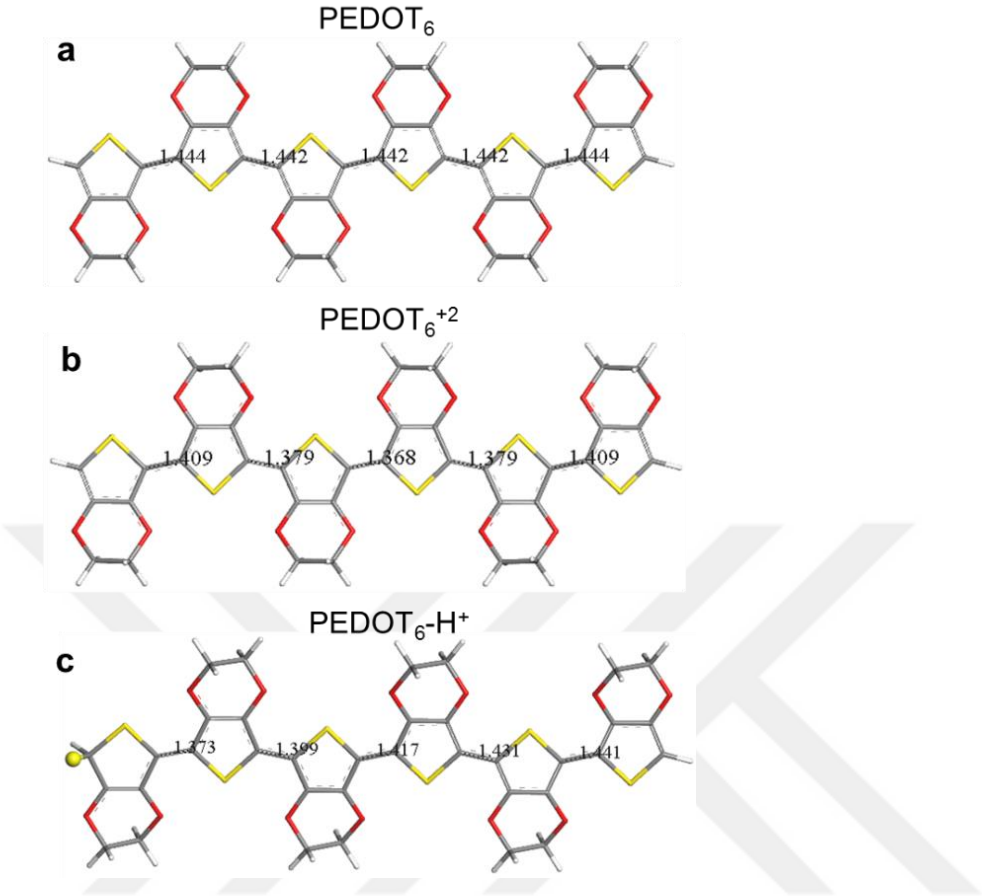


Figure 3.12. Backbone monomer (C-C bond) distances (in Å) for a) neutral $PEDOT_6$, b) $PEDOT_6^{2+}$ bipolaron, c) end group protonated $PEDOT_6$-H^+.

In Figure 3.13, the lowest energy structures determined for $PEDOT_6$-$2HSO_4^-$, $PEDOT_6^{2+}$-$2HSO_4^-$, $PEDOT_6^{2+}$-$2OH^-$, $PEDOT_6$-$2OH^-$ and Na^+-HSO_4^- are shown. M06-2X functional with 6- 31++G(d) basis set was used in Gaussian 09 software with tight convergence criteria for calculation as explained in the Methods (3.2.1) section. While neutral PEDOT can form hydrogen bond and CH---O=S interactions with HSO_4^-, electron-deficient $PEDOT_6^{2+}$ bipolaron interacts perpendicular with three oxygens of HSO_4^- with its positively charged H^+.

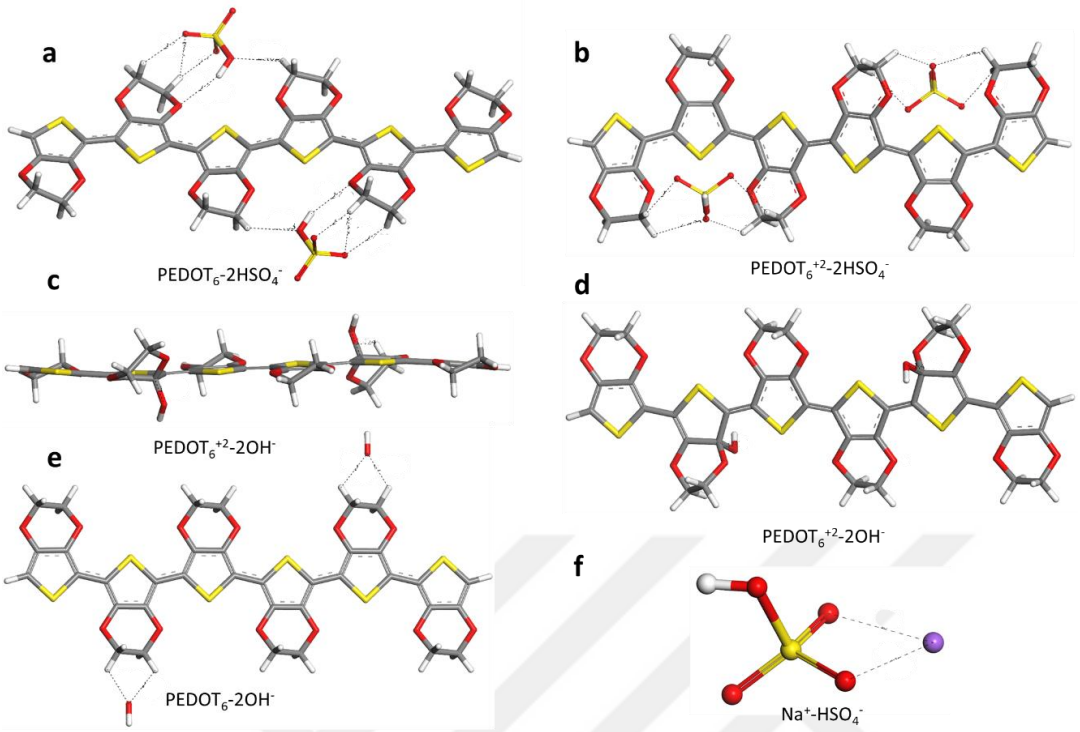


Figure 3.13. Geometry optimized lowest energy structures for a) $PEDOT_6\text{-}2HSO_4^-$, b) $PEDOT_6^{2+}\text{-}2HSO_4^-$, c-d) $PEDOT_6^{2+}\text{-}2OH^-$, e) $PEDOT_6\text{-}2OH^-$, f) $Na^+\text{-}HSO_4^-$ interactions.

As depicted in Figure 3.14, the $EDOT_3$ oligomer interacts with SS_3 oligomer via hydrogen bonding. On the other hand, when they are charged, i.e. $EDOT_3^+\text{-}PSS_3^-$ has strong ionic interaction via three hydrogens of $EDOT^+$ and three oxygens of SS^-.

In Table 3.3, interaction energies of possible structures of PEDOT and PSS with each other and with HSO_4^- and OH^- are listed. Details about calculation methods were given in the Methods (3.2.1) section. It can be verified from this data that PEDOT-PSS has weaker intermolecular interaction compared to $PEDOT\text{-}HSO_4^-$. Additionally, $PEDOT^+\text{-}PSS^-$ has weaker intermolecular interaction compared to $PEDOT^+\text{-}HSO_4^-$. It can be concluded from these data that acid treatment can induce phase separation between PEDOT-PSS in the PSS-rich shell since PSS and PSS^- can be replaced by HSO_4^- in PSS rich shell and PEDOT-rich core that will enhance the

crystallinity of PEDOT due to much smaller size of HSO_4^- compared to PSS^- as a dopant.

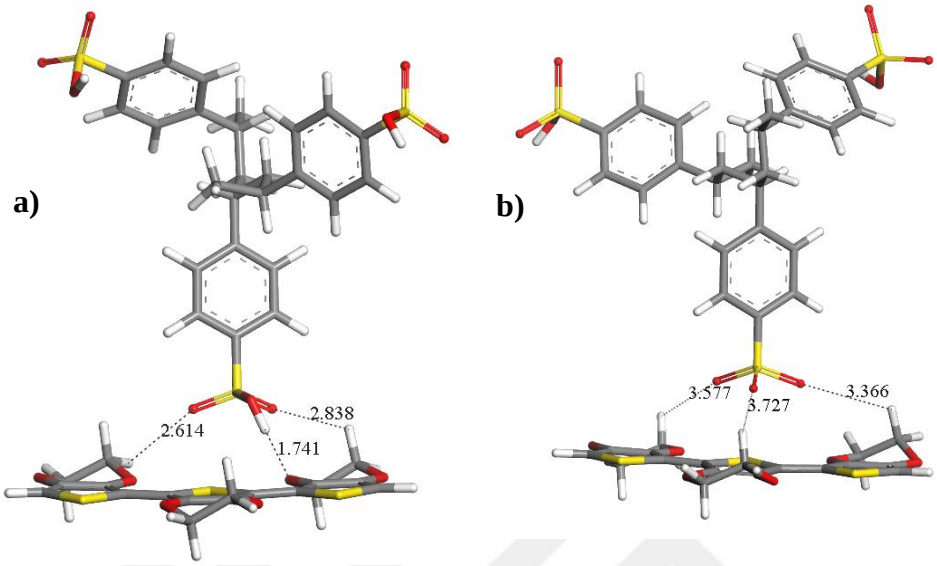


Figure 3.14. Geometry optimized lowest energy structures for a) $EDOT_3$-SS_3 b) $EDOT_3^+$-SS_3^-, interactions. Distances between the H atoms of EDOT and O atoms of SS are given in the figures in Å unit.

Table 3.3.Interaction energies calculated for possible interactions in A-PEDOT-PSS and AB-PEDOT-PSS.

Pair	**Interaction Energy (eV)**
$PEDOT^+$-HSO_4^-	-5.17
PEDOT-HSO_4^-	-0.91
$PEDOT^+$-OH^-	-9.65
PEDOT-OH^-	-1.30
$PEDOT^+$-PSS^-	-1.83
PEDOT-PSS	-0.69
Na^+-HSO_4^-	-5.83

Structures given in Figure 3.15, Figure **3.16** and Figure **3.17** were also geometry optimized by using M06-2X functional with 6-311+g(d) basis set using Grimme D3

dispersion correction. Calculations showed that there were not only two types of PSS in the form of PSS^- and PSSH. PSS^--Na^+ and PSSH-H_2O are the other two types of PSS structures present in the commercial PEDOT:PSS solution as confirmed by our DFT calculations as given in Figure 3.14.

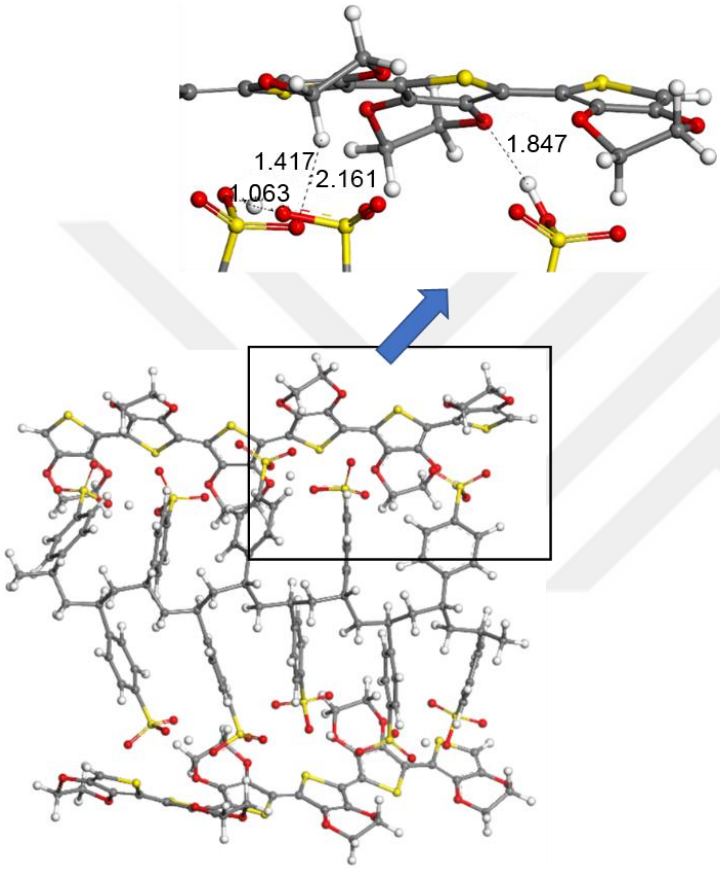


Figure 3.15. PEDOT:PSS where four PEDOT and four PSS are charged. Distances between the atoms of PEDOT and PSS are given in Å unit.

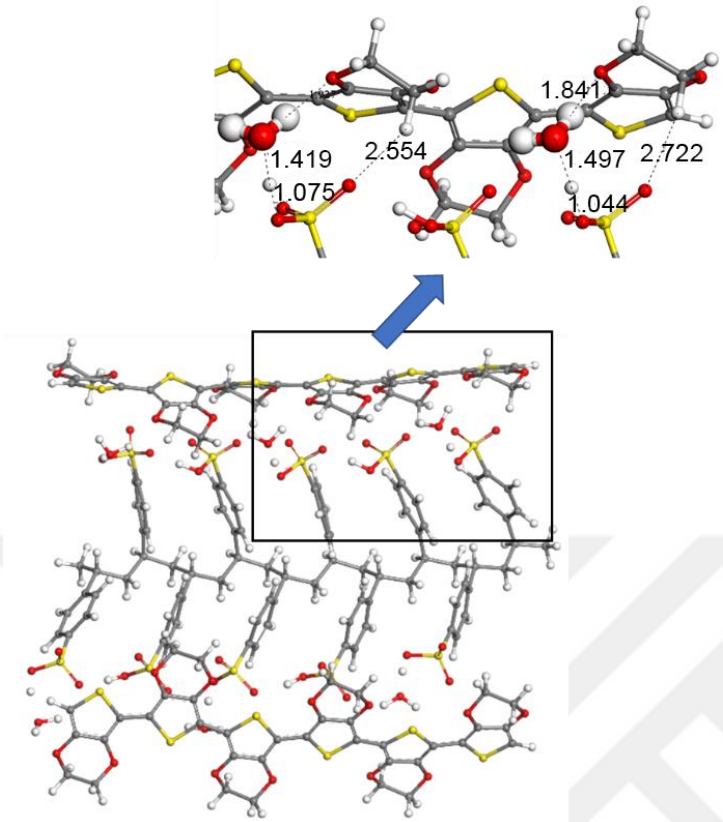


Figure 3.16. PEDOT: PSS where some of the PSSH units are coordinated by water molecules (PSSH-w). Distances between the atoms of PEDOT, H_2O and PSS are given in Å unit.

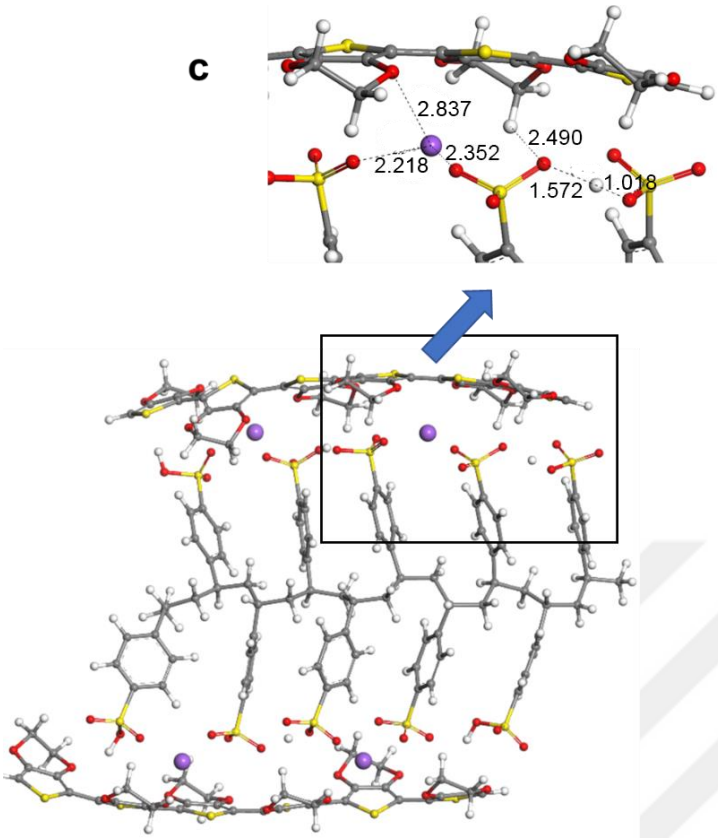


Figure 3.17. PEDOT: PSS where some of the PSS^- units are coordinated by Na^+ cations (PSS^--Na^+). Distances between the atoms of PEDOT, Na and PSS are given in Å unit.

It was demonstrated that PEDOT:PSS distance was the lowest and interaction was the strongest for $PEDOT^+$ and PSS^- demonstrated as the closest distance in Figure 3.15 (a). However, this interaction was weaker for the increasing percentage of PSSH, PSS^--Na^+ and PSSH-H_2O. It can be concluded that $PEDOT^+$ and PSS^- interaction stays intact during acid or other solvent treatments and other types of weakly interacting and insulating PSS and PEDOT types are the ones washed away. The mechanism of conductivity enhancement by acid and solvent treatment is elucidated in this way as

- End group protonation of PEDOT.
- Benzoid to quinoid transition of PEDOT via doping.

- PSS^- replacement by smaller HSO_4^- as dopant that leads to the more ordered PEDOT packing.
- The decreasing ratio of insulating soluble PSSH, PSS^--Na^+ and PSSH-H_2O units in the complex.

3.3.2 All-Atom MD Simulations

The aim of the first constructed simulation cell was to observe the behavior of the PEDOT and PSS chains in water with different concentrations of HSO_4^-, which is the main product of sulfuric acid dissociation in water. As given in Figure 3.4, initially, two PEDOT chains were placed together in the middle of PSS chains with π-stack distance to each other. The proposed mechanism in the literature is the separation of the PEDOT chains from the PSS phase[172]. After the separation of the PSS phase from PEDOT by washing out with water, the remaining PEDOT chains form an ordered structure which is the proposed mechanism of increased conductivity (Figure 3.18).

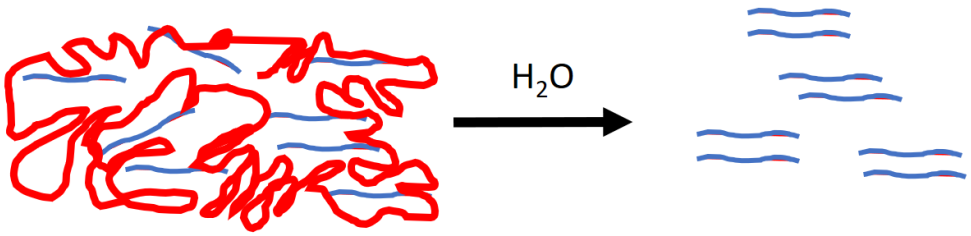


Figure 3.18. Phase separation of PSS (red) from PEDOT (blue) as suggested in the literature [172].

As explained in the Methods (3.2.2), the initial simulation cell was filled with certain amounts of water, HSO_4^- anion and H_3O^+ cation. Number of water was changed so that the density of the simulation cell equals to 1.0 and 1.2 in certain cases. Additionally, the number of HSO_4^- and H_3O^+ was changed so that the simulation cell contains an increasing percentage of acid. Hence, a comparison between the

changing concentration of acid and density of the solution by means of PEDOT-PEDOT aggregation, PEDOT-PSS and PEDOT-HSO_4^- interaction was made. Components of 10 cells used in the simulations are summarized in Table 3.1.

It was observed in the trajectories that, whether or not containing water, two PEDOT chains were separated from each other while the number of HSO_4^- anions was increased. Two of the final snapshots showing the close contact between the PEDOT chains and their separation are given in Figure 3.19 and Figure **3.20**, respectively.

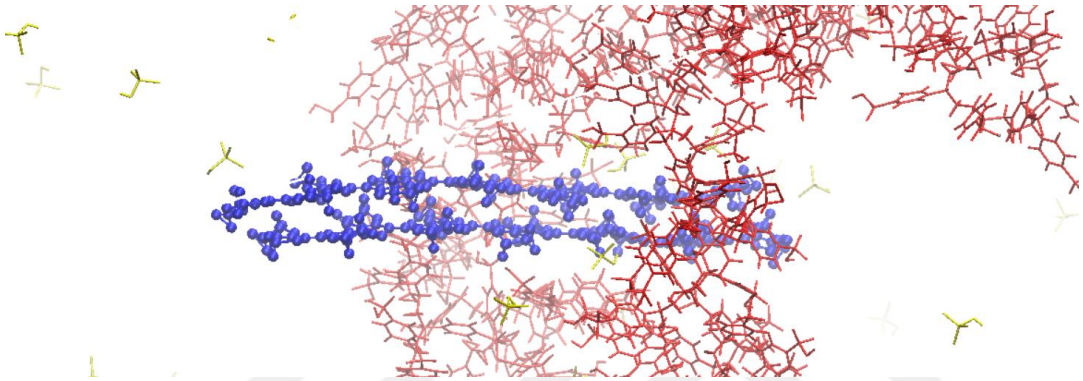


Figure 3.19. Final snapshot from the simulation cell containing 444 HSO_4^- (yellow) and 2008 water (hidden for simplicity). Blue: PEDOT, Red: PSS.

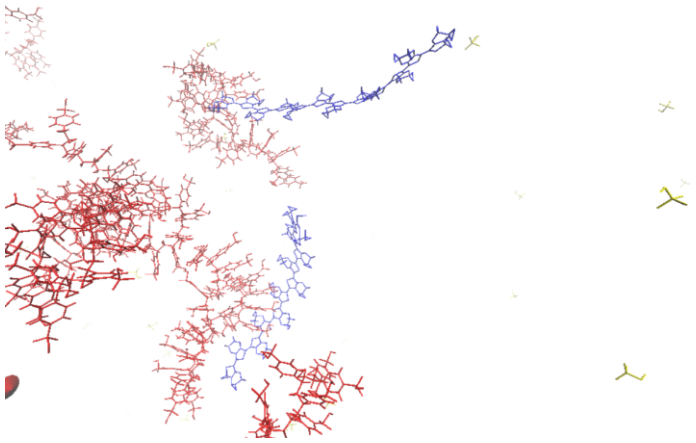


Figure 3.20. Final snapshot from the simulation cell containing 289 HSO_4^- (yellow) and 1001 water (hidden for simplicity). Blue: PEDOT, Red: PSS.

It can be seen in the RDF analysis given in Figure 3.21 that, PEDOT chains can be separated from each other in the presence of water, which looks like an independent process from the number of HSO_4^- anions present in the simulation cell.

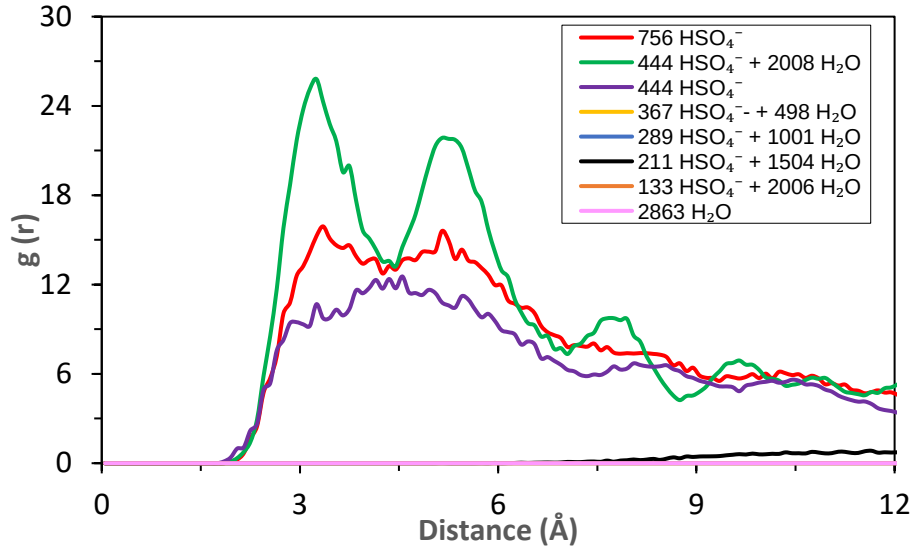


Figure 3.21. RDF analysis of two PEDOT chains in the simulation cells containing 756 HSO_4^- anions (red), 444 HSO_4^- anions and 2008 H_2O (green), 444 HSO_4^- anions (purple) and other combinations of H_2O and HSO_4^- listed in the caption of the figure.

In the RDF analysis given in Figure 3.22, the separation of PSS and PEDOT is observed in the presence of 2863 and 2008 water molecules. It can be concluded from this observation that PSS can be washed away with water from PEDOT chains when the number of water reaches a certain threshold. In the presence of 498 water molecules with 367 HSO_4^-, the peak value in the RDF analysis is in the order of 1.5 at 2.7-3.0 Å distance, due to hydrogen bonding between PEDOT and PSS.

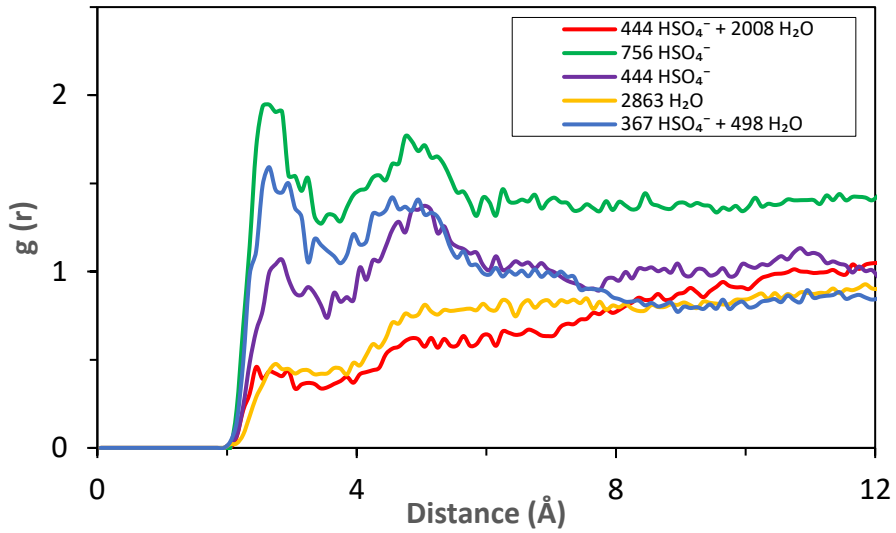


Figure 3.22. RDF analysis of O atoms of PSS with H atoms of PEDOT in the simulation cells containing 444 HSO_4^- anions and 2008 H_2O (red), 756 HSO_4^- anions (green), 444 HSO_4^- anions (purple), 2863 H_2O (yellow), 367 HSO_4^- anions and 498 H_2O (blue).

In Figure 3.23, RDF analysis for the system with HSO_4^- anions and PEDOT is given. The peak shows the number density of O atoms of HSO_4^- anions at about 2.8 Å distance to the PEDOT. Hydrogen bonding can be tracked from the RDF values at about 3-3.3 Å distance. It occurs between PEDOT and HSO_4^- in the presence of both HSO_4^- anion and water molecules.

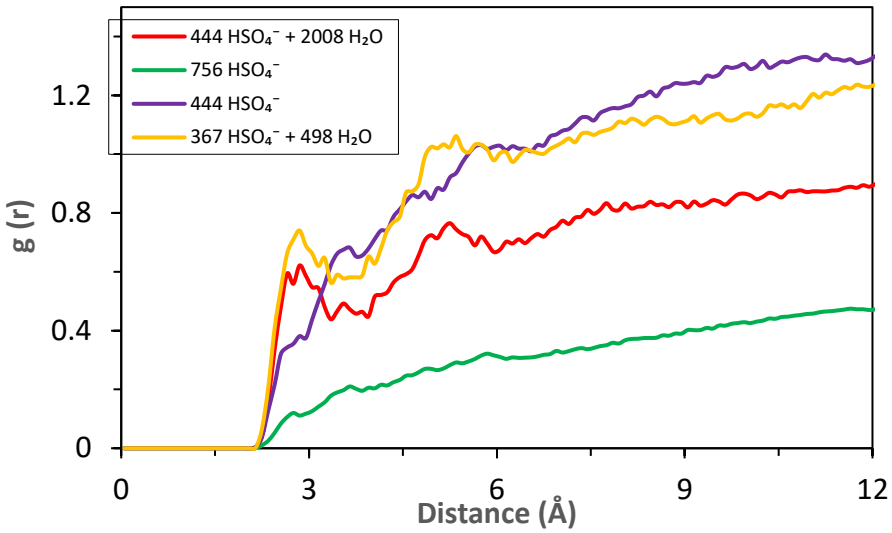


Figure 3.23. RDF analysis of O atoms of HSO_4^- anions with H atoms of PEDOT in the simulation cells containing 444 HSO_4^- anions and 2008 H_2O (red), 756 HSO_4^- anions (green), 444 HSO_4^- anions (purple), 367 HSO_4^- anions and 498 H_2O (yellow).

As a summary of the first set of MD simulations, we obtained three findings. Firstly, it was demonstrated that phase separation of PSS from PEDOT is independent of the presence of HSO_4^-. If the number of water molecules is enough, separation of PSS occurs independently from the number of HSO_4^- in the simulation cell. Secondly, the interaction of HSO_4^- with PEDOT requires the presence of both water and HSO_4^- in the simulation cell. As a third finding, the coalescence of PEDOT chains in the simulation cell does not seem to depend on the the presence or absence of HSO_4^- anions in the simulation cell. The π-stack of PEDOT chains, which is proposed to be one of the factors affecting the conductivity, is lost with the addition of certain amounts of water and HSO_4^- in the simulation cell. From these findings, it is difficult to construct a direct relation with the interactions of PEDOT and PSS chains and HSO_4^- anions.

In another set of all-atom MD simulations, 8 PEDOT chains, each having 12 monomers and +4 charge were placed close to each other and wrapped with 2 PSS chains, each having 96 monomers, 16 of them having -4 charge for charge equilibrium. The purpose of the construction of this structure was to observe the

behavior of an initially ordered PEDOT structure in the presence of HSO_4^- anions and water molecules. If this structure is close to the equilibrium state, it can be expected that the ordered PEDOT chains do not separate at the end of the simulation. This structure with the ordered PEDOT chains can be a good medium for electron transport via the hopping mechanism. A simulation cell containing two of these PEDOT:PSS structures is prepared to demonstrate whether the two bunches of PEDOT chains come closer to each other or not. Approach of the two sets of ordered PEDOT chains to each other may have a positive effect on the conductivity by electron hopping mechanism. Taking this purpose into consideration, a simulation cell containing two of these PEDOT:PSS structures was prepared for further studies.

The simulation cell defined above was minimized with the steepest-descent algorithm integrated into LAMMPS software. The stopping tolerance for energy was $1.0x10^{-4}$ (arbitrary units) and the stopping tolerance for force was $1.0x10^{-6}$ (kcal/mol)/Å. Usually, in minimization procedures, iterations are terminated when one of these tolerances is satisfied for the energy or force in subsequent time steps. The maximum number of iterations was set as 1000 and the maximum number of force and energy evaluations was set as 10.000 at which the minimization was terminated. Temperature was increased from 300 K to 1000 K in 1.0 ns, kept constant at 1000 K for 1.0 ns, decreased to 300 K in 5.0 ns and kept constant at 300 K for 3.0 ns. Three replicates of this structure were placed in a simulation cell. The first cell was filled with water until the density of the simulation cell was 1.2 g/cm^3. The number of water molecules in this cell was used as 7395. Other two simulation cells were prepared so that the cells contain 114 and 218 HSO_4^- anions and 13 and 16 SO_4^{2-} anions to ensure 1.0 and 2.0 mol/L sulfuric acid concentration, respectively.

As given in the final snapshots of the simulation cell containing 0.0, 1.0 and 2.0 mol/L H_2SO_4 in Figure 3.24, there is no visually observable distance in the final structures of PEDOT:PSS. As a first finding, organized PEDOT chains did not separate from each other and did not lose their organized structure in water with both the presence and absence of sulfuric acid. However, a long and most probably insoluble chain of PSS did not separate from PEDOT in all of the three cases, with

and without the presence of sulfuric acid. At the end of the simulations, the phase separation scheme illustrated in Figure 3.18 could not be verified by MD simulations.

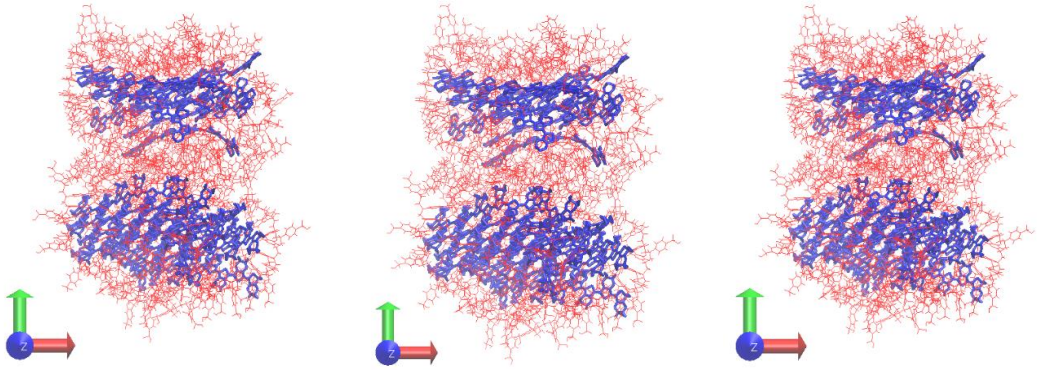


Figure 3.24. Final structures of PEDOT:PSS simulation cell with 0.0, 1.0 and 2.0 mol/L H_2SO_4.

RDF analysis of PEDOT chains with themselves was plotted in Figure 3.25. As seen in the RDF analysis, the closest distance between the two organized PEDOT blocks is about ~14.8 Å at 1 M sulfuric acid concentration. This distance does not seem to be enough for electron hopping and increasing electrical conductivity. Moreover, in the repeated simulations with different initial structures, this distance was not reproduced. In all of the simulations up to this point, the expected self-organization and ordered structure were not observed.

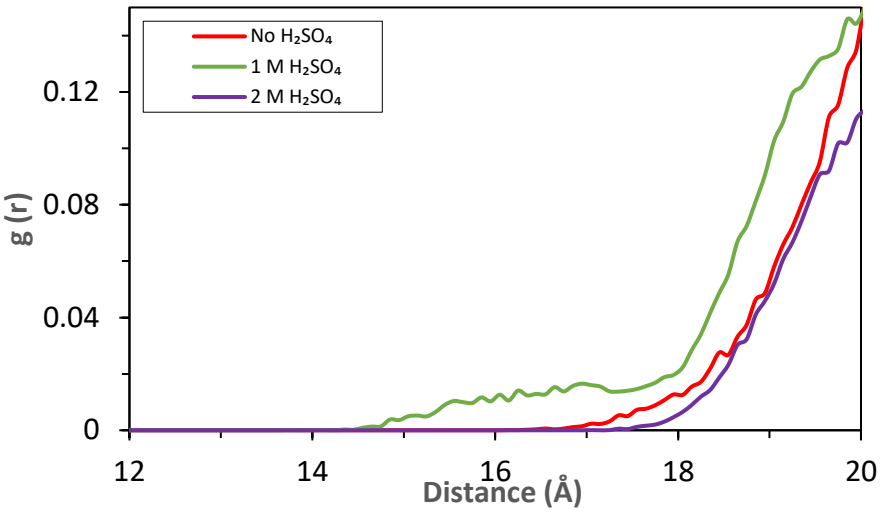


Figure 3.25. RDF of two PEDOT groups containing 8 PEDOT chains in each as described above with each other in the simulation cell containing 0.0, 1.0 and 2.0 M H_2SO_4.

In all-atom MD simulations in the cells containing water, phase segregation of PEDOT and PSS was observed in the presence of water regardless of the presence or absence of HSO_4^- anions in the simulation cell for the chain length of PSS is 24 monomers. On the other hand, when the number of monomers was 96, PSS surrounding the ordered PEDOT chains was not separated. In addition, the π-stacking of PEDOT chains, which is proposed to be one of the factors affecting the conductivity[92], is lost with the addition of certain amounts of water and HSO_4^- in the simulation cell. Aggregation of PEDOT chains and formation of an organized structure could not be demonstrated which is another proposed mechanism derived from the experimental studies reported in the literature[173]. It might require a longer time that would not be reached by all-atom MD simulations to highly ordered and densely packed structures as reported in the literature[174]. For this reason, a highly ordered structure of $EDOT_4$ chains is constructed. Details of the constructed cell were explained previously in the Methods (3.2.2) section.

In the literature, Ouyang and coworkers suggested that there is a strong Coulombic attraction between OH^- and $PEDOT^+$, so the charge carriers become more localized after OH^- treatment[175]. Okuzaki's group suggested that OH^- treatment of PEDOT:PSS films disrupts the stacking of PEDOT nanocrystals and therefore the electrical conductivity decreases[176]. Therefore, the simulation cell including the highly ordered structure of $EDOT_4$ is filled with HSO_4^- and OH^- anions both of which make strong interaction with EDOT monomers. On the contrary, treatment with HSO_4^- anions increases the conductivity where treatment with OH^- anions results in a decrease.

In contrast with HSO_4^-, NaOH treatment results in a decrease in the electrical conductivity. There may be three possible explanations for the decrease in electrical conductivity by NaOH treatment, which are;

1. Strong OH^- interaction and/or bonding with PEDOT that disrupts conjugation length and increases localization of charge carriers[175].
2. OH^- diffusion into PEDOT interlayer that disrupts packing and hopping mechanism[176].

$NaHSO_4$ formation by NaOH treatment, which results in the dedoping of $PEDOT^+$-HSO_4^-.

It is demonstrated that $PEDOT^+$-HSO_4^- has a well-packed structure compared to $PEDOT^+$-PSS^- core-shell morphology in all-atom MD simulations with a densely packed PEDOT system. All HSO_4^- molecules were placed between the interlayers of π-stacked PEDOT chains in interaction with the ethylenedioxy hydrogens as shown in Figure 3.26 (a,b). On the contrary, OH^- molecules were distributed both in the interlayers of π-stacked PEDOT chains as well as in the π-stacks that disrupt the packing of chains as shown in Figure 3.26 (c,d). This also explains the observed deterioration in the electrical conductivity in BA-PEDOT:PSS.

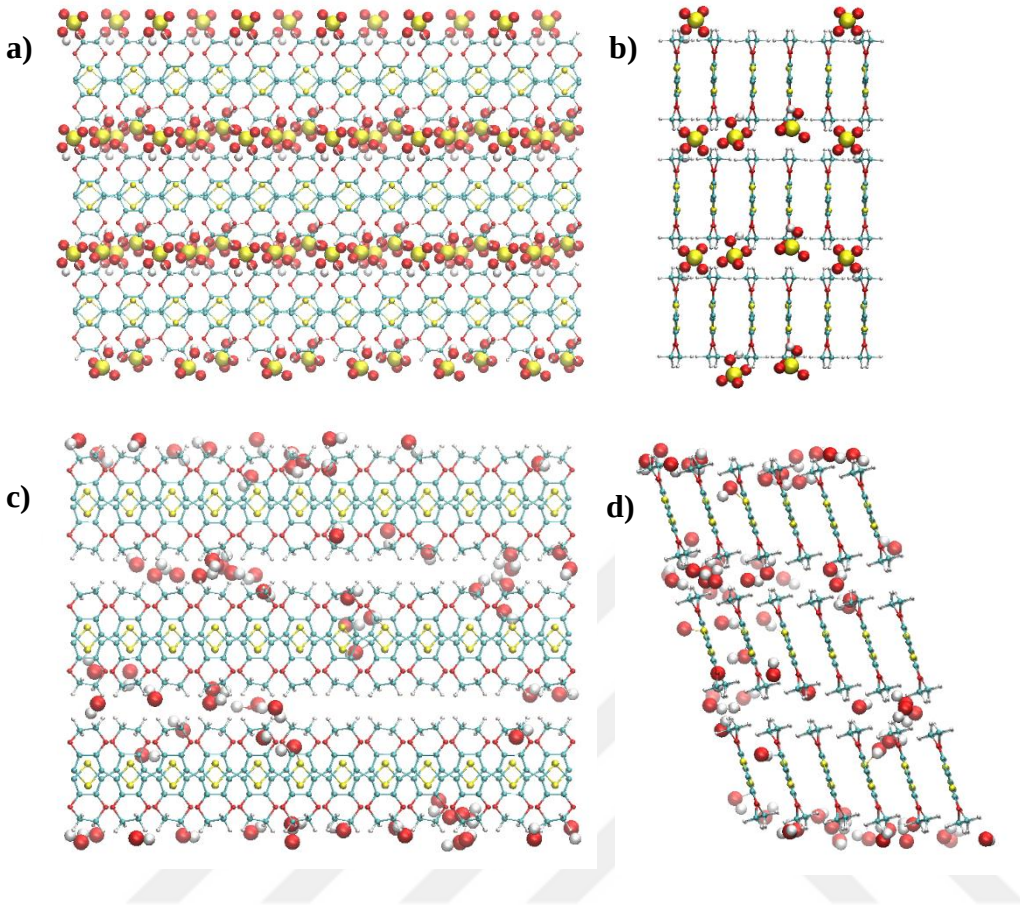


Figure 3.26. Equilibrium structure for 6x3x3 supercell with a-b) 72 HSO_4^- and c-d) 72 OH^- molecules (216 PEDOT monomer in the cell) for –xy (for a-c) and –yz (for b-d) directions.

Concentration profiles of HSO_4^- and OH^- perpendicular to the PEDOT chain orientation are plotted in Figure 3.27. It can be confirmed from this plot that HSO_4^- distributes regularly perpendicular to the PEDOT chains by placing between the edges of π-stacked PEDOT chains. On the other hand, OH^- anions have relatively irregular concentration profile between the faces of π-stacked PEDOT chains, possibly decreasing the electrical conductivity via the hopping mechanism.

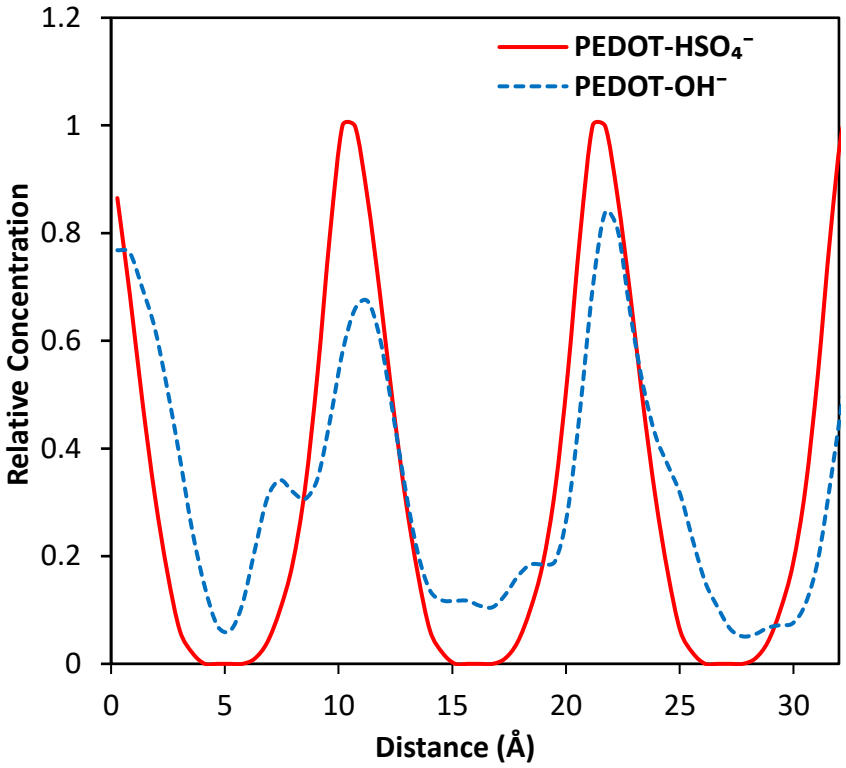


Figure 3.27. Concentration profile for HSO_4^- and OH^- molecules in-y direction.

The reason for the difference in the distribution of HSO_4^- and OH^- is mainly the interactions of these anions with PEDOT. HSO_4^- anions interact with the ethylenedioxy hydrogens of the PEDOT at the edge of the chains. On the other hand, OH^- anions interact with both the edge ethylenedioxy hydrogens and β-carbons in the thiophene from the face direction that agrees with DFT calculations.

The intermolecular distances between doped π-stacked PEDOT chains provide perfect distribution of HSO_4^- anions to the interlayer along the edges by interacting with four PEDOT monomers as demonstrated in Figure 3.28. Doping of PEDOT with HSO_4^- anions in this way increases the packing efficiency and electrical conductivity. Intermolecular distances are in units of Å and show a close intermolecular distance between these two components. This distribution is not possible for OH^- due to both the size and strong interaction of OH^- anion with electron-deficient β-carbon in thiophene.

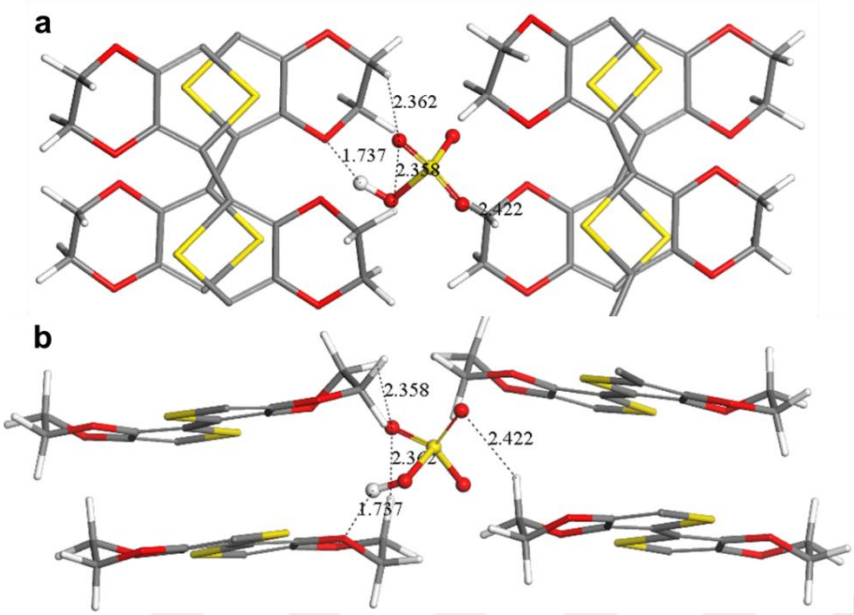


Figure 3.28. Average position of supercell from a) –xy and b) –yz directions for A-PEDOT:PSS. Distances between the atoms in the end group of PEDOT and HSO_4^- are given in Å.

The third reason for the decrease in the electrical conductivity with the NaOH treatment is the formation of Na^+- HSO_4^- acidic salt that might cause the dedoping of acid in PEDOT. In Figure 3.29, RDF for the hydrogen bond between PEDOT-HSO_4^- showed that the number of hydrogen bonds significantly decreased due to the Na^+- HSO_4^- ionic interactions. Interaction energies calculated by DFT methods agree well with the result that Na^+-HSO_4^- interactions were found to be slightly stronger than PEDOT-HSO_4^- interactions.

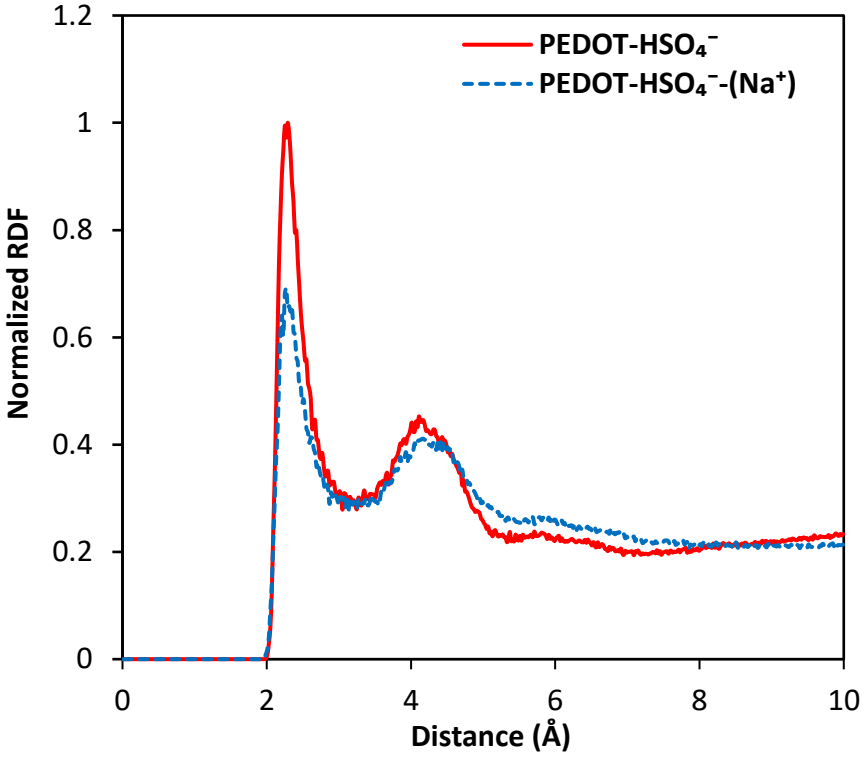


Figure 3.29. Radial distribution function for $PEDOT_6^-$-HSO_4^- hydrogen bond before (A-PEDOT:PSS) and after NaOH addition (BA-PEDOT:PSS).

In the study by Tounakti and coworkers, conductivity of the PEDOT:PSS was measured in situ during treatment with DMSO with and without water[106]. They concluded using XPS and IR measurements that PSS structure reorganized to a planar and stretched structure as soon as the PEDOT:PSS was in contact with the solvent. Additionally, short chains of neutral or charged PSS (HPSS, NaPSS) were removed with the help of the solvent. They proposed that remaining PEDOT:PSS chains after removal of HPSS and NaPSS were insoluble in any solvent and made an organized structure upon drying as depicted in Figure 3.30.

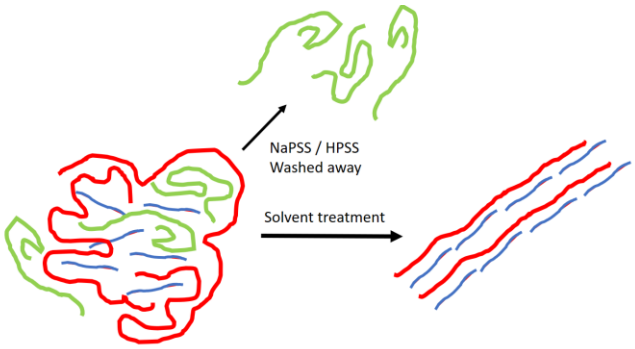


Figure 3.30. Proposed mechanism of Tounakti et.al.[106] for enhanced conductivity with solvent treatment (Green: PSS^-Na^+ and PSSH, Red: Insoluble PSS, Blue: PEDOT).

As was reported by Tounakti and coworkers that the reorganization of PSS and PEDOT occurs at the time when they are in contact with the solvent[106]. Another initial cell structure was constructed containing PEDOT and PSS chains with different numbers of monomers and different total charges of the chains to follow any reorganization with the addition of solvent to the system.

As it is depicted in the RDF analysis of PEDOT with water and hydronium ions in Figure 3.31 and Figure 3.32, the number density of water molecules around PEDOT decreases over time during the simulation. The simulation takes 20 ns and RDF values are plotted at 4, 8 and 20 ns.

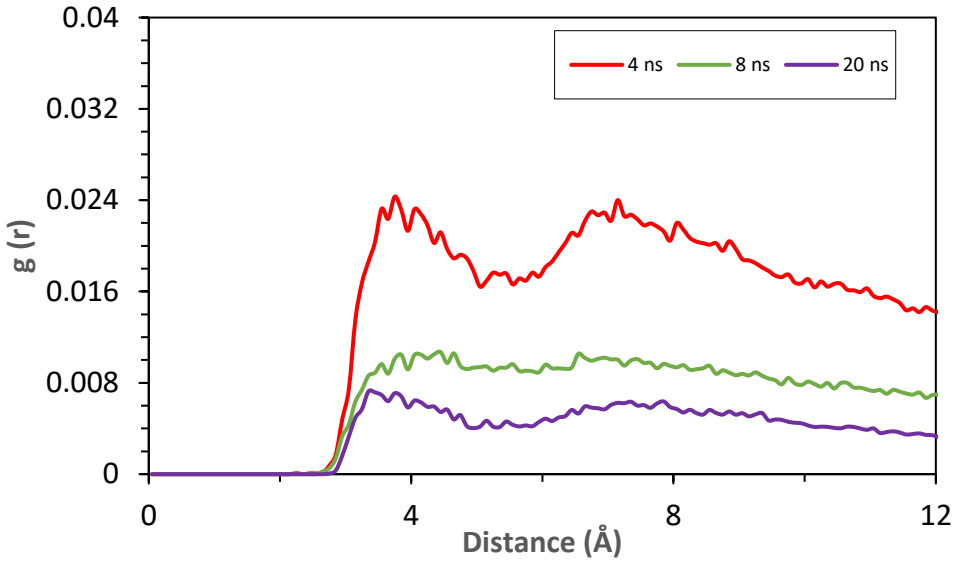


Figure 3.31. RDF analysis of backbone C of PEDOT with O atoms of H_2O molecules after 4 ns (red), 8 ns (green) and 20 ns (purple).

On the contrary to water molecules, the value of RDF peak at about 4 Å distance increases in time from about 0.02 to the value near 0.1, which corresponds to a 5-fold increase.

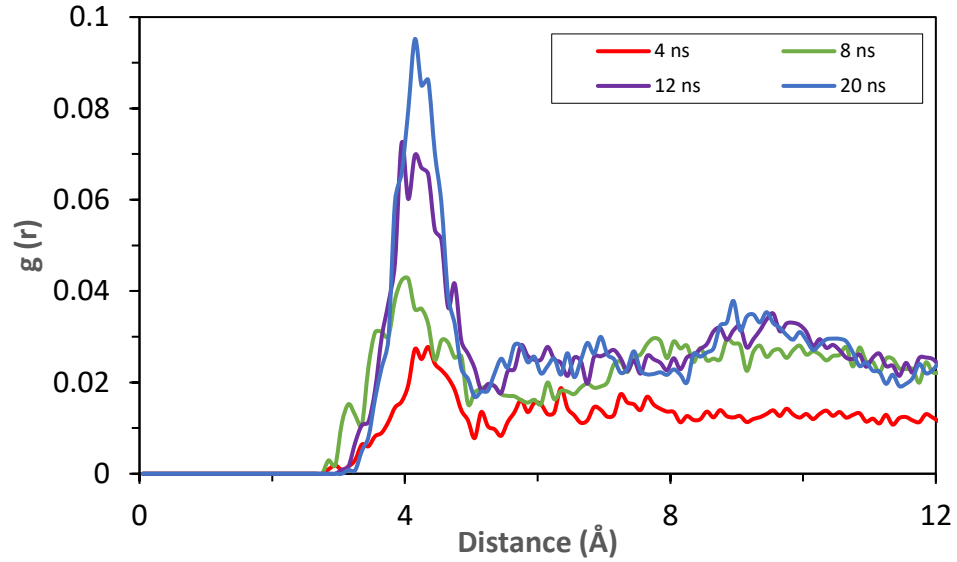


Figure 3.32. RDF analysis of backbone C of PEDOT with O atoms of H_3O^+ ions after 4 ns (red), 8 ns (green), 12 ns (purple) and 20 ns (blue).

Similar to PEDOT, an increase in the attraction was observed between H_3O^+ ions and PSS. In this case, however, the closest distance between H atoms of hydronium and O atoms of PSS was 1.75 Å as shown in Figure 3.33 which is close to an intermolecular attraction. In the report by Tounakti and coworkers, it was proposed that with the addition of water to DMSO, hydronium ions were formed by making bridges between SO_3^- groups of PSS monomers. This process was suggested to be the first step in the organization of PSS and PEDOT. Hydronium ions make bridges between the SO_3^- ends of the PSS, resulting in the reorganization of PSS to a planar stretched structure. The result is the reorganization of PEDOT chains to a linear structure. In the all-atom MD simulations, this whole process was not observed but the intramolecular bridges between SO_3 of the PSS chain can be observed in Figure 3.34.

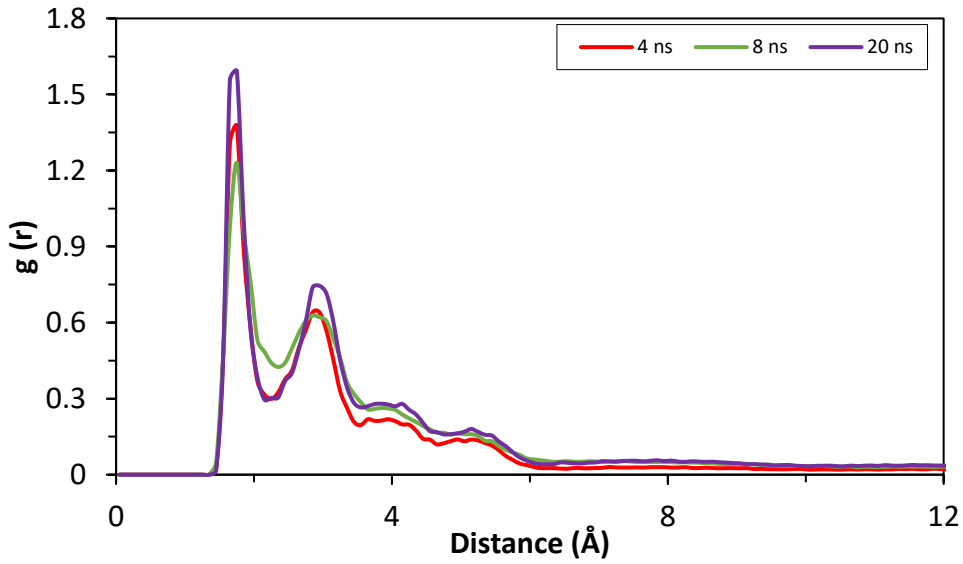


Figure 3.33. RDF analysis for O atoms of PSS with H atoms of H_3O^+ ions 4 ns (red), 8 ns (green) and 20 ns (purple).

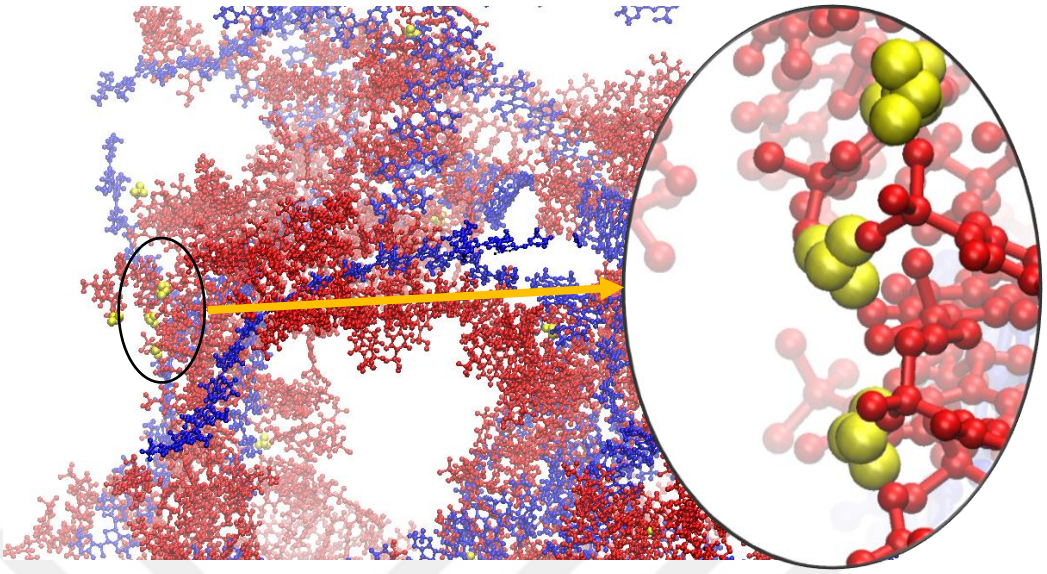


Figure 3.34. Positioning of H_3O^+ between the SO_3^- ends of a PSS chain.

For PEDOT and PSS, RDF values were decreasing with time during the simulation. As given in Figure 3.35, it can be seen that there was a 9-fold decrease in the number density of the DMSO molecules at about two Å distance from PSS. Yet, the extent of this interaction was decreased, however not totally lost, which is in agreement with the finding that some of the PSS chains were removed while there were insoluble PSS chains that were not removed. PEDOT seems to have a weak interaction with the solvent either as shown in Figure 3.36.

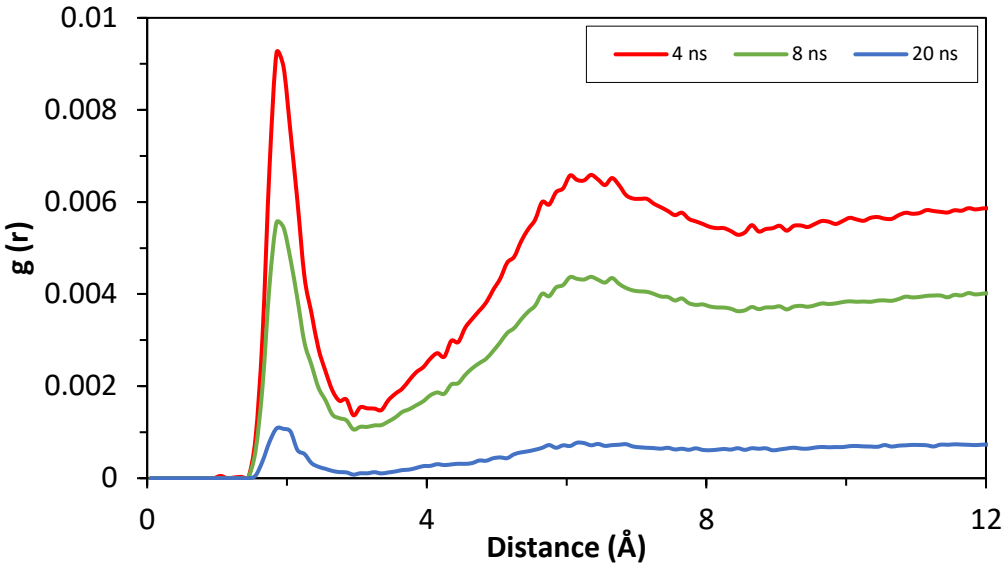


Figure 3.35. RDF analysis of PSS with DMSO molecules 4 ns (red), 8 ns (green) and 20 ns (blue).

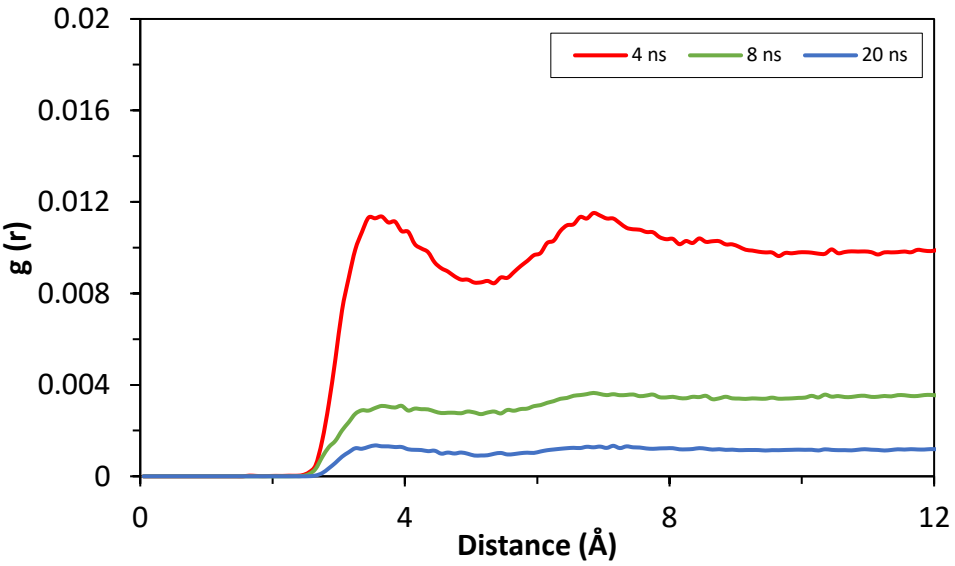


Figure 3.36. RDF analysis of PEDOT with DMSO 4 ns (red), 8 ns (green) and 20 ns (blue).

Finally, as it is demonstrated in Figure 3.37, there is a 1.5-fold increase in the g (r) value in the RDF of PEDOT-PSS. This finding shows that the insoluble PEDOT and PSS are interacting which is the first step to make an ordered structure.

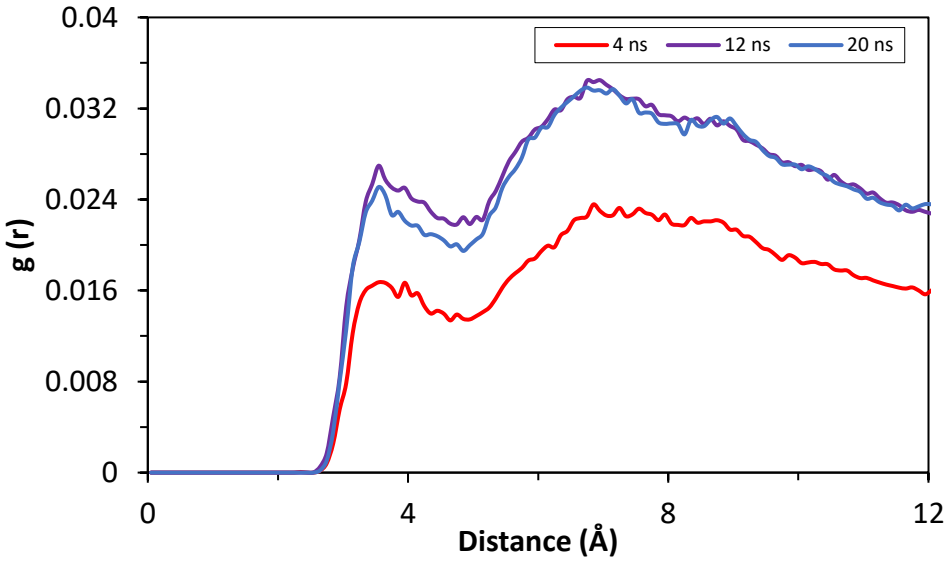


Figure 3.37. RDF analysis of O atoms of PSS with backbone C atoms of PEDOT.

CHAPTER 4

MECHANISM OF AGGREGATION CONTROL BY DETERGENT AND DISPERSANT IN ENGINE OIL

4.1 Aim of the Study

In this chapter, multiscale modeling methods were used to elucidate the mechanism of deposit formation in engine oil. As explained in the Introduction (1.5.1) chapter, these insoluble deposits, namely soot and sludge are formed as a by-product of incomplete fuel oxidation. Besides, control of deposit formation via detergents and dispersants was also simulated. The development of aggregates of insoluble deposits and the prevention of aggregation by model dispersants and detergents were studied.

It is important to note that, the aim of this study was not to conduct optimization studies that would give information or suggestions to increase the performance of detergent and dispersant in deposit control. Instead, as a first step, the aim of this study was to understand the deposit control mechanism. Once a successful model of the real situation is created, it can be possible to conduct optimization studies to acquire detergent and dispersant structures with improved performances in deposit control in the new studies.

The first objective of this study is the construction of an insoluble deposit model from scratch. The exact molecular structure of the insoluble deposit is not known. To the best of our knowledge, this study is the first in which an insoluble deposit model was constructed and aggregation of these insoluble deposit models was demonstrated. In addition, within the scope of this thesis, models for base oil, detergent and dispersant were developed for all-atom and coarse-grained molecular dynamics simulations.

4.2 Computational Methods

Computational methods used in this study including the pairwise interaction energy calculations with DFT, all-atom and coarse-grained MD simulations are explained below in detail.

4.2.1 First Principle Calculations

Most probable interactions and molecular configurations were determined by DFT. Interaction energies provide information about the experimental observations before any larger-scale simulations. All possible interaction energies between components were calculated based on the B3LYP/6-31+g(d) level DFT calculations starting from different initial structures. Detergents were represented by phenyl sulfonate (Psulfonate) group and alkyl tail. Dispersants were represented by bis-succinimide (bis-suc), polyisobutylene (PIB) and amine groups. Functional groups on the insoluble nanoparticle surface were represented by branched alkane groups substituted with carboxylic acid (Nacid), ketone (Nketone), alcohol (Nalcohol) and dialcohol (Nalcohol2). In the representation of the base oil, the limited contribution of branching and alkene groups was ignored and the alkyl group represented it.

4.2.2 All-Atom MD Simulations

Prior to the all-atom MD simulations, insoluble deposit, base oil, detergent and dispersant models were constructed. Construction of the simulation cells and procedure for all-atom MD simulations are described within this text below.

4.2.2.1 Construction of the Models

Initial all-atom structures for the insoluble deposit (which will be called “nanoparticles” throughout this chapter), base oil, bis-succinimide dispersant and

sulfonate detergent models were constructed throughout the thesis study by Esra Kan[177] in our group using Discovery Studio. The base of the models is described briefly below in this thesis.

4.2.2.1.1 Construction of Insoluble Deposit Model

The insoluble deposit was modeled by using C and O ratio based on the experimental elemental composition analysis results provided by the Lubrizol Corporation™. Elemental composition analysis showed that the land deposits contain 72% C and 25% O by mole ratio. Minor elements were Mg, P, S and others in smaller portions. For the drain insoluble, the mole ratio of C and O was found as 74% and 23%, respectively. Keeping these values in mind, the insoluble deposit model was constructed using 75% C and 25% O. These nanoparticles are formed as a by-product due to insufficient and unfinished combustion and they add up making aggregates, which can clog the filters and certain parts of the engine. A spherical-shaped nanoparticle with a diameter of about 2.2 nm was modeled as the smallest unit of the insoluble deposit as shown in Figure 4.1. The chemical formula of this insoluble deposit model was $C_{300}H_{599}O_{100}$. The molecular weight of the model was 5766.57 g/mol.

In order to mimic the aggregation process in the engine pistons, polar functional groups were placed on the surface. Non-polar functional groups were placed both in the center and on the surface. The spherical shape of these nanoparticles was kept throughout the simulations. Thus, the functional groups were connected to each other from the center of the sphere to the surface via chemical bonds.

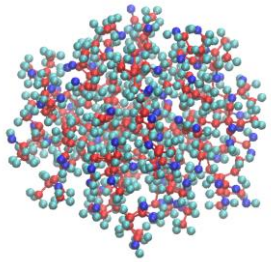


Figure 4.1. Insoluble deposit model. Molecular formula: $C_{300}H_{599}O_{100}$. 75% C, 25% O based on the experimental results provided by the company.

4.2.2.1.2 Construction of Base Oil Model

The average carbon number of isoparaffins and naphthenic groups is between 20 and 25. According to this information, base oil was modeled as a branched hydrocarbon structure having 24 C atoms[178]. The experimental density for the base oil is 0.86-0.87 g/cm^3. An alkene group at the center with short branching is preferred in order to reach the desired density. The structure of the base oil model used in this study is shown in Figure 4.2. The base oil is the major constituent of the lubricant additive according to the experimental results provided by the company. Care was taken in the preparation of the base oil structure to meet the experimental density provided by the company. The same density with the experimental value was calculated in MD simulations in constant pressure with the cell containing only base oil. Further information can be found in the thesis study by Esra Kan[177].

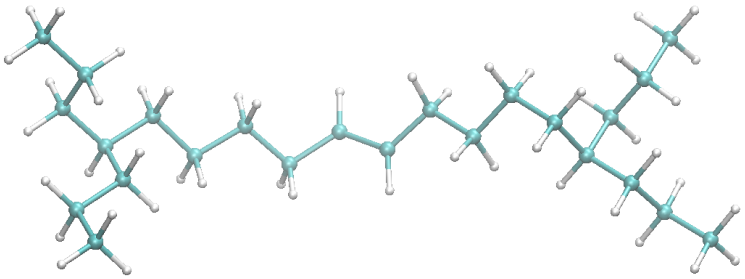


Figure 4.2. Base oil model used in this study.

4.2.2.1.3 Construction of the Dispersant Model

Dispersant having PIB tails containing 18 isobutylene units and polar amine groups in the center, connected with bis-succinimide was modeled as shown in Figure 4.3.

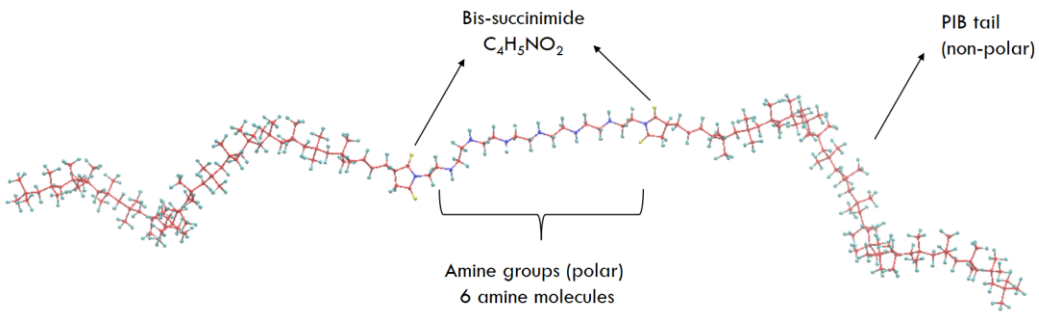


Figure 4.3. Dispersant model used in this study.

4.2.2.1.4 Construction of the Detergent Model

Detergent having a sulfonate head group with -1 charge and alkyl tail was modeled as shown in Figure 4.4.

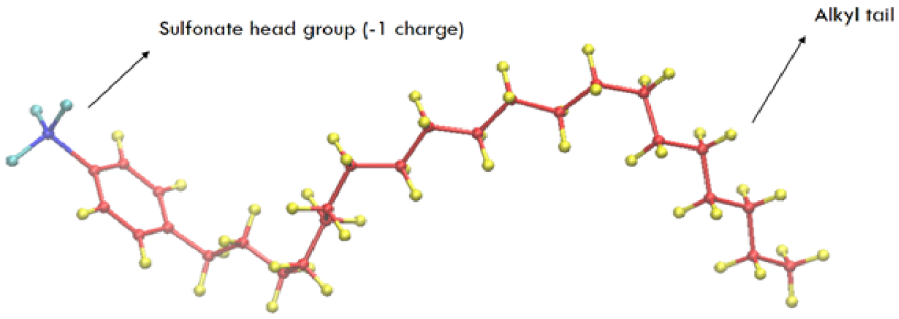


Figure 4.4. Sulfonate detergent model used in this study.

4.2.2.2 Modeling of the Simulation Cell

For all-atom molecular dynamics simulations, simulation cells were prepared with Discovery Studio. Scienomics MAPS 4.4 was used to apply the PCFF force field to the atoms in the constructed periodic models.

In the first part, three simulation cells containing two insoluble nanoparticles were prepared as shown in Figure 4.5. No dispersant or detergent was added to the first cell. In the second cell, two dispersants were added in the center of the simulation cell, in between two insoluble NP models. The positions of the detergents were chosen using Monte Carlo simulations. In the third cell, six detergents were placed. All the cells were filled with base oil.

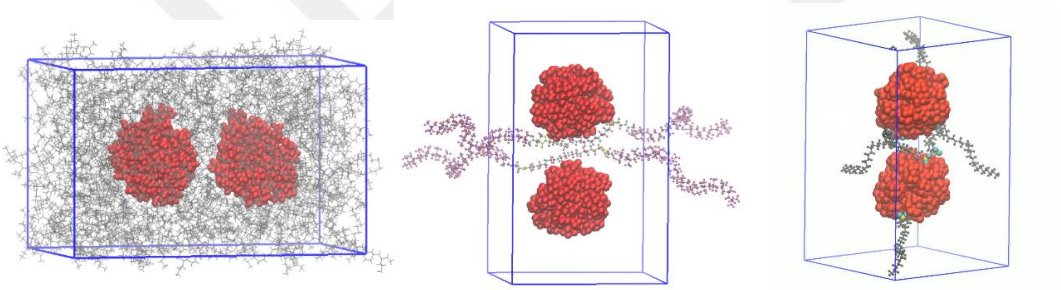


Figure 4.5. Three simulation cells containing a) 2 NPs, b) 2 NPs and 2 dispersants, c) 2 NPs and 6 detergents. Base oil molecules are hidden in the second and third cell for simplicity.

Simulation cells containing three nanoparticles were also prepared similarly as shown in Figure 4.6. No dispersant or detergent was added to the first cell. In the second and third cells, three and six dispersants were added in the center of the simulation cell, respectively. In the fourth and fifth cell, twelve and sixteen detergents are placed. All the cells were filled with base oil.

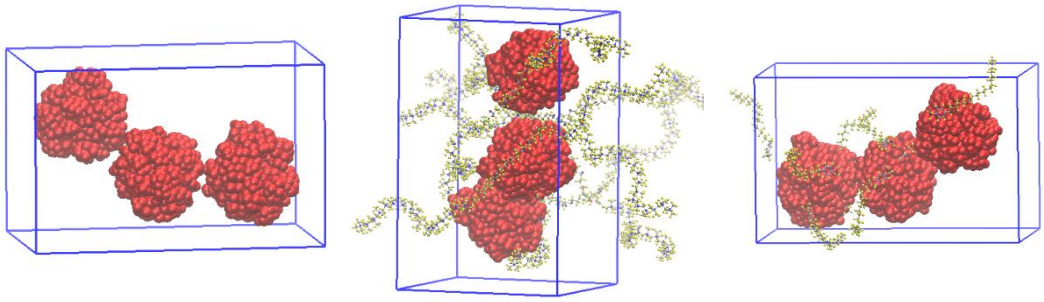


Figure 4.6. Three simulation cells containing a) 3 NPs, b) 2 NPs and 6 dispersants, c) 3 NPs and 12 detergents. Base oil molecules are hidden for simplicity.

4.2.2.3 Molecular Dynamics Simulation Procedure

Simulations were carried out by using LAMMPS (3 Mar 2020 version). 9−6 Lennard-Jones (LJ) was used for short-ranged repulsion-dispersion interactions. Particle-particle particle-mesh solver (PPPM) was used for long-range electrostatic interactions. Polymer consistent force field (PCFF) was used for bonded and non-bonded interactions. Data visualization and calculations were carried out with VMD visualizer. The simulation box has periodic boundary conditions (PBC) in the x, y and z directions. Initial structures were minimized using the steepest descent algorithm integrated into the LAMMPS package. The stopping tolerance for energy is $1.0x10^{-4}$ (arbitrary units) and the stopping tolerance for force is $1.0x10^{-6}$ (kcal/mol)/Å. As a general procedure in the minimization of the initial structures, iterations are terminated when one of these tolerances is satisfied for the energy or force in subsequent time steps. The maximum number of iterations was set as 1000 and the maximum number of force and energy evaluations was set as 10.000 at which minimization is terminated. The time step was 1 fs. An NVT ensemble and a Nose-Hoover thermostat at 423 K were used. Temperature was kept constant at 423 K for 6.0 ns.

4.2.3 Coarse-Grained MD Simulations

Similar to the all-atom MD simulations section, coarse-grained models of insoluble deposit, base oil, dispersant, salicylate and sulfonate detergents for the Martini force field were constructed before coarse-grained MD simulations.

4.2.3.1 Construction of the Models

Scienomics Atomeso Converter was utilized for mapping atoms of deposit model, base oil, dispersant and detergent to Martini 2.0 force field into coarse-grained beads or units for coarse-grained molecular dynamics simulations. Once the bead coordinates were gathered from the Scienomics Atomeso Converter, scripts written in Python and/or Excel were used to prepare Moltemplate input files. Packmol and Moltemplate programs were used for the preparation of simulation cells and LAMMPS input files. Data visualization and calculations were carried out with VMD.

4.2.3.1.1 Construction of the Insoluble Deposit Model

The diameter of the insoluble nanoparticle was 2.2 nm and number of beads in this coarse-grained particle was 123 in total. Type of the beads and mean distances between the center of the nanoparticle and number density of the beads based on the distance from the center are summarized in Table 4.1 and Table 4.2. The mean distances of apolar C1-4 beads to the center are between 7-8 Å. As explained in all-atom MD simulations section, polar functional groups were placed on the surface. Non-polar functional groups were placed both in the center and on the surface. Therefore, the mean distance of N_a, N_{da} and P_1-P_4 beads was between 9-10 Å. As defined in the “Introduction” part and summarized in Table 1.1, the C type of beads in Martini force-field represent apolar type of groups such as alkane, alkene and alkyne groups. P type beads represent polar types of groups such as water, DMSO,

ethanol, acetamide. For C and P type beads from 1 to 5 numbers represent the scale of the polarity. N type of beads represent non-polar groups such as 1-propylamine or 2-propanone and Q type of beads represent charged beads. For N and Q type of beads –da subscript represents both donor and acceptor character in hydrogen bonding where –d subscript represents donor, -a subscript represents acceptor and -0 represents the absence of hydrogen bonding character.

Table 4.1 Types of beads and their mean distances from the origin of the insoluble deposit model prepared in this study.

Type	**Mean Distance (Å)**
C_1	7.224
C_2	9.764
C_3	7.792
C_4	7.661
N_a	9.456
N_{da}	8.668
P_1	9.788
P_2	9.682
P_4	9.674

Table 4.2 Distance from the center of the insoluble deposit model and corresponding number of beads in the insoluble deposit model.

Distance (Å)	Number of Beads
0-1	0
1-2	1
2-3	1
3-4	3
4-5	7
5-6	12
6-7	8
7-8	13
8-9	24
9-10	34
10-11	20

Considering the data given in Table 4.1 and Table 4.2, insoluble deposit model with diameter 2.2 nm was modelled using Packmol software. Same number of beads listed in Table 4.2 were randomly placed in the given distance intervals.

As it was explained in the Computational Methods (4.2.2.1.1) section, the beads should keep their spherical structure during the simulations to meet the experimental results. Shortly, spherical structure is a convenient starting point to model large and porous deposit formation. A Python script was written to assign bonds randomly between the beads, beginning from the center bead and ensuring that each bead forms at least one and at most six bonds to conserve their integrity and shape. Next, Moltemplate package was utilized to prepare simulation cells for simulations in LAMMPS package. To verify that the nanoparticles remained in their spherical form throughout the simulation, 10 ps long NPT followed by 10 ps NVT simulations were performed until a NP with a satisfactory shape was obtained.

By using the same method, nanoparticles having diameters of 3.2 and 4.4 nm were prepared using Packmol software. The number of beads were increased based on the extension in the volume. Nanoparticles having 3.2 nm diameter contain 383 beads and those having 4.4 nm diameter contain 984 beads. Deposit models constructed for coarse-grained MD simulations are shown in Figure 4.7.

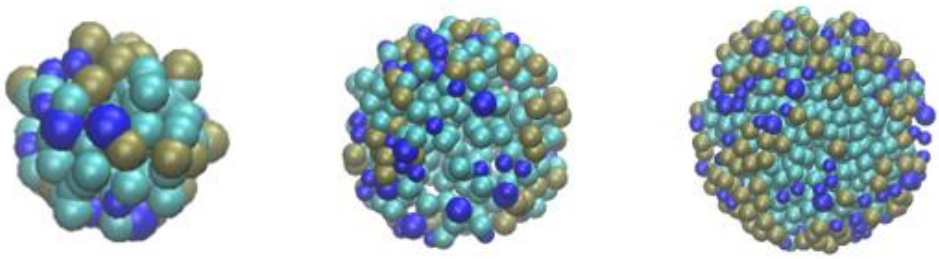


Figure 4.7. Martini model of nanoparticle, consisting of polar, apolar and non-polar beads in total. Total number of beads are 123, 383 and 984, respectively. Images are resized to fit in-line.

4.2.3.1.2 Construction of the Base Oil Model

Base oil was mapped consisting of seven apolar beads at different levels of polarity. The central bead containing the only alkene group in the structure was mapped to C4 apolar bead. Branching alkanes on the left and right sides of the structure were mapped as C3 and the beads connecting central bead to the branch beads were represented as C1 beads as shown in Figure 4.8.

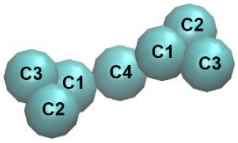


Figure 4.8. Martini model of base oil, consisting of 7 apolar (C1-C4) beads.

As expressed in the all-atom MD simulations part of this text, experimental density of the base oil, provided by the company is 0.86-0.87 g/cm^3 consistent with all-atom

MD simulations. Coarse-grained MD simulations in NPT ensemble were also run to check the density of coarse-grained base oil model. As shown in Figure 4.9, a satisfactory value of density, which is in between 0.86 and 0.87 g /cm3, was obtained beginning from ~0.17 ps from the starting configuration. This important step validated our model and simulation methodology.

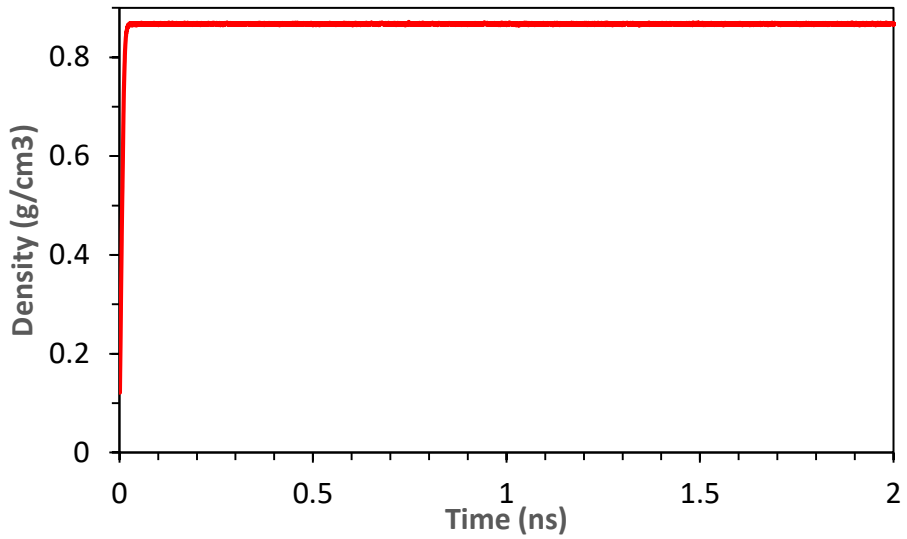


Figure 4.9. Density vs. time plot of the coarse-grained MD simulation of the cell containing only base oil model.

4.2.3.1.3 Construction of the Dispersant Model

Polyisobutylene-bis-succinimide (PIBSI) type dispersant was mapped into Martini coarse-grained force field consisting of three chemically different components as it is in the all-atom model. Polar P_5 beads depict the central amine group while P_3-P_5 couples represent the succinimide groups on either side of the amine group. These beads are connecting the amine group to two apolar tails as shown in Figure 4.10.

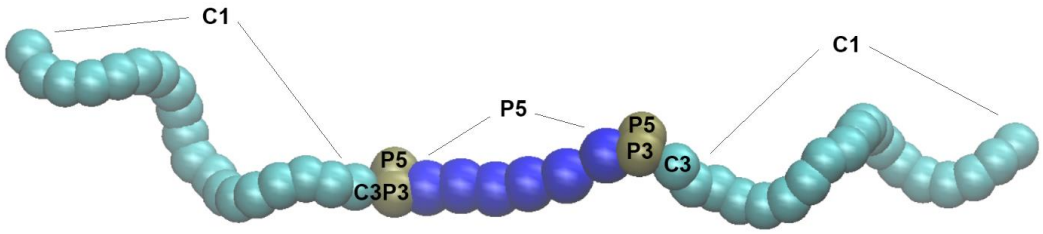


Figure 4.10. Martini model of bis-succinimide dispersant. 36 apolar (C_1, cyan) beads for ends, 6 polar (P_5, blue) beads in center, 4 polar (P_3, P_5; gray) and 2 apolar (C_3, cyan) beads for rings.

4.2.3.1.4 Construction of the Detergent Model

Sulfonate head group of the detergent is represented as a Q_a type bead having -1 charge. Aromatic ring connected to the sulfonate is represented as three STY beads which is an optimized version of SC_4 beads for phenyl surfactant studies, reported in the literature[179]. Tail of the detergent is represented as five apolar C_1 beads as shown in Figure 4.11. For charge equilibrium, one Q_0 type of bead with +2 charge is added to the simulation cells for every two detergents.

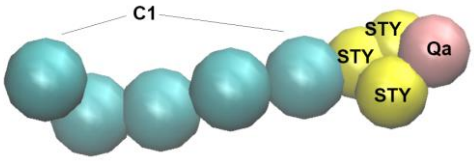


Figure 4.11. Martini model of sulfonate detergent. 5 apolar (C_1-C_4, green) beads for tail, 3 apolar (STY, yellow) beads for styrene and 1 charged (Qa, pink) bead for sulfonate with -1 charge.

For salicylate type of the detergent, salicylate head is represented as a Q_a type bead having -1 charge, similarly in sulfonate. The only difference in a salicylate detergent from sulfonate detergent is the SP_2 bead instead of STY bead for better representation –OH group connected to the aromatic ring as shown in Figure 4.12.

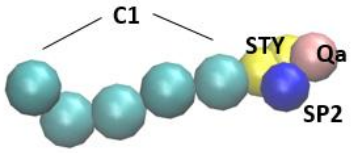


Figure 4.12. Martini model of salicylate detergent. 5 apolar (C_1, green) beads for tail, 2 apolar (STY, yellow) and 1 polar (SP_2, blue) beads for styrene and 1 charged (Qa, pink) bead for sulfonate with -1 charge.

4.2.3.2 Construction of the Simulation Cell

For coarse-grained MD simulations, ten of the insoluble deposit models were inserted in the center of the simulation box and the remaining 40 NPs were inserted into the surrounding as shown in Figure 4.13. Throughout the coarse-grained MD simulations, aggregation of the nanoparticles was monitored from RDF analysis between the polar groups of the central 10 NPs and those of the surrounding 40 NPs. It is important to consider that, the positions of the NPs at the end of the simulation depends strongly on the initial configurations. Hence, the trajectory files were also visualized by eye to check whether the aggregation between the central beads and the surround beads was a good representation of the aggregation inside the whole cell. Moreover, the initial positions of the NPs and the base oil molecules were prepared identical in the cells that contain a) only NPs and base oil, b) NPs, base oil, and dispersant, and c) NPs, base oil, and detergents. To ensure this, a simulation cell containing 100 NPs, 160 dispersants and 1600 detergents was prepared. Required number of these constituents were deleted from the simulation cell randomly to prepare the simulation cells for the control of each constituent.

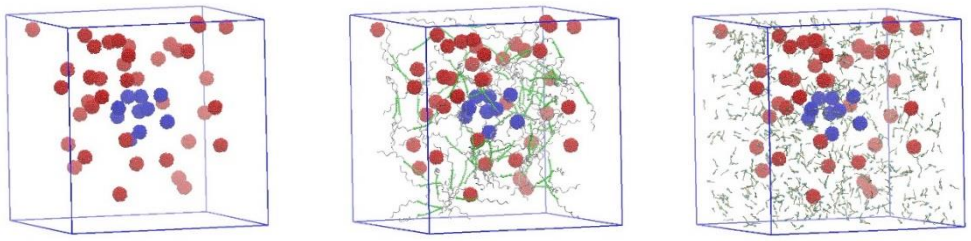


Figure 4.13. Initial structures in the first part of the study. a) 50 NPs, b) 50 NPs and 80 bis-succinimide dispersants c) 50 NPs and 800 sulfonate detergents. 5000 base oil molecules are hidden for simplicity.

4.2.3.3 Simulation Procedure

Steric clashes were removed with steepest-descent minimization algorithm integrated in LAMMPS package. Cell optimization was performed for 4.0 ns in the NPT ensemble at 300 K, followed by16.0 ns run in NVT ensemble at 423 K, with 10 fs time step. Atomic positions were recorded in a trajectory file in every 20 ps time intervals. Coordinates of the last 4.0 ns were used for RDF analysis in which atomic positions were relatively stable.

4.3 Results and Discussion

4.3.1 First Principle Calculations

Pairwise interaction energies for alkyl tail and polar head group of sulfonate detergent with possible functional groups that may be found on the surface of an insoluble deposit as demonstrated in Figure 4.14, were calculated with DFT. Details about calculation methods were given in Methods (4.2.1) section. Resulting interaction energies are listed in Table 4.3. The highest interaction energy was calculated between sulfonate head group of the detergent and –COOH functional group, which may exist on the surface of an insoluble deposit. These results showed

that the strongest interactions were the ones formed between phenyl sulfonate on the detergent with the polar functional groups on the insoluble nanoparticles. The weakest interactions were between the functional groups on the nanoparticle surface. It is worth to note that the number of interactions were ignored here that alkyl-alkyl interactions were dominant interactions due to the higher ratio of the base oil in the system.

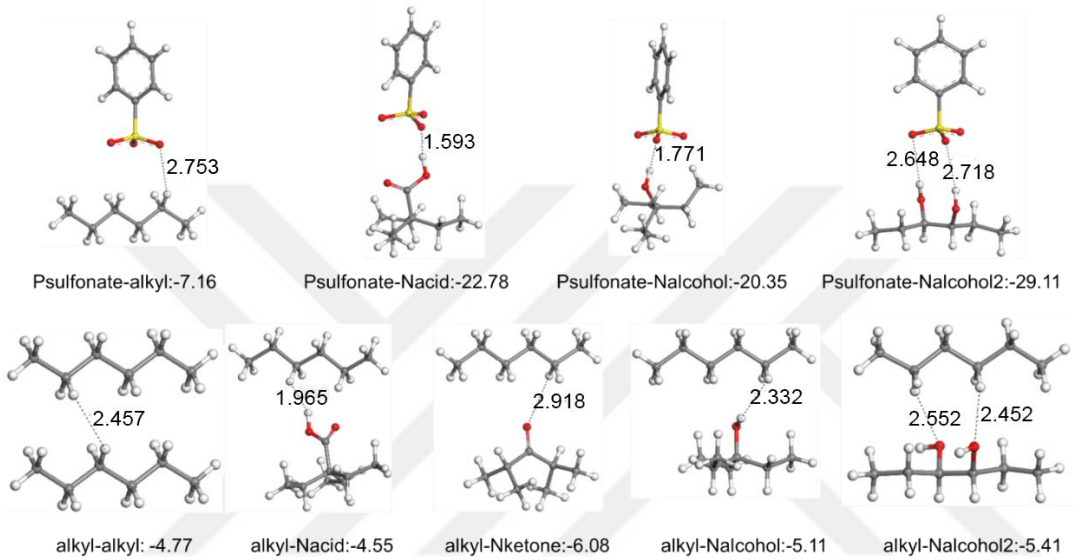


Figure 4.14. DFT calculation results for lowest energy structures and interaction energies of sulfonate detergent components with other constituents. Distances are given in Å unit.

Pairwise interaction energies for alkyl tail, polar polyisobutylene groups and polar amine center of detergent with possible functional groups that may be found on the surface of an insoluble deposit as demonstrated in Figure 4.15, were also calculated with DFT. Resulting interaction energies are listed in Table 4.4. The highest interaction energy was calculated between central amine group of the dispersant and $–R\text{-}(OH)_2$ functional group which may exist on the surface of an insoluble deposit. These results showed that the strongest interactions were the ones formed between polar functional groups of the dispersant with the polar functional groups on the insoluble nanoparticles. It can also be seen in Table 4.4 that there is a strong

interaction between PIB and amine groups of the dispersant and sulfonate head group of the detergent. This might result in a decreased aggregation control performance of the dispersant and detergent due to antagonistic effect or an increased performance because of synergistic effect. Mixing of the dispersant and possible synergistic/ antagonistic effect will be discussed throughout the coarse-grained MD simulations (4.3.3.7) section of this chapter.

Table 4.3. Interaction energies for all possible interactions of sulfonate detergent units with other constituents.

i	**j**	**ΔEij (kcal/mol)**		**i**	**j**	**ΔEij (kcal/mol)**
alkyl	R-COH	-4.43		alkyl	R=O	-6.08
alkyl	R-COOH	-4.55		alkyl	R-O-R	-2.75
alkyl	R-OH	-5.11		alkyl	Alkyl	-4.77
alkyl	$R-(OH)_2$	-5.41				
sulfonate	R-COH	-14.1		sulfonate	R=O	-9.96
sulfonate	R-COOH	-22.78		sulfonate	R-O-R	-11.35
sulfonate	R-OH	-20.35		sulfonate	alkyl	-7.16
sulfonate	$R-(OH)_2$	-29.11		sulfonate	sulfonate	+4.86

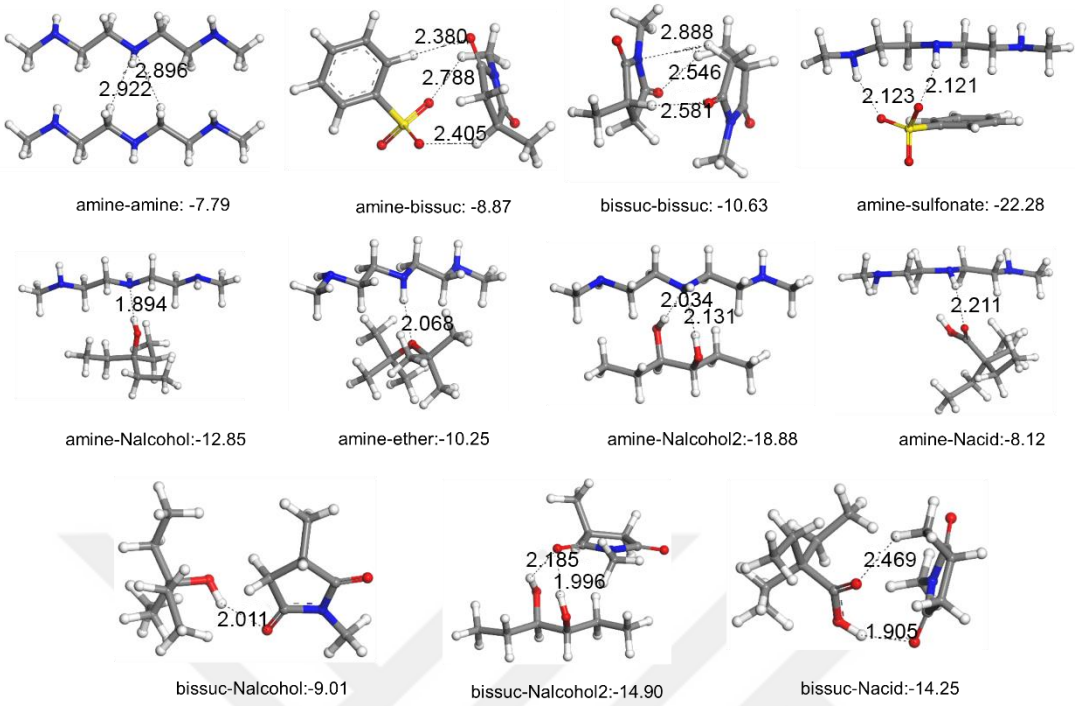


Figure 4.15. DFT calculation results for lowest energy structures and interaction energies of dispersant components with other constituents.

Table 4.4. Interaction energies for all possible interactions of dispersant units with other constituents.

i	**j**	**ΔEij (kcal/mol)**		**i**	**j**	**ΔEij (kcal/mol)**
PIB	R-COH	-6.44		PIB	R-$(OH)_2$	-7.09
PIB	amine	-8.56		PIB	R=O	-6.54
PIB	bis-suc	-6.62		PIB	R-O-R	-5.65
PIB	R-COOH	-6.82		PIB	PIB	-7.05
PIB	R-OH	-6.99		PIB	sulfonate	-12.88
amine	R-COH	-7.27		amine	R-O-R	-10.25
amine	R-COOH	-8.12		amine	alkyl	-5.76
amine	R-OH	-12.85		amine	amine	-7.79
amine	R-$(OH)_2$	-18.88		amine	sulfonate	-22.28
amine	R=O	-7.60				
bis-suc	R-COH	-9.29		bis-suc	R=O	-10.41
bis-suc	bis-suc	-10.63		bis-suc	R-O-R	-8.20
bis-suc	R-COOH	-14.25		bis-suc	amine	-8.87
bis-suc	R-OH	-9.01		bis-suc	sulfonate	-20.68
bis-suc	R-$(OH)_2$	-14.90				

4.3.2 All-Atom MD Simulations

Aim of this study is to demonstrate that the insoluble nanoparticles tend to coalesce and give rise to aggregates inside base oil matrix due to the polar nature of their surface. On the other hand, the role of different groups in dispersant and detergent additives such as bis-succinimide amine center and two polyisobutylene tails in dispersants as well as anionic sulfonate head group and alkyl tails in detergents was investigated.

4.3.2.1 Simulations with Two Insoluble Nanoparticles

In the RDF plot given in Figure 4.16, evolution of nanoparticle aggregation is shown. Without dispersant or detergent in the base oil matrix, the closest distance between hydrogen and oxygen atoms of each nanoparticles start at about 6 Å. The height of the RDF plot starts to increase beginning from the closest distance which is ~1.7 Å. The peak at 2.7-3.3 Å, which corresponds to hydrogen bonding, is at a g(r) value of nearly 0.20 in 1.2 ns simulation time. After 3.6 ns from the start, this value reaches orders of 0.27 and reaches 0.37 at the end of the simulation. This increase in the number density of atoms close to each other at about 3.0 Å distance is a strong indication of aggregation. Aggregation of the two NPs can be observed in Figure 4.19.

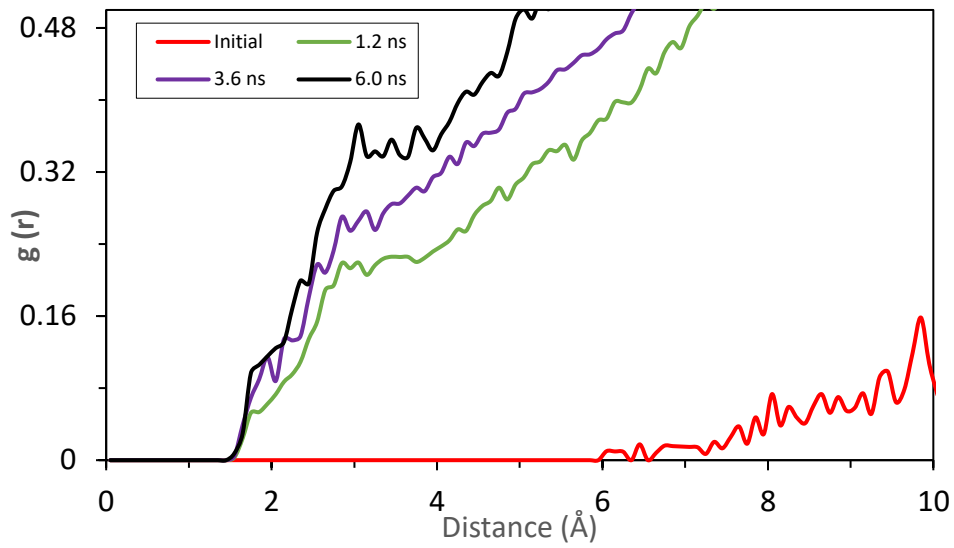


Figure 4.16. Time evolution of radial pair distribution function between oxygen and hydrogen atoms of two NPs.

In the presence of two dispersants, aggregation of NPs was slowed down as shown in Figure 4.17. The closest distance of two nanoparticles was about 4.7 Å in the presence of two dispersants at the end of the simulation. This distance was far away from the distance of hydrogen bonding. As shown in in Figure 4.19, polar amine and succinimide units in the center of dispersant (green) are either intercalated between particles or strongly interacted on the surface via hydrogen bonds and poly isobutylene groups (gray) are extended into the base oil.

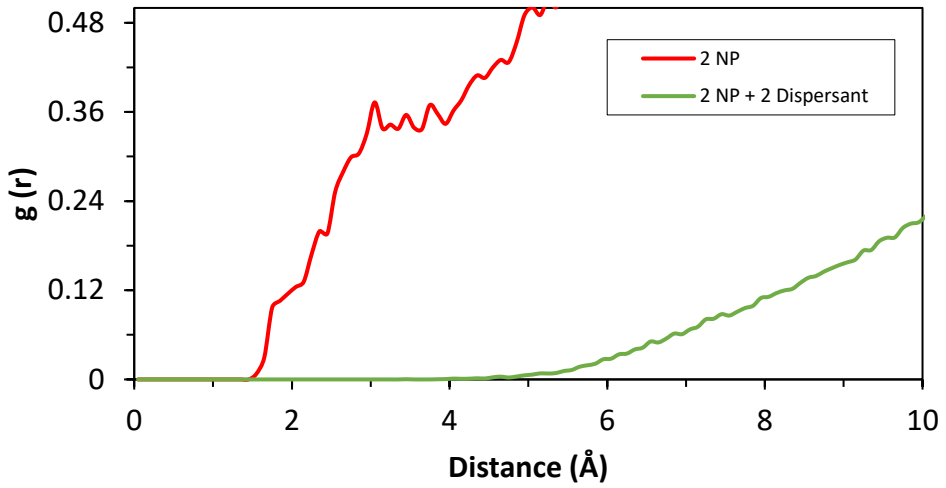


Figure 4.17. RDF of oxygen and hydrogen atoms of one NP with oxygen and hydrogen atoms of the other NP in the cell with two NPs, without dispersant (red) and with 2 dispersants (green).

Similar results were obtained in the presence of six detergents as shown in Figure 4.18. In the presence of six detergents, aggregation of nanoparticles is reduced which can be understood from decreased peak value of RDF. The closest distance between the two nanoparticles is at approximately 3.5 Å, which is again distant from hydrogen bonding distance. In the detergent case, the head group of the sulfonate detergent is interacting with NPs' surface where alkyl tails are interacting with the oil phase. They create a shear force to separate NPs, preventing aggregation of another NP.

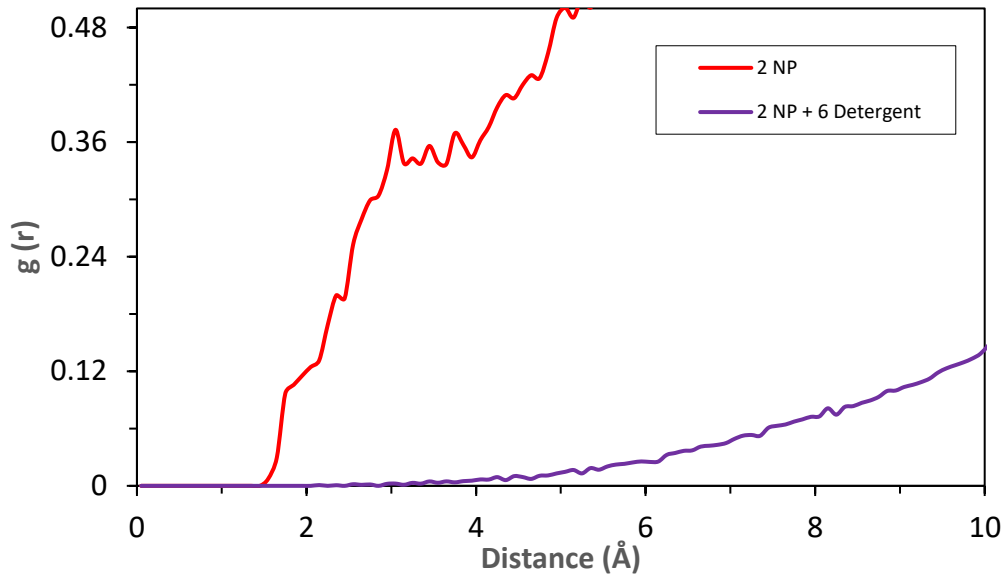


Figure 4.18. RDF of oxygen and hydrogen atoms of one NP with oxygen and hydrogen atoms of the other NP in the cell with two NPs, without detergent (red) and in the presence of 6 detergents and 3 calcium cations (purple).

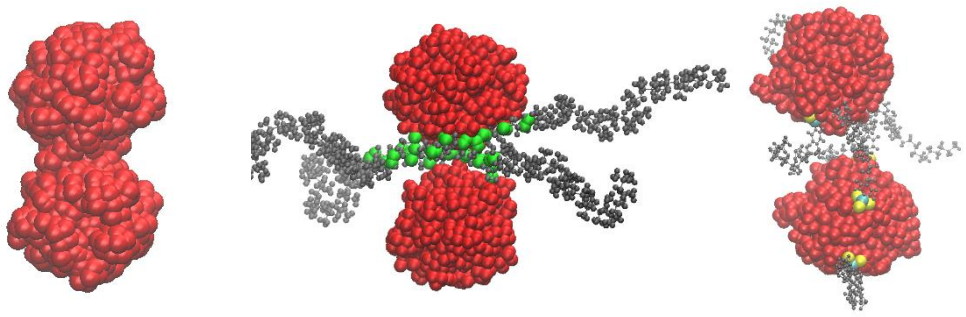


Figure 4.19. Final snapshot of NPs after all-atom simulations of 2 NPs (left), 2 NPs with 2 dispersants (center), and 2 NPs with 6 detergents (right).

4.3.2.2 Simulations with Three Insoluble Nanoparticles

The simulations were repeated with three NPs. In the absence of dispersant, closest distance between the central NP in the simulation cell and the other two NPs is ~1.9

Å as shown in Figure 4.20. At 3 Å distance, g(r) value is approximately 0.015 where it reaches up to 0.027 and 0.070 at 2.4 and 6.0 ns time in the simulation, respectively. The sharp increase in the height of RDF plot at 6.0 ns time in ~3 Å is a strong evidence of increased hydrogen bonding on the surface of the nanoparticles.

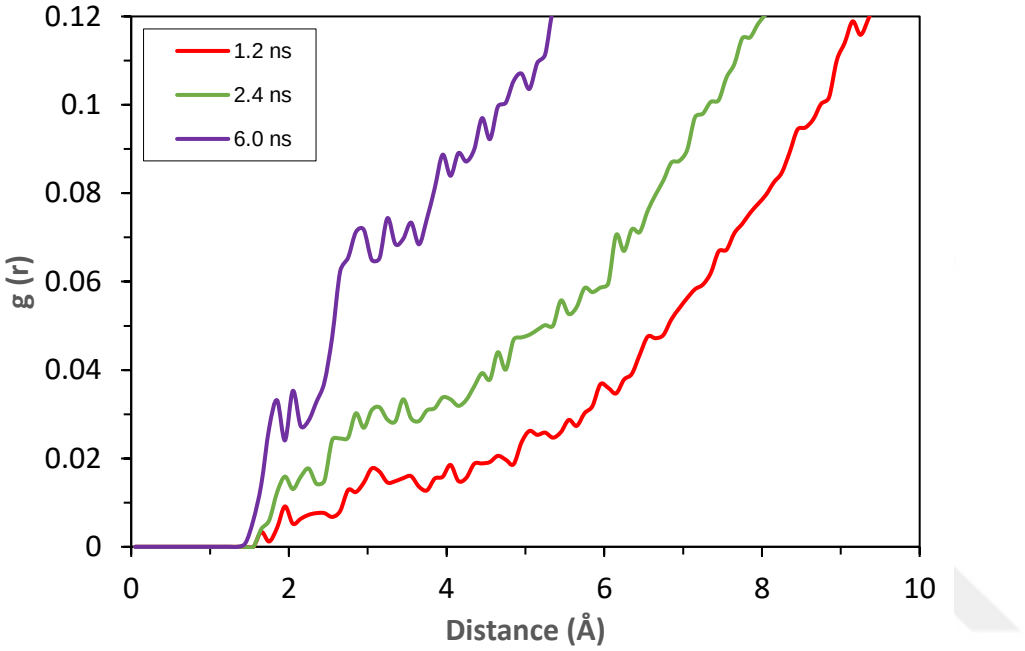


Figure 4.20. Time evolution of RDF of oxygen and hydrogen atoms of one NP with oxygen and hydrogen atoms of the remaining two NPs in the cell containing three NPs.

In the absence of dispersant or detergent, aggregation of the nanoparticles occurs inevitably as explained above. In the presence of 3 dispersants, as shown in Figure 4.21, a small decrease in the distance between the nanoparticles was observed. However, the height at 3 Å did not change significantly which means that NP aggregation still continued. In the presence of 6 dispersants, aggregation of the NPs was mitigated more efficiently. This implies that the amount of additives is another parameter to optimize for the real life applications. The closest distance between the NPs is about 3.7 Å, which is well distant from the hydrogen bonding distance.

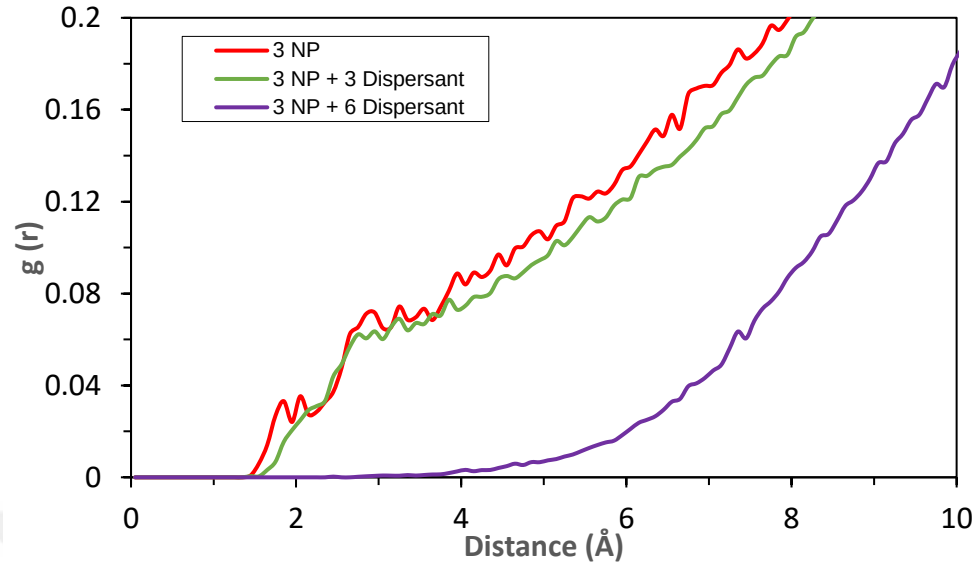


Figure 4.21. RDF of oxygen and hydrogen atoms of one NP with oxygen and hydrogen atoms of the remaining two NPs in the cell containing three NPs; in the absence of dispersant (red), in the presence of 3 dispersants (green) and 6 dispersants (purple).

It is worth to mention that; the initial positions of the dispersants are crucial in these simulations. RDF analysis was carried out between oxygen and hydrogen atoms of the central NP with those of the remaining two NPs. Initially amine center of the two dispersants were between the central NP and the NP on the left side in Figure 4.22, and the third dispersant was in between the central NP and the NP on the top of the central NP. It can be seen that two dispersants position themselves in between the NPs efficiently, preventing the aggregation. On the other hand, the remaining single dispersant was placed in between two NPs which was not sufficient to prevent the formation of intermolecular bonds in between the surfaces of two NPs. Even it was possible that it can help aggregation of the two NPs due to their polar surfaces allowing the formation of intermolecular bonds between NPs, bringing the two NPs together. Experiments showed that colloid-like structures were formed instead of solid precipitate indicating the formation of weakly interacting NPs in the presence of additives that can be washed away from the oil via filtration process as desired.

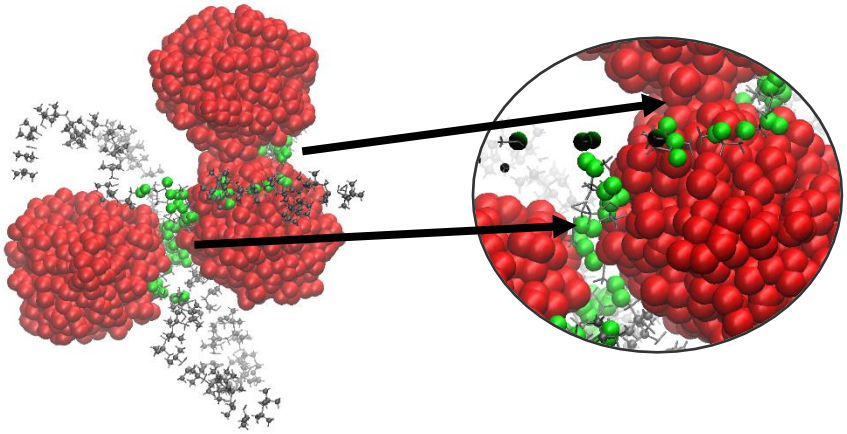


Figure 4.22. Final snapshot of NPs after all-atom simulations of three NPs (red) and three dispersants. Two dispersants can efficiently interrupt the contact of two NPs (bottom arrow) where remaining single dispersant cannot prevent aggregation of two NPs (top arrow). Polar amine center of the dispersants are shown as green colored beads to highlight their positioning.

Similar results were obtained with the detergent as shown in Figure 4.23. In the presence of 12 detergents a slight decrease in the height at about 3 Å was calculated. This showed that aggregation of NPs was mitigated however, the number of detergents was not sufficient for complete dispersion. In the presence of 18 detergents, the peak value of the RDF peak at about 3.0 Å that points out aggregation was decreased more efficiently. Similar to the results of the MD simulations with two NPs, dispersants and detergents prevented or mitigated the self-assembly of NPs to each other at the end of the simulation.

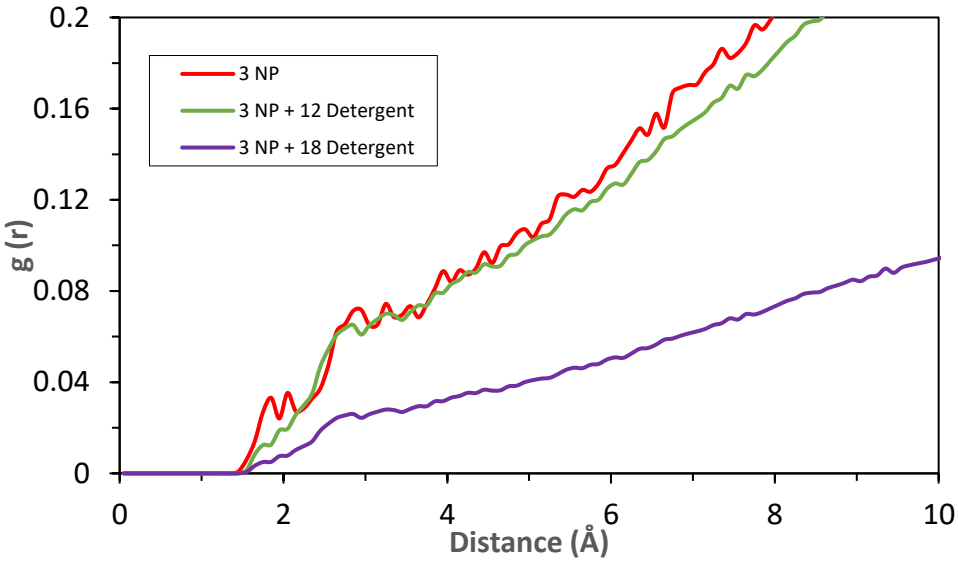


Figure 4.23. RDF of oxygen and hydrogen atoms of one NP with oxygen and hydrogen atoms of the remaining two NPs in the cell containing three NPs; in the absence of detergent (red), in the presence of 12 detergents (green) and 18 detergents (purple).

4.3.3 Coarse-Grained MD Simulations

In all-atom MD simulations, we demonstrated that nanoparticle aggregation occurs in the base oil matrix in the absence of dispersant and/or detergent. On the other hand, this aggregation of NPs can be prevented by the interaction of dispersant and detergent polar groups with the insoluble nanoparticles followed by the extension of hydrophobic tails into the oil phase that decreases coalesce further by forming a repulsive layer against the other nanoparticles. Moreover, we showed that, concentration of the dispersant and detergent is an important factor affecting the efficiency of aggregation control. The aim of the coarse-grained MD simulations is to observe the aggregation in a larger simulation cell containing 50 NPs. In addition, the effect of other parameters such as the structure and concentration of the dispersant, structure, type and concentration of the detergent and mixing the dispersant and detergent together was investigated in coarse-grained simulations.

4.3.3.1 Aggregation of the Insoluble Deposits

Aggregation of the insoluble deposits can occur due to the attraction between the polar beads present on the surface of the NPs. As explained in the Introduction (1.1.4.4.2.1) chapter, beads are representing 2 to 4 heavy atoms in Martini force field. In this case, polar beads on the surface of the NPs represent polar functional groups present on the surface of NPs. As shown in Figure 4.24, peak value of the RDF plot at 5.0 Å is about 1.8 after 4.0 ns simulation time. Equilibrium center-to-center distance of Martini FF based coarse-grained beads is 4.7 Å for regular beads and 4.3 Å for the ring type of beads (S). Hence, peak starting from g(r) values of 4.5 and ending at about 6 Å is an indication of a strong interaction between the polar beads on the surface of NPs resulting in aggregation. The RDF peak value continues increasing up to 3.2 and 4.7 Å after 12 and 20 ns simulation time, respectively. It should be noted that H-bonds could not be observed since these are not atoms and they are beads representing atom groups.

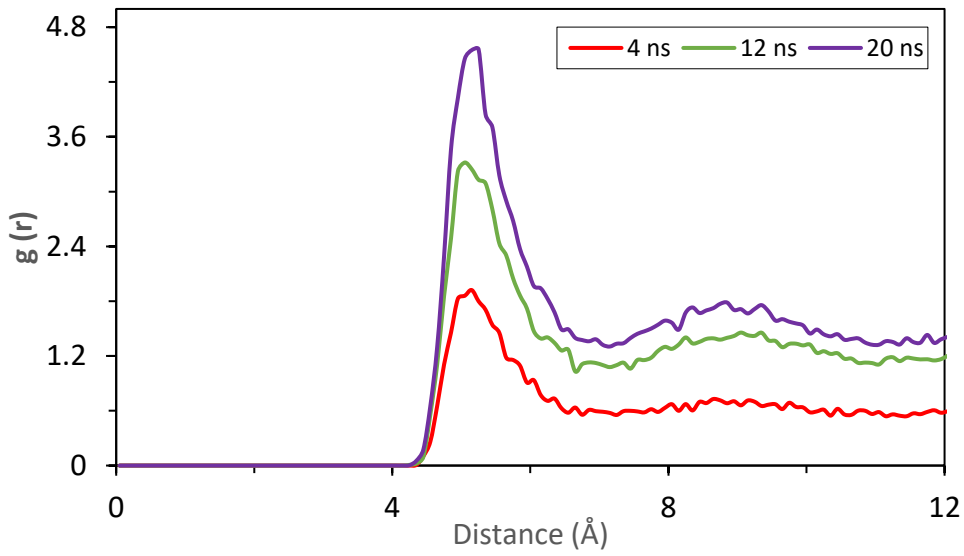


Figure 4.24. RDF plot for 50 NP (R=2.2 nm) in 5000 base oil, in the absence of dispersant after 4 (red), 12 (green) and 20 ns (purple) simulation time.

4.3.3.2 Effect of Different Structures of Dispersant on Aggregation

The dispersant, as mentioned in the Computational Methods (4.2.2.1.3) section, consists of polar center containing amine groups, which were mapped to Martini 2.0 force field as P5 beads, and two polyisobutylene tails represented as C1 beads.

Three versions of dispersant were created to study the effect of size of the amine center and PIB tails on the dispersant as shown in Figure 4.25.

1. The first model (Dispersant v1) has 6 beads located in the center and 18 beads located in the tails to test the effect of hydrophobic PIB tail.
2. In the second model (Dispersant v2), the number of beads in the center was increased to 12 amine beads to test the effect of polar group number.
3. In the third model (Dispersant v3), the number of beads in the tails was increased to 36, where the number of beads in the center was 12 to test effect of both amine and PIB sizes in the dispersant chains.

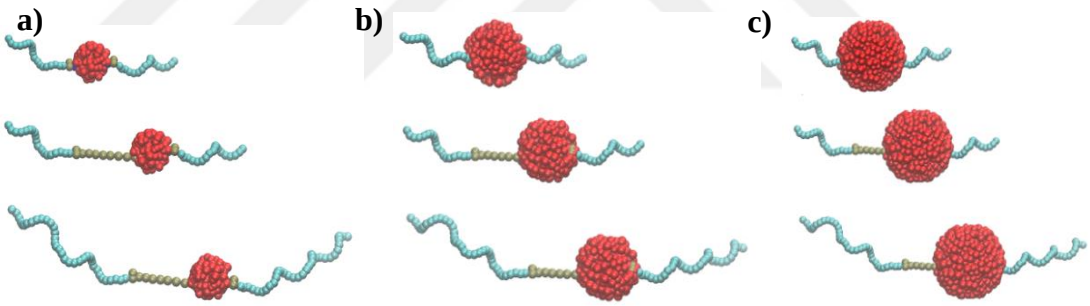


Figure 4.25. Insoluble deposit models with a) 2.2, b) 3.2 and c) 4.4 nm diameter, together with dispersant with 6 polar center and 18 apolar tail (top), with 12 polar center and 18 apolar tail (center), and with 12 polar center and 36 apolar tail (bottom), respectively. Green colored beads represent the alkyl tail of the dispersants, brown beads represent the polar beads in amine groups and succinimides and red color represent AuNPs.

Aggregation of nanoparticles was mitigated by the polar amine and succinimide beads at the center in the dispersants, which were intercalated between NPs via

hydrogen bonding, as discussed in the previous section in this chapter. For the simulation cell containing relatively small sized insoluble deposit models (R=2.2 nm), the peak value on the RDF graph, at approximately 5 Å distance, with 4.7 RDF value for the cell without any dispersants in the simulation contains 50 NPs in the base oil matrix. The peak intensity decreases to 3.3 in the presence of 80 dispersants having 6 polar P5 beads in the center and 18 apolar C1 beads in both tails. The size of polar center in the dispersant do not seem to have any effect on the efficiency of dispersant since the peak on the RDF graph decreases to a similar degree in both two versions of the dispersants, which contain similar hydrophobic tail sizes. This suggests that the distance between nanoparticles (NPs) are same when the size of the polar center of the dispersant changes. It should be noted that smaller size of NPs in simulations could be effective on this observation.

Extent of the decrease in the RDF peak given in Figure 4.26 increased when size of the apolar tails was increased to 36 (as it is 36 in Dispersant v3). RDF peak value at approximately 5 Å decreases down to value of 1.7. As can be visually observed in Figure 4.27 (left), the non-polar tails of NPs extend in the base oil environment, which creates a hydrophobic barrier and prevents other NPs from aggregating simultaneously. In addition to providing a hydrophobic barrier, extending of the non-polar tails inside the base oil matrix restrict the movement of NPs freely. This effect can be visualized in the RMSD plot given in Figure 4.28. It can be observed visually that noise of the plot is larger in the absence of dispersants which is indication of larger fluctuation in the nanoparticle positions.

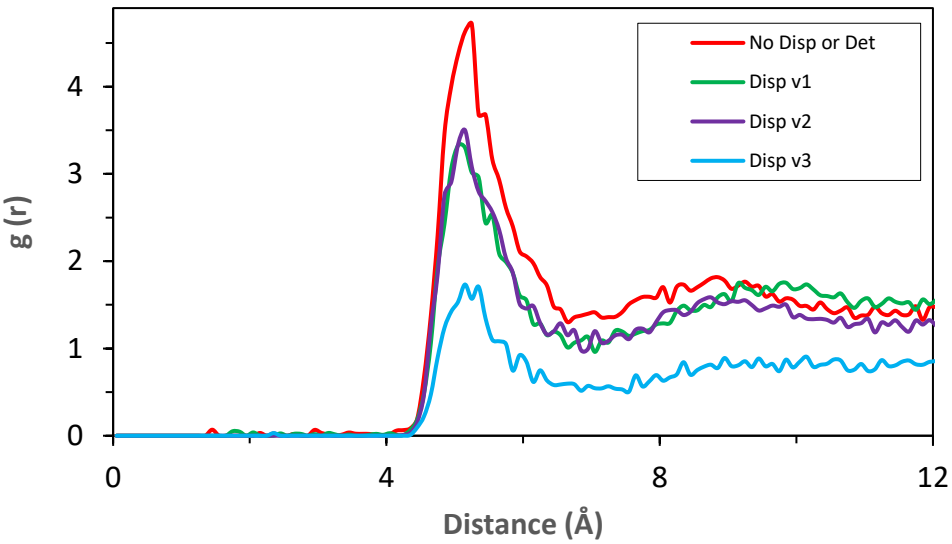


Figure 4.26. RDF plot for 50 NP (R=2.2 nm) + 5000 Base Oil, without dispersant (red), with 80 Dispersant v1 (green), with 80 Dispersant v2 (purple), and with 80 Dispersant v3 (blue).

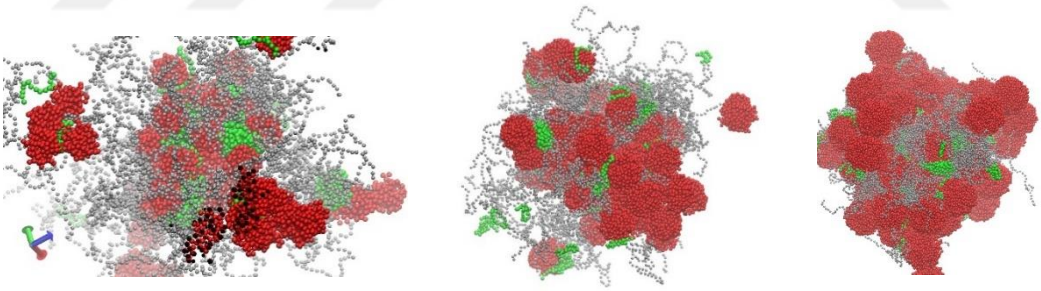


Figure 4.27. Final snapshot of NPs with 2.2 nm (left), 3.2 nm (center) and 3.2 nm (right) diameter. Polar beads of dispersants (green) intercalate between NPs (red) and apolar tails (gray) create a hydrophobic barrier preventing other NPs approaching in each case. While NPs size increases, relative size of the dispersant relative to that of NPs decreases which negatively affects the efficiency of mitigating the aggregation of NPs.

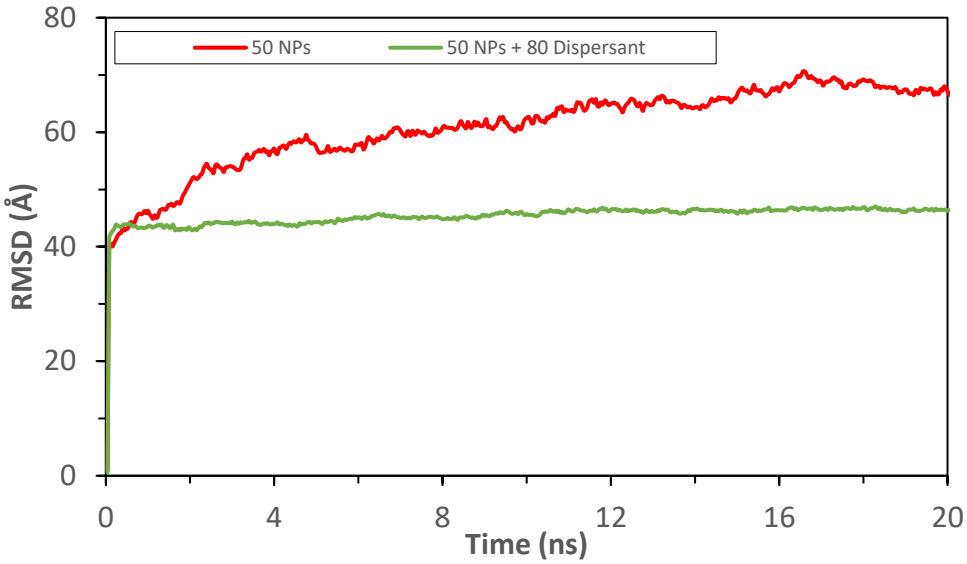


Figure 4.28. RMSD plot of 50 NPs having 2.2 nm diameter in 5000 base oil in the absence of dispersant (red) and in the presence of 80 dispersants (green).

The diameter of the initial NPs were increased to 3.2 nm and the simulations were repeated with the simulation cells prepared with this size of NPs. In this case, volumes of the simulation cells were increased and percentage of nanoparticles by means of number of beads was increased accordingly. Therefore, it is challenging to compare the results of the simulations by quantitative means.

In Figure 4.29, RDF plot for NPs with 3.2 nm is shown. It can be observed from this RDF plot that, the extent of aggregation is decreased with use of dispersant for larger NPs. In the RDF plot, peak value decreased from about 0.96 to 0.78 in the presence of 80 dispersants compared to the case in the absence of dispersants. Similar to the results of the smaller sized NP, size of the polar center of the dispersant did not create a remarkable difference by means of the peak height. Therefore, the interaction of the surfaces of the NPs were not interrupted more efficiently when the number of polar centers in the dispersants was increased. Dispersant v3 with 36 beads in the apolar tail resulted in a slightly higher decrease in the peak intensity at approximately five Å, similar with the case that the NPs having 2.2 nm diameter.

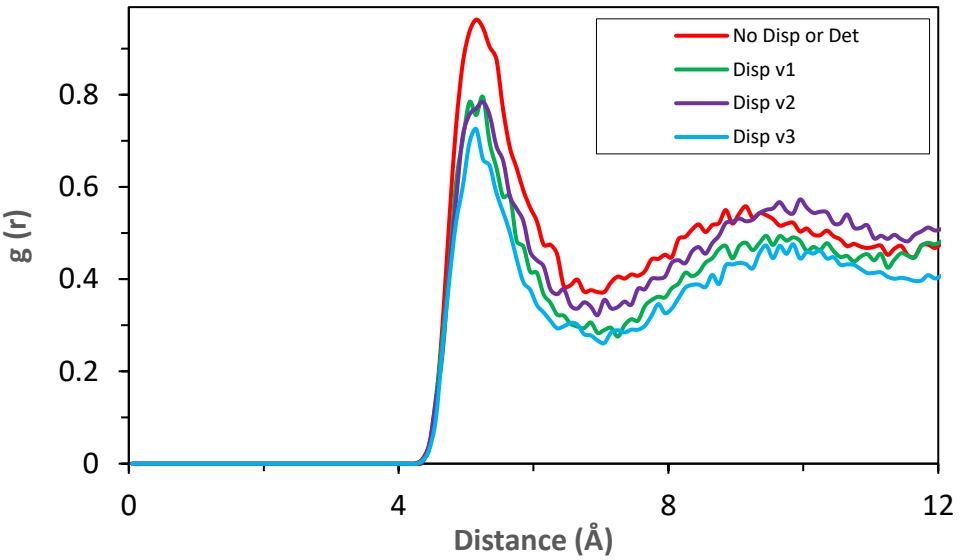


Figure 4.29. RDF plot for 50 NP (R=3.2 nm) + 5000 Base Oil, without dispersant (red), with 80 Dispersant v1 (green), with 80 Dispersant v2 (purple), and with Dispersant v3 (blue).

In the case of NPs, having 4.4 nm diameter RDF analysis is given in Figure 4.30. The difference in the peaks at 5 Å is insignificant compared to the results above. Peak heights decreased in the order of 0.04 approximately 8%. It is worth noting that the initial configuration is crucial in the final positions in our simulations. In some of the repeated simulations with different initial positions, it was observed that the size of the polar center and/or apolar tail in the dispersant did not make a considerable effect in the aggregation. As discussed above, volume of the simulation cells is increased and the percentage of NPs by means of number of beads was increased for the larger NPs. This resulted in the decrease in the concentration of dispersant in the simulation cell can be observed visually in Figure 4.27, which resulted in an inefficiency in mitigating the aggregation of NPs.

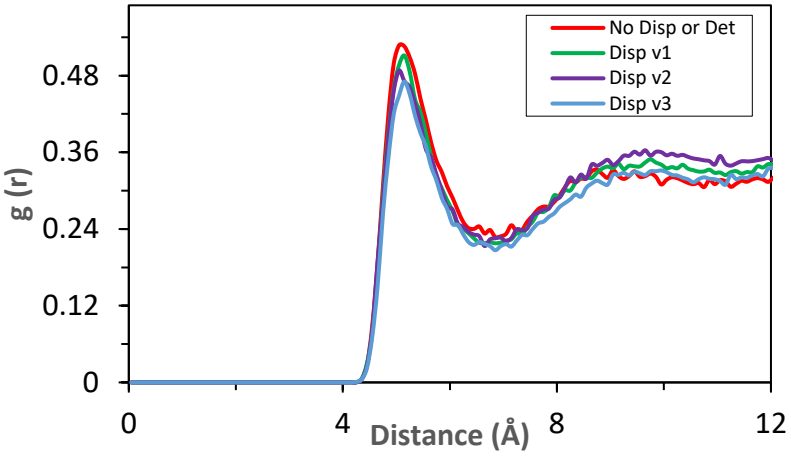


Figure 4.30. RDF plot for 50 NP (R=4.4 nm) + 5000 Base Oil, without dispersant (red), with 80 Dispersant v1 (green), with 80 Dispersant v2 (purple), and with Dispersant v3 (blue).

It can be seen in the RDF plots that, when the size of NPs increased, the efficiency of dispersant for NP separation decreases. It is clear in Figure 4.25 and Figure 4.27 that, the size of the dispersant molecule and hence the hydrophobic barrier created by the apolar tails of the dispersants relative to the size of NPs decreased with that of the NPs, which was possible to contribute to the decrease in the efficiency of dispersant type additives.

4.3.3.3 Effect of Dispersant Concentration on the Aggregation of Nanoparticles

Effect of the dispersant concentration is shown experimentally by TEM images provided by The Lubrizol ™ Corporation (Figure 4.31). In the base oil, addition of extra dispersant resulted in reduction of the NP aggregation, which are shown in the TEM image on the left.

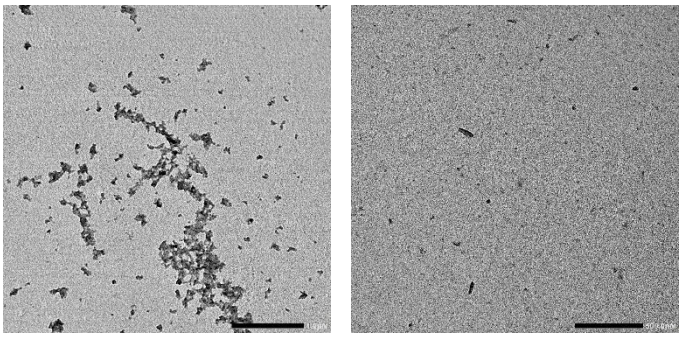


Figure 4.31. TEM images showing aggregation of insoluble deposit in the base oil (left) and reduced aggregation after addition of extra dispersant in the base oil (right). The Lubrizol ™ Corporation provided the TEM images.

To reproduce and analyze molecular details of this experimental results by computational methods, a simulation cell was prepared with 50 NPs, 5000 base oil and 80 dispersant having 12 polar center beads and 36 tail beads (Dispersant v3), which are shown to be the most effective version of the dispersant in the previous section. The number of the dispersant molecules were decreased to 40, 20 and 0 by simply deleting existing dispersants randomly from the first simulation cell. Initial positions of the NPs, base oils and dispersants existing in the simulation cell were the same in these four simulation cells. Within the simulation cell with 80 dispersants, the dispersants constitute 11.74% of the cell based on the number of beads present. Simulation cells having 40 and 20 dispersant constitute 6.23% and 3.22% of the cells, respectively.

In the RDF plot shown in Figure 4.32, addition of 20 dispersants in the simulation cell did not make any difference in the close contact between the existing 50 NPs. RDF peak values did not show significant difference.

Experimental findings provided by the company were reproduced computationally as shown in the RDF plot in Figure 4.32. The peak of RDF analysis observed at approximately 5 Å decreased gradually from 0.97 to 0.72 by the presence of higher dispersant amount. The number of dispersants in the simulation cell increased up to

40 and 80, where the RDF peak value in the analysis decreases to 0.83 and 0.72, respectively.

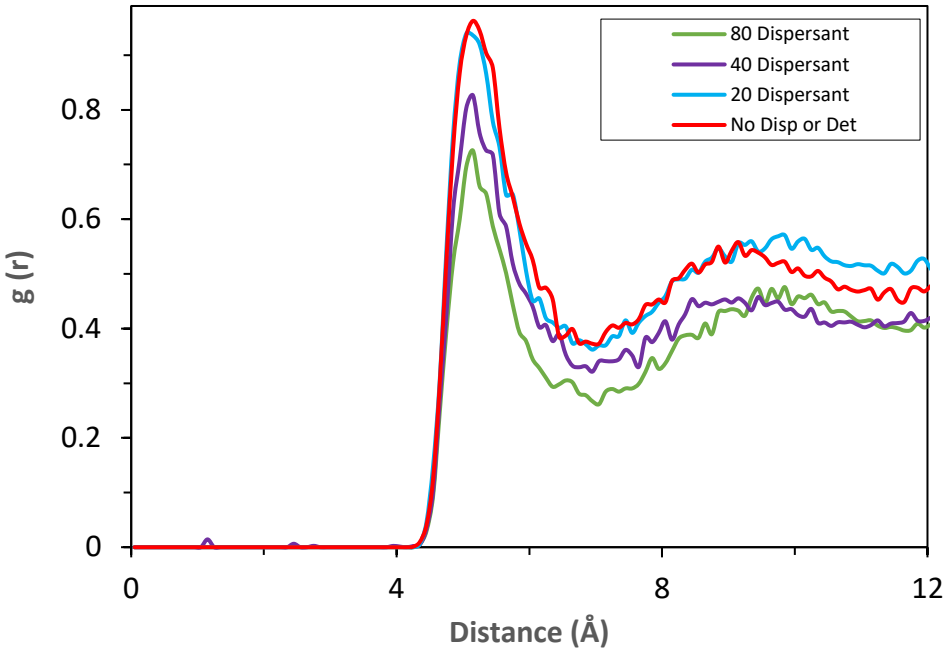


Figure 4.32. RDF plot for 50 NP (r = 3.2 nm) + 5000 Base Oil, without dispersant (red), with 20 dispersant (3.22% in the simulation cell), with 40 dispersant (6.23%) and with 80 dispersant (11.74%).

4.3.3.4 Effect of Detergent Type on the Aggregation of NPs

As mentioned in the Computational Methodology section, -1 charged head group of both salicylate and sulfonate are represented as -1 charged Q_a type beads. Difference in binding capability of the head groups in sulfonate and salicylate type cannot be efficiently differentiated by this method. Nevertheless, it was predicted that the surface of the insoluble deposits (NPs) could contain various type of functional groups with various polarity. Overall binding capability of sulfonate and salicylate type detergents depends strongly on the number of functional groups on the surface as well as the type of the functional groups in real situations. In the all-atom and coarse-grained MD simulations of this study, there is a single model of insoluble

deposit, which lack in representing the real situation. Considering all of these, it is believed that the loss of information in the head groups of sulfonate and salicylate would not impact the overall binding of the two detergent types to the NP surface.

In this part of the study, the only distinction between sulfonate and salicylate detergents was that the former had three apolar beads which represented the aromatic ring, whereas in the latter, one of these beads was polar. Simulation cells were prepared so that all of the initial positions of the beads were the same in sulfonate and salicylate detergent cases. Hence, the study aims to evaluate the impact of this single modification in the aromatic ring.

Final snapshot of the simulation cell containing NPs with 2.2 nm diameter with salicylate and sulfonate detergents are given in Figure 4.33. As shown in the RDF analysis in Figure 4.34, the peak value of RDF at about 5 Å decreases with the addition of detergent. Extent of this decrease is higher for salicylate, which implies that for the NPs with 2.2 nm diameter, salicylate detergent was more efficient in mitigating the aggregation of NPs. As mentioned before, the only difference between the two structures in coarse-grained models is that salicylate detergent has one polar bead instead of an apolar one in the aromatic ring. Therefore, based on the findings of this study, it can be inferred that the presence of additional binding sites in the detergent leads to an improvement in the efficiency when NPs are smaller (with 2.2 nm instead of 4.4 nm diameter in this study). On the other hand, when diameter of the NPs is 3.2 nm, sulfonate and salicylate detergents showed similar performance. Repeated simulations conducted with varying initial positions. These studies indicate that salicylate may result in further reduction of the RDF peak in some cases. We also showed that charged anionic head groups of detergents bind to the NPs and mitigate the aggregation by intercalating between them similar with the dispersant case. Additionally, some of the NPs were surrounded by detergent molecules and isolated in the simulations that can be easily cleaned from piston engines in real life. As it is observed for the results of dispersants, effect of detergent became limited with decrease in the size of NPs.

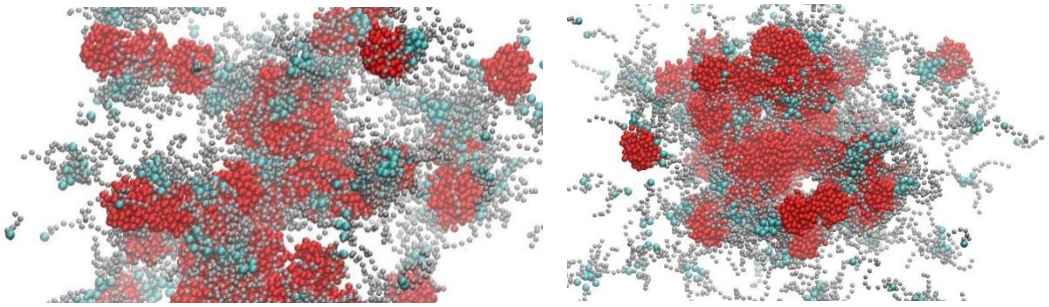


Figure 4.33. Final snapshot of NPs (2.2 nm diameter) with salicylate (left) and sulfonate (right) detergents. Difference in the extent of aggregation is not visible by eye.

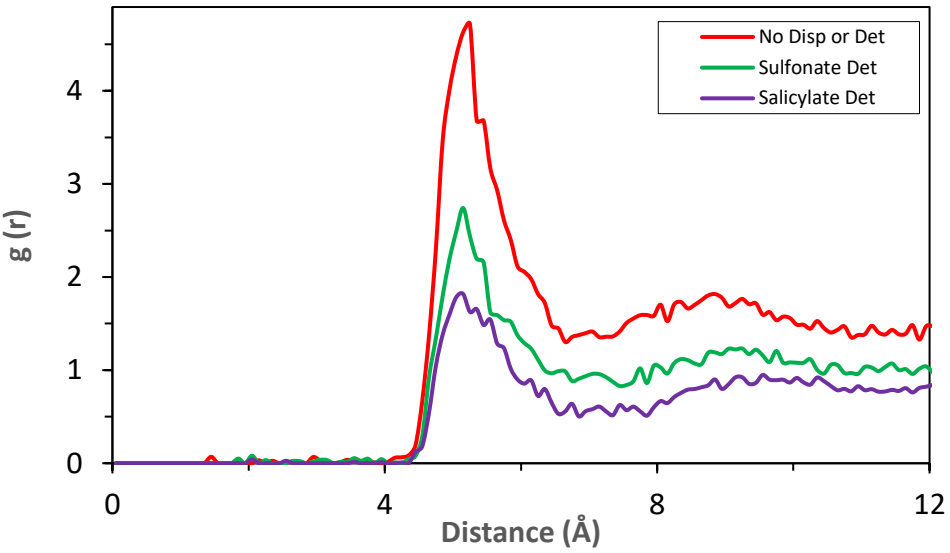


Figure 4.34. RDF plot for 50 NP (r = 2.2 nm) + 5000 Base Oil, without detergent (red), with sulfonate detergent (green) and with salicylate detergent (purple).

In Figure 4.35 and Figure 4.36, RDF plot for the simulation cells containing NPs with 3.2 nm and 4.4 nm diameters. Similar to the discussion in dispersant case, relative concentration of the detergent decreases with increasing number of beads of the NPs resulting in a decreased deposit control performance.

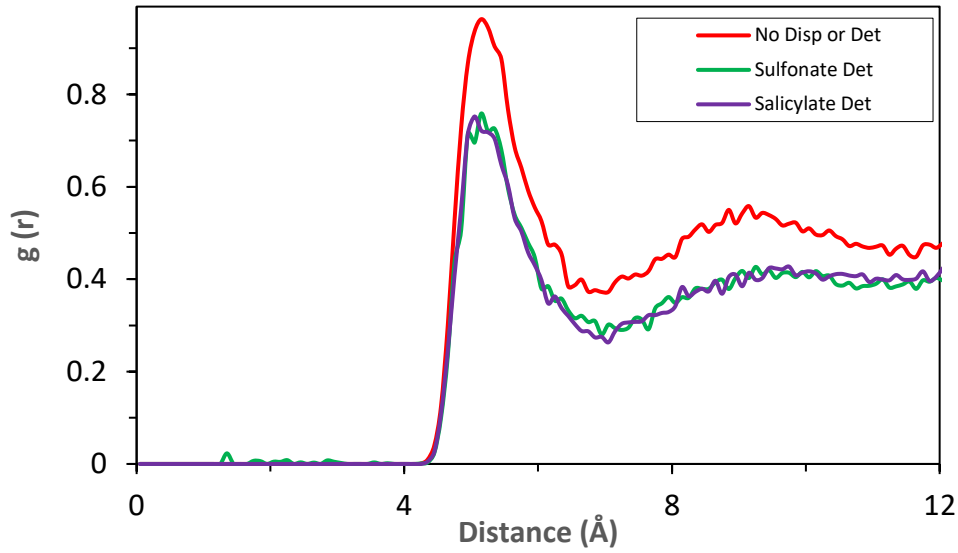


Figure 4.35. RDF plot for 50 NP (r = 3.2 nm) + 5000 Base Oil, without detergent (red), with sulfonate detergent (green) and with salicylate detergent (purple).

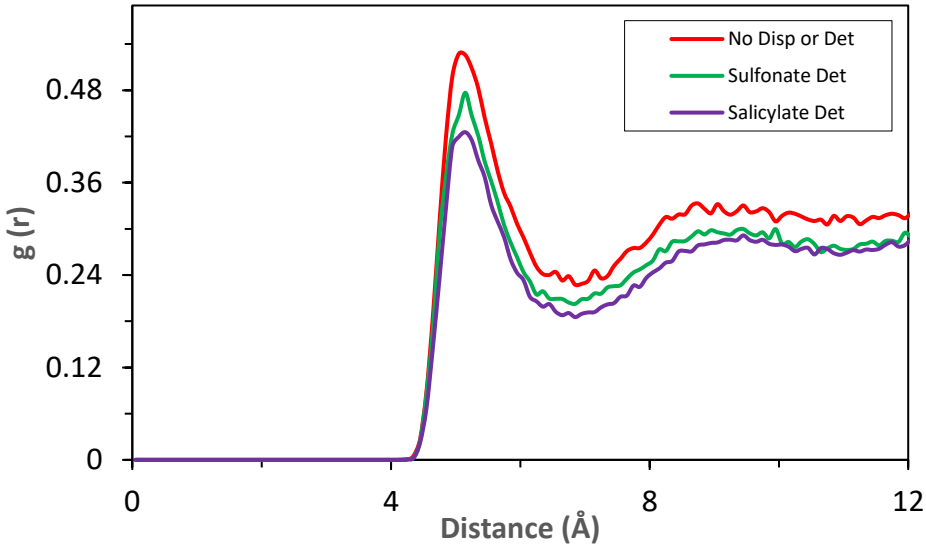


Figure 4.36. RDF plot for 50 NP (r = 4.4 nm) + 5000 Base Oil, without detergent (red), with sulfonate detergent (green) and with salicylate detergent (purple).

Comparison of the RDF analysis of NPs in the cells containing dispersant and salicylate detergent were given in Figure 4.37, Figure **4.38** and Figure **4.39**. Decrease in the RDF peak at about 5 Å are similar for dispersant and detergent. Moreover, the extent of decrease in the RDF peak decreases with increasing NP size, which was already discussed above.

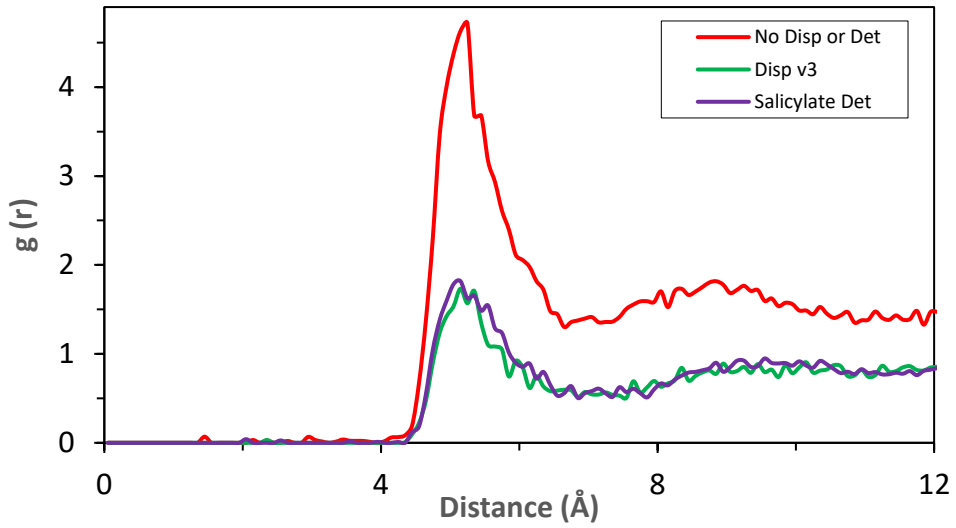


Figure 4.37. Comparison of RDF plot for 50 NP (r = 2.2 nm) + 5000 Base Oil, without detergent (red), with 80 Dispersant v3 (green) and with 800 Salicylate detergent (purple).

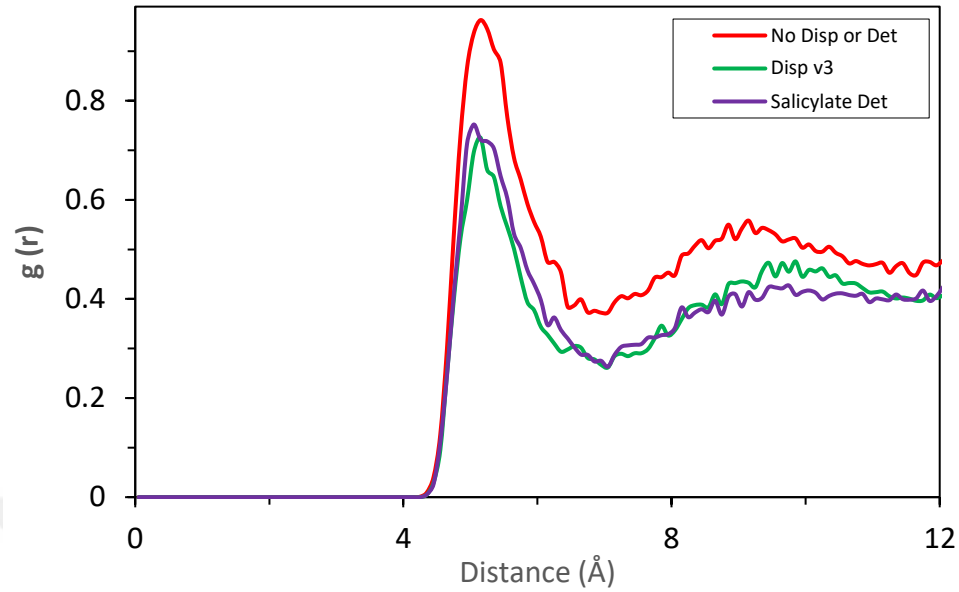


Figure 4.38. Comparison of RDF plot for 50 NP (r = 3.2 nm) + 5000 Base Oil, without detergent (red), with 80 Dispersant v3 (green) and with 800 Salicylate detergent (purple).

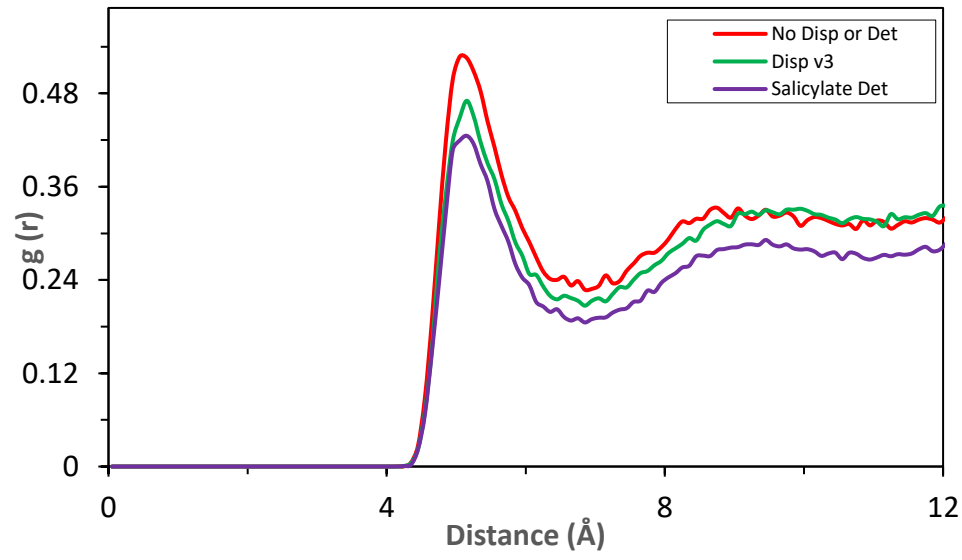


Figure 4.39. Comparison of RDF plot for 50 NP (r = 4.4 nm) + 5000 Base Oil, without detergent (red), with 80 Dispersant v3 (green) and with 800 Salicylate detergent (purple).

4.3.3.5 Effect of Tail Size of the Detergent on Aggregation of NPs

Tail of the detergent molecule is represented as five beads, in apolar C1 type in this study, by coarse graining of 20 carbon tails. With the aim of determination of the tail length effect in the detergent molecule, the last bead and the last two beads in the tail were simply deleted from the simulation cell in two cases. At the beginning, the position of the remaining beads in the detergents and position of base oil molecules and NPs were the same in three simulation cells. As apparent in the RDF analysis given in Figure 4.40, sulfonate detergent does not seem to be affected from the difference in the tail size whereas the efficiency of salicylate detergent slightly decreases with reduced sizes in the tail as shown in Figure 4.41. This very slight effect might be due to a decrease in the solubility of the tail together with the aromatic ring.

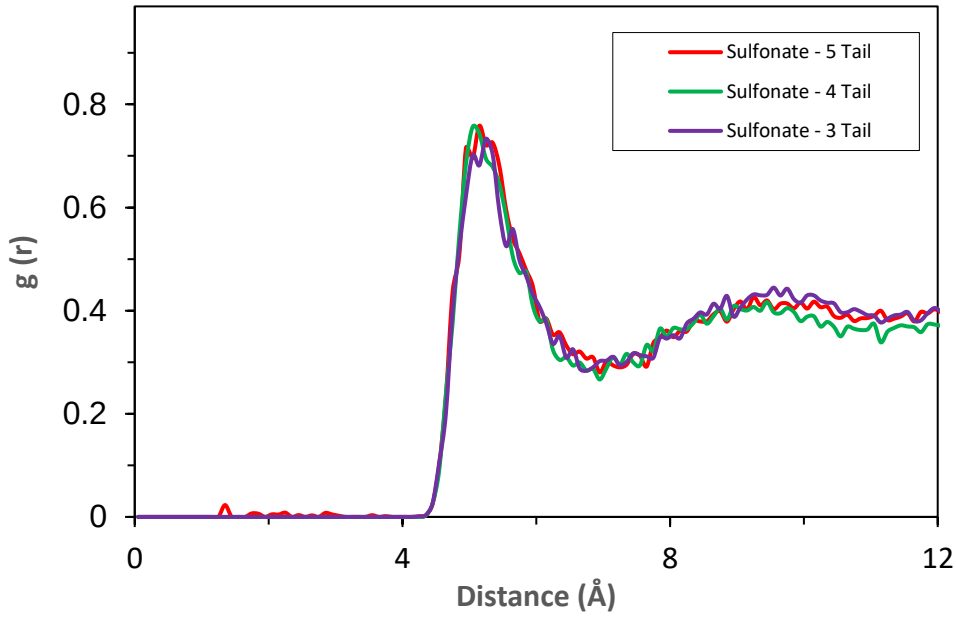


Figure 4.40. RDF plot for 50 NP (r = 3.2 nm) + 5000 Base Oil + 800 Sulfonate detergents having 5 beads (red), 4 beads (green) and 3 beads (purple) in the tail.

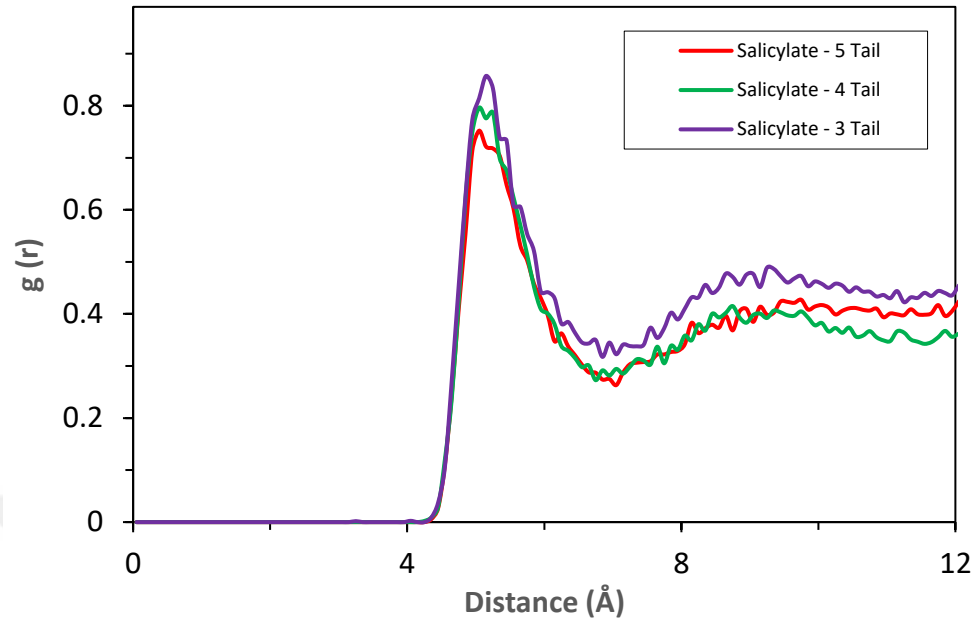


Figure 4.41. RDF plot for 50 NP (r = 3.2 nm) + 5000 Base Oil + 800 Salicylate detergents having 5 beads (red), 4 beads (green) and 3 beads (purple) in the tail.

4.3.3.6 Effect of Detergent Concentration on the Aggregation of NPs

Similar with the study on the dispersants, a simulation cell was prepared with 50 NPs, 5000 base oil and 800 detergent molecules. The number of the detergent molecules were then decreased to 400, 200 and 0 by simply deleting existing detergents randomly from the first simulation cell to keep consistency of all other molecules by means of initial positions. Initial positions of the NPs, base oils and detergent molecules existing in the simulation cell were the same in these four simulation cells. Number of beads in 800 detergents was 7200, which is equal to that of 80 dispersants to keep consistency in comparisons. Hence, the percentage of detergents in the simulation cells constructed are similar with those in the dispersant part of this study. The peak in RDF shown in Figure 4.42 and Figure 4.43 was observed at approximately 5 angstroms decrease gradually from 0.97 to 0.72 with increase in concentration of the detergents.

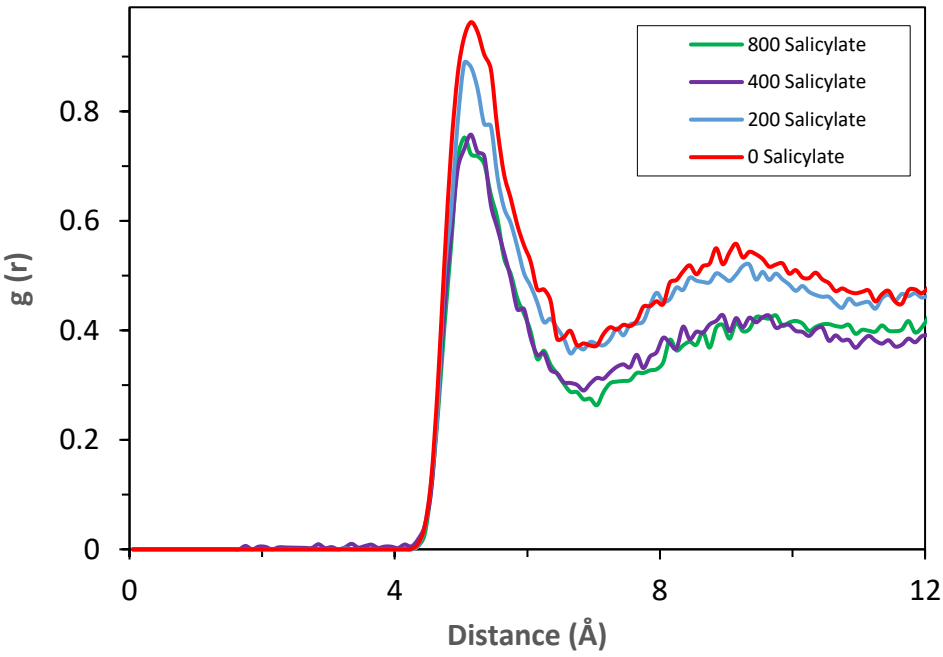


Figure 4.42. RDF plot for 50 NP (r = 3.2 nm) + 5000 Base Oil, without detergent (red), with 200 salicylate detergent (3.22% in the simulation cell), with 400 salicylate detergent (6.23%) and with 800 salicylate detergent (11.74%).

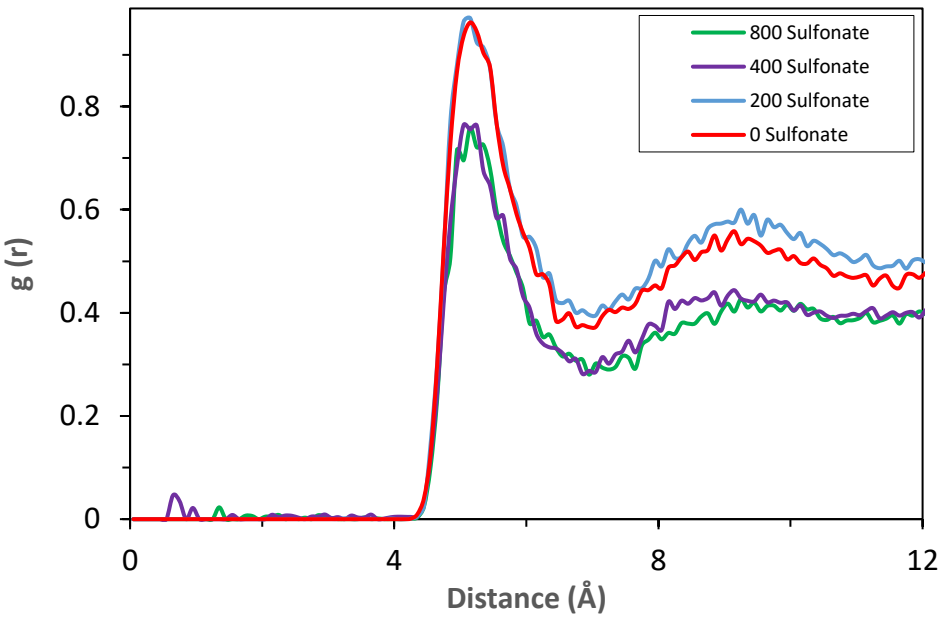


Figure 4.43. RDF plot for 50 NP (r = 3.2 nm) + 5000 Base Oil, without detergent (red), with 200 sulfonate detergent (3.22% in the simulation cell), with 400 sulfonate detergent (6.23%) and with 800 sulfonate detergent (11.74%).

4.3.3.7 Effect of Detergent and Dispersant in the Same Simulation Cell

As mentioned in the previous section of this chapter, the number of beads in 80 dispersants and 800 detergents are equal. Likewise, as revealed previously, the performance of 80 dispersants having 12 polar central beads and 36 tails is similar with that of 800 salicylate detergent in terms of reducing the aggregation of 50 NPs in base oil matrix. With the aim of illustrating a possible synergistic or antagonistic effect of using detergent and dispersant together, RDF plots of 800 detergents and 80 dispersants were compared with that of possible mixtures having a total of 7200 beads as it is in the case in 80 dispersants and 800 detergents as shown in Figure 4.44 and Figure 4.45. Results are shown for dispersant mixed with salicylate detergent and sulfonate detergent cases separately. As mentioned previously in this chapter, RDF is the plot of the number density of the polar beads on the surface of NPs. In salicylate case, mixing dispersant and detergent results in a decrease in peak value

in the RDF plot from about 0.75 to values as low as 0.53. In sulfonate case, there is a very slight decrease to about 0.70. In both cases, the peak value of the RDF plot for 0 dispersant and 800 salicylate detergents, 0 salicylate detergent and 80 dispersant and 40 dispersant and 40 salicylate detergents are almost the same. Hence, mixing in equal proportions (i.e. 40 dispersant and 400 detergents) does not seem to yield any synergistic effect in coarse-grained simulations.

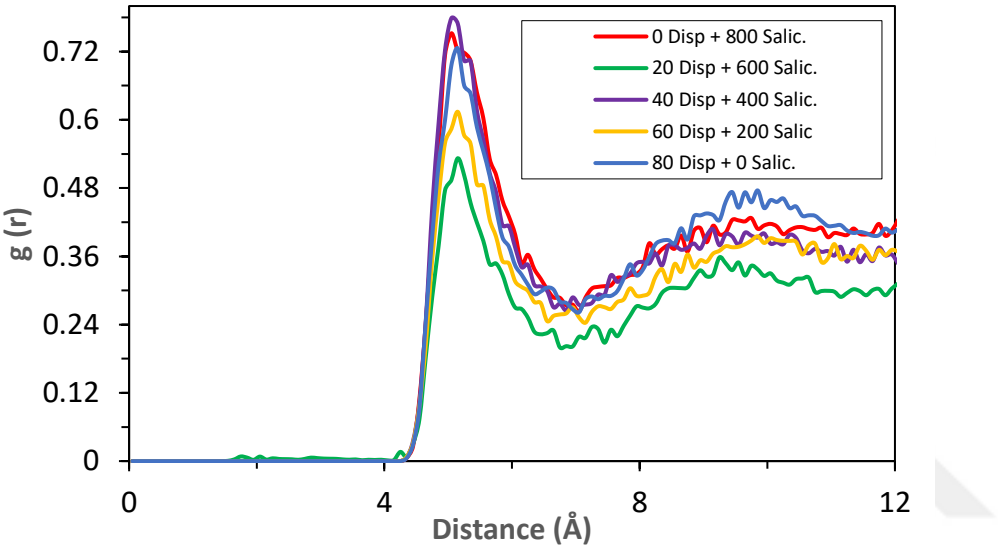


Figure 4.44. RDF plot for 50 NP (r = 3.2 nm) + 5000 Base Oil, with no dispersant and 800 salicylate detergent (red), 20 dispersant and 600 salicylate detergent (green), 40 dispersant and 400 salicylate detergent, 60 dispersant and 200 salicylate detergent, and 80 dispersant and no detergent (yellow).

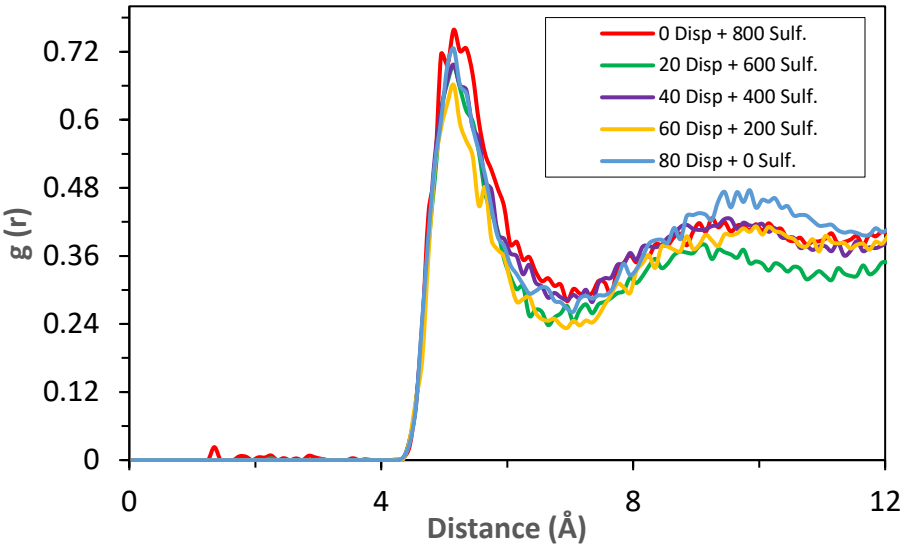


Figure 4.45. RDF plot for 50 NP (r = 3.2 nm) + 5000 Base Oil, with no dispersant and 800 sulfonate detergent (red), 20 dispersant and 600 sulfonate detergent (green), 40 dispersant and 400 sulfonate detergent, 60 dispersant and 200 sulfonate detergent, and 80 dispersant and no detergent (yellow).

Figure 4.46 shows the RDF analysis between polar beads of dispersant and polar bead in the aromatic ring in salicylate detergent and corresponding apolar bead in the sulfonate detergent. Figure 4.47 shows the RDF analysis between polar beads of dispersant and -1 charged head bead in the salicylate detergent and corresponding apolar bead in the sulfonate detergent. Referring to these figures, dispersant and detergent molecules make strong connection with each other as reported in the DFT calculations. The number density of detergent molecules around dispersant molecules increases with the increasing number of dispersant molecules as it is implied in this RDF analysis. As explained previously in the "Effect of Detergent Type on the Aggregation of NPs" (4.3.3.4) section, charged head groups of detergents intercalate between the NPs, reducing the aggregation. The salicylate detergents which are bound to the dispersant molecules participate to the intercalation process together with the dispersants. This fact can be confirmed in Figure 4.48, which is the final snapshot of the simulation cell containing 20

dispersant and 600 salicylate detergent. Synergistic effect demonstrated in the RDF plots given in Figure 4.44 and Figure **4.45** can be attributed to the increased size of the dispersant-detergent aggregate, which were intercalated between the NPs and sterically prevented aggregation of the NPs. In addition to intercalation between NPs, some of the detergents surround NPs isolate them. In the 20 dispersant together with 600 salicylate detergent case, number of free detergents are higher, which can contribute this second process. The reason of increased efficiency in mitigating the aggregation of NPs might be due to this second process with free salicylate detergent molecules.

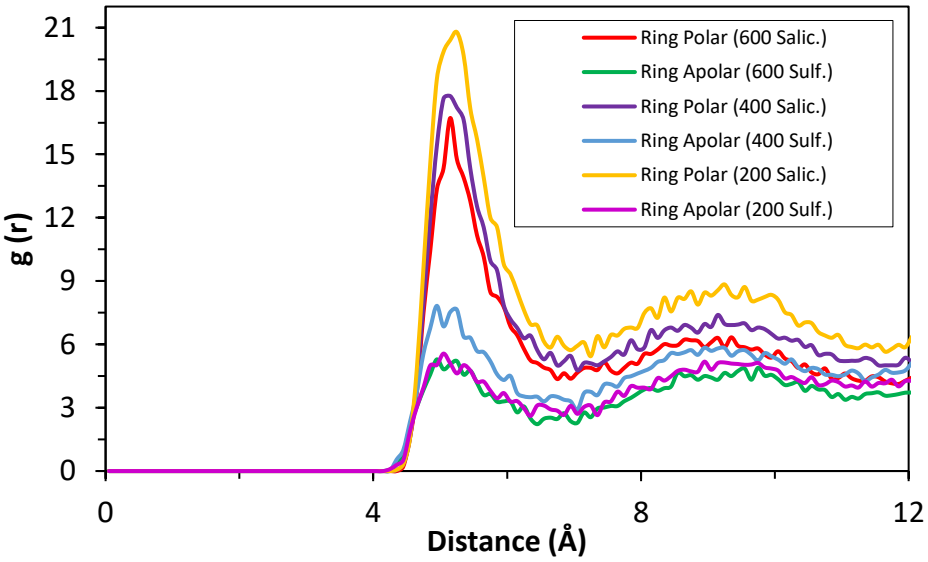


Figure 4.46. Plot of RDF between polar beads of dispersant and polar bead in the aromatic ring in salicylate detergent (red, purple and yellow) and corresponding apolar bead in the sulfonate detergent (green, blue and pink) for 20 dispersant and 600 detergent (red and green), 40 dispersant and 400 detergent (purple and blue), and 60 dispersant and 200 detergent (yellow and pink).

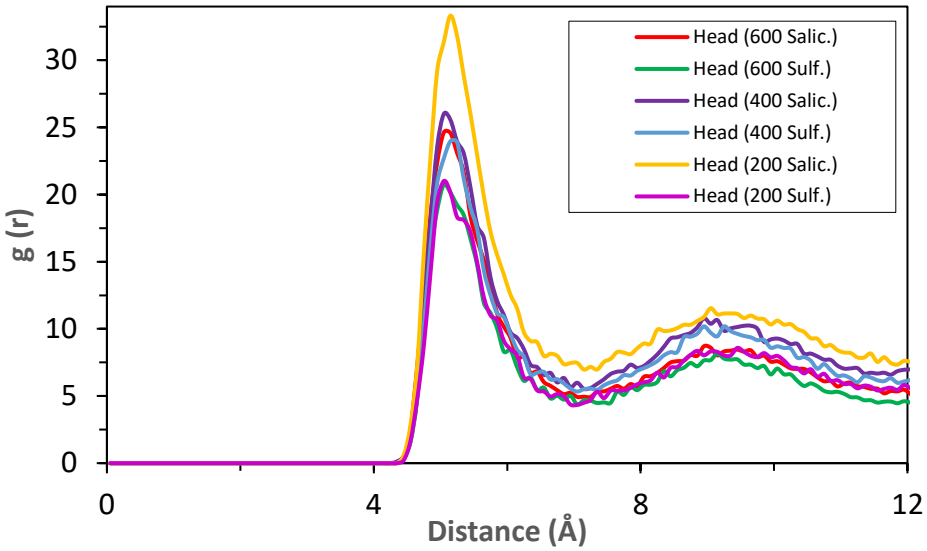


Figure 4.47. Plot of RDF between polar beads of dispersant and -1 charged head bead in the salicylate detergent (red, purple and yellow) and corresponding apolar bead in the sulfonate detergent (green, blue and pink) for 20 dispersant and 600 detergent (red and green), 40 dispersant and 400 detergent (purple and blue), and 60 dispersant and 200 detergent (yellow and pink).

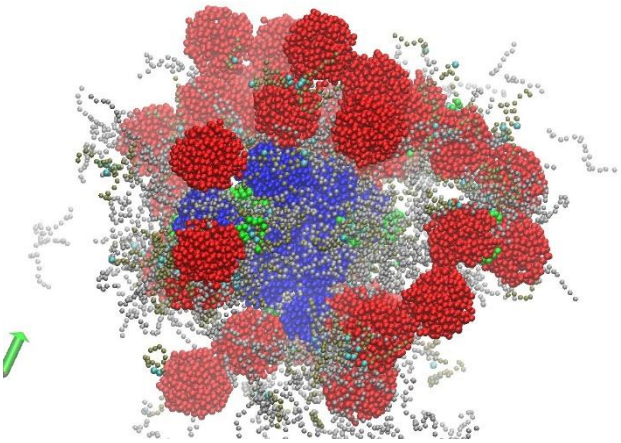


Figure 4.48. Final snapshot of the simulation cell including 50 NPs, 5000 base oil, 20 dispersant and 600 salicylate detergent.

To sum up, in both all-atom and coarse-grained MD simulations, it can be concluded that the NPs tend to aggregate regardless of presence or absence of detergent. Nevertheless, as the concentration of dispersant and or detergent molecules increases in the simulation cell, aggregation process was mitigated. However, it was not completely prevented. Main mechanism of mitigating the aggregation of NPs by dispersant is intercalation of polar center containing amine groups in the center in between the NPs and extension of hydrophobic tail in base oil matrix. Mechanism of aggregation control with detergent is preventing by interaction of head group of the sulfonate with NPs surface and extension of hydrophobic tail creating a sheer force around NPs. An important observation in the coarse-grained MD simulations is that, there is a synergistic effect of dispersant and detergent when they were used together.

CHAPTER 5

CONCLUSION

The aim of this thesis study was to investigate the self-assembly behaviour in different applications of polyelectrolytes. The advantages of computational methods at different scales were combined to better understand the role of PEs in three different applications at the molecular level within the scope of this study. With this general perspective, certain types of polyelectrolytes were modelled and all-atom and coarse-grained molecular dynamics simulations were conducted for three specific applications. Moreover, molecular and electronic properties and pairwise interactions of certain parts of the PEs with the surrounding components of the specific applications were calculated to understand their properties and their role in those specific applications. In the first part of this study, PEMs were modelled as SERS substrates and the relation with their structure properties and AuNPs mobility were investigated. In the second part, the electrical conductivity enhancement mechanism of PEDOT:PSS was studied. In the last part of the study, the insoluble deposit formed in the engine is modelled. Their aggregation and interaction with the oil additives such as dispersant and detergent were studied. As a general conclusion, coarse-grained MD simulations with Martini force field fitted with the applications where correlating structural changes with aggregation or mobility, i.e. deviation or fluctuation in the positions, of certain parts of the system is needed. On the other hand, the role of the molecular and electronic interactions can not be tracked with coarse-grained MD simulations. Hence, utilizing the advantages of computational methods at different scales, i.e. multiscale modeling, is a suitable method for studying the role of PEs in specific applications. Results specific to the applications were shared separately in the text below.

5.1 Investigation of Polyelectrolyte Multilayers for SERS

In the first part, Au immobilized PEs were used as a substrate to increase the Raman scattering with the help of surface plasmons generated on metal nanoparticles. The homogenous distribution of NPs on the SERS substrate is an important parameter affecting the SER signal. It was reported in the literature that the interaction of localized hot spots between the NPs and the analyte results in an enhancement in the SER signal and localization of the hot spots is affected by the mobility of the nanoparticles on the surface of the substrate. Owing to their fine-tunability for specific needs, polyelectrolyte multilayers are good candidates as a substrate for the homogenous distribution of NPs on the surface.

It was reported in the literature that SER signal increases with decreasing distance of nanoparticles and the highest enhancement can be achieved if one single analyte molecule is located in between two nanoparticles. In this study, rather than the distance between NPs, we focused on the mobility of the AuNPs. The number of AuNPs used in the initial model prepared for this study does not represent the number in experimental studies due to computational limitations. Moreover, the size of AuNPs in the experimental was more than 10 nanometers. On the other hand, modeling that size of AuNPs is not convenient for this study. Additionally, the number of layers can reach up to 40 in experimental studies whereas in this computational simulation study, a maximum of 18 layers were prepared. Hence, it is difficult to make a realistic estimation of the equilibrium distance of AuNPs, to relate with Raman signal enhancement. Rather, in this study, deviations in the mobility and fluctuations of AuNPs are analyzed and reported. The mobility of the AuNPs was shown to be depending on the exponential and linear grown PAH/PAA multilayers, exponential multilayers being superior in terms of decreased mobility of AuNPs. Moreover, increasing number of layers in the multilayer of PAH/TA was shown to further decrease the mobility of AuNPs. Moreover, the orientation of the analyte molecules on the surface of PEMs containing AuNPs and their interactions with the constituents of the surface were shown to be changing with different PEM

structures and number of layers. We first time in the literature studied the surface interaction of gold nanoparticles with PEM which can be a new generation material for SERS applications.

5.2 Electrical Conductivity Enhancement Mechanism of Acid and Solvent Treated PEDOT:PSS

In the second chapter of this thesis, the electrical conductivity enhancement mechanism of acid and solvent-treated PEDOT:PSS was investigated. The decision to examine this topic in the current study was driven by its increasing prominence in academic literature. There were two main objectives in this thesis, the first of which was the transition of the PEDOT structure from benzoid to quinoid. With DFT calculations, it was shown that bonds between PEDOT monomers decrease. In the literature, this transition is named as benzoid to quinoid structure change, which is one of the proposed mechanisms as summarized in the Introduction (1.4.1.2.3) chapter.

The second objective of this study was to demonstrate the segregation of PSS phase from PEDOT and formation of an ordered PEDOT structure as a result of acid treatment. With the calculation of pairwise interactions, HSO_4^- was shown to be interacting strongly with PEDOT monomers. Additionally, in all-atom MD simulations, the densely packed structure of PEDOT is shown to be resulting in a perfectly distributed HSO_4^- anion. This may result in an increase in the conductivity of PEDOT by doping with HSO_4^-. This perfect distribution was not achieved with OH^- anions. After many trials with different initial structures, separation of PSS from PEDOT was shown. However, the formation of the ordered structure of PEDOT could not be demonstrated with all-atom MD simulations.

The third objective of this chapter was to demonstrate the removal of PSS^-Na^+ and PSSH chains from PEDOT:PSS. PSS^-Na^+ and PSSH are expected to be the cause of the insulating character of pristine PEDOT:PSS. Intermolecular interactions between

PEDOT, PSS and other components in the DMSO solution were analyzed with DFT calculations and with all-atom MD simulations. As a result, it is proposed that PSS^- Na^+ and PSSH are washed away with DMSO. Additionally, PSS monomers were bound together with the help of H_3O^+ cations. This would be the first step to the organized structure of PEDOT:PSS chains from a disorganized starting structure.

5.3 Mechanism of Aggregation Control by Detergent and Dispersant in Engine Oil

Within the scope of the last chapter of this thesis, aggregation control in the lubricant oil by detergent and dispersant was investigated with first principle calculations, all-atom and coarse-grained MD simulations and the experimental details provided by the Lubrizol Corporation. From the experimental analysis, Deposits were shown to build up by aggregation of nanosized insoluble particles. Additionally, dispersants and detergents have a significant role in dispersing and stabilization of insoluble particles. From the all-atom MD simulations, the second reason for aggregation was hydrogen bonding formed between NPs. On the other hand, polar groups of dispersant and detergent intercalate between NPs via hydrogen bonding and non-polar tails were extended in base oil, preventing other NPs from aggregating by creating a hydrophobic barrier. From the CG Simulations, aggregation of NPs was shown to be inevitable without any detergents and dispersants. On the other hand, aggregation of NPs can be mitigated by the addition of dispersants and detergents.

It is important to note that, the aim of this study was not to conduct optimization studies that would give information or suggestions to increase the performance of detergent and dispersant in deposit control. The aim of this study was to create a model that resembles the experimental conditions of base oil in the passenger car engines. Once a successful model of the real system is created, it can be possible to conduct optimization studies to acquire detergent and dispersant structures with improved performances in deposit control in the new studies. The first important output of this study in this chapter was the construction of an insoluble deposit

model, which was the first in the literature. Additionally, aggregation of the insoluble deposit models was successfully simulated in both all-atom and coarse-grained MD simulations. Moreover, mitigation of the insoluble deposit formation was shown with the use of detergents and dispersants by using different structures at different concentrations.

5.4 Outlook and Future Perspective

This thesis study includes the investigation of the self-assembly behavior of polyelectrolytes in specific applications with computational methods at different scales. In the first part of the study for SERS applications, the movement of NPs on the PEM surface on a large scale required coarse-grained MD simulations. In the second part, electrical conductivity mechanism of the selected PEs is more related to the intrinsic electronic and molecular properties of PEDOT, which require first principle calculations instead of molecular mechanics studies or larger scale simulations. In the last part, calculations at the molecular or electronic level and larger size simulations feed each other to improve the construction of a better representation of the whole system.

The versatility and multifunctionality of polyelectrolytes draw attention of the researchers for their potential to be used in various fields. With the advancements in polymer science, the potential applications and importance of polyelectrolytes are expected to increase further in the future. Moreover, multiscale modeling and simulation is a powerful tool in the study of complex systems, particularly in polyelectrolytes in this study. Thanks to the sophisticated nature of the PEs, understanding their contribution to specific applications requires a perspective including multiple length and time scales. Hence, multiscale modeling and simulation techniques are suitable for studying polyelectrolytes in various application fields and it is expected to extend their place in the field of polyelectrolyte studies.

REFERENCES

(1) Karabasov, S.; Nerukh, D.; Hoekstra, A.; Chopard, B.; Coveney, P. V. Multiscale Modeling: Approaches and Challenges. *Philos. Trans. R. Soc. A Math. Phys. Eng. Sci.* **2014**, *372* (2021), 20130390. https://doi.org/10.1098/rsta.2013.0390.

(2) Foresman, J. B.; Frisch, A. E.; Gaussian, I. *Exploring Chemistry with Electronic Structure Methods*; Gaussian, Incorporated, 1996.

(3) Tamar Schlick. *Molecular Modeling and Simulation: An Interdisciplinary Guide*, 2nd ed.; Marsden, S. S. A. J. E., Sirovich, L., Eds.; London, 2010.

(4) Thompson, J. M. T.; van Mourik, T. First–Principles Quantum Chemistry in the Life Sciences. *Philos. Trans. R. Soc. London. Ser. A Math. Phys. Eng. Sci.* **2004**, *362* (1825), 2653–2670. https://doi.org/10.1098/rsta.2004.1469.

(5) Pople, J. A. Nobel Lecture: Quantum Chemical Models. *Rev. Mod. Phys.* **1999**, *71* (5), 1267–1274. https://doi.org/10.1103/RevModPhys.71.1267.

(6) Hohenberg, P.; Kohn, W. Inhomogeneous Electron Gas. *Phys. Rev.* **1964**, *136* (3B), B864–B871. https://doi.org/10.1103/PhysRev.136.B864.

(7) Kohn, W.; Sham, L. J. Self-Consistent Equations Including Exchange and Correlation Effects. *Phys. Rev.* **1965**, *140* (4A), A1133–A1138. https://doi.org/10.1103/PhysRev.140.A1133.

(8) Zhang, I. Y.; Wu, J.; Xu, X. Extending the Reliability and Applicability of B3LYP. *Chem. Commun.* **2010**, *46* (18), 3057–3070. https://doi.org/10.1039/C000677G.

(9) Kohn, W.; Becke, A. D.; Parr, R. G. Density Functional Theory of Electronic Structure. *J. Phys. Chem.* **1996**, *100* (31), 12974–12980. https://doi.org/10.1021/jp960669l.

(10) Grimme, S.; Antony, J.; Ehrlich, S.; Krieg, H. A Consistent and Accurate Ab Initio Parametrization of Density Functional Dispersion Correction (DFT-D) for the 94 Elements H-Pu. *J. Chem. Phys.* **2010**, *132* (15), 154104. https://doi.org/10.1063/1.3382344.

(11) Dawe, G. B.; Musgaard, M.; Aurousseau, M. R. P.; Nayeem, N.; Green, T.; Biggin, P. C.; Bowie, D. Distinct Structural Pathways Coordinate the Activation of AMPA Receptor-Auxiliary Subunit Complexes. *Neuron* **2016**, *89* (6), 1264–1276. https://doi.org/https://doi.org/10.1016/j.neuron.2016.01.038.

(12) Manglik, A.; Lin, H.; Aryal, D. K.; McCorvy, J. D.; Dengler, D.; Corder, G.; Levit, A.; Kling, R. C.; Bernat, V.; Hübner, H.; Huang, X.-P.; Sassano, M. F.; Giguère, P. M.; Löber, S.; Duan, D.; Scherrer, G.; Kobilka, B. K.; Gmeiner, P.; Roth, B. L.; Shoichet, B. K. Structure-Based Discovery of Opioid Analgesics with Reduced Side Effects. *Nature* **2016**, *537* (7619), 185–190. https://doi.org/10.1038/nature19112.

(13) Hollingsworth, S. A.; Dror, R. O. Molecular Dynamics Simulation for All. *Neuron* **2018**, *99* (6), 1129–1143. https://doi.org/10.1016/j.neuron.2018.08.011.

(14) Zhao, J.; Cao, Y.; Zhang, L. Exploring the Computational Methods for Protein-Ligand Binding Site Prediction. *Comput. Struct. Biotechnol. J.* **2020**, *18*, 417–426. https://doi.org/https://doi.org/10.1016/j.csbj.2020.02.008.

(15) Venable, R. M.; Krämer, A.; Pastor, R. W. Molecular Dynamics Simulations of Membrane Permeability. *Chem. Rev.* **2019**, *119* (9), 5954–5997. https://doi.org/10.1021/acs.chemrev.8b00486.

(16) Comer, J.; Schulten, K.; Chipot, C. Permeability of a Fluid Lipid Bilayer to Short-Chain Alcohols from First Principles. *J. Chem. Theory Comput.* **2017**, *13* (6), 2523–2532. https://doi.org/10.1021/acs.jctc.7b00264.

(17) Marquardt, D.; Kučerka, N.; Wassall, S. R.; Harroun, T. A.; Katsaras, J.

Cholesterol's Location in Lipid Bilayers. *Chem. Phys. Lipids* **2016**, *199*, 17–25. https://doi.org/https://doi.org/10.1016/j.chemphyslip.2016.04.001.

(18) Parisio, G.; Stocchero, M.; Ferrarini, A. Passive Membrane Permeability: Beyond the Standard Solubility-Diffusion Model. *J. Chem. Theory Comput.* **2013**, *9* (12), 5236–5246. https://doi.org/10.1021/ct400690t.

(19) Lin, F.; Xiang, Y.; Shen, H.-S. Temperature Dependent Mechanical Properties of Graphene Reinforced Polymer Nanocomposites – A Molecular Dynamics Simulation. *Compos. Part B Eng.* **2017**, *111*, 261–269. https://doi.org/https://doi.org/10.1016/j.compositesb.2016.12.004.

(20) Rasul, M. G.; Kiziltas, A.; Arfaei, B.; Shahbazian-Yassar, R. 2D Boron Nitride Nanosheets for Polymer Composite Materials. *npj 2D Mater. Appl.* **2021**, *5* (1), 56. https://doi.org/10.1038/s41699-021-00231-2.

(21) Ganesan, V.; Jayaraman, A. Theory and Simulation Studies of Effective Interactions, Phase Behavior and Morphology in Polymer Nanocomposites. *Soft Matter* **2014**, *10* (1), 13–38. https://doi.org/10.1039/C3SM51864G.

(22) Scocchi, G.; Posocco, P.; Fermeglia, M.; Pricl, S. Polymer−Clay Nanocomposites: A Multiscale Molecular Modeling Approach. *J. Phys. Chem. B* **2007**, *111* (9), 2143–2151. https://doi.org/10.1021/jp067649w.

(23) Smith, J. S.; Bedrov, D.; Smith, G. D. A Molecular Dynamics Simulation Study of Nanoparticle Interactions in a Model Polymer-Nanoparticle Composite. *Compos. Sci. Technol.* **2003**, *63* (11), 1599–1605. https://doi.org/https://doi.org/10.1016/S0266-3538(03)00061-7.

(24) Leveugle, E.; Zhigilei, L. V. Molecular Dynamics Simulation Study of the Ejection and Transport of Polymer Molecules in Matrix-Assisted Pulsed Laser Evaporation. *J. Appl. Phys.* **2007**, *102* (7), 74914. https://doi.org/10.1063/1.2783898.

(25) Sharma, S.; Kumar, P.; Chandra, R. Chapter 1 - Introduction to Molecular

Dynamics. In *Micro and Nano Technologies*; Sharma Lammps and Gromacs, S. B. T.-M. D. S. of N. U. B. M. S., Ed.; Elsevier, 2019; pp 1–38. https://doi.org/https://doi.org/10.1016/B978-0-12-816954-4.00001-2.

(26) Kimber, I.; Humphris, C.; Westmoreland, C.; Alepee, N.; Negro, G. D.; Manou, I. Computational Chemistry, Systems Biology and Toxicology. Harnessing the Chemistry of Life: Revolutionizing Toxicology. A Commentary. *J. Appl. Toxicol.* **2011**, *31* (3), 206–209. https://doi.org/10.1002/jat.1666.

(27) Verlet, L. Computer "Experiments" on Classical Fluids. I. Thermodynamical Properties of Lennard-Jones Molecules. *Phys. Rev.* **1967**, *159* (1), 98–103. https://doi.org/10.1103/PhysRev.159.98.

(28) Allen, M. P.; Tildesley, D. J. Computer Simulation of Liquids. Oxford University Press June 22, 2017. https://doi.org/10.1093/oso/9780198803195.001.0001.

(29) Hünenberger, P. H. Thermostat Algorithms for Molecular Dynamics Simulations BT - Advanced Computer Simulation: Approaches for Soft Matter Sciences I; Dr. Holm, C., Prof. Dr. Kremer, K., Eds.; Springer Berlin Heidelberg: Berlin, Heidelberg, 2005; pp 105–149. https://doi.org/10.1007/b99427.

(30) Mayo, S. L.; Olafson, B. D.; Goddard, W. A. DREIDING: A Generic Force Field for Molecular Simulations. *J. Phys. Chem.* **1990**, *94* (26), 8897–8909. https://doi.org/10.1021/j100389a010.

(31) Marrink, S. J.; Risselada, H. J.; Yefimov, S.; Tieleman, D. P.; De Vries, A. H. The MARTINI Force Field: Coarse-grained Model for Biomolecular Simulations. *J. Phys. Chem. B* **2007**, *111* (27), 7812–7824. https://doi.org/10.1021/jp071097f.

(32) Jorgensen, W. L.; Maxwell, D. S.; Tirado-Rives, J. *Development and Testing of the OPLS All-Atom Force Field on Conformational Energetics and*

Properties of Organic Liquids; 1996.

(33) Radosinski, L.; Labus, K. Molecular Modeling Studies of Structural Properties of Polyvinyl Alcohol: A Comparative Study Using INTERFACE Force Field. *J. Mol. Model.* **2017**, *23* (11). https://doi.org/10.1007/s00894-017-3472-z.

(34) Barnoud, J.; Monticelli, L. Coarse-Grained Force Fields for Molecular Simulations. *Methods Mol. Biol.* **2014**, *1215*, 125–149. https://doi.org/10.1007/978-1-4939-1465-4_7.

(35) Vögele, M.; Holm, C.; Smiatek, J. Coarse-Grained Simulations of Polyelectrolyte Complexes: MARTINI Models for Poly(Styrene Sulfonate) and Poly(Diallyldimethylammonium). *J. Chem. Phys.* **2015**, *143* (24). https://doi.org/10.1063/1.4937805.

(36) Hansen, J.-P.; McDonald, I. R. Chapter 4 - Distribution Function Theories; Hansen, J.-P., McDonald, I. R. B. T.-T. of S. L. (Fourth E., Eds.; Academic Press: Oxford, 2013; pp 105–147. https://doi.org/https://doi.org/10.1016/B978-0-12-387032-2.00004-0.

(37) Frenkel Daan, S. B. *Understanding Molecular Simulation*, 2nd ed.; 2002.

(38) Mackoy, T. Tools for Understanding Static Structure Factors and Their Application to Simulations of Liquids, Northern Illinois University, 2019. Graduate Research Theses & Dissertations.

(39) Flory, P. J. *Principles of Polymer Chemistry*; Cornell University Press Ithaca, N.Y.: Ithaca, N.Y. SE -, 1953. https://doi.org/LK - https://worldcat.org/title/542497.

(40) Bowers, K. J.; Chow, E.; Xu, H.; Dror, R. O.; Eastwood, M. P.; Gregersen, B. A.; Klepeis, J. L.; Kolossvary, I.; Moraes, M. A.; Sacerdoti, F. D.; Salmon, J. K.; Shan, Y.; Shaw, D. E. Scalable Algorithms for Molecular Dynamics Simulations on Commodity Clusters. In *Proceedings of the 2006 ACM/IEEE*

Conference on Supercomputing; SC '06; Association for Computing Machinery: New York, NY, USA, 2006; pp 84–es. https://doi.org/10.1145/1188455.1188544.

(41) Case, D. A.; Cheatham III, T. E.; Darden, T.; Gohlke, H.; Luo, R.; Merz Jr., K. M.; Onufriev, A.; Simmerling, C.; Wang, B.; Woods, R. J. The Amber Biomolecular Simulation Programs. *J. Comput. Chem.* **2005**, *26* (16), 1668–1688. https://doi.org/https://doi.org/10.1002/jcc.20290.

(42) Abraham, M. J.; Murtola, T.; Schulz, R.; Páll, S.; Smith, J. C.; Hess, B.; Lindahl, E. GROMACS: High Performance Molecular Simulations through Multi-Level Parallelism from Laptops to Supercomputers. *SoftwareX* **2015**, *1–2*, 19–25. https://doi.org/https://doi.org/10.1016/j.softx.2015.06.001.

(43) Thompson, A. P.; Aktulga, H. M.; Berger, R.; Bolintineanu, D. S.; Brown, W. M.; Crozier, P. S.; in 't Veld, P. J.; Kohlmeyer, A.; Moore, S. G.; Nguyen, T. D.; Shan, R.; Stevens, M. J.; Tranchida, J.; Trott, C.; Plimpton, S. J. LAMMPS - a Flexible Simulation Tool for Particle-Based Materials Modeling at the Atomic, Meso, and Continuum Scales. *Comput. Phys. Commun.* **2022**, *271*, 108171. https://doi.org/10.1016/j.cpc.2021.108171.

(44) Phillips, J. C.; Braun, R.; Wang, W.; Gumbart, J.; Tajkhorshid, E.; Villa, E.; Chipot, C.; Skeel, R. D.; Kalé, L.; Schulten, K. Scalable Molecular Dynamics with NAMD. *J. Comput. Chem.* **2005**, *26* (16), 1781–1802. https://doi.org/https://doi.org/10.1002/jcc.20289.

(45) Humphrey, W.; Dalke, A.; Schulten, K. VMD: Visual Molecular Dynamics. *J. Mol. Graph.* **1996**, *14* (1), 27-28,33-38. https://doi.org/10.1016/0263-7855(96)00018-5.

(46) Stukowski, A. Visualization and Analysis of Atomistic Simulation Data with OVITO–the Open Visualization Tool. *Model. Simul. Mater. Sci. Eng.* **2010**, *18* (1), 15012. https://doi.org/10.1088/0965-0393/18/1/015012.

(47) Jewett, A. I.; Stelter, D.; Lambert, J.; Saladi, S. M.; Roscioni, O. M.; Ricci,

M.; Autin, L.; Maritan, M.; Bashusqeh, S. M.; Keyes, T.; Dame, R. T.; Shea, J.-E.; Jensen, G. J.; Goodsell, D. S. Moltemplate: A Tool for Coarse-Grained Modeling of Complex Biological Matter and Soft Condensed Matter Physics. *J. Mol. Biol.* **2021**, *433* (11), 166841. https://doi.org/10.1016/j.jmb.2021.166841.

(48) Martínez, L.; Andrade, R.; Birgin, E. G.; Martínez, J. M. PACKMOL: A Package for Building Initial Configurations for Molecular Dynamics Simulations. *J. Comput. Chem.* **2009**, *30* (13), 2157–2164. https://doi.org/10.1002/jcc.21224.

(49) Oosawa, F. *Polyelectrolytes*; Marcel Dekker: New York, 1971.

(50) Barrat, J.-L.; Joanny, F. Theory of Polyelectrolyte Solutions. In *Advances in Chemical Physics*; Advances in Chemical Physics; 1996; pp 1–66. https://doi.org/https://doi.org/10.1002/9780470141533.ch1.

(51) Rabiee, A.; Ershad-Langroudi, A.; Zeynali, M. E. A Survey on Cationic Polyelectrolytes and Their Applications: Acrylamide Derivatives. **2015**, *31* (3), 239–261. https://doi.org/doi:10.1515/revce-2014-0056.

(52) Schwoyer, W. L. K. *Polyelectrolytes for Water and Wastewater Treatment*; SE -, 1981. https://doi.org/LK - https://worldcat.org/title/475431050.

(53) Rabiee, A.; Ershad-Langroudi, A.; Jamshidi, H. Polyacrylamide-Based Polyampholytes and Their Applications. **2014**, *30* (5), 501–519. https://doi.org/doi:10.1515/revce-2014-0004.

(54) Bohrisch, J.; Eisenbach, C. D.; Jaeger, W.; Mori, H.; Müller, A. H. E.; Rehahn, M.; Schaller, C.; Traser, S.; Wittmeyer, P. New Polyelectrolyte Architectures BT - Polyelectrolytes with Defined Molecular Architecture I; Schmidt, M., Ed.; Springer Berlin Heidelberg: Berlin, Heidelberg, 2004; pp 1–42. https://doi.org/10.1007/b11266.

(55) Lyklema, J. *Fundamentals of Interface and Colloid Science. Volume I:*

Fundamentals.; Academic Press, 1991.

(56) van der Gucht, J.; Spruijt, E.; Lemmers, M.; Cohen Stuart, M. A. Polyelectrolyte Complexes: Bulk Phases and Colloidal Systems. *J. Colloid Interface Sci.* **2011**, *361* (2), 407–422. https://doi.org/10.1016/j.jcis.2011.05.080.

(57) Izumrudov, V. A.; Mussabayeva, B. K.; Murzagulova, K. B. Polyelectrolyte Multilayers: Preparation and Applications. *Russ. Chem. Rev.* **2018**, *87* (2), 192–200. https://doi.org/10.1070/rcr4767.

(58) Fares, H. M.; Wang, Q.; Yang, M.; Schlenoff, J. B. Swelling and Inflation in Polyelectrolyte Complexes. *Macromolecules* **2019**, *52* (2), 610–619. https://doi.org/10.1021/acs.macromol.8b01838.

(59) Dobrynin, A. V.; Rubinstein, M. Theory of Polyelectrolytes in Solutions and at Surfaces. *Progress in Polymer Science (Oxford)*. Elsevier Ltd 2005, pp 1049–1118. https://doi.org/10.1016/j.progpolymsci.2005.07.006.

(60) Mermut, O.; Barrett, C. J. Effects of Charge Density and Counterions on the Assembly of Polyelectrolyte Multilayers. *J. Phys. Chem. B* **2003**, *107* (11), 2525–2530. https://doi.org/10.1021/jp027278t.

(61) Decher, G.; Hong, J. D.; Schmitt, J. Buildup of Ultrathin Multilayer Films by a Self-Assembly Process: III. Consecutively Alternating Adsorption of Anionic and Cationic Polyelectrolytes on Charged Surfaces. *Thin Solid Films* **1992**, *210–211* (PART 2), 831–835. https://doi.org/10.1016/0040-6090(92)90417-A.

(62) Rončević, I. Š.; Krivić, D.; Buljac, M.; Vladislavić, N.; Buzuk, M. *Polyelectrolytes Assembly: A Powerful Tool for Electrochemical Sensing Application*; 2020; Vol. 20. https://doi.org/10.3390/s20113211.

(63) Das, B. P.; Tsianou, M. From Polyelectrolyte Complexes to Polyelectrolyte Multilayers: Electrostatic Assembly, Nanostructure, Dynamics, and

Functional Properties. *Adv. Colloid Interface Sci.* **2017**, *244*, 71–89. https://doi.org/10.1016/j.cis.2016.12.004.

(64) Zhao, S.; Caruso, F.; Dähne, L.; Decher, G.; De Geest, B. G.; Fan, J.; Feliu, N.; Gogotsi, Y.; Hammond, P. T.; Hersam, M. C.; Khademhosseini, A.; Kotov, N.; Leporatti, S.; Li, Y.; Lisdat, F.; Liz-Marzán, L. M.; Moya, S.; Mulvaney, P.; Rogach, A. L.; Roy, S.; Shchukin, D. G.; Skirtach, A. G.; Stevens, M. M.; Sukhorukov, G. B.; Weiss, P. S.; Yue, Z.; Zhu, D.; Parak, W. J. The Future of Layer-by-Layer Assembly: A Tribute to ACS Nano Associate Editor Helmuth Möhwald. *ACS Nano* **2019**, *13* (6), 6151–6169. https://doi.org/10.1021/acsnano.9b03326.

(65) Zhang, W.; Pan, C.; Ge, Q.; Zhang, L.; Wang, X. Fabrication and Characterization of Chitosan/Alginate Multilayer Composite Membrane Supported by a Porous Poly (Acrylonitrile) Substrate for Pervaporation Dehydration of Alcohol. *J. Membr. Sci. Res.* **2017**, *3* (4), 272–280. https://doi.org/10.22079/jmsr.2016.18586.

(66) Ariga, K.; Ahn, E.; Park, M.; Kim, B.-S. Layer-by-Layer Assembly: Recent Progress from Layered Assemblies to Layered Nanoarchitectonics. *Chem. – An Asian J.* **2019**, *14* (15), 2553–2566. https://doi.org/https://doi.org/10.1002/asia.201900627.

(67) Das, B. P.; Tsianou, M. From Polyelectrolyte Complexes to Polyelectrolyte Multilayers: Electrostatic Assembly, Nanostructure, Dynamics, and Functional Properties. *Adv. Colloid Interface Sci.* **2017**, *244*, 71–89. https://doi.org/10.1016/j.cis.2016.12.004.

(68) Laugel, N.; Betscha, C.; Winterhalter, M.; Voegel, J.-C.; Schaaf, P.; Ball, V. Relationship between the Growth Regime of Polyelectrolyte Multilayers and the Polyanion/Polycation Complexation Enthalpy. *J. Phys. Chem. B* **2006**, *110* (39), 19443–19449. https://doi.org/10.1021/jp062264z.

(69) Hoda, N.; Larson, R. G. Modeling the Buildup of Exponentially Growing

Polyelectrolyte Multilayer Films. *J. Phys. Chem. B* **2009**, *113* (13), 4232–4241. https://doi.org/10.1021/jp809959j.

(70) Kudelski, A. Analytical Applications of Raman Spectroscopy. *Talanta* **2008**, *76* (1), 1–8. https://doi.org/10.1016/j.talanta.2008.02.042.

(71) Kneipp, K.; Moskovits, M.; Kneipp, H. *Surface-Enhanced Raman Scattering*; Springer-Verlag: Berlin, 2006.

(72) Willets, K. A.; Van Duyne, R. P. Localized Surface Plasmon Resonance Spectroscopy and Sensing. *Annu. Rev. Phys. Chem.* **2007**, *58* (1), 267–297. https://doi.org/10.1146/annurev.physchem.58.032806.104607.

(73) Michaels, A. M.; Nirmal, M.; Brus, L. E. Surface Enhanced Raman Spectroscopy of Individual Rhodamine 6G Molecules on Large Ag Nanocrystals. *J. Am. Chem. Soc.* **1999**, *121* (43), 9932–9939. https://doi.org/10.1021/ja992128q.

(74) Kneipp, K.; Wang, Y.; Kneipp, H.; Perelman, L. T.; Itzkan, I.; Dasari, R. R.; Feld, M. S. Single Molecule Detection Using Surface-Enhanced Raman Scattering (SERS). *Phys. Rev. Lett.* **1997**, *78* (9), 1667–1670. https://doi.org/10.1103/PhysRevLett.78.1667.

(75) Stiles, P. L.; Dieringer, J. A.; Shah, N. C.; Van Duyne, R. P. Surface-Enhanced Raman Spectroscopy. *Annu. Rev. Anal. Chem. (Palo Alto. Calif).* **2008**, *1*, 601–626. https://doi.org/10.1146/annurev.anchem.1.031207.112814.

(76) Campion, A.; Kambhampati, P. Surface-Enhanced Raman Scattering. *Chem. Soc. Rev.* **1998**, *27* (4), 241–250. https://doi.org/10.1039/A827241Z.

(77) McNay, G.; Eustace, D.; Smith, W. E.; Faulds, K.; Graham, D. Surface-Enhanced Raman Scattering (SERS) and Surface-Enhanced Resonance Raman Scattering (SERRS): A Review of Applications. *Appl. Spectrosc.* **2011**, *65* (8), 825–837. https://doi.org/10.1366/11-06365.

(78) Banholzer, M. J.; Millstone, J. E.; Qin, L.; Mirkin, C. A. Rationally Designed

Nanostructures for Surface-Enhanced Raman Spectroscopy. *Chem. Soc. Rev.* **2008**, *37* (5), 885–897. https://doi.org/10.1039/B710915F.

(79) Xu, H.; Aizpurua, J.; Kall, M.; Apell, P. Electromagnetic Contributions to Single-Molecule Sensitivity in Surface-Enhanced Raman Scattering. *Phys. Rev. E, Stat. physics, plasmas, fluids, Relat. Interdiscip. Top.* **2000**, *62* (3 Pt B), 4318–4324. https://doi.org/10.1103/physreve.62.4318.

(80) CREIGHTON, J. A. The Selection Rules for Surface-Enhanced Raman Spectroscopy. *Adv. Spectrosc.* **1988**.

(81) Hill, W.; Wehling, B.; Gibbs, C. G.; Gutsche, C. D.; Klockow, D. Detection of Aromatics in Aqueous Solution by Surface-Enhanced Raman Scattering by Substrates Chemically Modified with p-Tert-Butylcalix[4]Arenetetrathiol. *Anal. Chem.* **1995**, *67* (18), 3187–3192. https://doi.org/10.1021/ac00114a014.

(82) Moskovits, M. Surface-Enhanced Spectroscopy. *Rev. Mod. Phys.* **1985**, *57* (3), 783–826. https://doi.org/10.1103/RevModPhys.57.783.

(83) Semin, D. J.; Rowlen, K. L. Influence of Vapor Deposition Parameters on SERS Active Ag Film Morphology and Optical Properties. *Anal. Chem.* **1994**, *66* (23), 4324–4331. https://doi.org/10.1021/ac00095a032.

(84) He, L.; Musick, M. D.; Nicewarner, S. R.; Salinas, F. G.; Benkovic, S. J.; Natan, M. J.; Keating, C. D. Colloidal Au-Enhanced Surface Plasmon Resonance for Ultrasensitive Detection of DNA Hybridization. *J. Am. Chem. Soc.* **2000**, *122* (38), 9071–9077. https://doi.org/10.1021/ja001215b.

(85) Zhang, L.; Sun, J. Layer-by-Layer Deposition of Polyelectrolyte Complexes for the Fabrication of Foam Coatings with High Loading Capacity. *Chem. Commun.* **2009**, No. 26, 3901–3903. https://doi.org/10.1039/B907691C.

(86) Viswanathan, P.; Kim, Y. J.; Hong, J. D. Nanoporous Silver Submicrocubes Layer by Layer Encapsulated with Polyelectrolyte Films: Nonenzymatic Catalysis for Glucose Monitoring. *Langmuir* **2020**, *36* (13), 3452–3460.

https://doi.org/10.1021/acs.langmuir.9b03972.

(87) Xiang, Y.; Lu, S.; Jiang, S. P. Layer-by-Layer Self-Assembly in the Development of Electrochemical Energy Conversion and Storage Devices from Fuel Cells to Supercapacitors. *Chem. Soc. Rev.* **2012**, *41* (21), 7291–7321. https://doi.org/10.1039/C2CS35048C.

(88) Shirakawa, H.; Ito, T.; Ikeda, S. Simultaneous Polymerization and Formation of Polyacetylene Film on the Surface of Concentrated Soluble Ziegler-Type Catalyst Solution. *J. Polym. Sci. Part A Polym. Chem.* **1996**, *34* (13), 2533–2542. https://doi.org/10.1002/pola.1996.854.

(89) Shirakawa, H.; Louis, E. J.; MacDiarmid, A. G.; Chiang, C. K.; Heeger, A. J. Synthesis of Electrically Conducting Organic Polymers: Halogen Derivatives of Polyacetylene{,} (CH). *J. Chem. Soc.{,} Chem. Commun.* **1977**, No. 16, 578–580. https://doi.org/10.1039/C39770000578.

(90) Heeger, A. J. Semiconducting and Metallic Polymers: The Fourth Generation of Polymeric Materials (Nobel Lecture). *Angew. Chemie Int. Ed.* **2001**, *40* (14), 2591–2611. https://doi.org/https://doi.org/10.1002/1521-3773(20010716)40:14<2591::AID-ANIE2591>3.0.CO;2-0.

(91) Rozlosnik, N. New Directions in Medical Biosensors Employing Poly(3,4-Ethylenedioxy Thiophene) Derivative-Based Electrodes. *Anal. Bioanal. Chem.* **2009**, *395* (3), 637–645. https://doi.org/10.1007/s00216-009-2981-8.

(92) Jiang, Y.; Liu, T.; Zhou, Y. Recent Advances of Synthesis, Properties, Film Fabrication Methods, Modifications of Poly(3,4-Ethylenedioxythiophene), and Applications in Solution-Processed Photovoltaics. *Adv. Funct. Mater.* **2020**, *30* (51), 2006213. https://doi.org/https://doi.org/10.1002/adfm.202006213.

(93) Billingham, N. C.; Calvert, P. D. Electrically Conducting Polymers — A Polymer Science Viewpoint BT - Conducting Polymers/Molecular Recognition; Springer Berlin Heidelberg: Berlin, Heidelberg, 1989; pp 1–104.

(94) Wessling, B. From Conductive Polymers to Organic Metals. *Chem. Innov.* **2001**, *31* (1), 34–40.

(95) Kudoh, Y.; Akami, K.; Matsuya, Y. Solid Electrolytic Capacitor with Highly Stable Conducting Polymer as a Counter Electrode. *Synth. Met.* **1999**, *102* (1), 973–974. https://doi.org/https://doi.org/10.1016/S0379-6779(98)01012-1.

(96) Bayer, A. J. E. P. Polythiophenes, Process for Their Preparation and Their Use. US-4959430-A, 339340, 1988.

(97) Seymour, R. B. Conductive Polymers BT - Applications of Polymers; Seymour, R. B., Mark, H. F., Eds.; Springer US: Boston, MA, 1988; pp 69–71. https://doi.org/10.1007/978-1-4684-5448-2_11.

(98) Qiu, Z.; Hammer, B. A. G.; Müllen, K. Conjugated Polymers – Problems and Promises. *Prog. Polym. Sci.* **2020**, *100*, 101179. https://doi.org/https://doi.org/10.1016/j.progpolymsci.2019.101179.

(99) McGehee, M. D.; Heeger, A. J. Semiconducting (Conjugated) Polymers as Materials for Solid-State Lasers. *Adv. Mater.* **2000**, *12* (22), 1655–1668. https://doi.org/https://doi.org/10.1002/1521-4095(200011)12:22<1655::AID-ADMA1655>3.0.CO;2-2.

(100) Kumar, D.; Sharma, R. C. Advances in Conductive Polymers. *Eur. Polym. J.* **1998**, *34* (8), 1053–1060. https://doi.org/https://doi.org/10.1016/S0014-3057(97)00204-8.

(101) Fonseca, S. M.; Moreira, T.; Parola, A. J.; Pinheiro, C.; Laia, C. A. T. PEDOT Electrodeposition on Oriented Mesoporous Silica Templates for Electrochromic Devices. *Sol. Energy Mater. Sol. Cells* **2017**, *159*, 94–101. https://doi.org/https://doi.org/10.1016/j.solmat.2016.09.002.

(102) Kang, J.-H.; Oh, Y.-J.; Paek, S.-M.; Hwang, S.-J.; Choy, J.-H. Electrochromic Device of PEDOT–PANI Hybrid System for Fast Response and High Optical Contrast. *Sol. Energy Mater. Sol. Cells* **2009**, *93* (12), 2040–2044.

https://doi.org/https://doi.org/10.1016/j.solmat.2009.08.007.

(103) Zhou, H. Recent Advancements in the Synthesis and Application of PEDOT and PEDOT:PSS. **2021**, No. January 2021, 82. https://doi.org/10.1117/12.2592828.

(104) Sun, K.; Zhang, S.; Li, P.; Xia, Y.; Zhang, X.; Du, D.; Isikgor, F. H.; Ouyang, J. Review on Application of PEDOTs and PEDOT:PSS in Energy Conversion and Storage Devices. *J. Mater. Sci. Mater. Electron.* **2015**, *26* (7), 4438–4462. https://doi.org/10.1007/s10854-015-2895-5.

(105) Spiteri, M. N.; Williams, C. E.; Boué, F. Pearl-Necklace-Like Chain Conformation of Hydrophobic Polyelectrolyte: A SANS Study of Partially Sulfonated Polystyrene in Water. *Macromolecules* **2007**, *40* (18), 6679–6691. https://doi.org/10.1021/ma060896d.

(106) Tounakti, C.; Decorse, P.; Kouki, F.; Lang, P. Relationship between Enhancement of PEDOT:PSS Conductivity by Solvent Treatment and PSS Chain Reorganization. *J. Polym. Sci.* **2023**. https://doi.org/10.1002/pol.20220605.

(107) Greczynski, G.; Kugler, T.; Salaneck, W. R. Characterization of the PEDOT-PSS System by Means of X-Ray and Ultraviolet Photoelectron Spectroscopy. *Thin Solid Films* **1999**, *354* (1), 129–135. https://doi.org/https://doi.org/10.1016/S0040-6090(99)00422-8.

(108) Takano, T.; Masunaga, H.; Fujiwara, A.; Okuzaki, H.; Sasaki, T. PEDOT Nanocrystal in Highly Conductive PEDOT:PSS Polymer Films. *Macromolecules* **2012**, *45* (9), 3859–3865. https://doi.org/10.1021/ma300120g.

(109) Elschner, A.; Kirchmeyer, S.; Lövenich, W.; Merker, U.; Reuter, K. *PEDOT: Principles and Applications of an Intrinsically Conductive Polymer*; 2010. https://doi.org/10.1201/b10318.

(110) Franco-Gonzalez, J. F.; Rolland, N.; Zozoulenko, I. V. Substrate-Dependent Morphology and Its Effect on Electrical Mobility of Doped Poly(3,4-Ethylenedioxythiophene) (PEDOT) Thin Films. *ACS Appl. Mater. Interfaces* **2018**, *10* (34), 29115–29126. https://doi.org/10.1021/ACSAMI.8B08774/ASSET/IMAGES/MEDIUM/AM-2018-08774J_M004.GIF.

(111) Zozoulenko, I.; Felipe Franco-Gonzalez, J.; Gueskine, V.; Mehandzhiyski, A.; Modarresi, M.; Rolland, N.; Tybrandt, K. Electronic, Optical, Morphological, Transport, and Electrochemical Properties of PEDOT: A Theoretical Perspective. *Macromolecules* **2021**, *54* (13), 5915–5934. https://doi.org/10.1021/acs.macromol.1c00444.

(112) Brédas, J. L.; Wudl, F.; Heeger, A. J. Polarons and Bipolarons in Doped Polythiophene: A Theoretical Investigation. *Solid State Commun.* **1987**, *63* (7), 577–580. https://doi.org/https://doi.org/10.1016/0038-1098(87)90856-8.

(113) Stafström, S.; Brédas, J. L. Evolution of the Electronic Structure of Polyacetylene and Polythiophene as a Function of Doping Level and Lattice Conformation. *Phys. Rev. B* **1988**, *38* (6), 4180–4191. https://doi.org/10.1103/PhysRevB.38.4180.

(114) Burke, K. Perspective on Density Functional Theory. *J. Chem. Phys.* **2012**, *136* (15), 150901. https://doi.org/10.1063/1.4704546.

(115) Salzner, U. Investigation of Charge Carriers in Doped Thiophene Oligomers through Theoretical Modeling of Their UV/Vis Spectra. *J. Phys. Chem. A* **2008**, *112* (24), 5458–5466. https://doi.org/10.1021/jp800606m.

(116) Bredas, J. L.; Street, G. B. Polarons, Bipolarons, and Solitons in Conducting Polymers. *Acc. Chem. Res.* **1985**, *18* (10), 309–315. https://doi.org/10.1021/ar00118a005.

(117) Ouyang, W.; Mandelli, D.; Urbakh, M.; Hod, O. Nanoserpents: Graphene Nanoribbon Motion on Two-Dimensional Hexagonal Materials. *Nano Lett.*

2018, *18* (9), 6009–6016. https://doi.org/10.1021/acs.nanolett.8b02848.

(118) Xia, Y.; Ouyang, J. Salt-Induced Charge Screening and Significant Conductivity Enhancement of Conducting Poly(3,4-Ethylenedioxythiophene):Poly(Styrenesulfonate). *Macromolecules* **2009**, *42* (12), 4141–4147. https://doi.org/10.1021/ma900327d.

(119) Shi, H.; Liu, C.; Jiang, Q.; Xu, J. Effective Approaches to Improve the Electrical Conductivity of PEDOT:PSS: A Review. *Adv. Electron. Mater.* **2015**, *1* (4), 1–16. https://doi.org/10.1002/aelm.201500017.

(120) Kim, J. Y.; Jung, J. H.; Lee, D. E.; Joo, J. Enhancement of Electrical Conductivity of Poly(3,4-Ethylenedioxythiophene)/Poly(4-Styrenesulfonate) by a Change of Solvents. *Synth. Met.* **2002**, *126* (2), 311–316. https://doi.org/https://doi.org/10.1016/S0379-6779(01)00576-8.

(121) Ouyang, J.; Chu, C.-W.; Chen, F.-C.; Xu, Q.; Yang, Y. High-Conductivity Poly(3,4-Ethylenedioxythiophene):Poly(Styrene Sulfonate) Film and Its Application in Polymer Optoelectronic Devices. *Adv. Funct. Mater.* **2005**, *15* (2), 203–208. https://doi.org/https://doi.org/10.1002/adfm.200400016.

(122) Onorato, A.; Invernale, M. A.; Berghorn, I. D.; Pavlik, C.; Sotzing, G. A.; Smith, M. B. Enhanced Conductivity in Sorbitol-Treated PEDOT–PSS. Observation of an in Situ Cyclodehydration Reaction. *Synth. Met.* **2010**, *160* (21), 2284–2289. https://doi.org/https://doi.org/10.1016/j.synthmet.2010.08.021.

(123) Cruz-Cruz, I.; Reyes-Reyes, M.; López-Sandoval, R. Formation of Polystyrene Sulfonic Acid Surface Structures on Poly(3,4-Ethylenedioxythiophene): Poly(Styrenesulfonate) Thin Films and the Enhancement of Its Conductivity by Using Sulfuric Acid. *Thin Solid Films* **2013**, *531*, 385–390. https://doi.org/https://doi.org/10.1016/j.tsf.2012.12.050.

(124) Kong, F.; Liu, C.; Song, H.; Xu, J.; Huang, Y.; Zhu, H.; Wang, J. Effect of Solution PH Value on Thermoelectric Performance of Free-Standing

PEDOT:PSS Films. *Synth. Met.* **2013**, *185–186*, 31–37. https://doi.org/https://doi.org/10.1016/j.synthmet.2013.09.046.

(125) Xia, Y.; Sun, K.; Ouyang, J. Solution-Processed Metallic Conducting Polymer Films as Transparent Electrode of Optoelectronic Devices. *Adv. Mater.* **2012**, *24* (18), 2436–2440. https://doi.org/https://doi.org/10.1002/adma.201104795.

(126) Kim, N.; Kee, S.; Lee, S. H.; Lee, B. H.; Kahng, Y. H.; Jo, Y.-R.; Kim, B.-J.; Lee, K. Highly Conductive PEDOT:PSS Nanofibrils Induced by Solution-Processed Crystallization. *Adv. Mater.* **2014**, *26* (14), 2268–2272. https://doi.org/https://doi.org/10.1002/adma.201304611.

(127) Gueye, M. N.; Carella, A.; Massonnet, N.; Yvenou, E.; Brenet, S.; Faure-Vincent, J.; Pouget, S.; Rieutord, F.; Okuno, H.; Benayad, A.; Demadrille, R.; Simonato, J. P. Structure and Dopant Engineering in PEDOT Thin Films: Practical Tools for a Dramatic Conductivity Enhancement. *Chem. Mater.* **2016**, *28* (10), 3462–3468. https://doi.org/10.1021/acs.chemmater.6b01035.

(128) Xia, Y.; Ouyang, J. Significant Conductivity Enhancement of Conductive Poly(3,4-Ethylenedioxythiophene): Poly(Styrenesulfonate) Films through a Treatment with Organic Carboxylic Acids and Inorganic Acids. *ACS Appl. Mater. Interfaces* **2010**, *2* (2), 474–483. https://doi.org/10.1021/am900708x.

(129) Ouyang, J. Solution-Processed PEDOT:PSS Films with Conductivities as Indium Tin Oxide through a Treatment with Mild and Weak Organic Acids. *ACS Appl. Mater. Interfaces* **2013**, *5* (24), 13082–13088. https://doi.org/10.1021/am404113n.

(130) McCarthy, J. E.; Hanley, C. A.; Brennan, L. J.; Lambertini, V. G.; Gun'ko, Y. K. Fabrication of Highly Transparent and Conducting PEDOT:PSS Films Using a Formic Acid Treatment. *J. Mater. Chem. C* **2014**, *2* (4), 764–770. https://doi.org/10.1039/C3TC31951B.

(131) Kang, K. S.; Chen, Y.; Han, K. J.; Yoo, K. H.; Kim, J. Conductivity Enhancement of Conjugated Polymer after HCl–Methanol Treatment. *Thin*

Solid Films **2009**, *517* (20), 5909–5912. https://doi.org/https://doi.org/10.1016/j.tsf.2009.04.030.

(132) Crispin, X.; Marciniak, S.; Osikowicz, W.; Zotti, G.; van der Gon, A. W. D.; Louwet, F.; Fahlman, M.; Groenendaal, L.; De Schryver, F.; Salaneck, W. R. Conductivity, Morphology, Interfacial Chemistry, and Stability of Poly(3,4-Ethylene Dioxythiophene)–Poly(Styrene Sulfonate): A Photoelectron Spectroscopy Study. *J. Polym. Sci. Part B Polym. Phys.* **2003**, *41* (21), 2561–2583. https://doi.org/https://doi.org/10.1002/polb.10659.

(133) Alemu Mengistie, D.; Wang, P.-C.; Chu, C.-W. Effect of Molecular Weight of Additives on the Conductivity of PEDOT:PSS and Efficiency for ITO-Free Organic Solar Cells. *J. Mater. Chem. A* **2013**, *1* (34), 9907–9915. https://doi.org/10.1039/C3TA11726J.

(134) Ouyang, J.; Xu, Q.; Chu, C. W.; Yang, Y.; Li, G.; Shinar, J. On the Mechanism of Conductivity Enhancement in Poly(3,4-Ethylenedioxythiophene):Poly(Styrene Sulfonate) Film through Solvent Treatment. *Polymer (Guildf).* **2004**, *45* (25), 8443–8450. https://doi.org/10.1016/j.polymer.2004.10.001.

(135) Yildirim, E.; Wu, G.; Yong, X.; Tan, T. L.; Zhu, Q.; Xu, J.; Ouyang, J.; Wang, J. S.; Yang, S. W. A Theoretical Mechanistic Study on Electrical Conductivity Enhancement of DMSO Treated PEDOT:PSS. *J. Mater. Chem. C* **2018**, *6* (19), 5122–5131. https://doi.org/10.1039/c8tc00917a.

(136) Ahmed, N. S.; Nassar, A. M.; Abdel-Azim, A. A. A. Synthesis and Evaluation of Some Detergent/Dispersant Additives for Lube Oil. *Int. J. Polym. Mater. Polym. Biomater.* **2008**, *57* (2), 114–124. https://doi.org/10.1080/00914030701392385.

(137) Seddon, E. J.; L., F. C.; Roski, J. P. Detergents and Dispersants. In *Chemistry and Technology of Lubricants*; Springer Netherlands, 1997; pp 213–236. https://doi.org/10.1007/978-94-017-1021-3_3.

(138) J. F. Kunc Jr.; J. P. Hamer. LUBRICANTS — THE SURFACE SAVERS. *SAE Trans.* **1953**, *61*, 378–385.

(139) Smiechowski, M. F.; Lvovich, V. F. Characterization of Non-Aqueous Dispersions of Carbon Black Nanoparticles by Electrochemical Impedance Spectroscopy. *J. Electroanal. Chem.* **2005**, *577* (1), 67–78. https://doi.org/10.1016/j.jelechem.2004.11.015.

(140) Smith, G. W. Kinetic Aspects of Diesel Soot Coagulation. *SAE Tech. Pap.* **1982**, No. 3, 299–309. https://doi.org/10.4271/820466.

(141) Bunting, B. G. An Analysis of Intake Valve Deposits from Gasolines Containing Polycyclic Aromatics. *SAE Tech. Pap.* **1991**, *100* (1991), 1051–1057. https://doi.org/10.4271/912378.

(142) Dimkovski, Z.; Bååth, L.; Rosén, S.; Ohlsson, R.; Rosén, B. G. Interference Measurements of Deposits on Cylinder Liner Surfaces. *Wear* **2011**, *270* (3–4), 247–251. https://doi.org/10.1016/j.wear.2010.10.066.

(143) McGeehan, J. A. Effect of Piston Deposits, Fuel Sulfur, and Lubricant Viscosity on Diesel Engine Oil Consumption and Cylinder Bore Polishing. *SAE Trans.* **1983**, *92*, 848–869.

(144) Ahmed, N. S.; Nassar, A. M. Lubricating Oil Additives Based on Polyalkylpolyamines. *Int. J. Polym. Mater. Polym. Biomater.* **2009**, *58* (3), 178–190. https://doi.org/10.1080/00914030701551071.

(145) Havet, L.; Blouet, J.; Robbe Valloire, F.; Brasseur, E.; Slomka, D. Tribological Characteristics of Some Environmentally Friendly Lubricants. *Wear* **2001**, *248* (1), 140–146. https://doi.org/https://doi.org/10.1016/S0043-1648(00)00550-0.

(146) Barnes, A. M.; Bartle, K. D.; Thibon, V. R. A. A Review of Zinc Dialkyldithiophosphates (ZDDPS): Characterisation and Role in the Lubricating Oil. *Tribol. Int.* **2001**, *34* (6), 389–395.

https://doi.org/https://doi.org/10.1016/S0301-679X(01)00028-7.

(147) Dörr, N.; Agocs, A.; Besser, C.; Ristić, A.; Frauscher, M. Engine Oils in the Field: A Comprehensive Chemical Assessment of Engine Oil Degradation in a Passenger Car. *Tribol. Lett.* **2019**, *67* (3), 1–21. https://doi.org/10.1007/S11249-019-1182-7/FIGURES/13.

(148) Castro, W.; Weller, D. E.; Cheenkachorn, K.; Perez, J. M. The Effect of Chemical Structure of Basefluids on Antiwear Effectiveness of Additives . *Tribology International* . March 2005, pp 321–326. https://doi.org/10.1016/j.triboint.2004.08.020.

(149) Lashkhi, V. L.; Leimeter, T.; Nemsadze, G. G.; Smirnov, K. Y.; Shor, G. I.; Evseev, A. A. Theoretical Principles of Lube Oil Qualimetry. *Chem. Technol. Fuels Oils* **2003**, *39* (4), 197–200. https://doi.org/10.1023/A:1025442213074.

(150) Pawlak Z. Role of Detergent & Dispersant. In *Tribochemistry of Lubricating Oils*; Elsevier: Amsterdam, 2003; p 25.

(151) Colyer, C. C.; Gergel, W. C. Detergents/Dispersants BT - Chemistry and Technology of Lubricants; Mortier, R. M., Orszulik, S. T., Eds.; Springer US: Boston, MA, 1992; pp 62–82. https://doi.org/10.1007/978-1-4615-3272-9_3.

(152) Singh, A. K.; Singh, R. K. A Search for Ecofriendly Detergent/Dispersant Additives for Vegetable-Oil Based Lubricants. *J. Surfactants Deterg.* **2012**, *15* (4), 399–409. https://doi.org/10.1007/S11743-011-1321-0.

(153) Abramo, I. G. P.; Blain, A.; Laurel, M.; Angeline, B.; J, N. Modified Succinimides as Dispersants and Detergents and Lubricant and Fuel Compositions Containing Same, 1996.

(154) Mekewi, M. A. Synthesis and Characterization of Antioxidants and Detergent Dispersant Based on Some Polyisobutylene Copolymers. *Mater. Res. Innov.* **2002**, *6* (4), 214–217. https://doi.org/10.1007/s10019-002-0194-2.

(155) Kotov, N. A. Layer-by-Layer Self-Assembly: The Contribution of

Hydrophobic Interactions. *Nanostructured Mater.* **1999**, *12* (5), 789–796. https://doi.org/https://doi.org/10.1016/S0965-9773(99)00237-8.

(156) Netz, R. R.; Joanny, J.-F. Adsorption of Semiflexible Polyelectrolytes on Charged Planar Surfaces: Charge Compensation, Charge Reversal, and Multilayer Formation. *Macromolecules* **1999**, *32* (26), 9013–9025. https://doi.org/10.1021/ma990263h.

(157) Cranford, S. W.; Ortiz, C.; Buehler, M. J. Mechanomutable Properties of a PAA/PAH Polyelectrolyte Complex: Rate Dependence and Ionization Effects on Tunable Adhesion Strength. *Soft Matter* **2010**, *6* (17), 4175–4188. https://doi.org/10.1039/c0sm00095g.

(158) Alechinsky, L.; Favreau, F.; Cechova, P.; Inal, S.; Faye, P. A.; Ory, C.; Thuillier, R.; Barrou, B.; Trouillas, P.; Guillard, J.; Hauet, T. Tannic Acid Improves Renal Function Recovery after Renal Warm Ischemia–Reperfusion in a Rat Model. *Biomolecules* **2020**, *10* (3). https://doi.org/10.3390/biom10030439.

(159) Heinz, H.; Vaia, R. A.; Farmer, B. L.; Naik, R. R. Accurate Simulation of Surfaces and Interfaces of Face-Centered Cubic Metals Using 12-6 and 9-6 Lennard-Jones Potentials. *J. Phys. Chem. C* **2008**, *112* (44), 17281–17290. https://doi.org/10.1021/jp801931d.

(160) Salassi, S.; Caselli, L.; Cardellini, J.; Lavagna, E.; Montis, C.; Berti, D.; Rossi, G. A Martini Coarse-grained Model of Citrate-Capped Gold Nanoparticles Interacting with Lipid Bilayers. *J. Chem. Theory Comput.* **2021**, *17* (10), 6597–6609. https://doi.org/10.1021/acs.jctc.1c00627.

(161) Bastos, H.; Bento, R.; Schaeffer, N.; Coutinho, J. A. P.; Pérez-Sánchez, G. Using Coarse-Grained Molecular Dynamics to Rationalize Biomolecule Solubilization Mechanisms in Ionic Liquid-Based Colloidal Systems. *Phys. Chem. Chem. Phys.* **2020**, *22* (42), 24771–24783. https://doi.org/10.1039/d0cp04942e.

(162) Chatzidaki, M. D.; Papavasileiou, K. D.; Papadopoulos, M. G.; Xenakis, A. Reverse Micelles As Antioxidant Carriers: An Experimental and Molecular Dynamics Study. *Langmuir* **2017**, *33* (20), 5077–5085. https://doi.org/10.1021/acs.langmuir.7b00213.

(163) Modarresi, M.; Mehandzhiyski, A.; Fahlman, M.; Tybrandt, K.; Zozoulenko, I. Microscopic Understanding of the Granular Structure and the Swelling of PEDOT:PSS. *Macromolecules* **2020**, *53* (15), 6267–6278. https://doi.org/10.1021/acs.macromol.0c00877.

(164) Zheng, H.; Wu, K.; Shi, J. Effective Enhancement of Thermal Conductivity and Electrical Conductivity with Poly(3,4-Ethylenedioxythiophene):Poly(4-Styrenesulfonate) through Solvent Treatment. *Macromol. Chem. Phys.* **2023**, *224* (2), 1–8. https://doi.org/10.1002/macp.202200305.

(165) Jain, K.; Mehandzhiyski, A. Y.; Zozoulenko, I.; Wågberg, L. PEDOT:PSS Nano-Particles in Aqueous Media: A Comparative Experimental and Molecular Dynamics Study of Particle Size, Morphology and z-Potential. *J. Colloid Interface Sci.* **2021**, *584*, 57–66. https://doi.org/10.1016/j.jcis.2020.09.070.

(166) Modarresi, M.; Zozoulenko, I. V. Why Does Solvent Treatment Increase Conductivity of PEDOT:PSS? Insight from Molecular Dynamics Simulations. *Phys. Chem. Chem. Phys.* **2022**, *7*, 22073–22082. https://doi.org/10.1039/d2cp02655d.

(167) Yildirim, E.; Zhu, Q.; Wu, G.; Tan, T. L.; Xu, J.; Yang, S. W. Self-Organization of PEDOT:PSS Induced by Green and Water-Soluble Organic Molecules. *J. Phys. Chem. C* **2019**, *123* (15), 9745–9755. https://doi.org/10.1021/acs.jpcc.9b01716.

(168) Choi, C.; De Izarra, A.; Han, I.; Jeon, W.; Lansac, Y.; Jang, Y. H. Hard-Cation-Soft-Anion Ionic Liquids for PEDOT:PSS Treatment. *J. Phys. Chem. B* **2022**, *126* (7), 1615–1624. https://doi.org/10.1021/acs.jpcb.1c09001.

(169) Guan, X.; Yildirim, E.; Fan, Z.; Lu, W.; Li, B.; Zeng, K.; Yang, S. W.; Ouyang, J. Thermoelectric Polymer Films with a Significantly High Seebeck Coefficient and Thermoelectric Power Factor Obtained through Surface Energy Filtering. *J. Mater. Chem. A* **2020**, *8* (27), 13600–13609. https://doi.org/10.1039/d0ta05324d.

(170) Volkov, A. V.; Wijeratne, K.; Mitraka, E.; Ail, U.; Zhao, D.; Tybrandt, K.; Andreasen, J. W.; Berggren, M.; Crispin, X.; Zozoulenko, I. V. Understanding the Capacitance of PEDOT:PSS. *Adv. Funct. Mater.* **2017**, *27* (28), 1–10. https://doi.org/10.1002/adfm.201700329.

(171) Wang, J.; Cai, K.; Shen, S. Enhanced Thermoelectric Properties of Poly(3,4-Ethylenedioxythiophene) Thin Films Treated with H2SO4. *Org. Electron.* **2014**, *15* (11), 3087–3095. https://doi.org/10.1016/j.orgel.2014.09.012.

(172) Ouyang, L.; Musumeci, C.; Jafari, M. J.; Ederth, T.; Inganäs, O. Imaging the Phase Separation Between PEDOT and Polyelectrolytes During Processing of Highly Conductive PEDOT:PSS Films. *ACS Appl. Mater. Interfaces* **2015**, *7* (35), 19764–19773. https://doi.org/10.1021/acsami.5b05439.

(173) Shi, W.; Zhao, T.; Xi, J.; Wang, D.; Shuai, Z. Unravelling Doping Effects on PEDOT at the Molecular Level: From Geometry to Thermoelectric Transport Properties. *J. Am. Chem. Soc.* **2015**, *137* (40), 12929–12938. https://doi.org/10.1021/JACS.5B06584/ASSET/IMAGES/LARGE/JA-2015-065846_0007.JPEG.

(174) Kim, J.; Jang, J. G.; Hong, J. I.; Kim, S. H.; Kwak, J. Sulfuric Acid Vapor Treatment for Enhancing the Thermoelectric Properties of PEDOT:PSS Thin-Films. *J. Mater. Sci. Mater. Electron.* **2016**, *27* (6), 6122–6127. https://doi.org/10.1007/s10854-016-4538-x.

(175) Fan, Z.; Li, P.; Du, D.; Ouyang, J. Significantly Enhanced Thermoelectric Properties of PEDOT:PSS Films through Sequential Post-Treatments with Common Acids and Bases. *Adv. Energy Mater.* **2017**, *7* (8), 1602116.

https://doi.org/https://doi.org/10.1002/aenm.201602116.

(176) Mochizuki, Y.; Horii, T.; Okuzaki, H. Effect of PH on Structure and Conductivity of PEDOT/PSS. *Trans. Mater. Res. Soc. Japan* **2012**, *37* (2), 307–310. https://doi.org/10.14723/tmrsj.37.307.

(177) Kan, E. A Multiscale Modeling Approach to Understand Mechanism of Deposit Control by Lubricant Detergents and Dispersants, Middle East Technical University, 2022.

(178) Sarpal, A. S.; Sastry, M. I. S.; Bansal, V.; Singh, I.; Mazumdar, S. K.; Basu, B. Correlation of Structure and Properties of Groups I to III Base Oils. *Lubr. Sci.* **2012**, *24* (5), 199–215. https://doi.org/https://doi.org/10.1002/ls.1172.

(179) Rossi, G.; Monticelli, L.; Puisto, S. R.; Vattulainen, I.; Ala-Nissila, T. Coarse-Graining Polymers with the MARTINI Force-Field: Polystyrene as a Benchmark Case. *Soft Matter* **2011**, *7* (2), 698–708. https://doi.org/10.1039/c0sm00481b.

CURRICULUM VITAE

Surname, Name: Özdemir, Erhan

EDUCATION

Degree	Institution	Year of Graduation
MS	METU Chemistry	2013
BS-MS	METU Chemistry Education	2010
High School	Şehitler Science High School, Yozgat	2004

FOREIGN LANGUAGES

English

PUBLICATIONS

1. Aydemir U., Ugur E., Ermis C., Aydemir F. N., Ozdemir E., Banerjee S., Yildirim E., Akdag A., Erel-Göktepe I. " Boron Cage Triggered Micellization of a Neutral–Cationic Block Copolymer and Preparation of Boron-Containing Layer-by-Layer Microparticles", ACS Applied Polymer Materials, 4(5), 3448-3461 (2022)

2. Özdemir, E., Kan, E., Guo, B.. Pashkovski, E., Agiral, A. Yıldırım, E. "A Multiscale Modeling Approach to Understand Mechanism of Deposit Control By Sulfonate Based Lubricant Detergents", In Preparation.